Effect of Leading Edge Blowing for Aerofoil Subjected to Laminar and Turbulent Inflows

A thesis submitted for the degree of

Doctor of Philosophy

Yasir Al-Okbi

College of Engineering, Design and Physical Sciences

Brunel University London

Uxbridge, UB8 3PH

United Kingdom

2020

I. Abstract

The aim of this thesis is the investigation on the aerodynamic performance, flow pattern and aeroacoustics of a NACA65(12)-10 aerofoil with different straight blowing as an active flow-control device and serrated leading edges as a passive flow-control device leading edges at high and low turbulent flow. Aerofoil subjected to leading edge blowing can be regarded as one of the effective flow control approaches that can harvest multiple benefits. In this thesis, small orifices are implemented at the leading edge of an aerofoil to facilitate injection of mass flow against the incoming flow with low and elevated freestream turbulence intensities. The aeroacoustics investigation reveals that the largest level of reduction in the turbulence–leading edge interaction noise is associated with a larger concentration of orifices per unit span before reaching a critical velocity, whilst a lower concentration of spanwise orifices is more desirable after the critical velocity. There also exists an optimal blow rate to tackle this particular noise source.

It is envisaged that leading edge blowing, an active flow control approach, could produce the same mechanisms as those produced by a serrated leading edge to enhance the aerodynamic and aeroacoustic performances of aerofoil.

It is interesting to note that the effective margin of the leading edge blowing volume flow rate is so narrow that small variation in Q' from the most optimised value would produce a large difference in the noise performance. The concept of the leading edge blowing is to minimise the interaction of an incoming turbulent flow with the leading edge of the aerofoil. Through blowing, the leading edge jet continuously opposes, and possibly dissipates the incoming turbulent eddies by either displacing the leading edge stagnation point of the aerofoil, or creating a “buffer zone” over the region around the aerofoil leading edge. It seems that one, or possibly both of these mechanisms could be very sensitive to the blowing volume flow rate, which

is related to the exit jet velocity. Although not shown here, ΔPWL as high as 9 dB can be achieved by one of the leading edge blowing configurations.

NACA 65(12)-10 was chosen as the baseline aerofoil in this experimental study. Four types of serrated leading edge in different combinations of serration wavelength λ and amplitude A, as well as straight leading edge with different blow rates Q' and spanwise air hole spacing λ', were investigated. Based on the results so far, there exists an explicit relationship between the A and Q', as well as λ and λ' for the aerodynamic lift and drag coefficients across a wide range of angle of attack, it is improved the stall angle and larger lift coefficient. However, at the post-stall regime, the most effective configuration switches back to the one with larger concentration of orifices per unit span.

Additionally, active and passive flow control techniques for serrated-blowing (Hybrid) leading edge designs with superior aerodynamic or aeroacoustic performance with the influencing a number of serrated-blowing leading edge devices were implemented.

For high turbulent intensity and the serration-blowing leading edge is clearly beneficial, with a significant reduction in the turbulent broadband noise, up to 4 dB in some cases with the influencing factors blowing rate (Q'=0.5-4.5 liter/min) and the sound power level reduction of the noise up to 3.7 dB for low turbulent intensity. The sound reduction involves the elimination of tonal effects. Thus, a noise reduction jump from 12 dB in elevated turbulent instances to 33 dB in the case of low Tu compares with basline case. Through noise and velocity measurements close to the leading and trailing edges of an aerofoil, the reduction of the noise is found to be primarily caused by the serration geometry. The new serrated-blowing (hybrid) leading edges have the potential to enhance serration technology's industrial worthiness in obtaining low noise radiation.

II. Acknowledgments

First of all, I would like to express my genuine appreciation to my supervisor, Dr. Tze Pei Chong, for his continued support and assistance of my Ph.D. study and for sharing with me his research, patience and enormous expertise. His advice and encouragement assisted me conduct my research, write this thesis and overcome the problems I encountered during my Ph.D. study. I couldn't ask for a stronger supervisor and mentor for my research.

I would also like to thank the research fellow, Dr. Seyed Mohammad Hasheminejad, for his support, feedback, friendship and cooperation. My sincere thanks go to Assistant Professor. Oksana Stalnov for his assistance and valuable comments in the first stage of my reaserch.

I would like to acknowledge the financial support provided by Prime Minster office of Iraq and through The Higher Committee of Education Development in Iraq in support of my Ph.D.

I would also like to thank the PhD students and friends Auris Juknevicus, Jonne Jeyalingam and Chioma Muhammad for their amazing support and company during my time at Brunel University.

I would like to thank William, Michael and Kevin Robinson for their technical support and advice in the laboratories.

Finally, I am likewise grateful to my office mates and best friends, Dr. Ahmed Almurshedi and Mr. Ali Aldujaili who stood beside me through the hardest times during my study. They are the perfect instances of true friends.

I would like to thank my family with all my heart for supporting me spiritually through my life in general and my study. I donate this thesis to my parents, Mrs. Najiyah for their everlasting faith. I am very grateful to my brother son Hussein Mohammed and my son , Ahmed, for inspiring me with their care and love.

To my wife, Mrs. Rana Al-dujele, words are inadequate to express my appreciation to and feelings for you. Thank you for your enduring love, for having believed in me long when I lost faith in myself and for your patience. Praise be to God for your presence in my life.

III. Author's Declaration

I hereby declare that the research contained in this thesis has not been submitted for any other prize and is my own work. I also confirm that this work fully acknowledges the opinions, ideas and contributions of other individuals/works.

Signature:

Yasir Al-Okbi

IV. Publications Work

- **Yasir Al-Okbi**, Tze Pei Chong, Seyed Mohammad Hasheminejad ‘’ Effect of Straight and serrated-Leading Edges Blowing for Aerofoil Subjected to High and Low Turblent Intensity.” AIAA Journal, under preparation ,2019.
- **Yasir Al-Okbi**, Tze Pei Chong, Oksana Stalnov ‘’ Mimicking the serration effects on aerofoil by leading edge blowing.” AIAA/CEAS Aeroacoustics Conference, Atlanta, Georgia,USA, 2018.
- **Yasir Al-Okbi**, Tze Pei Chong, Seyed Mohammad Hasheminejad ‘’ Effect of Leading Edge Blowing for Aerofoil Subjected to Laminar and Turbulent Inflows at Low Reynolds Numbers.” 54th 3AF International Conference on Applied Aerodynamics, Paris, France, 2019.
- **Yasir Al-Okbi**, Tze Pei Chong ‘’ Aerodynamic Performance Enhancement and Study Technique for Thermochromic Liquid Crystal Temperature Measurements on Aerofoil.” Poster conference in Brunel University, London, UK, 2017.
- **Yasir Al-Okbi**, Tze Pei Chong ‘’ Aerofoil noise reduction by leading edge treatments.” Poster conference in Brunel University, London, UK, 2018.
- **Yasir Al-Okbi**, Ahmed Almurshedi, Tze Pei Chong ‘’ Shear Strength and Behaviour of Pentagonal Flange Beams with Web Openings.” Young researcher conference, London, UK, 2019.
- **Yasir Al-Okbi**, , Tze Pei Chong ‘’ Effect of Straight and Serrated Blowing Leading Edges for Aerofoil Subjected to Laminar and Turbulent Inflows”. First Annual Research Students Conference, Brunel University London, UK, 2019.

V. Table of Contents

VI. List of Figures

VII. List of Tables

VIII. Nomenclature

a	Mean-line loading designation	**[-]**
a_0	Lift force aft zero reading	[N]
A	Amplitude of serrations	[mm]
A_u	Lift force aft (uncorrected)	[N]
C	Chord length	[m]
CD	Drag coefficient	[-]
CD_u	Uncorrected drag coefficient	[-]
CfL	Lift coefficient in frictionless flow	[-]
CL	Lift coefficient	[-]
CLu	Uncorrected lift coefficient	[-]
Cp	Static pressure coefficient	[-]
d	Distance between hot wire probe an aerofoil surface	[m]
d_{GRID}	Mesh bar diameter	[m]
d_0	Drag force fore zero reading	[N]
D	Drag force	[N]
D_u	Drag force fore (uncorrected)	[N]
f	Frequency	[Hz]
F_u	Lift force fore (uncorrected)	[N]
f_0	Lift force fore zero reading	[N]
h	Test section height	[m]
h_{GRID}	Grid height	[mm]
k^2	Yaw-coefficient	[-]
K_x	Normalised streamwise wavenumber	[-]
K_η	Constant factor	[m^{-1}]
L	Lift force	[N]
m_{GRID}	Mesh size of grid	[mm]
pi	Static pressure measured at location i	[Pa]
p∞	Atmospheric pressure	[Pa]
ps	Static pressure	[Pa]
P	Pressure [kPa]	
pt	Total pressure	[Pa]
p	Sound pressure	[Pa]
Rec	Chord based Reynolds number	[-]
Rspecific	Universal gas constant	[J kg^{-1} K^{-1}]
R0	Sensor resistance at ambient temperature	[Ω]
Rw	Sensor resistance at operating temperature	[Ω]
S	Surface area baseline leading edge	[m^2]
Sm	Surface area serrated leading edge (measured)	[m^2]
t	Aerofoil thickness	[m]
T	Temperature	[K]
U_∞	Free stream velocity	[m/s]
w_{GRID}	Grid width	[mm]
U_o	Jet velocity	[m/s]

y	Vertical displacement of Aerofoil tip	[mm]
u', v'	Ensemble-averaged rms velocity fluctuations	[m/s]
α	Angle of attack	[°]
α_0	Temperature coefficient of resistance	[%/C]
$\Gamma(x)$	Gama function	[-]
Δ	Absolut difference	[various]
k_e	Wavenumber	[m^{-1}]
ε_{sb}	Solid blockage correction factor	[-]
ε_{wb}	Wake blockage correction factor	[-]
η	Dynamic fluid viscosity	[kg m^{-1} s^{-1}]
δ	Boundary layer thickness	[mm]
δ^*	Boundary layer displacement thickness	[mm]
λ	Wavelength of serrations (also W)	[mm]
λ_2	Body shape factor	[-]
Λ_{uu}	Spanwise integral length scale	[mm]
ρ	Fluid density	[kg m^{-3}]
$\emptyset_{uu}^{VK}(\omega)$	Longitudinal power-density spectrum Von Karman	[dB/ Hz]
$\emptyset_{uu}^{L}(\omega)$	Longitudinal power-density spectrum Liepmann	[dB/ Hz]
ω	Angular frequency	[rad/s]
Q	Mass flow rate	[liter/min]
Q'	Blow rate per hole	[liter/min]
λ'	Spanwise spacing of the orifice	[mm]
θ	Angle of the microphone array	[°]

List of Abbreviations

ACARE	Advisory Council for Aeronautical Research
A/D	Analog to Digital converter
BNC	British Navy Connector
AoA	Angle of Attack
AGI	Airfoil Gust Interaction
BSLN	Baseline (straight leading edge)
CTA	Constant Temperature Anemometer
HWA	Hot-Wire Anemometry
ISAVE	Institute of Sound And Vibration Engineering
ISVR	Institute of Sound and Vibration Research
LE	Leading Edge
LES	Large Eddy Simulation
N	Number of samples
NACA	National Advisory Committee for Aeronautics
Re	Reynolds number
Re_c	Chord based Reynolds number
RMS	Root Mean Square
RPM	Rounds Per Minute [min^{-1}]
SLS	Selective Laser Sintering

PWL	Sound Power Level [dB]
SR	Sampling Rate
T	Sampling Time
TCR	Sensor Temperature Coefficient
TE	Trailing Edge
Tu	Turbulence Intensity
NX9.0	Siemens PLM software
OAPWL	Overall sound power level, dB
PIV	Particle Image Velocimetry
RANS	Reynolds Averaged Navier Stokes
TS	Tollmien-Schlichting waves/ instabilities
TS	Integral Time Scale (see also t_L) [ms]

Chapter 1 : Introduction

1.1 Background

The impact of man-made noise sources has become a major concern among the ever-growing global population. Aircraft, helicopters, and all types of air transport are required to comply with certain noise standards. Moreover, renewable energy sources like wind power, which is an important theme in recent political trends, has been suffering from issues of aerodynamic noise radiation. This environmental problem has become a major obstacle to achieve greater proliferation of onshore wind turbines.

Millions of people in Europe are affected by noise pollution every day. A high level of industrialisation and a strong demand for transportation lead to an inexorable increase in noise emissions. With the growing aircraft industry and the use of new sources of energy like wind turbines, regulations on environmental pollution, especially in terms of fuel emissions and noise, arise continuously. Aerodynamic sound generation from surfaces that rotate as propulsive devices (e.g. rotors or fan blades) are recognised as one of the main sources of aircraft-related noise.

Political and industrial regulations and guidelines have emerged demanding a reducion in aviation-related air pollution, which was one of the targets of the EU's 7th Environment Action Programme [1]. The Advisory Council for Aeronautical Research published a report to reduce noise levels by 50% from their 2000 level through to 2020 [2]. The European Commission set targets to reduce aircraft noise emissions by 65% in the Flight Path 2050 programme [3]. In addition, renewable sources of energy, such as wind power, are an increasingly important political topic. However, wind turbine noise is the main drawback to more widespread applications. The aerodynamic noise from the blades is generally considered to be the predominant noise source, as shown in Figure 1-1. A 3-blade wind turbine with a rotor diameter of 58 m was measured for acoustic field measurements to characterize the source of noise and to check whether the trailing edge sound from the turbines was controlled. One blade was cleaned, one blade was tripped, and one blade stayed untreated to evaluate the influence of blade roughness. A big horizontal microphone array was used to assess the allocation the sources of noise in the rotor plane and on the individual blades, placed around one rotor diameter upwind from the turbine. The results of the array reveal that in addition to a minor source at the rotor hub, basically all noise (radiated to the ground) is generated during the blades ' downward movement. This highly asymmetric source pattern can be described by convective amplification and direction of trailing edge noise. The noise is generated in the external part of the blades, but not the very tip.

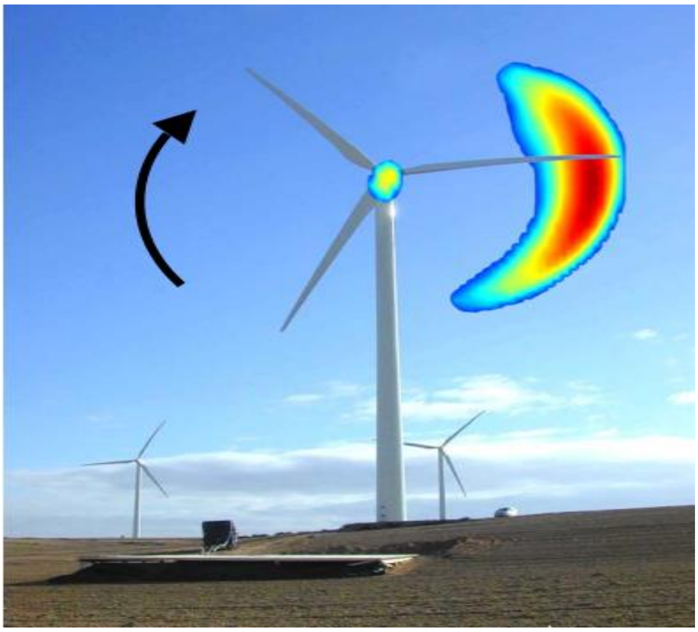

Figure 1-1: Wind turbine with microphone array platform of the noise sources in the rotor plane (averaged over some rotations) [4].

New technologies and approaches are needed to reduce the emitted aerofoil sound and achieve the future goals set by the European Commission, supporting the wind turbine and aviation industries. Since nature has always inspired human achievements and has led to effective systems, materials, structures and other benefits, scientists are trying to adopt mechanisms from nature to the fields of aerodynamic and aeroacoustics. The study of bio-inspired technologies, known as biomimetics, was first examined extensively by Schmitt [5]. He defined biomimetics as the study of the functions of biological systems as models for the design and engineering of materials and machines.

Many recent studies related to the aerodynamics and aeroacoustics of investigated the silent flight of the owl and tried to transpose similar mechanisms to aerofoil geometry. The wings of an owl are equipped with wavy comb-type leading edges and fringe type trailing edges, which can reduce the flow-induced noise (Figure 1-2). Galvez [6] concluded that the sound pressure level difference, compared to non-silently flying birds, is significant at medium and high frequencies.

Both the geometrical modification of the aerofoil leading edge and trailing edge are of high interest in ongoing research. The application of leading edge undulations is also due to another inspiration from nature.

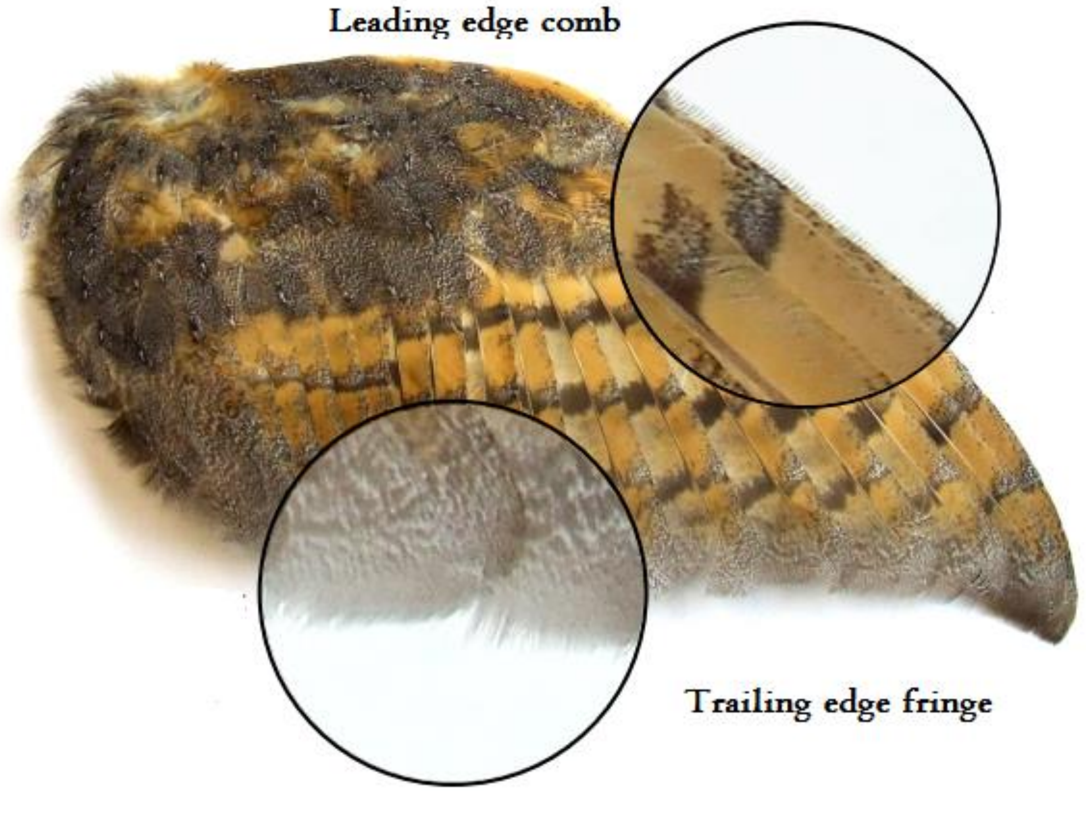

Figure 1-2: Barn owl wing [6].

The stall-delaying properties of the humpback whale flipper have been observed and quantified, both experimentally and numerically. Fish et al. [7] undertook a detailed study to understand the mode of operation of the tubercles and suggested that they may act as a passive flow-control device, delaying the stall angle. The tubercles on the leading edge of the flipper can be described as rounded protuberances that alter the flow-field. Figure 1-3 shows humpback whales' flippers with undulations on the leading edge. The mechanism behind these undulations can be compared to that of a vortex generator, whereby the boundary layer is reenergised. As a result, the application of "leading edge" tubercles for passive flow-control has potential in the design of wind turbines, and may be particularly appropriate for wings at a high angle of attack. The maintenance of lift at high angles of attack leads to enhanced performance and manoeuvrability. However, leading edge undulations can also be applied to reduce aerofoil gust interaction noise, whereby the free stream turbulence interacts with the aerofoil leading edge, and thus leads to broadband noise radiation. In the context of this work, the focus is on the aerodynamic mechanism and the aeracoustics of different "leading edge" configurations subjected to laminar and turbulent flow.

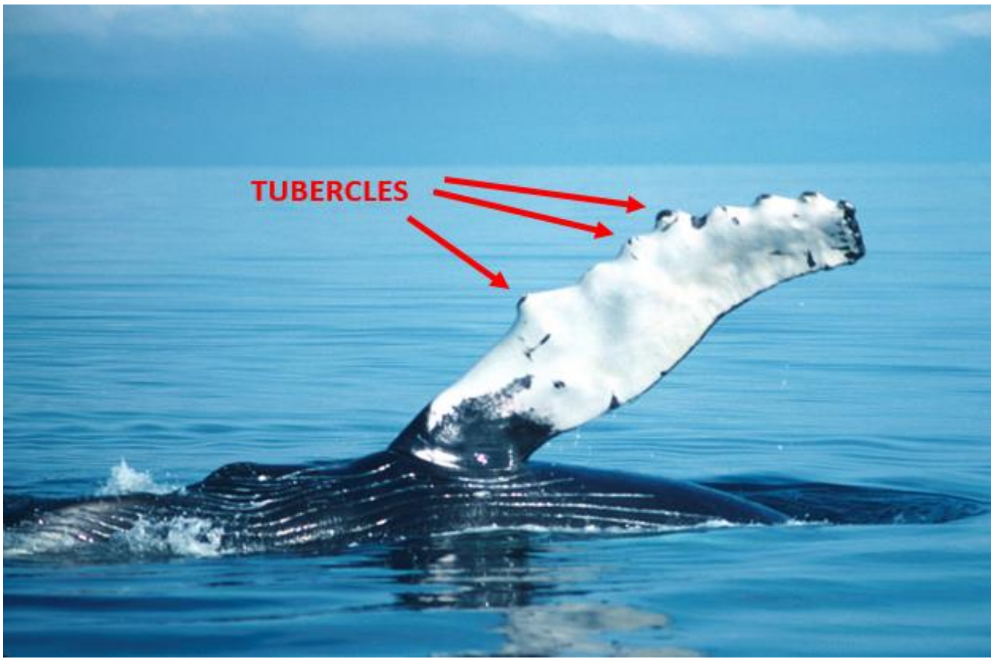

Figure1-3: Humpback whale filppers showing the leading edge with tubercles [8].

The continual increase in air traffic and expansion of airport facilities and associated infrastructure creates strong political commitment to reducing noise pollution (among other impacts) from the aviation industry, posing major design challenges. As a result, many airplane and aero-engine manufacturers are prioritising efforts to reduce airplane and turbomachinary noise.

Noise related to the hydrodynamic interaction between the incoming turbulent flow and the leading edge of fan blades is of particular interest. This mechanism is perhaps the most relevant at the rotor-stator stage of the aero-engine, where the wake generated from the upstream rotor impinges on the downstream stator (or the outlet-guided-vanes OGV) to radiate the broadband interaction noise. Currently, the fan is the main source of noise for an approaching turbofan engine.

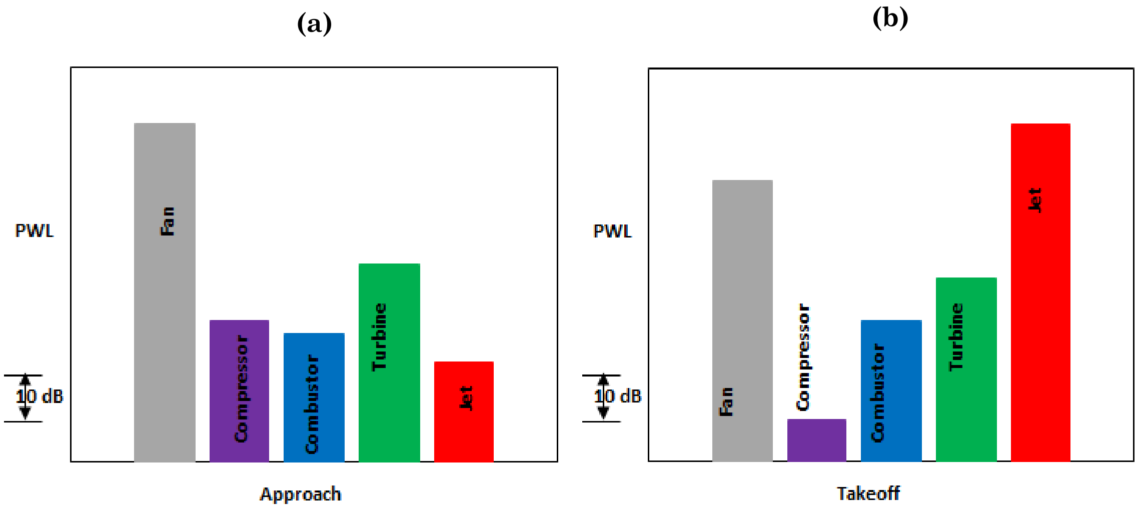

Figure 1-4: Relative sound power levels of noise sources at (a) approach and takeoff (b) in modern aircraft engines [9].

The relative noise contribution by the major components of a modern engine to a takeoff and approach condition is illustrated in Figure 1-4 [9]. Fan noise at takeoff is as important as jet noise, and is clearly dominant at the approach.

The analytical work by Amiet et al. [10] describes the turbulence–leading edge interaction noise ϕ, as a function of angular frequency ω, as:

$$\phi(\omega) = \frac{2b}{\pi c}\left(\frac{2\Lambda_{uu}}{3\pi R}\right) Tu^2 \rho_0^2 U_0^4 \left[\frac{\Gamma\left(\frac{1}{3}\right)}{\Gamma\left(\frac{5}{6}\right)}\right]^2 \frac{\widehat{K}_x^2}{\left(1+\widehat{K}_x^2\right)^{\frac{7}{3}}}\, exp\left(\frac{-\omega \cdot d}{2U_0}\right) \tag{1-1}$$

where Λuu is the longitudinal integral length scale of the turbulence, Tu is the turbulence intensity, Uo is the velocity, $\Gamma(x)$ is the gama function, R is the observer distance, b the aerofoil semi-span, d is the airfoil thickness and $\widehat{K}_x =$

$\frac{k_x}{k_e}$ is the normalised longitudinal wavenumber where $k_x = \frac{\omega}{U_0}$ and $k_e = \frac{\sqrt{\pi}}{L} . \frac{\Gamma(\frac{5}{6})}{\Gamma(\frac{1}{3})}$. From this expression, apart from the aerofoil geometry and physical configuration, the level of the interaction noise can be governed by the external factors in flow, such as the longitudinal turbulence length scale and the turbulence intensity.

Inspired by the ability of owls to hunt with acoustic stealth, there is now great interest to reproduce the features of owl's wings in aircraft, centring on three phenomena: The First, the "leading edge" (primary feathers on the owls' wings) is serrated. Second, the trailing feathers on the back end of the wing are tattered. And third, the rest of the owls' wings are covered in velvety feathers. It is believed that the "leading edge" serrations are responsible for the reduction of the "leading edge" noise. When the "leading edge" of a blade is undulated, it can affect the acoustical response with the incoming turbulent flow. Many studies have already been performed on the effect of "leading edge" serrations on broadband noise. In a joint experimental-numerical investigation by Clair et al. [11] on the "leading edge" interaction noise of a NACA 65(12)-10 aerofoil, the wavy "leading edge" was found to achieve noise reduction between 3–4 dB.

Narayanan et al. [12] performed a fundamental study to assess the effects of a serrated "leading edge" on the interaction noise characteristics of a flat plate and an aerofoil. A nearly isotropic turbulence was produced using mesh grid positioned inside a nozzle. They demonstrated significant noise reduction of 5–8 dB, with the largest noise reduction being achieved with a flat plate configuration. The level of broadband noise reduction was a strong function of the serration amplitude (i.e. the distance between the peak and trough), and less sensitive to the serration wavelength (the distance between successive peaks).

Many studies used high-fidelity numerical flow simulation to provide physical insights into the noise reduction mechanisms by serration [13, 14]. These studies found that the surface pressure fluctuation and the far field noise on a serrated "leading edge" are de-correlated by the serrated "leading edges". In particular, the noise source at the mid-region of the oblique edge becomes ineffective across the mid- to high-frequency range. The serration could cause a significant decrease in the surface pressure fluctuations around the tip and mid-regions of the serration, and subsequently reduce the broadband noise level. Another noise reduction mechanism is attributed to the phase interference and destruction effect between the serration peak and the mid-region of the oblique edge. Accordingly, the serration root could still remain effective in the noise radiation.

Aerodynamically, work performed by Fish et al. [7] showed that the humpback whale benefits from tubercles along the "leading edge" of its flippers (similar concept as a serrated leading edge), enhancing its maneuverability by delaying flow separation. Despite the delayed aerodynamic stall and improved post-stall lift performance, the serrated leading edges also reduce the maximum lift coefficient and increase the drag coefficient, resulting in lower lift-to-drag ratio. Johari et al. [15] performed experimental evaluation of the effects of various wavelength and amplitude configurations on the aerodynamic force characteristics of a full-span NACA 634-021 aerofoil at a Reynolds Number of 1.83 x10^5. Despite the increased post-stall lift up to 50%, serrated leading edges also produce a reduction in both stall angle and lift coefficient, as well as a significant increase in drag coefficient.

Miklosovic et al. [16] replicated several aerofoil models with tapered wing possesses having similar aspect ratios to the humpback whale flipper, and measured the lift and drag coefficients in a wind tunnel. They described an increase above the baseline configuration of the maximum lift coefficient by 6% and a delay of the stall angle by about 40% for the flipper model with the bumps. The consensus of the serrated "leading edge" is that, though the stall angle and the maximum lift coefficient can be increased by an optimised serrated-configuration, the lift coefficients at the pre-stall regime will be lower than those produced by an unmodified, baseline "leading edge". The momentum exchange as a result of mixing between the streamwise vortices and the boundary layer is regarded as one of the main enhancement mechanisms to prevent or delay stall and improve the post-stall recovery and performance. The streamwise vortices in the form of counter-rotating pairs are predominantly generated at the troughs of the serration as a direct consequence of the serration geometry [17]. Skillen et al. [18] highlighted that secondary flow can be induced by the spanwise pressure gradient, where near-wall low-momentum fluid is transported away from the serration peak towards the trough. Conversely, high-momentum fluid from the freestream is drawn to re-energise the boundary layer downstream of the serration peaks. Hansen et al. [17] focused on the evolution of vorticity near the serration troughs, where they observed that the external pressure force transforms the initial vorticity near the "leading edge" into pairs of counter-rotating streamwise vortices via a three-dimensional process (comprising stretching, tilting, and diffusion).

The discussion above concerns the aeroacoustic and aerodynamic performance of aerofoils with serrated "leading edge" acting as a simple and effective passive flow control device. A question worth exploring is whether the underpinning physical mechanisms can be replicated by a completely different flow control approach. More specifically, active flow control has the advantage of being versatile, as the flow condition can change considerably over a short period of time, and producing minimal parasite drag when implemented in an aerofoil system.

The analytical solution of Amiet [10] provides a relationship between the level of "leading edge" noise radiation on one hand, and the incoming flow turbulence intensity and integral length scale on the other. One avenue to reduce the "leading edge" noise, therefore, is to weaken the fluid-structure interaction. Leading edge blowing is an attractive method to achieve this objective because the injection of mass flow from the "leading edge" (against the incoming flow) could potentially decrease the turbulence intensity, and hence the level of noise radiation. Depending on the blow rate of the leading edge jet, once mixed with the incoming flow it can be entrained and propagated as the streamwise vortices in the downstream direction along the aerofoil surface. These streamwise vortices are generated indirectly as a result of the “leading edge” blowing, and are similar to those produced by a serrated leading edge.

1.2 Classifications of Flow Control

The energy consumption of flow control device is the major specification to be considered for the purposes of this thesis. If no additional power input is required, the device is classified as passive; in contrast, it is classified as active when additional energy is required for operation. Changing the aerofoil geometry or adding non-moving elements on the aerofoil surface achieves passive flow control, while active flow control includes the use of additional energy in operating devices, such as actuators. Active flow control techniques offer different advantages in terms of performance over passive flow control methods. These include switching on and off, increased adaptability to changing flight conditions, capacity to target specific instabilities, and less drag. However, the execution of active control is often more complicated and expensive than passive control, due to manufacturing-related problems of complexity and maintenance. There are some examples of the successful transfer of active flow control techniques from laboratory models to full-scale applications [19]. Therefore, research into the viability of passive flow control devices remains relevant for modern design, as these devices are generally more reliable and economically viable to implement.

Another useful classification is whether the flow control device has been designed to improve lift or reduce drag, which is often directly related to applications for aerofoils. In order to increase the lift generated by an aerofoil, the shape can be modified, the flow orientation can be changed, the tip stall can be minimised, or the flow attachment and circulation can be improved. Generally speaking, the lift can be improved by increasing the wing area, the angle of attack, the camber, the increase in circulation, and the exchange of momentum in the boundary layer. Furthermore, the lift can be improved by minimizing or avoiding the tip stall and prolonging the flow attachment to the suction surface.

Flow control techniques for drag reduction aim to reduce the most important drag component. The principal drag components for subsonic flows are the formed drag, induced drag, and skin friction drag. Some drag reduction methods for subsonic flow focus on the avoiding / delaying of the flow separation (form drag); and decreasing spanwise flow (caused drag); avoiding / delaying the transition towards turbulence (skin friction drag), decreasing the consistency of turbulent structures (skin friction drag) and producing favourable contact with turbulent fluctuations of skin friction drag.

1.3 Passive Techniques

The aerofoil profile shape optimisation includes flow control without spanwise differences in the aerofoil geometry, which precludes performance-improving attachments. Circulation increase includes flow control methods that enhance the flow movement around the aerofoil. An improved momentum exchange in the boundary layer can delay flow separation, thus allowing operations at high angle of attack to increase the maximum lift coefficient before stall. This mechanism is responsible for the performance improvements observed for serrated aerofoils. Other methods can be used to achieve separation delays, including the variation of pressure gradients or the provision of a barrier that restricts the movement of the separation line to the leading edge. Restriction spanwise flow is an important goal where there is a risk of a tip stall. The transition delay is intended to ensure a laminar boundary layer formal is maintained, and to reduce the skin friction drag for as long as possible. When the turbulent boundary layer exists, drag reduction methods involve reducing turbulent fluctuations.

1.3.1 Lift Improvement

1.3.1.1 Optimisation of Aerofoil Profile Shape

The traditional method of optimizing the lift performance involves changing the aerofoil design. In general, if the wing has a greater camber and chord length in a given angle of attack and span, the generate a lift will be greater. Furthermore, a laminar boundary layer is sometimes associated with reduced skin friction drag, the delayed transition approach is therefore required in such cases. Aerofoil with the maximum thickness can be designed to position at as far aft as possible [20]. The contouring of aerofoil must also be carefully designed in accordance to the minimum pressure point, to ensure transition rather than separation [21]. The advantages of changing aerofoil design should generally be weighed against the disadvantage of off-design performance degradation.

1.3.1.2 Momentum Exchange or Separation Delay

Vortex generators are small rectangular or delta wings used to delay separation and stall, as shown in Figure 1-5. These devices extend in the chord direction and conventionally have the same height as the boundary layer's thickness [22]. In recent years, it has been shown that devices with a height of approximately 10 percent of the thickness of the boundary layer can still prove to be quite effective [22, 23].

Depending on the orientation of the device, the vortex generators may protrude into the boundary layer and have discontinuities. These can create counter- or co-rotating vortices, which encourge the momentum exchange in the boundary layer, resulting in an effective mixing region of more than three times the height of the device at some distances downstream [24]. It has been reported that vortex generators decrease the intensity of acoustic disturbances in the wake region tonal noise by suppressing the formation of the Kármán vortex [25]. Vortex generators have the advantages of being simple, robust, and cheap.

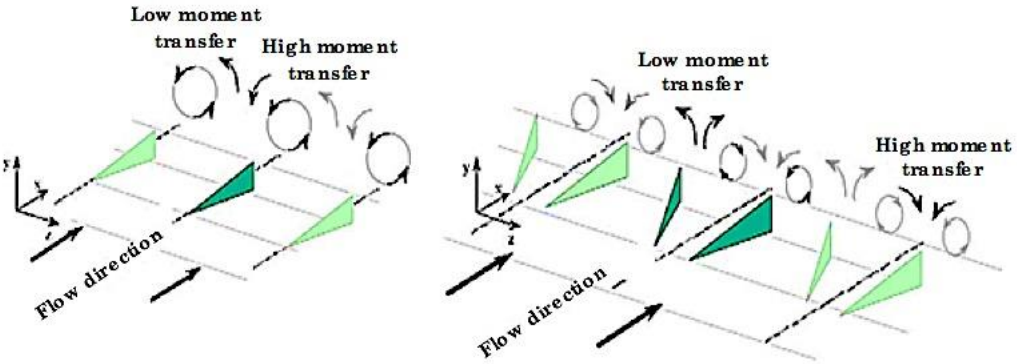

Figure 1-5: Two vortex generators, passive device (left) co-rotating and (right) counter-rotating configurations (reproduced from Kuethe) [25].

However, in situations where stall suppression is not necessary, such as cruise, they can increase parasitic drag. Most aeroplanes are fitted with vortex generators as a standard part of their initial manufacture, but vortex generators can also be retrofitted to existing designs.

Another way to generate counter-rotating streamwise vortices on the suction on an aerofoil is by placing small serrations on the pressure surface slightly in front of the stagnation point [26], as shown in Figure 1-6. While the serrations are located on the aerofoil's pressure surface, they actually affect the flow through the suction surface, as the stagnation point is known to move downstream at the pressure surface as the angle of attack increases. In addition, performance improvements by somthings are related to the

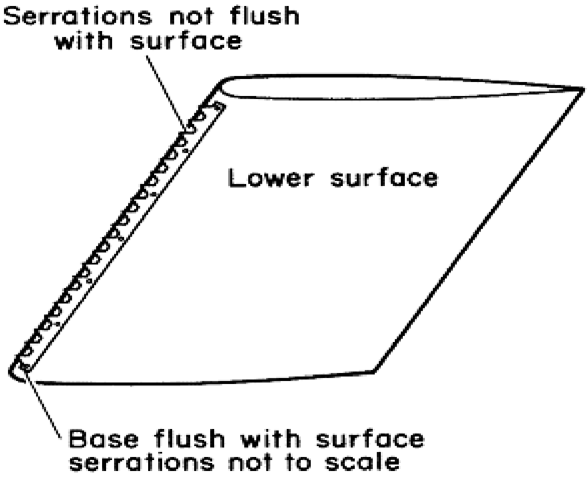

Figure 1-6: Serration leading edge [26].

increased maximum lift coefficient with negligible drag influences at low angles of attack, and decreased drag at high angles of attack [26].

It was also found that the greatest improvements are achieved when the smallest wavelength serrations are placed as close as possible in front of the stagnation point. In addition, the size, position, and spacing of the wavelength were noted as important parameters. leading edge extensions or strakes (the aerodynamic surface usually installed on the fuselage of an airplane acting as big vortex generators) are little influenced by airplane performance in cruising conditions; on the other hand, at moderate to high angles of attack each extension of the “leading edge” begins to produce a high-swirl vortex, as shown in Figure 1-7, which helps to maintain the flow attachment to the upper surface of the wing (At a high angle of attack, the vortex core deformation produced by the fence is less apparent than at a lower angle of attack). The vortex breakdown happens in the area of the fence location at an angle of attack, and the fence does not influence the form of the vortex core upstream of the breakdown [27], allowing the wing to make a lift past the expected stall angle. The penalty associated with “leading edge” extensions is that the process of vortex bursting can occur, which can cause structural damage to the airplane tail section [28], and wing rock, due to the high degree of flow instability.

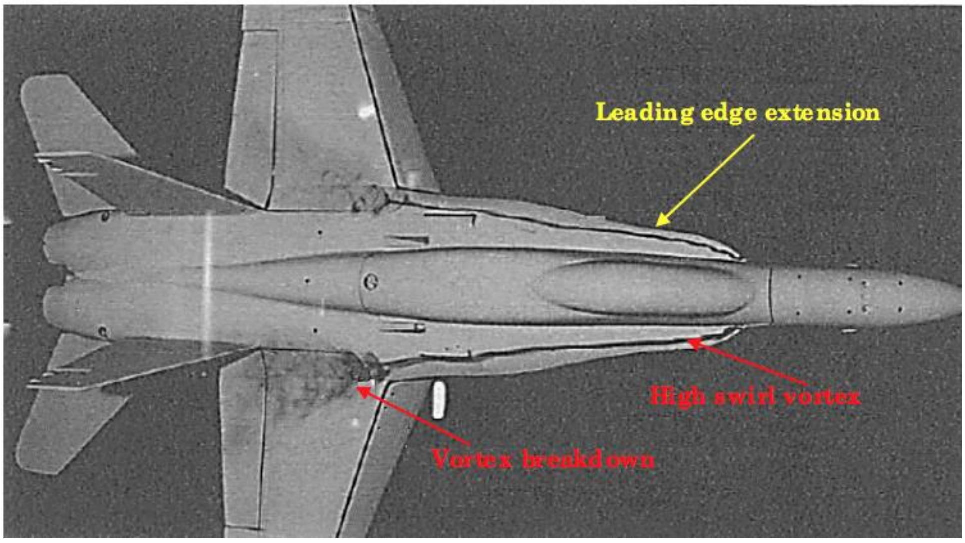

Figure 1-7: Diagram of flow visualization patterns near extension leading edge [27].

For a turbulent boundary layer, there is greater momentum exchange with the freestream flow, and therefore less likelihood of separation when the boundary layer meets an adverse pressure gradient [29]. This can be obtained by using a turbulator, that often takes the shape of a slim raised tape, as shown in Figure 1-8.

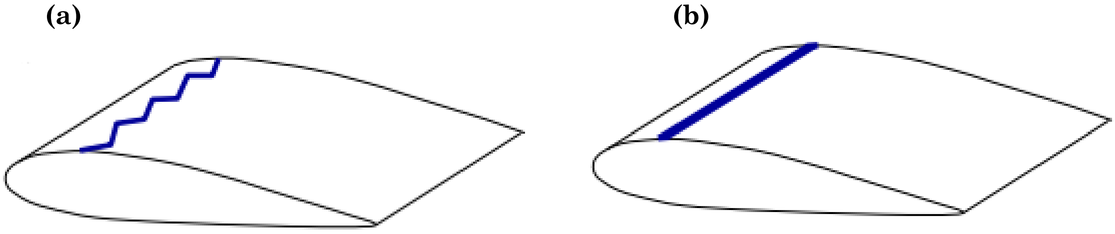

Figure 1-8: illustrates (a) Zig zag trip tape turbulator, (b) Straight trip tape turbulator.

Turbulators can also be developed using distributed roughness components. The drag at cruise is increased by turbulators (A typical mechanical turbulator is a tripe tape, attached to the surface of the aerofoil. The location of the tape in accordance with the form of the airfoil), relative to the laminar boundary layer (where drag is minimal if the system is well executed), plus the skin friction drag increases at the turbulent boundary layer.

Hence, the height and location of turbulators are essential parameters to be optimized in order to ensure their success. Separation delay can also be achieved when the pressure gradients on the aerofoil surface are altered. This happens when a ribbed trailing edge is integrated into the aerofoil (The fabric between the ribs of full-scale aircraft is pulled upwards by the reduced pressure range on the upper aerofoil surface, the rib idea enabled the smooth variation and continuous in camber along the aerofoil span, decreasing drag and improving lift at any specific step of the flight task). In this case, the serrations are perpendicular to both the freestream flow and the aerofoil chord as shown in Figure 1-9. The aerofoil waviness is thought to be small but important lateral pressure gradients directly related to a bifurcation line somewhere between the trough and the peak, with a low momentum boundary layer of fluid on the suction surface [30].

Furthure details are provided in section 2.4.3. Experiments have shown that the maximum lift coefficient and stall angle can be increased with a minimum drag penalty using this particular device [30]. In comparison to the conventional wings at 0° angle of attack, [31], found significant variations in the structure of boundary layer sublocted to serrated edges. The transition from laminar to turbulent was 30 percent further downstream than that of a trough for the peak. Furthermore, there were no separation bubbles at these locations in the flow over humps, and the separation bubble was confined to the troughs. as shown in Figure 1-9. It was concluded that a serrated wing could support a higher adverse pressure gradient than an unmodified wing, and thus improve the aerodynamic performance [31]. The observation that the covering feathers on the suction surface of their wings rise when birds land was inspired by a further method of separation delay.

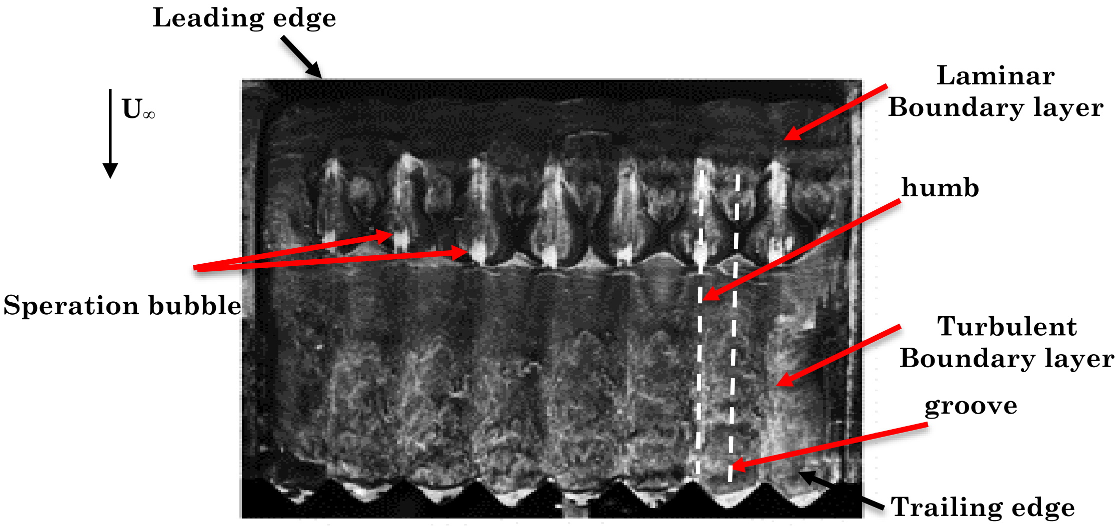

Figure 1-9: presents the flow visualisation and its clarification for the serrated aerofoil at $\alpha = 0^\circ$ [31].

In experiments where moving plastic and metal flaps were attached to an aerofoil's suction surface and pivoted at a limited angle, a simplified design was tested [32]. In order to avoid increasing drag associated with premature boundary layer transitions, the flaps were placed near the trailing edge of the aerofoil as shown in Figure 1-10a [32]. If flow separation starts, the devices lift in response to the reversed local flow, as shown in Figure 1-10b. This creates a physical barrier to promote flow movement to the "leading edge" [32].

Problems with premature flap raising have been overcome by the porosity of the devices, with a jagged trailing edge, allowing the static pressure to be equalised on each side of the flap. The comb-like fixtures found on the "leading edge" of owl wings offer another method of separation delay from nature.

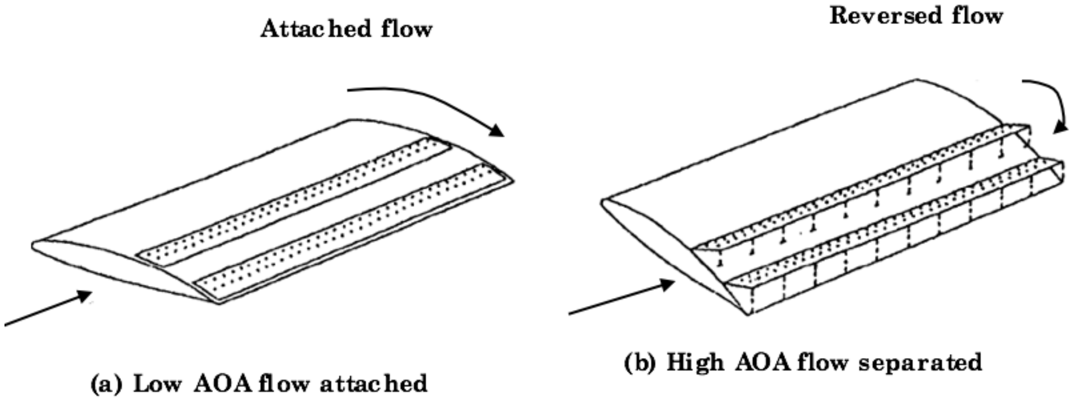

Figure 1-10: Sketch of flexible flaps at high and low angle of attack (reproduced from Meyer et al.) [32].

Flow visualisation experiments found that the comb creates a spanwise vortex on the wing's "leading edge" at a large angle of attack, which seems to delay the flow separation in the outer wing half [33]. It is assumed that this vortex creates a low-pressure region on the surface of the wing, achieving a vortex lift commonly seen on delta wings. The amount of the vortex lift increases with the angle of attack, until the vortex collapse occurs [33]. Flow separation delay is expected to be linked with higher maximum lift values.

1.3.2 Drag Reduction

1.3.2.1 Transition Delay

Passive compliant coating can be applied to delay the transition from laminar to turbulent boundary layer by interacting with instability modes, such as Tollmien-Schlichting wave, traveling wave flutters, and static divergence [34]. Three possible modes of instability have been recognised and studied, First type oscillations are Tollmien-Schlichting- this type of waves in the boundary layer changed by the compliance with the wall, in other words by the movement of the solid in response to the fluctuations of shear stress and pressure in the flow. The disruption eignenfunction for T-S waves has the highest amplitude within the fluid area. Those waves are stabilized by the irreversible transition of energy from the fluid to the layer but destabilized by dissipation in the wall. Second type waves are discovered in both the wall and the fluid. However, the disruption eignenfunction has its highest amplitude at the solid- fluid interface and thus these waves are primarily wall based modes of instability. This kind of instability would not occur if the wall were rigid. The instability is as a result of the downstream free wave in the solid being changed by the fluid loading. The destabilization of category waves is caused by the phase difference between the perturbation of the pressure and the deformation of the wall, which enables a flow of energy from the fluid to the wall. Second type wave conduct is the opposite of that for first type waves, stabilized by the wall damping but destabilized by hydrodynamical nonconservative forces. Essentially second category waves are improved when the flow provides adequate energy to counterbalance the inner dissipation of the coating. Last category waves are similar to the inviscid instability of Kelvin-Helmholtz and happen when conservative hydrodynamic forces induce a unidirectional transition of energy to the solid. The pressure distribution over a wavy wall in an inviscid flow is in precise anti-phase with the height. In that case, third type waves can only grow on the solid surface if the amplitude of pressure is so large that it outweighs the stiffness of the coating. Third type waves are the consequence of a modal coalescence instability where the flow velocity is sufficiently large that the initially upstream wall-free waves are turned to move downstream and combine with the altered downstream wall waves. Irreversible procedures in both the fluid and the solid have a negligible impact on the instability of the third type. Figure 1-11 shows the configuration of a passive compliant coating used in experimental research [35]. Suppression of a given mode of instability can lead to transition delays and thus reduction of skin friction, provided that other modes do not increase in response to the fluid - structure interaction [36]. A multi panel design in which each compatible panel was tuned for the local flow environment conjecture that boundary layer at high Reynolds numbers could be suppressed with this design [37].

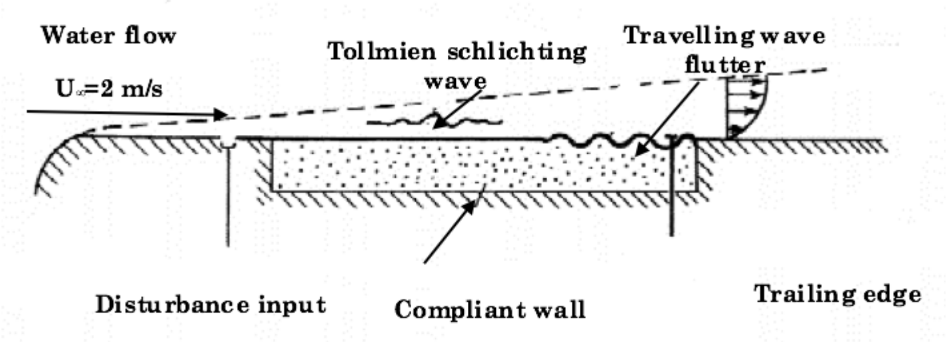

Figure 1-11: Reaction of compliant coatings to the Tollmien-Schlichting waves created by a disturbance input (reproduced from Gaster) [35].

Compliant coatings thus provide a simple and cost-effective flow control method, although their design optimisation can some low be complex.

1.4 Active Techniques

For the category of active flow control, one way to improve the lift is to increse the planform area, as it is proportional to the lifting force if other variables are kept constant. Circulation increase is a technique that promotes greater flow movement around an aerofoil, which also leads to increased lift. The application of mechanical-suction changes the stability characteristics of the boundary layer, which if applied puperly can restrict its growth. Enhanced momentum exchange can prolong the flow attachment and, correspondingly, increase the stall angle and the maximum lift coefficient. The periodic forcing of the velocity field supports entrainment and mixing, which leads to the reattachment of the boundary layer [38]. Body force generation in the air can facilitate separation control and re-attachment. The introduction of a vorticity source in a boundary layer can reduce wall shear stress in both the laminar and turbulent boundary layers. Altering the near-wall viscosity influences the position where the boundary layer transitions from laminar to turbulent. It may be desirable to delay or accelerate the transition, depending on the application. Several different mass injection methods have been investigated, such as those examined here. Vakili and Gauthier [39] used a drilled plate to inject air into the near boundary layers upstream of the cavity. They reported a reduction of 27 dB in the cavity's peak tones, and concluded that mass injection can altere the cavity feedback. Bueno et al. [40] studied various longitudinal cavities within Mach 2 flow under steady, pulsed blowing found that constant blowing to reduce the surface pressure fluctuations was the most effective configurtion, with microjets used at the "leading edge" in order to change the shear layer across the cavity. The pulsed mass injection is also efficient in decreasing the amplitude by drawing energy from resonant modes. However, it appears that injection at a constant pulsing frequency improve the overall of the noise in the cavity. The continuous injection becomes more active than pulsed injection as it results in a greater reduction of both tones and overall noise.. The cavity tones could be reduced by 20 dB, whilst the broadband noise was reduced by 9 dB. Visualisation of shadows and velocimetry of particulate images was also used to show that the injection reduced the cavity's flow unsteadiness [41].

Microjets and span-wise slots are also used for cavity flow control and fluctuating surface pressure reductions. Ukeiley et al. [42] employed a complex cavity geometry, but found that the spectra of surface pressure changed by the momentum injection was very similar to that of a rectangular cavity. The best blowing settings were discovered when the injectors did not completely fully span the cavity's leading edge. In this research, the outcomes of an experimental study in which different settings of leading edge blowing actuators were used to change the shear layer above the cavity. As a result, fluctuations in surface pressure in the cavity were significantly reduced. Numerical simulations including RANS-LES of supersonic flow over a non-rectangular cavity when L/D = 5.6 has been presented with control perceptions involving blowing through slot jets and microjets and a fence spoiler. As a consequence, changes in the cavity's surface pressure were noticeably reduced. The blowing concepts are seen to yield as good or better suppression of the fluctuating pressure levels compared with the spoiler, and, although the spoiler was not optimized, the blowing concepts are significantly more amenable to working at varying freestream conditions. The blowing techniques are seen to produce as excellent or superior suppression of instable pressure levels relative to the spoiler, and although the spoiler has not been optimized, the blowing techniques are noticeably more likely to work under differing freestream conditions. Because the mass/momentum of these concepts can be tuned or adjusted for different flow conditions, these are more effective and practical than the spoiler perception. The results showed that the aft fluctuating surface pressures on the cavity wall were reduced by 55 percent. In addition, the tonal and broadband components of the fluctuating pressures were reduced. This was based on the observation that the surface pressure on the aft wall was significantly reduced in the span-wise wall by the “leading edge” blowing.

A numerical study of similar conditions was reported by Arunajatesan et al. [43], achieving reductions in the surface pressure and certain flow control effects in the cavity shear layer. In particular, there was a change in the span-wise coherence of turbulent structures and significantly more three-dimensional flow impinging on the aft wall, less than in the flap of the cavity shear layer. It was also observed that an increase in the production of turbulences in the first part of the shear layer, and the main effect of “leading edge” blowing, was a redistribution of turbulent energy from larger to smaller vortex structures.

1.4.1 Lift Improvement

1.4.1.1 Increased Wing Area or Camber

Leading edge slats and trailing edge flaps both provide a means of simultaneously increasing the camber and wing area, as shown in Figure 1-12. Through take-off and landing procedures, these devices can be angled down to generate the necessary lift. Slat deployment also creates a gap known as a slot that further improves the performance, as discussed in more detail in Section 1.7.2. Large modern aircraft use a triple slotted flap that generates significantly higher lift during departure, which is required for greater weight [44]. Both flaps and slats are retracted into the wing to decrease drag during cruise conditions. On the other hand, the drag associated with these devices cannot be completely eliminated, and the actuation mechanism increases the aircraft’s weight. A leading edge flap, as shown in Figure 1-13, is an alternative device to a slat, which also increases the wing’s effective camber.

Figure 1-12: The extended trailing edge flaps on an aircraft (Airbus A310-300) and the position of the leading edge slats; the slats are drooped [45].

These devices are stopped at the wing's "leading edge" and have no associated slot, resulting in lower performance compared to slats [46]. However, they are mechanically simpler and particularly suitable for thin wing sections [47]. They are often utilised on the wing's inboard section in combination with outboard slats to enhance longitudinal stability [47].

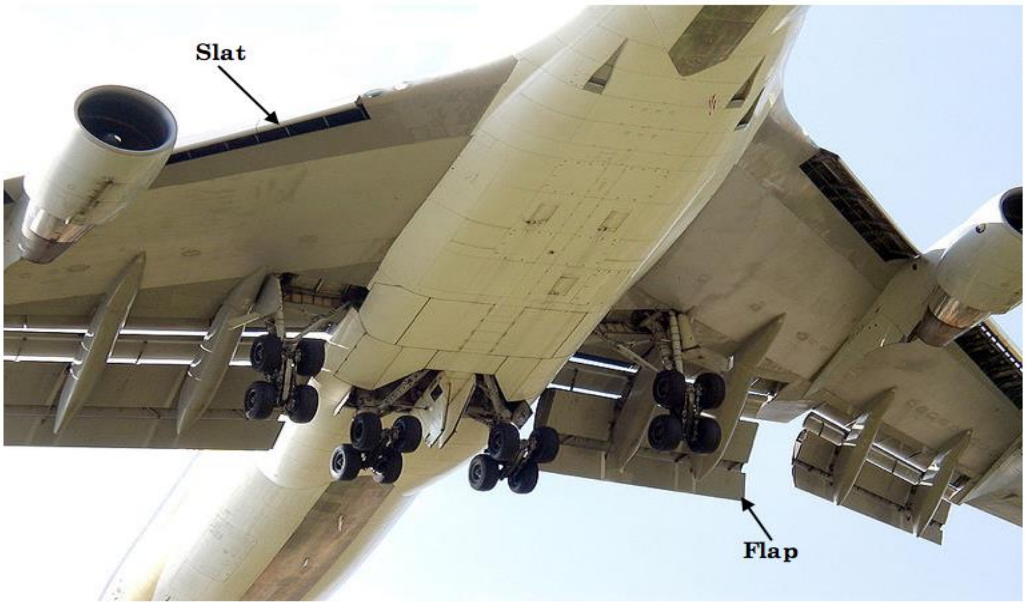

Figure 1-13: Leading edge flap [46].

1.4.1.2 Momentum Exchange or Separation Delay

Zero-net mass flow jet or synthetic jet are a more cost-effective alternative to separation control than the previous methods of steady suction and steady blowing [48]. Usually, they consist of a sinusoidally oscillating membrane, which is embedded under a row of holes or a spanwise slot, can be seen in Figure 1-14.

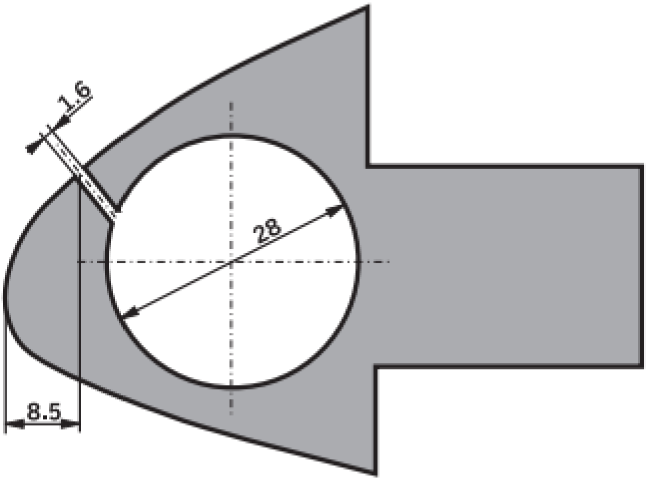

Figure 1-14: Schematic of zero-net mass flow-actuator with loudspeakers on the ends [48].

Within each sinusoidal cycle, there is no net fluid flow into or out of the actuator, but the fluid drawn from the boundary layer is forced back into the flow at higher trajectory, as seen in Figure 1-15 [49].

Zero-net mass flow jets support increased mixing and lead to a higher entrainment rate in the boundary layer. Additionally, streamlines are deflected from the surface, which decrease the local upstream pressure gradient, thereby reducing forces that lead to the separation of the boundary layer. These characteristics significantly delay the stall, allowing the aerofoil to generate a larger lift with reduced pressure drag [50].

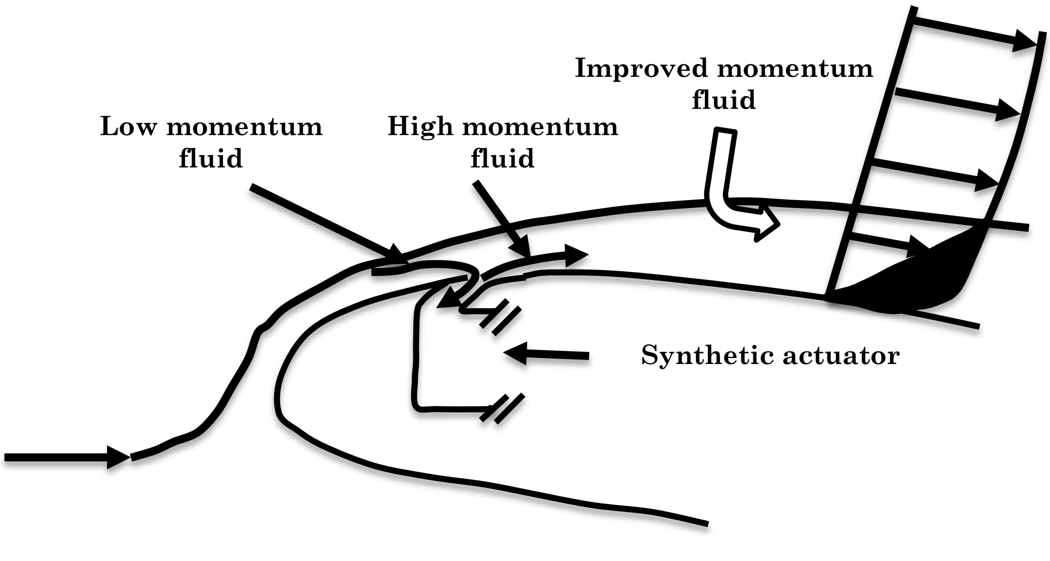

Figure 1-15: Schematic of zero-net mass flow (ZNMF) jet with acoustic actuator (reproduced from Gillaranz et al.) [49].

The best results have shown by studies that located the control actuators closest to the separation point. The control mechanism changes the dynamics of the separated shear layer, as lift improvement is not improved at angles of attack below the stall.

A larger degree of attachment can be achieved using synthetic jets, as shown in Figure 1-16. Slots enable flow from the pressure side of the aerofoil to be guided onto the suction side, increasing the momentum exchange at the suction surface. One possible problem with zero-net mass flow (ZNMF) jets is that the holes are at risk of being blocked by dirt, moisture, and polish [50].

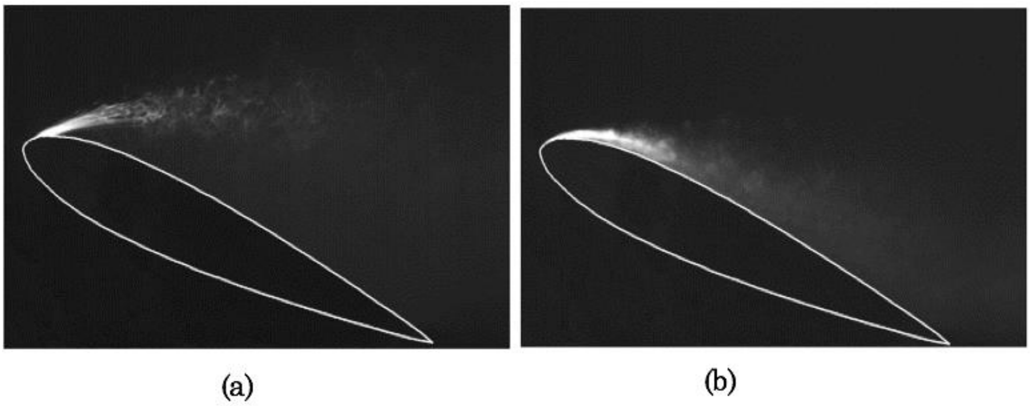

Figure 1-16: Flow visualisation NACA0015 aerofoil at 18° degree. for (a) uncontrolled and (b) controlled flow [50].

The slots can be suitably formed by apertures, as shown in Figure 1-17 [51], which can be incorporated into the wing during the production process.

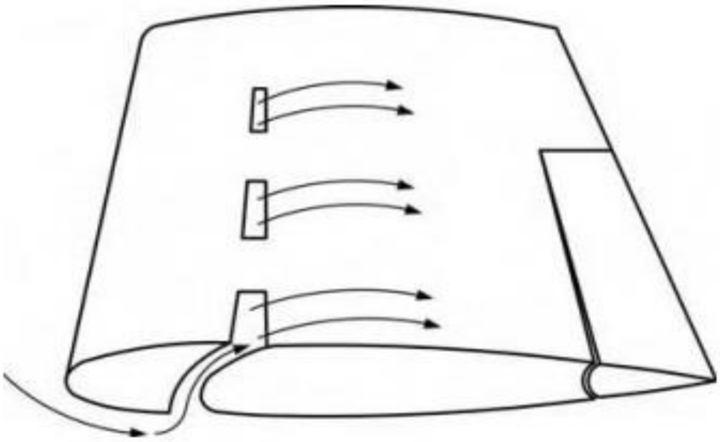

Figure 1-17: Leading edge tips slots [51].

They are also deliberately made by the deployment of slats, with small gaps between the “leading edge” and the slat. Slots remain closed during cruises, but they are opened to allow higher lift generation at higher angles of attack [46]. In nature, thumb-pinion of a pheasant, split tail of the falcon, and layered feathers of certain other birds display similar flow control mechanisms [52].

Vortex generators jets an improve momentum exchange, but they are more controllable and less intrusive compared to the traditional vortex generators [53]. They are positioned on the suction surface of the aerofoil at a certain pitch and a certain angle of yaw. The typical configuration of the vortex generator jet is shown in Figure 1-18 [54]. The optimum configuration of these parameters allows the separation to be delayed, thereby increasing the maximum lift and stall angle, and reducing the form drag. Streamwise vortices produced by the jets seem to resemble a weak vortex produced by a solid vortex generator, but not a stronger vortex created by a solid vortex generator [55]. The operating vortex jets in pulsed mode have been found to reduce the power needs for a certain lift by as much as an order of magnitude [56].

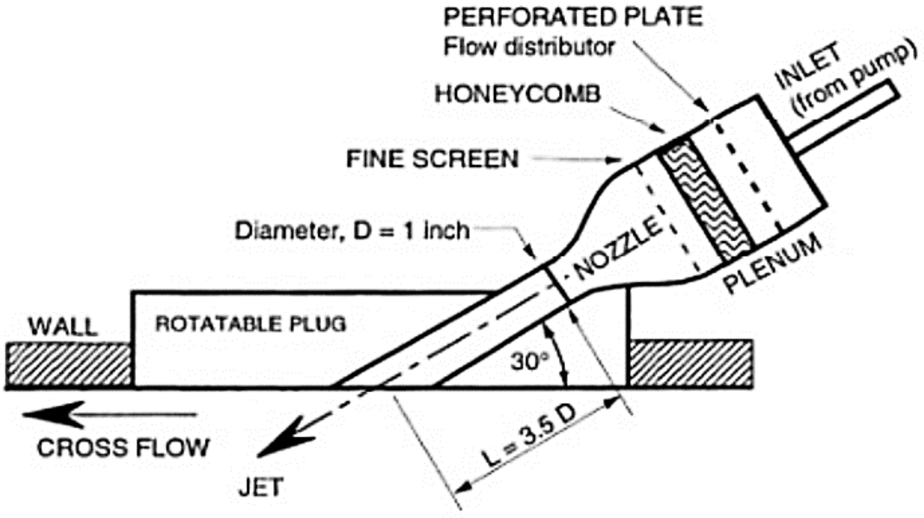

Figure 1-18: Diagram of a vortex generator jet actuator with a pitch angle of 30 deg. and a rotatable connector to change the angle of skewing [54].

Internal acoustic excitation includes sound radiations from one or more narrow gaps or slots close to the “leading edge”, which reduces the extent of the separated area, thereby decreasing the drag and increasing the lift [57, 58]. The flow control mechanism was described as an increase in the momentum exchange, leading to a suction peak on the suction surface of the aerofoil [58]. The early section of the separated shear layer, which narrows the separation region, has also been indicated as an increase in entrainment [57]. The results of internal acoustic excitation show that the sound pressure level required for effective control was much lower than those required for external excitation, with reducing energy needs [58]. It was noticed that separation control most effective when the sound amplitude is higher close to the initial separation region [57, 58 , 59].

1.4.1.3 Application of Body Force to Air

Plasma actuators can be used for a wide range of internal and external flow control applications, including aerofoil lift increase [60, 61], turbulent boundary layer control, and aerofoil “leading edge” separation [59]. The most widely used plasma actuator is based on a single dielectric barrier discharge mechanism, which includes two electrodes separated by dielectric material [61, 62, 63]. When high AC voltage is applied between the electrode it ionizes the air, and the collisions of the ionised air creates a body force [64].

By optimising the configuration of the electrodes, the body force can be adapted to specific requirements [63]. The air heating due to plasma generation is believed to be insignificant [65]. Important parameters for the optimisation of the plasma actuator include the geometry of the electrode, AC waveform, AC frequency, and dielectric thickness [63]. Plasma was successfully used for the separation control of an unmanned aerial vehicle equipped with plasma actuators subjected to high voltage generator [66]. Roth [67] used flow visualisation of the NACA0015 aerofoil with plasma actuators, at 12° an angle of attack, the excitation of all eight electrodes on the panel generated in a significant reattachment of the flow of air, making the air flow downstream of the aerofoil less turbulent, and the results can be seen in Figure 1-19.

However, the need to produce high voltage accompanied by associated losses of energy and increased weight is one of the disadvantages of plasma actuators [68].

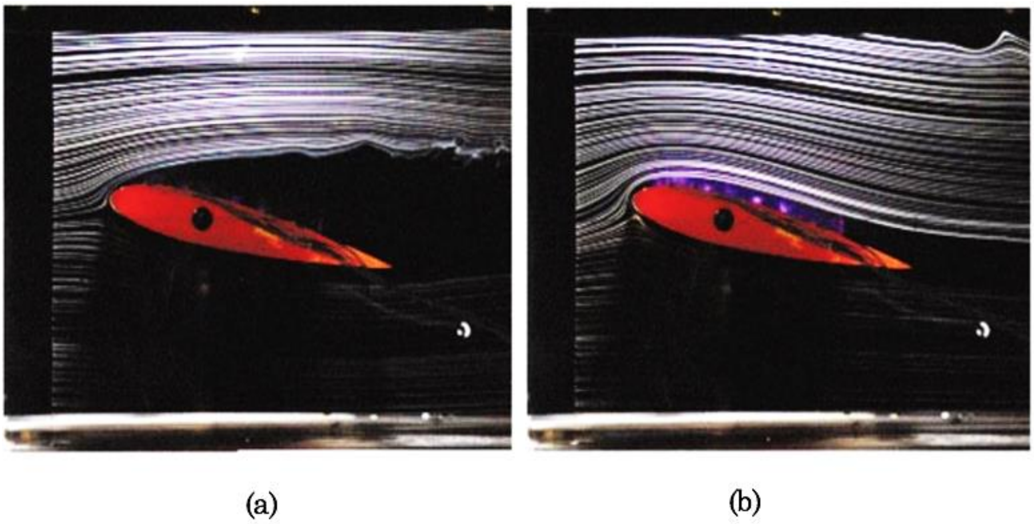

(a) (b)

Figure 1-19: Flow visualisation showing (a) separation of flow control with plasma off, and (b) re-attachment with plasma on at high angle of attack for NACA0015 aerofoil at a= 12° [67].

1.4.1.4 Source of Vorticity in Boundary Layer

It is possible to use a magnetohydrodynamic flow control to effect the flow of electrically conductive fluids, such as seawater. Flush mounted electrode arrays and subsurface magnets can be used to persuade a field of current-density and magnetic field in a wall region. The resulting three-dimensional Lorentz body forces are a source of vorticity that can be controlled both spatially and temporally to influence the field of vorticity of the boundary layer.

Wall shear stress reduction was measured for both laminar and turbulent boundary layers [69]. It has been proposed that the drag reduction mechanism for laminar boundary layers should be the restructuring of the vorticity field, and interfering with coherent motions responsible for turbulence generation for turbulent boundary layers [69].

1.5 Summary and Discussion of Active or Passive Techniques

This brief flow control introduction to gives an overview of the most popular devices available. The main purpose was to create a relevant context for serrations, whereby it has been highlighted that they are a passive flow control unit, and to increase the momentum exchange of the boundary layer. Other devices, such as vortex generators, synthetic jets, and "leading edge" serrations, were identified as belonging to this category. Section 2.4 provides further details on alternative mechanisms that have been proposed to improve the performance of aerofoils with serrations. The comparison of the performance features and flow patterns of flow control devices was expected to improve understanding of serrations. Furthermore, the development of a knowledge base of flow control methods allows associated advantages and disadvantages of different devices to be considered. On the other hand, The serrated leading edge in different combinations of serration wavelength λ and amplitude A, as well as straight leading edge with different blow rates Q' and spanwise air hole spacing λ', were investigated. Based on the results, there exists an explicit relationship between the A and Q', as well as λ and λ' for the aerodynamic lift and drag coefficients across a wide range of angle of attack. Aeroacoustically, it can also be concluded at this stage that there exists a correlation between the A and Q' for the noise reduction, it can be confirmed that the serration effect on aerofoil can be mimicked by leading edge blowing. Applications for specific devices can also be identified, therefore a suitable niche for "leading edge" serrations can be established. The different flow control devices, their effect on flow, and the associated benefits are summarised in Table 1-1.

Table 1-1: Flow control devices with their corresponding influences and advantages.

Devices	**Advantages**	**Influence on Flow**
Serrations leading edge, vortex generators and rippled trailing edges, and Movable flaps	Delay separation	Drag reduction, increased lift or stall angle
Flaps, leading edge flaps, slats	Increased speed on suction side	Increased lift or stall angle
Wing fences, notched “leading edge”, sawtooth “leading edge” and vortex generator	Restricted spanwise flow	Minimization or avoidance of tip stall
Manipulation of near wall viscosity and turbulator	Accelerated transition	Avoidance of stall
Compliant coating, manipulation of near wall viscosity	Delay transition	Reduced skin friction drag
Large eddy break up and riblets	Reduced momentum exchange	Reduced skin friction drag
Vortex generator jets, slots, plasma and external or internal acoustic excitation	Delay separation	Drag reduction, increased lift or stall angle
Mangnetohydrodynamic flow control	Restructuring of boundary layer vorticity	Reduced skin friction drag
Guney flap and blown flap	Circulation augmentation	Increased lift or stall angle

1.6 Thesis Structure

This thesis describes the results of an experimental study performed at Brunel University London, aiming to investigate the aeroacoustics and flow pattern of a NACA65(12)-10 aerofoil with straight and serrated leading edges. The organisation of this thesis is as follows.

Chapter 1 is the introductory chapter that presents an overview of the worldwide concerns concerning aeroacoustics and flow pattern, particularly its reducing emission noise and environmental impact. This chapter also briefly presents the working principle of blowing systems and the demand for a mean-line model to enhance aerofoil performance and reduce noise.

Chapter 2 presents a comprehensive literature review of aeroacoustics technologies that focus on “leading edge” aerofoil. This chapter also presents state-of-the-art studies on serration leading edge. The main aim of Chapter 2 is to intensively review the different types of expansion machines, both straight and serration models, and discuss the detailed phenomena like laminar separation bubble and full laminar flow separation, concerning characteristics of the low Reynolds number regime and effects of aerofoil geometry, topology flow, and flow control mechanism.

Chapter 3 presents a detailed description of the experimental facility and measurement techniques implemented to perform the noise and aerodynamics measurements presented in this thesis. describes the apparatus and instrumentation used to perform this study, mainly utilising the Brunel University London Wind Tunnel, with a novel anechoic test section and surrounding anechoic chambers. A detailed comparison of the airfoil and turbulence parameters used in the generation of leading edge noise is also discussed. The microphone system used for the measurement of the far-field noise and successful measurement of these quantities required calibrated arrays. Also, the data acquisition, reduction, and the characterization of jet profile are discussed in depth in this chapter.

Chapter 4 is an introductory presentation of the experimental study performed to understand the influence of aerofoil geometry on turbulence-aerofoil interaction noise on isolated aerofoils. Systematic noise measurements were carried out with varying serrated and straight leading edge, with and without blowing. The chapter provides the results of the measurements of the far-field noise as a result of the interaction of turbulence with the “leading edge” of a series of airfoils. The effects of blow rate (Q') and angle of attack on the radiated noise are discussed in detail, along with the effects of wavelength, and amplutuide. Results are presented for a range of angles of attack, up through and including stall. The tunnel background noise levels were fully documented and are used to eliminate the background noise from the “leading edge” noise spectra.

Chapter 5 presents the aerodynamic measurements conducted in the open circuit suction type wind tunnel of ten different leading edges. Lift and drag coefficients for a set of NACA65(12)-10 are calculated and presented, along with optimised serration wavelength and amplitude parameters based on lift and drag performance. An alternative modification is tried in the form of blowing the leading edge and comparing the results of the four “leading edge” serration types.

Chapter 6 presents the new hybrid “leading edge” device, referred to as a ‘serration-blowing’ “leading edge”, with comprehensive acoustic and aerodynamic tests on the ‘serration-blowing’ “leading edge” will be introduced . The effects of blow rate (Q') and angle of attack on the radiated noise are discussed in detail, along with the effects of wavelength and amplutuide in this chapter.

Chapter 7 summarises the thesis and the concludes the work presented in previous chapters, with the author’s suggestions for future work.

Chapter 2 : Literature Review

2.1 Introduction

This literature review focuses on leading edges subjected to low and high turbulent flow and on the theory of their manipulation. In order to maintain the original terminology of the researchers and authors active in this field, as cited in this chapter, the terms sinusoidal, undulating, serrated, and straight blowing are used to describe the shape of the leading edges. However, in the following chapters these variants are abridged to blowing and serrated leading edges, which best describes the designed leading edges. Recent fundamental publications are reviewed in this chapter to provide an overview of existing research on this study's subject.

The dipole sound theory of Curle [70] represents an extension of the aerodynamic theory of sound [71]. The latter presented that the fluctuating fluid stresses of a turbulent flow act as a volume quadruple distribution, despite the absence of a solid surface. Curle [70] showed that strong surface forces occur when a solid surface in the flow exists. These forces are added to the quadruples, but in comparison they are much stronger and radiate like dipoles in nature. As dipoles radiate more efficiently than quadrupoles, the sound is dominated by the surface forces. Due to the interaction between fluid and solid structures, the sound radiation occurs mainly by a fluctuating force field through an aerofoil exposed to a flow. Given a current-exposed aerofoil, Geyer et al. [72] described both leading and trailing edges sound generation.

Two principles of sound generation have been identified: incoming flow turbulence intensity, and the turbulence generation within the aerofoil boundary layer. Turbulence is the defining feature in both, and the distinction between the two principles lies in the position of its generation, whether externally (before aerofoil contact) or within the boundary layer.

The distinction between the noise generation at the leading and trailing edges of an aerofoil is a function of the current dominant principle. If the incoming flow turbulence exceeds that generated within the boundary layer, the leading edge noise is dominant, thus causing pressure fluctuations on the surface. These differences in pressure are propagated at sound velocity and cause broadband noise emissions. Leading edge noise occurs in the low frequency region, where turbulent structures are larger. Alternatively, if the incoming flow feature is characterised by low turbulence intensity, sound generation occurs at the trailing edge, due to turbulence and trailing edge interaction, with a potential acoustic feedback mechanism.

As Oerlemans and Migliore [73] indicated, trailing edge effects dominate the noise emitted by a clean tunnel flow. Otherwise, the leading edge represents the sound source at high incoming turbulence intensity. Furthermore, no interaction with the trailing edge was detected in the latter case, because experiments with and without tripping devices used to secure the transition from the laminar to the turbulent boundary layer produced the same results. The emission noise can have a broadband or a tonal character, as illustrated in Figure 2-1. Broadband noise includes both self-noise, generated by boundary layer turbulence at the trailing edge of the blade, or noise caused by tip leakage in unsteady flows and turbulence-ingestion [74].

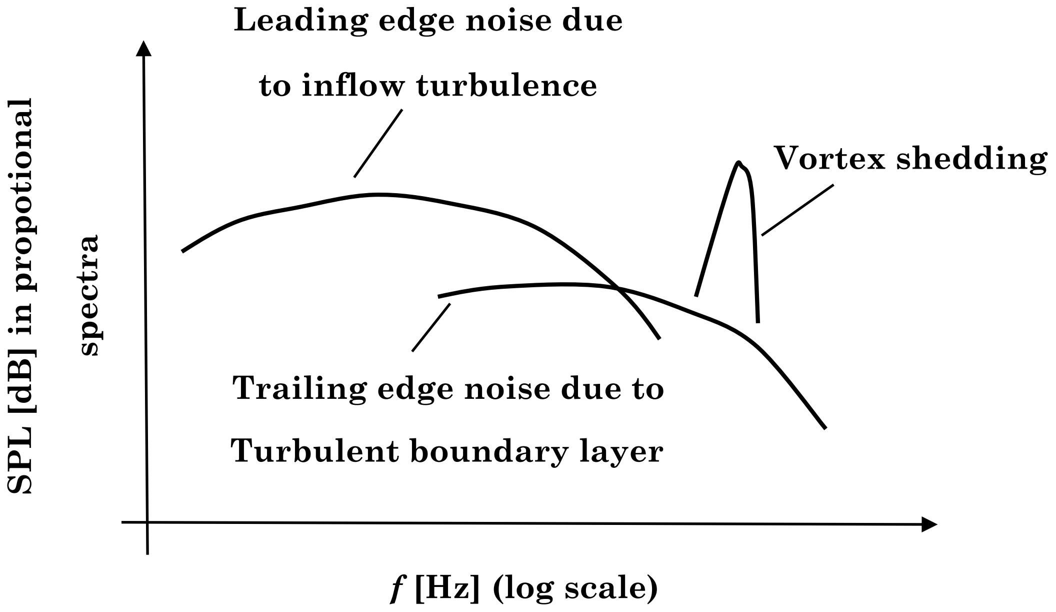

Figure 2-1: Illustration of flow-induced noise, radiated by a rigid aerofoil supported [75, 76].

According to Gershfeld [77], an aerofoil generates acoustic dipoles primarily at the leading and trailing edges in a turbulent flow. In these regions, due to the surface shape, the dipole surface normal stresses caused by the turbulence have not been cancelled by their images. When the chord length of the aerofoil is acoustically uncompact, the dipole sound produced by the diffraction of the turbulence by the leading or trailing edges is subsequently dispersed back by the opposite edge of the foil [77].

Aeolian tones or tonal noise are mainly limited to the presence of periodic vortex shedding (or any other periodical occurrence). The frequency of vortex shedding is equal to the frequency of tonal noise emission, according to Strouhal's law. The sources aerodynamics and underlying principles of the vortex shedding can be of a different nature. On the other hand, the development of an aeroacoustic feedback loop is primarily attributable to the significant tonal noise in low turbulent flow aerofoils.

2.2 Leading edge noise

Given the incoming flow of high turbulence, the incident turbulence affects the aerofoil's leading edge, and thus causes pressure fluctuations on the surface. These differences of pressure fluctuate propagate at sound velocity and cause broadband noise emissions. Several previous studies have been undertaken on the fluctuating lift forces of turbulent incoming flows and subsequent sound radiation into the far-field [78, 79]. The forces of action are the result of an unsteady pressure field generated by the aerofoil as a response to impinging turbulence. The pressure field develops due to an interaction of turbulence and the aerofoil. Given the freestream, the convection of the turbulent structures through the turbulent flow causes an interaction with the leading edge of the aerofoil. The turbulent eddies bend and curve around the leading edge, inducing pressure fluctuations on both sides of the aerofoil, thus resulting in noise radiation (Figure 2-2).

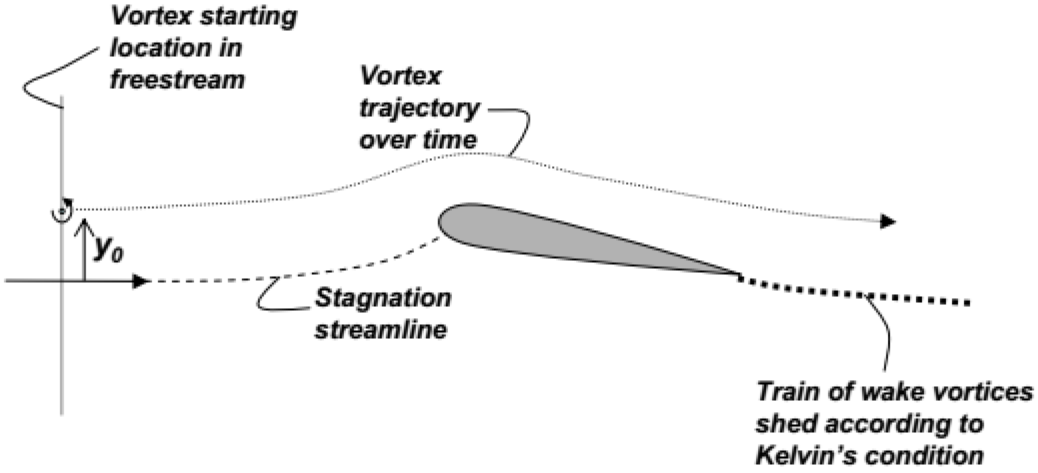

Figure 2-2: Schematic of a vortex interacting with the aerofoil and unsteady loading created as the vortex approaches the aerofoil, which is directly responsible for generating the noise heard in the far-field [80].

Carolus [76] reported that the transitory velocity relative to the aerofoil surface is a key problem with regard to sound generation on curved surfaces. The velocity profile depends highly on the aerofoil's position (accelerated versus delayed flow); consequently, the mechanisms for sound generation are also dependent on this position. The sound source location depends on the acoustic and aerodynamic compactness of the aerofoil treated. An aerofoil chord length of less than the integral length scale provides aerodynamic compactness (Figure 2-3 left). The flow leads to an oscillating angle of attack (AoA) for the aerofoil surface in the case of aerodynamics compactness, which responds with oscillating lift and drag forces. The aerofoil radiates the sound as a whole in this case [76]. If no aerodynamic compactness is observed (Figure 2-3 right), a discrete area on the leading edge that radiates noise is developed. The profile length ℓ is less than the length scale of the turbulent structure Λ (see the left of Figure 2-3 for aerodynamically compact profile), and the profile length ℓ is larger than the length scale of the turbulent structure Λ (non-compact aerodynamics, as shown on the right of Figure 2-3), whilst acoustic compactness is defined for the frequency range at which sound emissions happen.

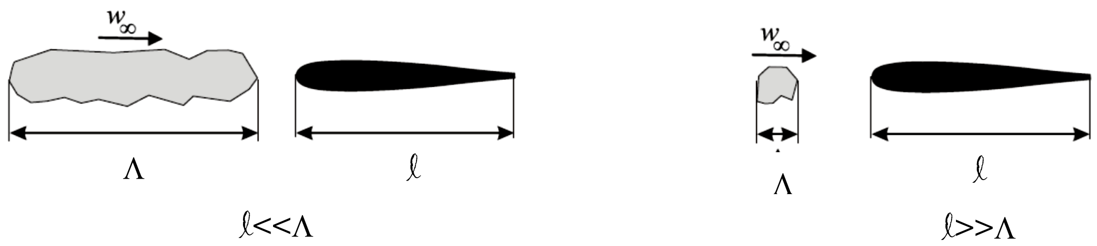

Figure 2-3: Left, profile aerodynamically compact (eddy dimensions larger than profile length) and right, profile aerodynamically not compact (eddy dimensions significantly smaller than profile length) [76].

The aerofoil is regarded as acoustically compact if the chord length is considerably smaller than the acoustic wave length. A body is generally defined as acoustically compact when it has a small characteristic dimension compared to the wavelength of the acoustic waves, or this dimension interacts with the wavelength (Eq. 2-1) [81].

$$\ell \ll \lambda \;\text{ with } \lambda = c_0/f \tag{2-1}$$

Assuming a wavelength of $1/4\lambda$ to satisfy the above equation, the frequency is limited to an acoustically compact aerofoil (Eq. 2-2).

$$f = c_0/\lambda = c_0/4\,\ell \tag{2-2}$$

This is consistent with earlier studies showing that leading edge noise occurs primarily at lower frequencies [79, 73]. This means that the larger turbulent content is responsible for leading edge sound generation, and the integral length scale can be described. To summarise, the sound source can be assumed to be located on the aerofoil surface or at a distance equal to an acoustic wavelength subset [72].

Oerlemans and Migliore [73] observed that leading edge noise prevails for all investigated aerofoils in the event of high inflow turbulence. They also measured an increasing broadband sound level and the sharpness of the leading edge. The moderate flow velocities of a low Mach number lead to moderate frequencies, and hence high wavelengths, resulting in acoustic compactness. The fluctuating forces of pressure function as a dipole source in this case.

2.3 Trailing edge noise

The flow field of turbulence and the aerofoil interaction is highly complex. The dynamic of this interaction process has many different parameters, such as boundary layer development and transition. Due to the boundary layer, transition is formed of small eddies (relative to incoming structures in the turbulent flow), which migrate to the aerofoil surface downstream and cause pressure changes. A laminar boundary layer vortex shedding noise occurs with a low to moderate Reynolds number (Re), in which instability waves of Tolmien-Schlichting (T-S) disturb the aerofoil's laminar boundary layer, thus resulting in the vortex shedding noise. Separation bubble is expected to amplify the unstable T-S modes close to the trailing edge.

2.3.1 Aerofoil tonal noise generation

From low to moderate Reynolds number and with low turbulence intensity, T-S instability waves are confirmed after reaching a critical Reynolds number. On a sharp-edged aerofoil, the T-S waves are established to propagate downstream towards the trailing edge and scatter into instability tonal noise. The regular shedding of vortices on the trailing edge of the aerofoil results in noise generation at distinct frequencies, which can be termed tonal effects, where the development of a Kármán vortex street and vortex shedding occurs, according to the Reynolds numbers. The development of an aerofoil trailing edge vortex street also depends on the Reynolds number. Usually, the development of a Kármán vortex street occurs at relatively low Reynolds numbers ($Re < 1\times10^5$), as illustrated in Figure 2-4. T-S instability waves are promoted after reaching a high Reynolds number. In general, a vortex shedding takes place at the aerofoil trailing edge, if a boundary layer is laminar to this edge on at least one side of the aerofoil. In the case of laminar flow with a chord-based Reynolds between $8 \times10^5< Re < 3 \times 10^5$, Hersh and Hayden [83] have observed loud distinct tones caused by fluctuating surface forces.

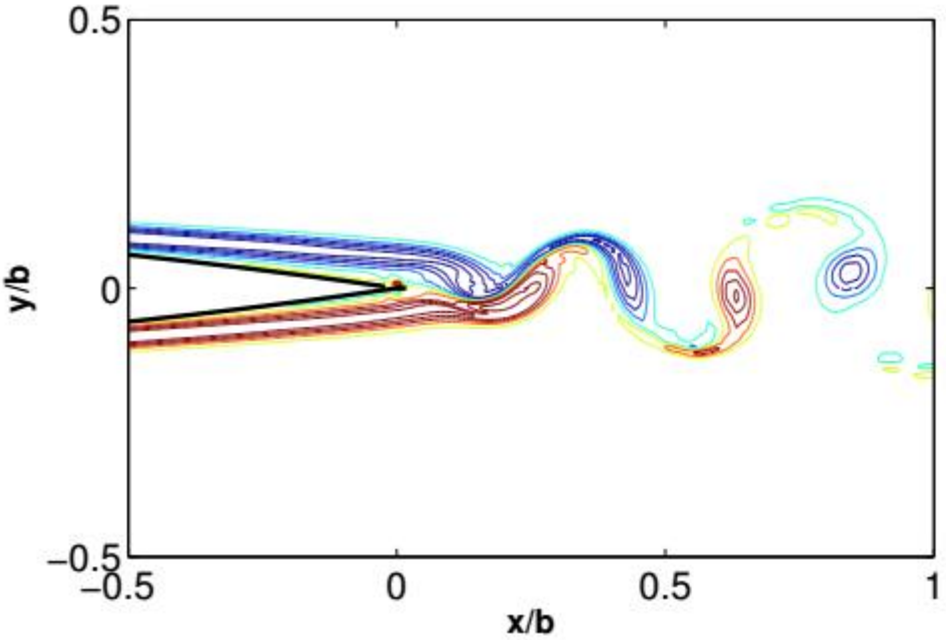

Figure 2-4: Instantaneous vorticity field in the boundary layer and the near wake of a symmetric NACA0018 (2% truncation) at (0°) AoA. The Reynolds number is 2×10^5 [82].

They also placed a tripping wire at the pressure side of the aerofoil's laminar boundary layer, and acknowledged the disappearance the tonal effects. When the boundary layer becomes turbulent, the vortex shedding is suppressed, because the wake vortex shedding character changes from coherent to random.

Various studies of the trailing edge flow have found that the noise source is near to it. In 1974, Tam noted that the vortex develops at an important distance from the aerofoil trailing edge even at a present vortex street, thus it cannot be a source of distinct tones on the trailing edge [84]. Hence, the tonal effect is responsible for another sound generation principle. Many researchers have suggested different principles of sound generation in recent years. Tam and Ju [85] and Arbey and Bataille [86] referred to self-exciting the acoustic feedback loop [87, 79].

McAlpine et al. [88] found that the separation bubble can be an essential source to generate tonal noise. A tonal frequency was detected in almost all calculations performed in this work, which provided additional data in the field, especially for conditions with lower Reynolds numbers. The experimental and numerical data contributed by different researchers on the presence of a tonal noise in under different Reynolds numbers and the AoAs are summarised in Figure 2-5. The solid line is an estimate of the zone in which tonal noise is produced [89].

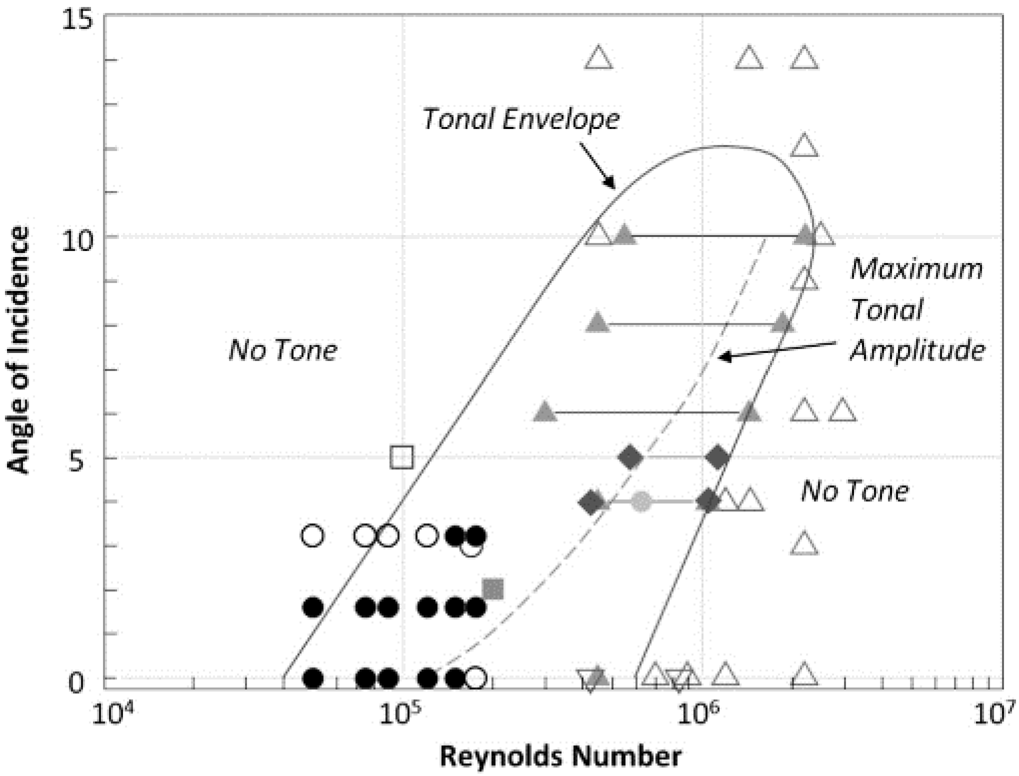

Figure 2-5: Pattern proposed by Lowson et al. [89] in which the tonal noise phenomenon is likely to occur. Filled symbols indicate the presence of a tone, while empty symbols indicate non tone was detected. Experimental data from various works.

Tam's [85] research revealed the first explanation of a so-called self excited aeroacoustic feedback loop [84]. Current instabilities in the laminar boundary layer on the pressure side of the aerofoil become amplified, while converging downstream the aerofoil. When exceeding a certain amplitude, instabilities cause a wake oscillation that leads to an induction of acoustic waves in all directions. As soon as these waves reach the pressure surface near the trailing edge, the boundary layer is excited and starts to oscillate. A reinforcing

influence is reached if the phase change turns out to be a multiple of 2π. In summary, the instabilities are amplified if the instabilities are in phase.
In conclusion, instabilities are amplified when they are in a phase of instabilities. Paterson and Amiet [79] tried to predict the frequency of the radiated tonal noise by applying a formula for the boundary layer to a flat plate while defining a scaling law, as presented in Equation 2-3.

$$f_0 = k.U_\infty^{1.5}/(C.\ \nu)^{0.5} \tag{2-3}$$

where, f_0 is the frequency of the acoustic tone, U_∞ is the freestream velocity, C is the chord length of the aerofoil, ν is the kinematic viscosity, and k represents the arbitrary factor (often set to $k = 0.011$). Nash et al. [87] proposed an acoustic feedback loop where the vortex shedding occurrence is produced by massively amplified T-S instability waves (Figure 2-6). A four-part process defines the acoustic principle:

1. A negative pressure gradient on the pressure surface causes a flow region with inflectional velocity profiles, and hence a maximum amplification of T-S instabilities.

2. Discrete frequencies of instability continue to be amplified with propagation to the aerofoil's trailing edge, and start rolling into a vortex. In order to retain a coherent structure, the inflectional or separated flow has to be located near the trailing edge, whereby it can generate tonal noise.

3. The interaction between this roll-up instability and the trailing edge results leads to a scattered oscillating field that oscillates around the aerofoil at the same frequency as the more amplified instability.

4. Installations roll up into the Kármán Vortex Street regularly, which is shed at the acoustic tone frequency at the trailing edge.

A new tonal noise generation mechanism was introduced by McAlpine et al. [88] concatenated by a separation bubble near the aerofoil's trailing edge. In this configuration, tonal noise can be generated only when the boundary layer is transformed into turbulence taking place close enough to the trailing edge

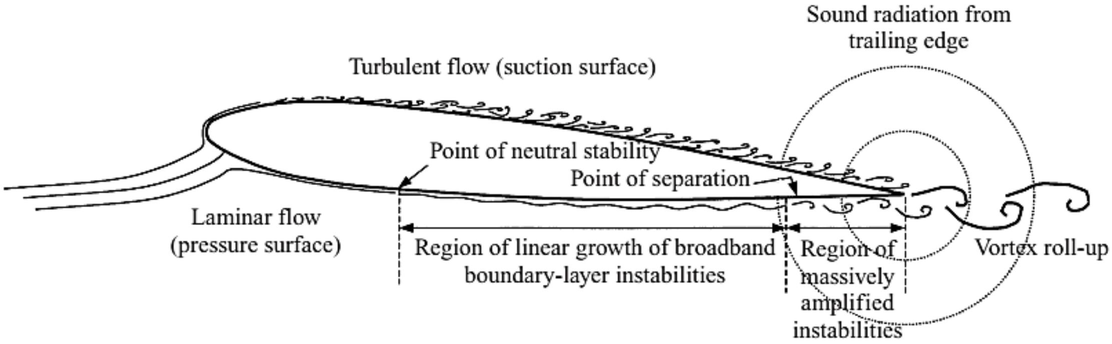

Figure 2-6: Diagram of a feedback model [87].

[88]. This supports Tam and Ju’s [85] conclusion that a turbulent boundary layer is necessary for a no-tone regime. This is also confirmed by the fact that tonal noise is produced at low AoA, and thus only when the boundary layer passes near the trailing edge.

It is assumed that these vortices generate increased momentum exchange through the boundary layer, changing the stability characteristics of the boundary layer and therefore the frequency of velocity fluctuations in the shear layer close the trailing edge. A numerical study describing an aeroacoustic feedback loop to verify Nash et al.’s work was recently proposed by Desquesnes et al. [89], who also wanted to explain some previously unexplained aspects, such as the existence of secondary vortices or frequencies [86]. The flow around a 2D NACA0012 aerofoil was investigated. In a previous study, it was indicated that two different acoustic response phenomena had been observed, depending on the Reynolds number and the AoA [89]:

1- A spectrum with broadband, but dominant frequency, and some other important peaks at equal distances.

2- A spectrum with a broadband character.

The initial acoustic response is considered to be the aerofoil trailing edge’s tonal effect. The authors confirmed that the pressure side of the aerofoil had a separation bubble that developed in the mean flow (Figure: 2-7) [89]. In addition, the main tonal frequency was observed close to the most amplified frequency of the boundary layer. The study showed that no separation occurred on the suction side of the aerofoil.

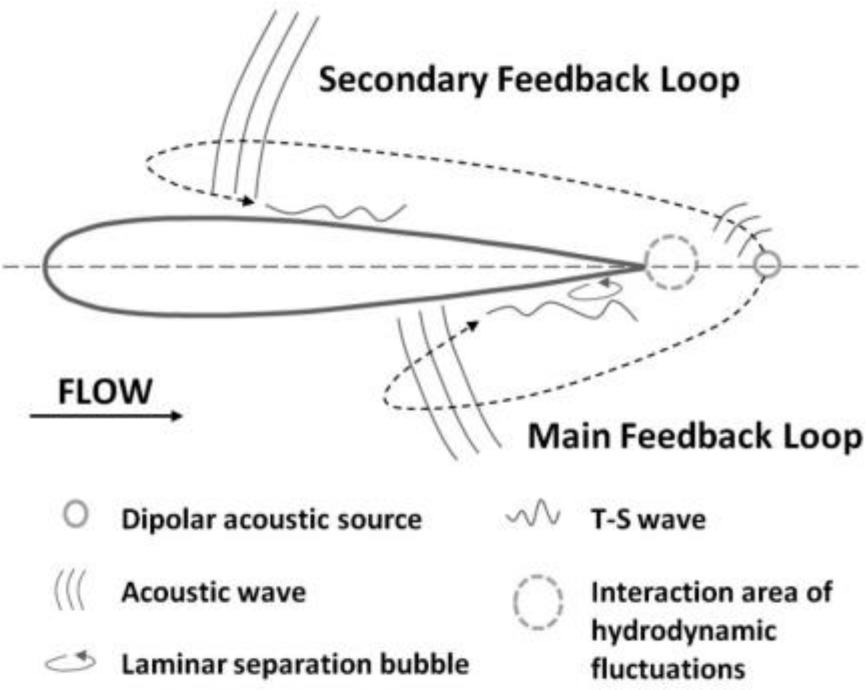

Figure 2-7: Sketch of the tonal noise mechanisms proposed by [89].

Furthermore, in comparison with the emitted tonal frequency, the most amplified frequency was different, as a result of which the laminar separation bubble is formed on the suction surface and is constituted through the reattached shear layer of the aerofoil. In these situations, the separation bubble is unsteady, switching between small and open bubbles.

Finally, Desquesnes et al. [89] found that a bifurcation of the wake aerofoil led to the existence of secondary tonal-frequencies, which changed the vortex development from symmetrical to unsymmetrical. Bifurcation may exist, because the main tone mechanism induces the interaction of the most amplified disturbances in the suction side boundary layers as well as those caused by the suction side pressures [89]. The flow visualisation of the trailing edge showed that the instability of π between the pressure and suction sides had an optimal phase difference, thus resulting in the radiation of the maximum acoustic wave amplitude.

Desquesnes et al.'s [89] findings were consistent with those of Arbey and Bataille [86], who undertook numerical and experimental research that identified a laminar flow noise from an aerofoil consisting of a broadband contribution with a maximum frequency and a set of equidistant discerning frequencies.

The diffraction of the Tollmien-Schlichting waves at the aerofoil's trailing edge was observed, as in other studies. It should be noted that no tonal noise is generated at the trailing edge in the case of highly turbulent inflow. Due to the high level of turbulence intensity, a bypass transition to a turbulent boundary layer occurs and any tonal noise generation at the trailing edges is suppressed, as a laminar boundary layer to the trailing edge of the aerofoil pressure side would be a necessary attribute in tonal emissions. A theoretical model based on the Orr-Sommerfield equation and likened to current empirical patterns was developed by Kingan and Pearse [90], with predictions of tonal noise frequencies for four different sets of experimental results [86, 91, 92, 98]. The theoretical model purported that the boundary layer instability noise could be predicted with reasonable accuracy for arbitrary aerofoil forms. However, the empirical results gave different predictions, since they were derived for a particular aerofoil shape. The authors contended that the theoretical model has become much more applicable [90].

Some aspects are still to be explained or experimentally confirmed in tonal aerofoil noise generation, and several studies have been carried out to classify and underlying the understand physical mechanisms. The mean flow on the pressure side of the aerofoil displays a separation bubble close the trailing-edge, and the main tone frequency is near to the most amplified frequency of the boundary layer. In addition, no study has been conducted on the effect of leading edge modifications on tonal noise. A link has been observed between the coherence of rake and tonal noise generation [89]. Furthermore, the importance of the suction surface in tonal noise generation has been highlighted [86, 89]. Also, the phase difference between instabilities on the trailing edge is thought to have a significant impact on the amplitude of tonal noise [89].

2.3.2 Aerofoil self-noise

Aerofoil self-noise is also known as trailing edge noise, which is caused in its own boundary layer as well as near the wake region by the interactions between the aerofoil and generated turbulence [90]. In 1959, Powell [93] attempted to identify the source of trailing edge noise, and this has subsequently been extensively investigated [92, 94, 95, 96]. Trailing edge noise is characterised as a minimum fan noise, assuming installations have no substantial effect, since the leading edge noise is not prominent, having low pressure load and turbulence configurations [97]. Five different aerofoil noise mechanisms, four of which are related to the hydrodynamic interaction between the boundary layer and the trailing edge, were identified by Brooks [92].

The geometrical discontinuity of the sharp trailing edge disperses these vortical disturbances in the sound, leading to a radiation with a significant increase in the noise generated compared with fluctuations in free space [98, 99]. For this reason, trailing edge noise is considered one of the main sources of noise, and it has received great attention in the development of trailing edge noise theories. Brooks et al. [92], through comprehensive experimental research, identified five aerofoil self-noise mechanisms, which were indistinct through their extensive experimental research. The first two from the noise mechanisms listed below are of interest for the present investigation.

Firstly, trailing edge noise of high levels of Reynolds numbers occurs as the turbulent boundary layer created over an aerofoil convects past the trailing edge and emits noise (Figure 2-8I). This source of noise is known for its broadband character, and is the main one for unseparated turbulent boundary layer flows. In a turbulent boundary layer, the structures are highly complex and often viewed as “random”. However, some repeatable recognisable patterns can also explain the phenomena of certain noise observations, reviewed in subsections 2.2 and 2.3 to obtain a deeper understanding of turbulent boundary layers and the corresponding noise mechanisms.

Secondly, a laminar boundary layer vortex shedding noise occurs in low to moderate Reynolds numbers (Figure 2-8II), in which instability waves of T-S disturb the aerofoil’s laminar boundary layer, thus resulting in the vortex shedding noise. The noise is of a tonal nature, with a narrow band, and it has been observed that the T-S waves alone are no longer the only mechanism for noise generation. Furthermore, a separation bubble is expected to be an amplifier for the unstable T-S modes close to the trailing edge.

Thirdly, a bluntness-trailing edge vortex shedding noise occurs in a small separate area past the blunt trailing edge of an aerofoil, which can be a significant noise source (Figure 2-8III). The radiated noise has a tonal nature superimposed on the frequency spectrum on a distinct broadband peak. In turbulent boundary layer flows, the audible bluntness noise usually dominates over the turbulent broadband noise as a distinct source, which depends on the thickness of the aerofoil's boundary layer and the ratio of actual bluntness at the trailing edge.

Fourthly, separation of the stall noise (Figure 2-8IV) becomes clear at high AoA, under separated flow conditions. As Brooks pointed out, an assessment by Paterson et al. [91] suggests that the dominant noise source originates from the trailing edge for lightly separated flows, while the broadband noise originates from the chord as a whole when the aerofoil experiences a deep stall.

Fifthly, a tip vortex formation noise generates a separate local flow close to the tip of the blade point region (Figure 2-8VI).

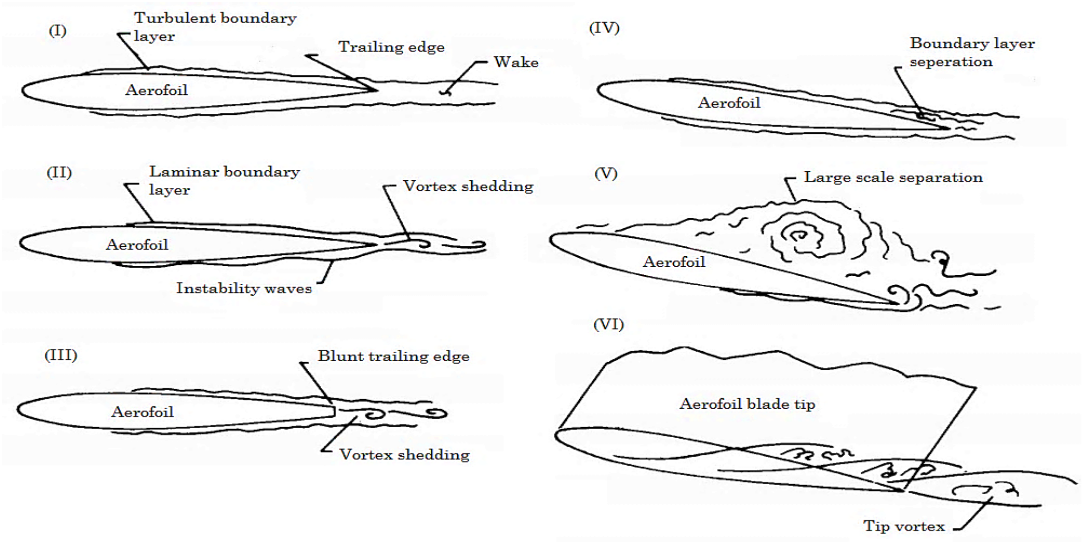

Figure 2-8: Five mechanisms of aerofoil self-noise, as identified by Brooks et al. [100]; (I) trailing edge turbulent boundary layer noise, (II) trailing edge laminar boundary layer noise, (III) bluntness vortex shedding noise, (IV and V) separation stall noise and (VI) tip vortex shape noise.

The vortex generates a thick, viscous, and highly turbulent core when the flow passes through the blade tip. Brooks and Marcolini's [100] investigation was able quantitatively to isolate the specific noise source, and to investigate the noise generation of aerofoil models in two and three dimensions under different conditions.

2.3.3 Broadband noise generation

Depending on the source, the frequency spectrum of the aerofoil's radiated sound differs. Turbulent inflow generally causes broadband noise at the leading edge and boundary layer turbulence, including the sound feedback loop, and the interaction with the trailing edge results in broadband noise as well as tonal noise, as shown in Figure 2-9 [72]. The broadband noise contribution, generated at the trailing edge, is located mainly in the average to high frequency regions. The reasoning for this principle of sound generation often appears to be of minor importance in recent research. However, Arbey and Bataille's [86] measurements confirm Fink's [101] discovery that the broadband contribution is the result of boundary layer instability with hydrodynamic fluctuations. Concerning the energy spectrum of the turbulent boundary layer, a theoretical illustration is shown in Figure 2-9a, and an actual set of experimental measurements can be seen in Figure 2-9b, in which kinetic-energy per mass is presented across various turbulence length scales.

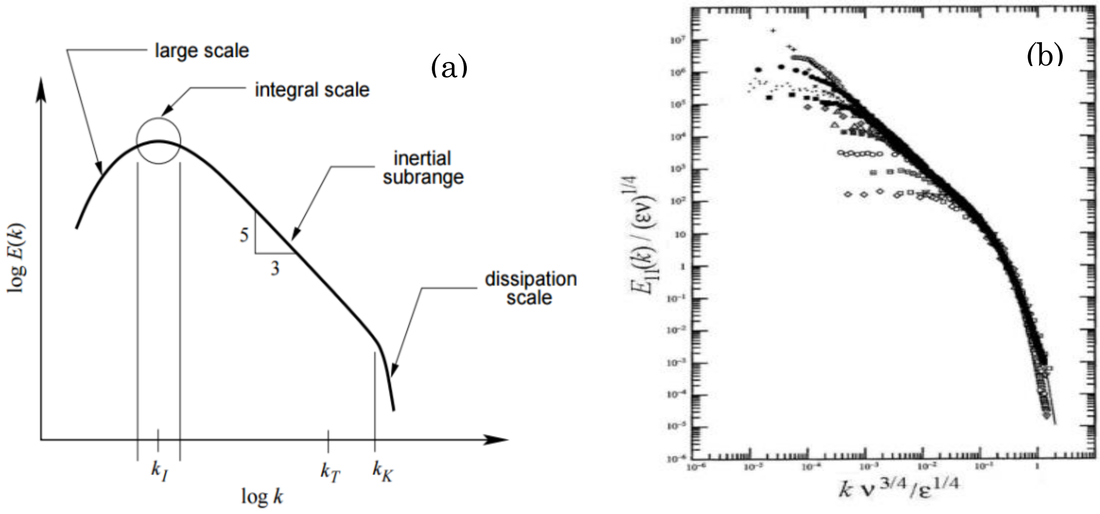

Figure 2-9: Turbulent energy wavenumber spectra (a) theoretical representation [102] (b) experimental results [103].

In addition, it was observed that an energy spectrum decay rate of $-5/3$ power law holds well within the inertial range. This is relevant for intermediate eddy diameters, which are remote from both the shortest and the largest scales [103].

2.3.4 Bluntness noise

Vortex shedding noise is often of a distinct narrow-band nature and occurs as a hump centred around the dominating frequency, superimposed with a broadband noise in the acoustic spectra. Noise from bluntness is generated in a small, separate area past the blunt trailing edge of the aerofoil. Both far-field noise spectra and fluctuation of the surface pressure, as measured by Brooks and Hodgson [103] and investigated by Blake [104], can be observed in the above mentioned hump. The intensity of the bluntness noise is based on the ratio between the thickness of the boundary layer and the bluntness at the aerofoil's trailing edge.

The noise bluntness can be found when the bluntness parameter of trailing edge $\varepsilon/\text{б}^{*}$ is above 0.3, where bluntness is ε and thickness б^{*} (with bluntness being in mm). A Strouhal number nondimensional dependency is expressed by the f_d shedding frequency, the bluntness parameter ε, and by the flow velocity U_{∞}, through:

$$\mathrm{St} = (f_d\ \varepsilon)/U_{\infty} \tag{2-4}$$

A constant number of Strouhals is seen throughout the velocity range for the straight trailing edge of a certain bluntness [92, 103].

2.4 Influence of the wavy leading edges on aerodynamic performance

The performance of the wavy leading edge depends on the type of stall of the aerofoil. The stall behaviour is also influenced by the geometry of the aerofoil (thickness and camber) and the condition of the Reynolds number. The results of the force and moment measuring are provided to quantify the geometric parameters of the aerofoil by evaluating the effects of the aerofoil thickness on the wavy aerodynamic performance of the leading edge. Furthermore, the Reynolds number effect on wavy performance is also investigated. The studies were performed in both cases with lift, drag, and moment curve evaluations during pre- and post-stall regimes. Equation 2-5 defines the lift coefficient.

$$C_L = 2 \times F/(\rho U_\infty^2 \times A) \tag{2-5}$$

Where, F is the lift force, ρ is fluid density, U_∞ *is* the flow velocity, and A is the area of the surface. When the lift coefficient is determined with a baseline case and compared with a lift coefficient for the same aerofoil with serrated leading edges and a constant maximum chord length, the coefficient of the serrated case is higher, if a surface is adapted to its actual (smaller) values. This could cause the lift coefficients to increase, but not the acting lift forces. However, a direct comparison between the two cases requires a constant surface area by means of aerodynamic performance. The resulting lift coefficients with serrations are in this case smaller than the baseline.

The aerodynamic features are extremely sensitive to the serration position. Many studies on the aerodynamic characteristics of serrated leading edges have been carried out. Leading edge geometry has been modified to a wavy leading edge from a sawtooth shape. While Ito [105] found that the aerodynamic benefit of serrated leading edge was only observed after installation at a low Reynolds number (2.1×10^4), several other authors showed that leading edge undulations might give rise to more advantageous post-stall and stall performance in a wide range of flow velocities [15, 18, 106]. Weakened performance of pre-stall has been observed, but the optimisation of the leading edge can be reduced [106]. The serrated leading edge attaching also has the same effectiveness as the increase of vortex generators at certain degrees of AoA. Fine serrations are conducive to fine longitudinal vortices on the suction side of the aerofoil, and the turbulent transition carried on the suction side of the aerofoil delays the separation region by the fine longitudinal vortices.

The aerodynamic performance of leading edge undulations is also part of the present work, along with the aerodynamic performance of leading edge serration.

Five different leading edges are tested to obtain information for the effect on the characteristic values of amplitude and wavelength. The morphology of the humpback whale flipper, which highlights geometrical parameters determining its hydrodynamics performance, has been studied in this regard [7]. The design suggests high manoeuvrability compared with the singular feeding habits of the humpback whale. In addition, Fish and Battle [7] analysed the characteristics of the tubercle and reviewed the literature of the tubercle function. They suggested that the morphology and placement of the leading edge the tubercle operates as a lift improvement device to regulate flow over the surface of the flipper, and keep the high lift values at a high angle. In order to enhance the hydrodynamic and aerodynamic performance, this pioneering work was a motive for interest in mimicking cetacean tubercles.

Watts and Fish [107] were also inspired by whale flippers' tubercles and carried out research of the sinusoidal leading edge, which showed a potential increase in aerodynamic and hydrodynamic efficiencies. The NACA 63021 aerofoil with its finite span to aspect ratio (AR) of 2.04 was used to simulate inviscid and viscous flow with a large Reynolds number. At 10 degrees, the wavy form built on the leading edge increased lift by 4.8 percent, whilst induced drag decreased by 10.9 percent, improving the lift-to-drag ratio by 17.6 percent. At modest angles, the wavy leading edge improves aerofoil performance, without any adverse effect at zero degree. However, drag increased by 11 percent with $\alpha = 10^{\circ}$ for a viscous calculation form. Miklosovic et al. [16] carried out the first experimental study on the wavy leading edge. The aerofoil NACA0020 was used to create a scale model of the pectoral flipper of a humpback whale tested with Reynolds number ranging from 5.5 $x10^5$ to 5.2 $x10^5$ in a wind tunnel. The tests showed promising results (Figure 2-10), in that the stall angle increased by 40 percent and the maximum lift by 6 percent, while the post-stall drag decreased by 32 percent for the tubercles configuration (compared to the smooth flipper model). The lift and drag showed similar results at a low AoA compared to the smooth model. Furthermore, the scalloped flipper has a better ratio between lift and drag (L/D), with a higher performance at all AoA, except for $10^{o} < \alpha < 12^{o}$.

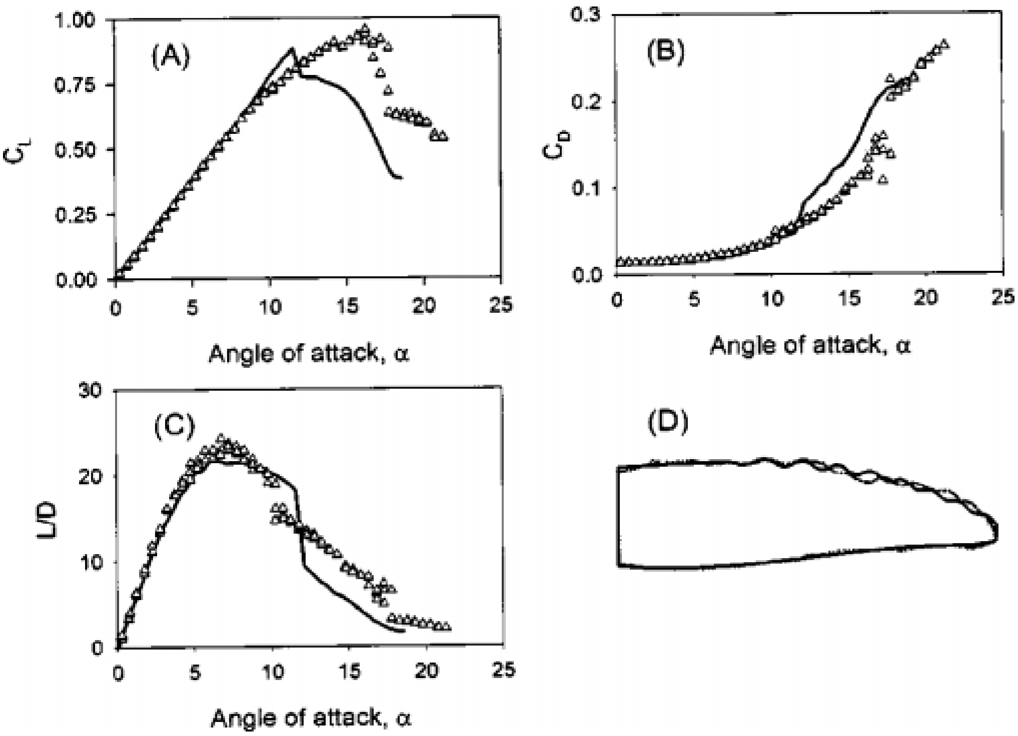

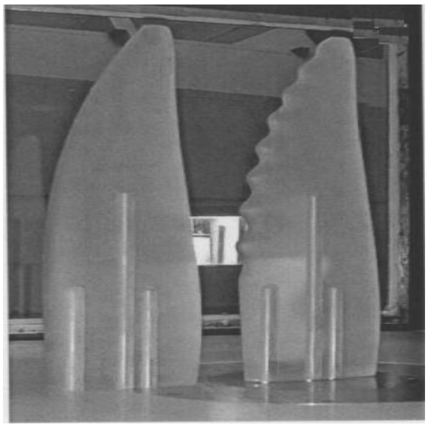

Figure 2-10: (A and B) lift and drag coefficients for flipper model of the whale with tubercles against AoA (solid lines – unmodified, triangles – modified), (C) lift-to-drag ratio (L/D) against AoA at 12°, (D) the profile of the flipper model compared with actual model (dot-line) without (solid line) [16].

Miklosovic et al. [16] found that the whale flipper's scalloped leading edge has the function of delaying the stall, by providing a higher lift at higher attack angles. These results inspired a rapid increase in research interest concerning the study of wavy leading edge phenomena.

Stein and Murray [108] were the first to conduct experimental tests with full-span models to show tubercles performance. The results presented an increase in drag and decrease in lift compared to the smooth aerofoil. Experiments were conducted at Reynolds number 2.5×10^5 for a particular AoA, range $0^\circ < \alpha < 12^\circ$, using a full-span model, with a sinusoidal leading edge with amplitude and wavelength equal to the mean values found in humpback whale flippers.

Levshin et al. [109] and Johari et al. [15] conducted experimental tests with a full-span model to examine in detail the nature of the flow imposed by the wavy-leading edge and the performance of the tubercle. The experiments were performed in a water tunnel using NACA634021, similar to the morphology of the humpback whale, for various wavy-leading edge geometries (i.e. 4S = λ0.5CA0.025C, 8S = λ0.25CA0.025C, 4M = λ0.5CA0.05C, 8M = λ0.25CA0.05C, 4L = λ0.5CA0.12C, and 8L = λ0.25CA0.12C), with a Reynolds number of 1.83×10^5. The results in Figure 2-11 present a deterioration in pre-stall performance with a reduction in lift and increased drag being observed for the modified aerofoil.

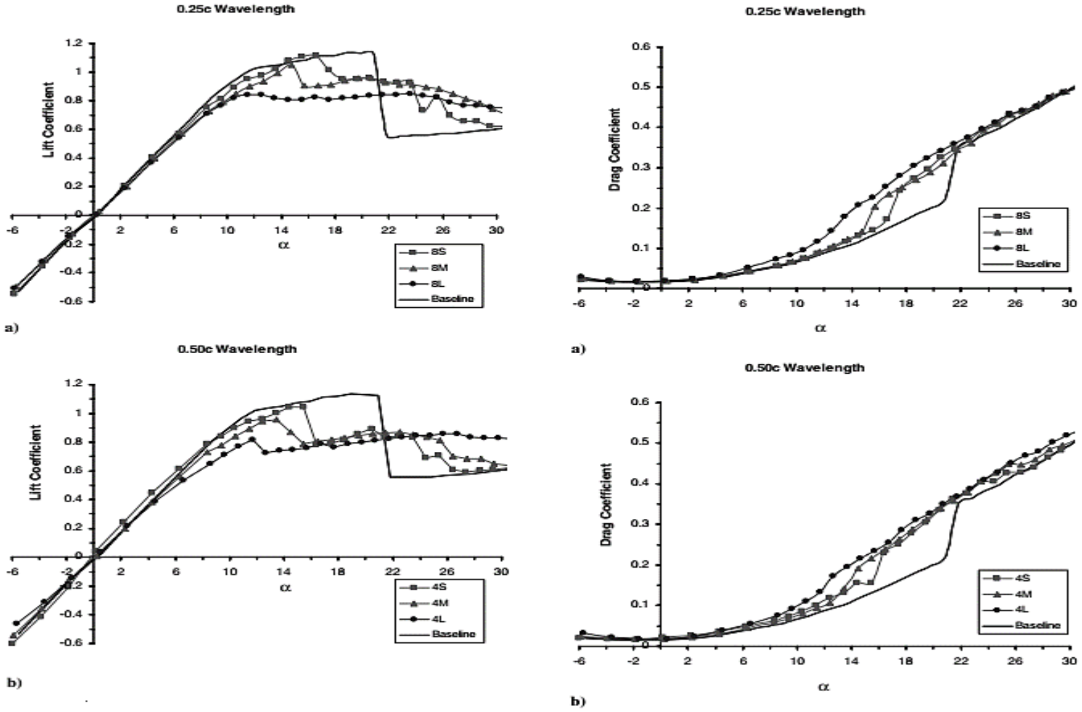

Figure 2-11: The tubercle influence on the pre and post-stall regime for different amplitudes (S, M, and L for 0.025C, 0.05C, and 0.12C) and wavelengths (4 for 0.5C, and 8 for 0.25C) [15].

However, smoother stall progression was observed, and the post-stall performance advantage was reverted to the wavy aerofoil, with a lift increase of 50% and a low (or no) drag penalty.

Miklosovic et al. [110] investigated the wavy leading edge influence in full and partial span models. Wind tunnel tests were conducted with geometries based on the NACA0020 aerofoil at Reynolds numbers from 2.74×10^5 to 2.77×10^5 for 2D, and 53.4×10^5 to 63.1×10^5 for 3D geometries. The 2D results showed apparent delay in the stall angle, together with reduced lift and increased drag. The 3D results also presented a delay in stall angle by 5°, with the maximum lift increased by 4 percent, but the drag also increased. In the Reynolds range of 1.2×10^5 to 4.4×10^5 in a water tunnel, Stanway [111] performed tests using a model similar to Miklosovic et al. [16], based on the NACA0020 aerofoil. Also, for all Reynolds numbers, the configuration of the tubercle showed smooth stall characteristics and delayed stall initiation. In all cases except for the highest Reynolds number the maximum lift was reduced, while the drag plots showed that the range of the low drag coefficient was decreased (Figure 2-12). Figure 2-13 compares the velocity fields of the two foils at 3 angles. With $\alpha = 10°$, the flow velocity reach to 2.3 m/s over the midchord of both foils. The control foil slows back to 1.5 m/s downstream. There are small spanwise fluctuations, but no net spanwise transport is obvious. Small areas of lower velocity (1.2 m/s) are noted on the test foil downstream of the roots between the serrations.

Nierop et al.'s [112] study is considered significant as the experimental data are similar to those obtained in their theoretical models. Wavy leading edge phenomena were designed, because the tubercle causes a cyclical change in chord and thickness along the span, and causes a variation in circulation. This results in a sheet of streamwise vortices behind the aerofoil. Using lifting theory and using a smooth elliptical aerofoil model, they defined pre- and post-stall aerodynamic characteristics for tubercle configurations.

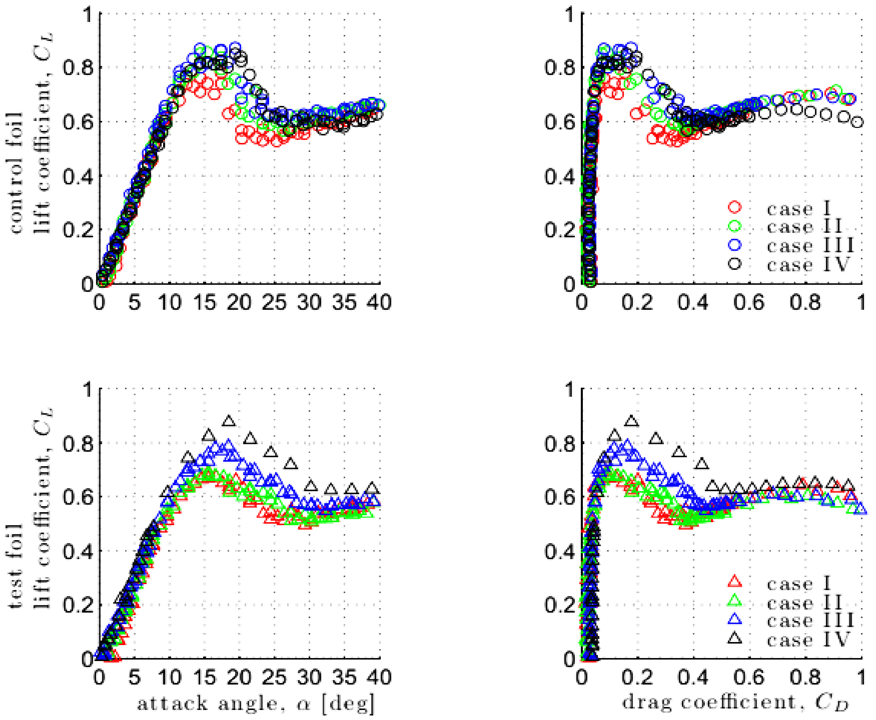

Figure 2-12: Lift and drag coefficient results for a smooth aerofoil [circle] and serrated aerofoil [triangle], introduced as lift curves and drag polar. The Reynolds numbers for each case were: case I: 44648, case II: 59530, case III: 89295 and case IV: 119060 [110].

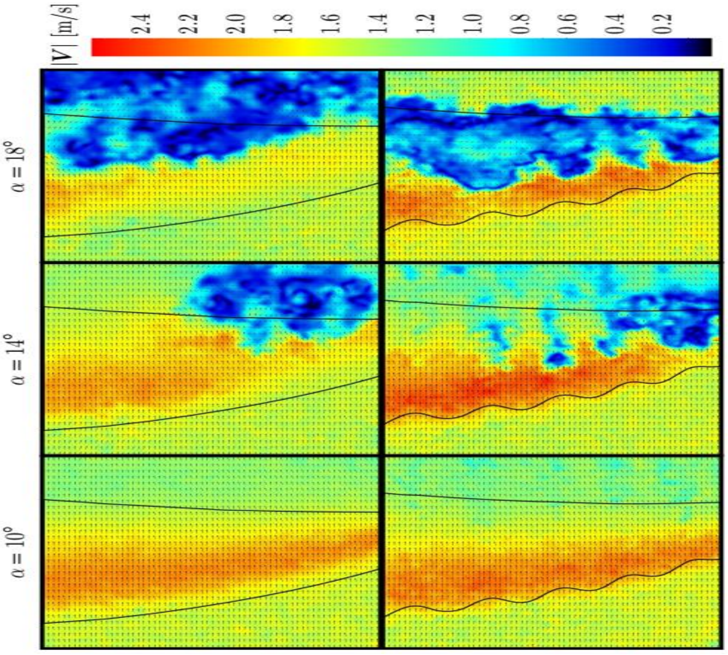

Figure 2-13: Comparison of instantaneous representative velocity fields at $\alpha = 10°$, 14 °, and 18 °. Top row: control foil, bottom row: test foil. Freestream speed = 1.5 m/s (Case III, Re = 89295). Low velocity areas in blue suggest separation and stall [110].

In 1998, Bearman and Owen [113] conducted some basic research on leading edge serrations. They carried out an experimental investigation of wavy thin plates and rectangular cylinders with spanwise sinusoidal forms and sinusoidal shaped front faces, with flat rear ones.
In the form of aerodynamic measurements of the drag forces, they analysed the effect of these modifications and observed two significant modifications in the flow properties [113]. First, vortex shedding formed a regular pattern of cells over the span of each cell with a predominant frequency. The frequency differences led to the occurrence of two distinct shedding frequencies and dislocation of the vortex between the cells. The increase of the sinusoidal peak-to-peak quotient and wavelength from 0.0 to 0.9 was the result of a complete suppression of vortex shedding for the thin plate.
A rectangular cylinder with peak-to-peak quotients and wavelengths ranging from 0.06 to 0.09 was utilised with an identical physical process. Secondly, with increasing steepness (the quotient of the peak-to-peak value and the wavelength serration value), the base pressure increased by waves, which led to a drag reduction of up to 30 percent. At quotients 0.06 to 0.09, the drag coefficient measured was at its lowest and the vortex shedding was completely suppressed in this region [113].

Soderman [25] studied spring brass leading edge serrations with a thickness of 0.254 mm. It was found that vortices on the aerofoil were created at the locations of the serrations. These vortices delayed the flow separation, and thus improved the maximum lift coefficient as well as the pre-stall AoA. Soderman [25] also noted continuously that the introduction of serrations on an aerofoil would not increase the drag to smaller angles, and would reduce it to larger angles. A similar observation was made by Polacsek et al. [114], with a key finding that undulations lead to delayed aerodynamic stall and improved post-stall lift performance. The delay of the separation boundary layer can be addressed by leading edge undulation to generate spanwise vortices, which improves the lift and delay stall. Thus, aerofoil undulations influence the growth of the boundary layer on the surface of the aerofoil, where serrations cause a delayed flow separation.

Hansen et al. [115] conducted full-span experimental tests for NACA 0021 aerofoils with the Reynolds number 1.2 x 10^5 (Figure 2-14), investigating the effects of variation of amplitude (6-11%C) and wavelength (20-86%C). Within the pre-stall range, the smallest amplitude (6%C) with a wavelength of 43%C achieved a higher CLmax and larger maximum stall angle between the wavy aerofoils. Furthermore, with a decreasing amplitude, this increased the lift in the second linear range of the lift curve for the symmetrical aerofoil. The larger amplitudes achieved smoother stall characteristics during the post-stall regime. In terms of drag characteristics, the drag values were approximately similar in various amplitudes at lower AoA ($\alpha < 8^{\circ}$). The lowest amplitude was achieved at an intermediate AoA of $8^{\circ} < \alpha < 15^{\circ}$, while the largest amplitude showed a lower drag coefficient at $\alpha > 15^{\circ}$. Flow visualisation indicates that streamwise vortices form between serrations on either side of the roots, downstream of the leading edge (Figure 2-15(a)). It is also clear that the flow separates behind the serration roots earlier than it separates after the tips. In Figure 2-15, (b) and (c) indicate that the wake is wider behind the root, while (a) and (d) propose that the flow is accelerated in the roots at the leading edge, as indicated by the meeting of streak lines in these areas.

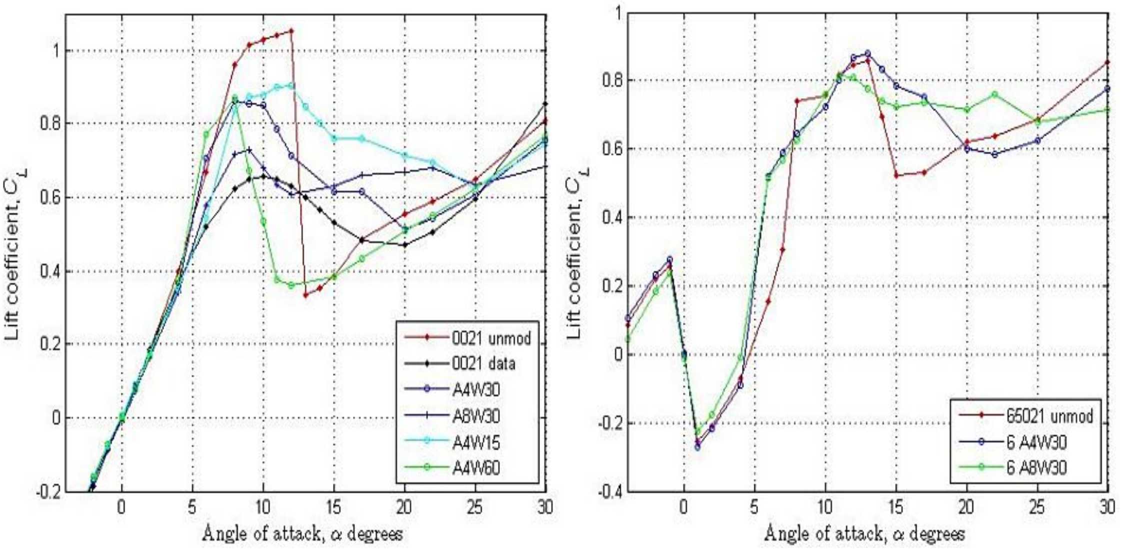

Figure 2-14: Effect of tubercle geometries for different amplitudes (4 for 0.06C and 8 for 0.11C) and wavelengths (15 for 0.21C, 30 for 0.43C and 60 for 0.86C) in both pre- and post-stall conditions [115].

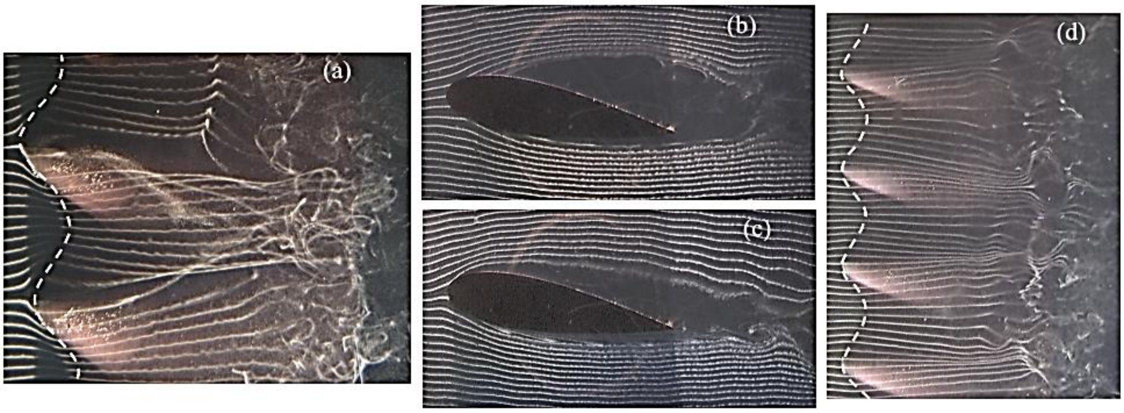

Figure 2-15: Visualization of hydrogen bubbles (a) top-view of streamwise vortices, (b) side-view in root plane, (c) side-view in tip plane, and (d) top view of acceleration regions [115].

The effects of the streamwise vortices are shown in the convergence of streak lines towards the serrations. Streamlines and pressure distributions schemed for the numerical results found by Watts and Fish [107] are presented in Figure 2-16.

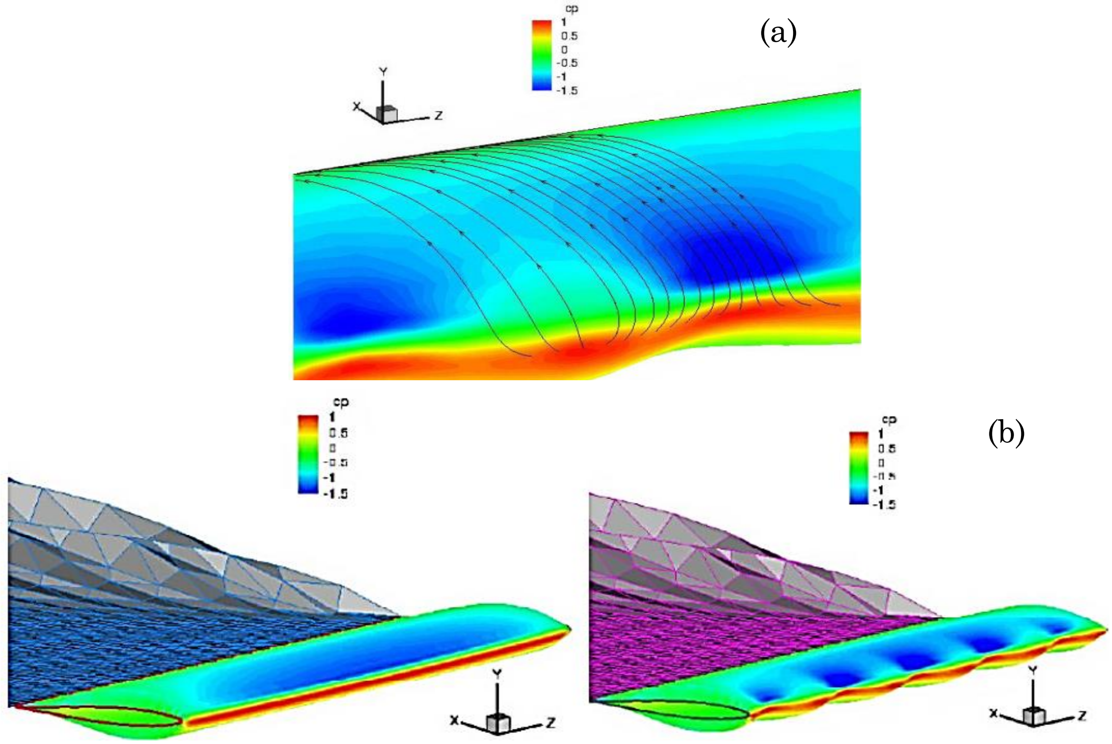

Figure 2-16: Colours represent (a) streamlines at the edge of the boundary layer, (b) the pressure differences flow over a finite span wing at $\alpha = 10°$ with serration leading edge (right) and straight baseline leading edge (left) [107].

It can be seen that the pressure behind the roots is lower than that behind the tips. Furthermore, the streamlines are nearer in the root region, representative of higher flow speed, consistent with predictions [7]. The limitation of this research is that the numerical simulation ignored the effects of viscosity, thus streamwise vorticity and boundary layer development were not modelled [107].

Viscous effects were, however, accounted for in a numerical research which used the same aerofoil and AoA, but an unsteady Reynolds number averaged Navier Stokes equation [116]. It has been observed that separation was delayed almost to the trailing edge for regions downstream of the serration peaks, as shown in Figure 2-17. As predicted by Fish and Battle [7], streamline contours indicate the development of large streamwise vortices in the regions behind the roots between serrations.

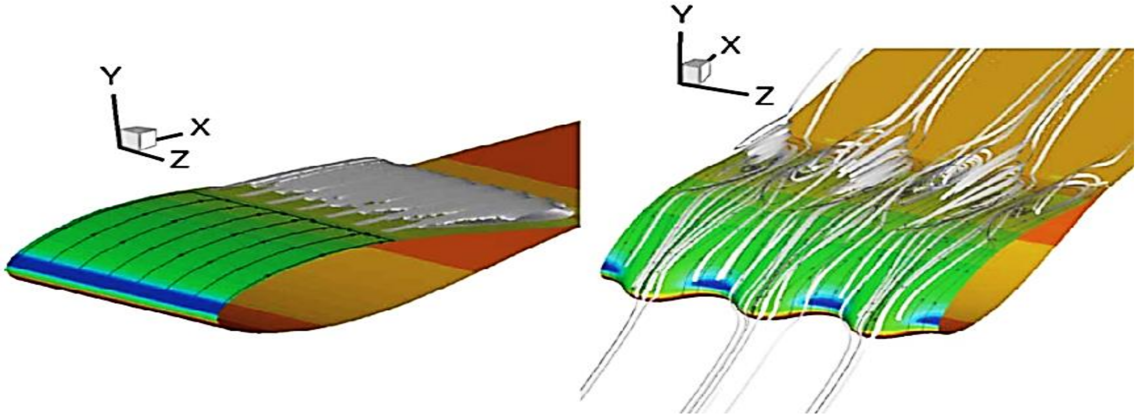

Figure 2-17: Streamlines and pressure contours for aerofoil NACA 63-021 with and without serration [116].

Dye visualization experiments presented in Figure 2-18 [117], using the same aerofils as Johari et al. [15], indicate that pairs of counter-rotating streamwise vortices were created in the roots between serrations when Re = 1500. The figures also show that flow remains on attached behind serration tips in the post-stall region, in spite of the fact that it was separated after the roots. Streamwise vortices were supported by computational research at Re = 500000 [117].

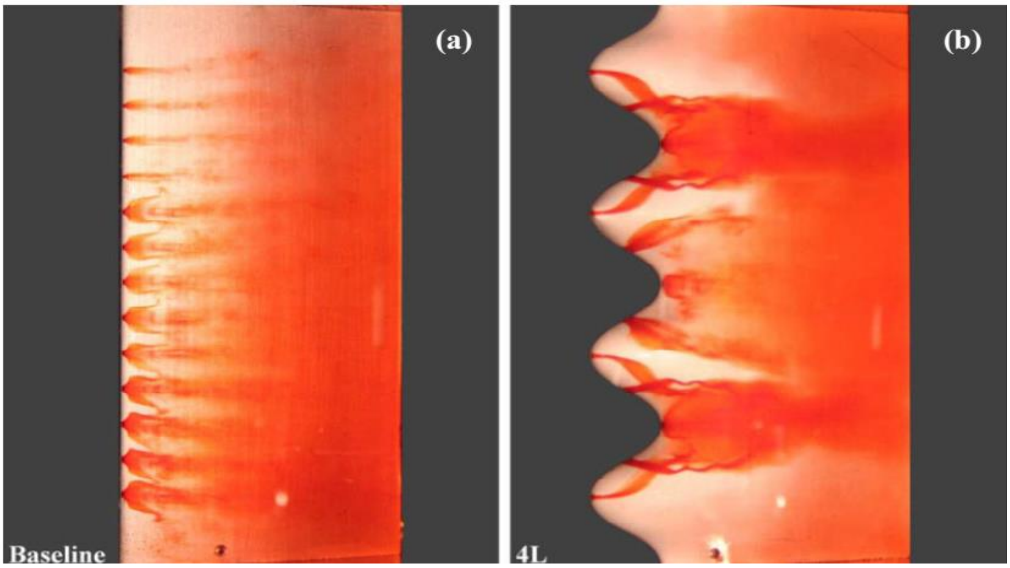

Figure 2-18: Flow visualisation presenting formation of the streamwise vortices at $\alpha = 24^o$ after stall. (a) Unchanged aerofoil and (b) aerofoil with serrations, $\lambda = 0.05C$ and $A = 0.12C$ [117].

Investigations revealed that serrations changed the vorticity distribution along the span of the humpback whale-flipper at α = 15°, as presented in Figure 2-19(a) [118]. In contrast, in an identical case except for a smooth leading edge, the model with serrations experienced improved vorticity downstream of the serrations, and a reduction in peak vortex strength at the same AoA. It was also found that the spanwise extent of leading-edge separation in the peak region decreased, and there was a much more irregular trailing edge separation line on the central third of the span in the area behind the serrations, as indicated in Figure 2-19(b) [118].

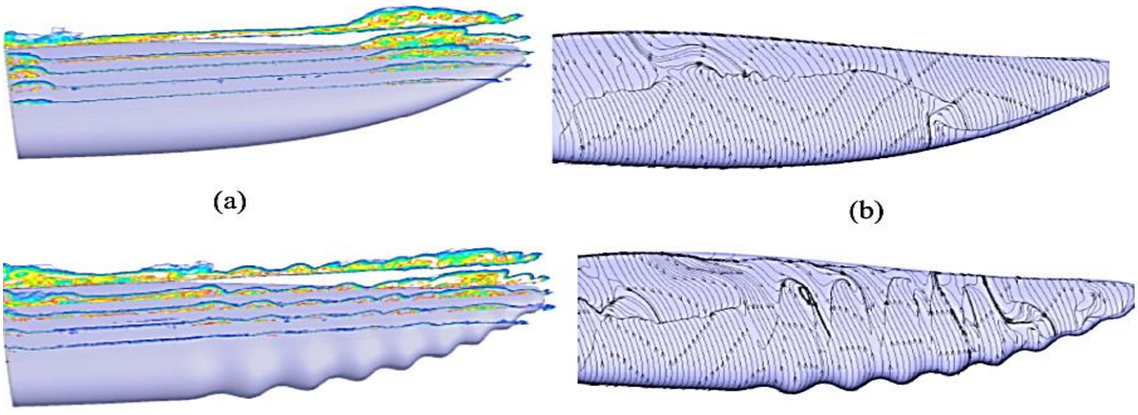

Figure 2-19: (a) Vorticity magnitude slices in span direction and (b) Averaged shear stress lines for Re = 500.000 and $\alpha = 15^o$ [117].

Custodio [117] presented another reason for the lift improvements, suggesting that counter-rotating stream-wise vortices migrate towards the roots between tubercles, according to the image method. This trend is presented in Figure 2-20, and the arrows reflect the velocity direction caused by the vortex of the appearance.

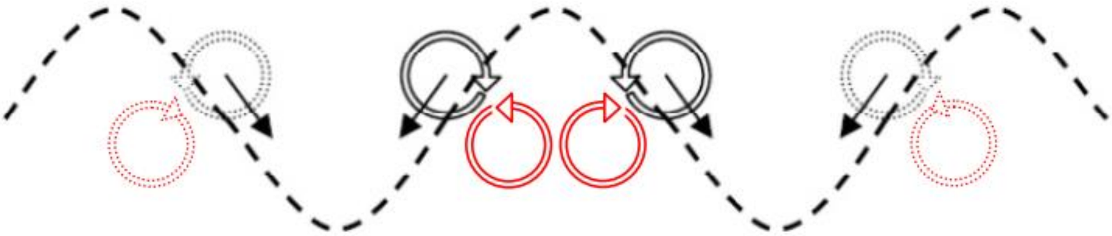

Figure 2-20: Diagram presenting movement of vortices towards roots as predicted using imaging technique. Vortices shown in red [117].

Weber et al. [119] observed that leading edge serrations increased cavitation initiation and changed the location of initial occurrence, as shown in Figure 2-21. Cavitation was found in the roots between serrations for the changed rudders instead of spreading along the entire of the leading edge (as for the unchanged rudder). The peak vortex for the rudder with serrations can also be seen to be smaller, indicating a reduced induced drag force.

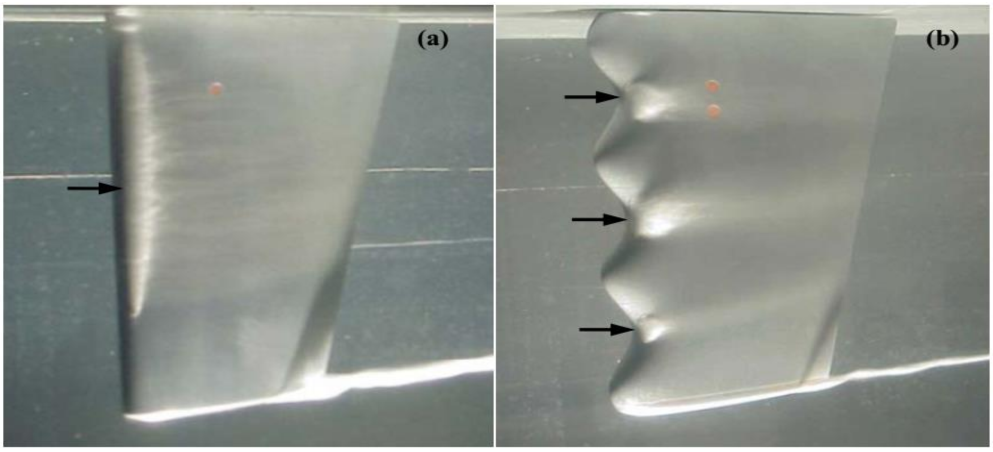

Figure 2-21: (a) Leading edge cavitation and peak vortex cavitation on the smooth rudder, $\alpha = 17°$ and (b) cloud cavitation in roots between serrations and peak vortex cavitation on changed rudder, $\alpha = 15.8°$. Re = 786000 [119].

2.5 Influence of wavy leading edges on aeroacoustic performance

Further understanding of the aeroacoustic effects of undulated leading edge is required. A study demonstrated that narrow band vortex shedding noise from stationary and rotating aerofoils with leading edge serrations can effectively be reduced by four to eight dB [120]. It also indicated that leading edge serrations reduce tones generated by the regular fluctuating pressures close to the trailing edge. Such tones arise from the formation of vortices which alter the wake, changing velocity fluctuations from periodical to random.

Migliore and Oerlemanns [73] also noticed that when the turbulence level affecting the aerofoil is sufficiently high the aerofoil gust interaction noise could dominate. Hansen et al. [17] made similar observations. Aerofoil tonal noise is reduced due to the application of an undulated leading edge to an aerofoil NACA0021 at a Reynolds number of 1.2×10^5. The vortices behind the root tend to break the coherence of the vortex generation on the trailing edge, and can be seen as the cause of a reduction in tonal self-noise. Longhouse [121] and Arndt and Nagel [122] confirmed these observations.

Numerical simulations performed by Lau et al. [123] to investigate the effects on aerofoil gust interaction noises of wavy leading edges found that the primary factor determining the performance of noise reduction is the ratio between the leading edge (A) amplitude and the wavelength of the gust. Noise reductions were significantly achieved when the amplitude to the wavelength ratio of the gust exceeded 0.3. Far-field noise reductions can be made, because the wavy leading edge causes a faster phase variation in the leading edge pressure fluctuations (compared to the baseline leading edge). The computational results show the ratio between the wavy amplitude and the gust length scale as being the main effect factor characterising the acoustic performance of leading edge noise reduction. With increasing ratio A / Λ, a maximum sound reduction is achieved, which is saturated to $A / \Lambda = 1.0$. They also defined a minimum wavelength to ensure an effective sound reduction.

With a minimum wavelength of up to 0.3, the sound reduction becomes significant. Interestingly, the definition of a range of 1.0 to 1.5, where the effect of the serrated wavelength λ is much greater than outside this range, is a controversial issue in many studies [123].

Clair et al. [11] conducted a numerical and experimental study into the effect of sinusoidal leading edges on aerofoil gust interaction noise, showing a reduction in sound power levels of approximately 3-4 dB, without any effect on aerodynamic performance. Further studies have been carried out describing the noise reduction dependence on the geometric parameters of the leading edge. Roger et al. [74] noted that the AoA is independent of the noise radiation, but it is strongly dependent on the chord based Strouhal number. Regarding the impact of the freestream speed, the authors referred to the Mach number, instead of the often quoted Reynolds number, to describe the influence of noise reduction. The integral length scale of the isotropic turbulence generated by the grid appears to play a significant role in noise generation, and hence also in its reduction.

Haeri et al. [124] and Narayanan et al. [12] have shown that the serration amplitude is primarily the factor determining noise control performance. Chong et al. [125] carried out a study with twelve sinusoidal leading edges of turbulence leading edge interaction noise. They showed that greater aerofoil reduction noise can be connected with the largest amplitude leading edge and the smallest wavelength, whereas a small amplitude and large wavelength is preferred regarding aerodynamic performance.

In recent years, Biedermann et al. [126] conducted an experimental aeroacoustic study to determine the influences of the five affecting parameters on broadband noise emission, and to reduce the turbulent flow of serrated leading edges. It was noted that the Reynolds number (Re) and the turbulence intensity (Tu) contribute to the emissions of broadband noise.

The main factors for the effective broadband noise reduction were the amplitude of the serration (A/C), the Reynolds number, (Re) and the wavelength of the serration (λ/C). The broadband noise was most efficiently reduced by large serration amplitudes and small to medium wavelengths. In addition, counter-rotating vortices on the lower edges of the pressure side could be visualised, and are thought to be the principal mechanism for reducing broadband noise radiation. Camara [127] conducted detached eddy simulations for passive stall control of a sinusoidal leading edge. The flow topology on the suction side of the leading edge of the aerofoil is shown in Figure 2-22. Immediate vortical structures were visualised, with these streamwise structures being seen to form in the valley(s) of the leading edge and propagating to the trailing edge. Skillen et al. [18] performed LES simulations for the flow over a symmetrical NACA0021 aerofoil with leading edge undulations. Figure 2-23 shows slices of the streamwise vorticity providing an insight concerning the strong spanwise velocity gradients and the formation of secondary flow. It is believed that low-inertia near-wall fluid is transported away by the secondary flow, whereas high-momentum fluid is drawn from above, re-energising the boundary layer.

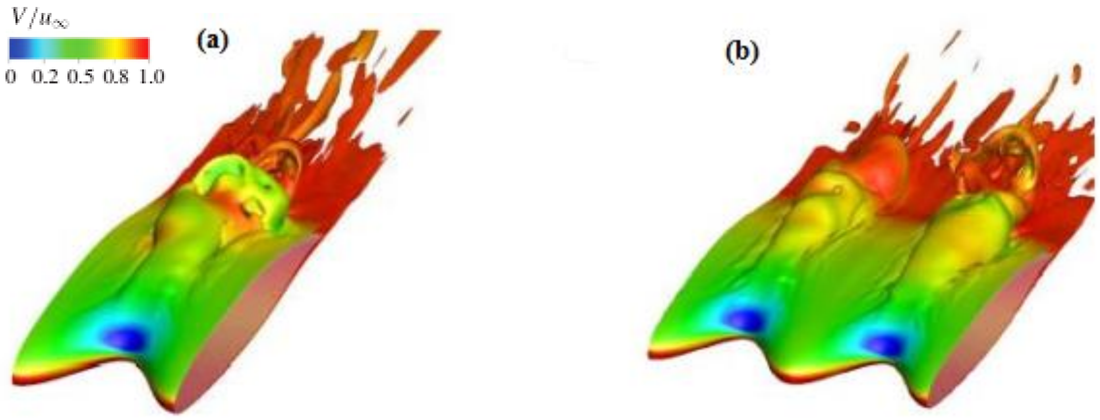

Figure 2-22: Instaneous flow fields NASA LS(1)-0417 of the serrated leading edge at an AoA of 7.5 deg.; (a) S1 model single wavelength, (b) S2 model double wavelength [127].

Figure 2-23 shows streamwise vorticity slices that provide an insight into the high spanwise velocity gradients and the secondary flow formation. The secondary fluid is believed to be transported away by low inertia close to the wall, while high momentum fluid from above is drawn in to re-energise the boundary layer behind each chord peak, and delaying separation. The surface flow along the suction side, showing the average time wall shear stress lines, has also been provided by Skillen et al. [18], as shown in Figure 2-24, which depicts the direction of flow, and its separation and reattachment. A strong flow acceleration between the undulating peaks can be identified, which is supposed to increase turbulence levels. The main separation line in the midchord of the aerofoil shows a strong spanwise variation (possible in this region) to a complex 3D flow field. Shear flow is supposed to generate a large vortex system along this separation. The results of experiments have shown a large noise reduction in the frequency range between 0.3Hz and 4 kHz. With increasing serration amplitude, the reduction of the ΔPWL is generally increased. The effect of amplitude and wavelength seem mainly to follow a continuous dependency. The larger the amplitude, the higher the noise reduction. The apparently opposing effect of the wavelength is of minor influence. In addition, it has been noticed that the higher the velocity, the lower the noise reduction influence [124].

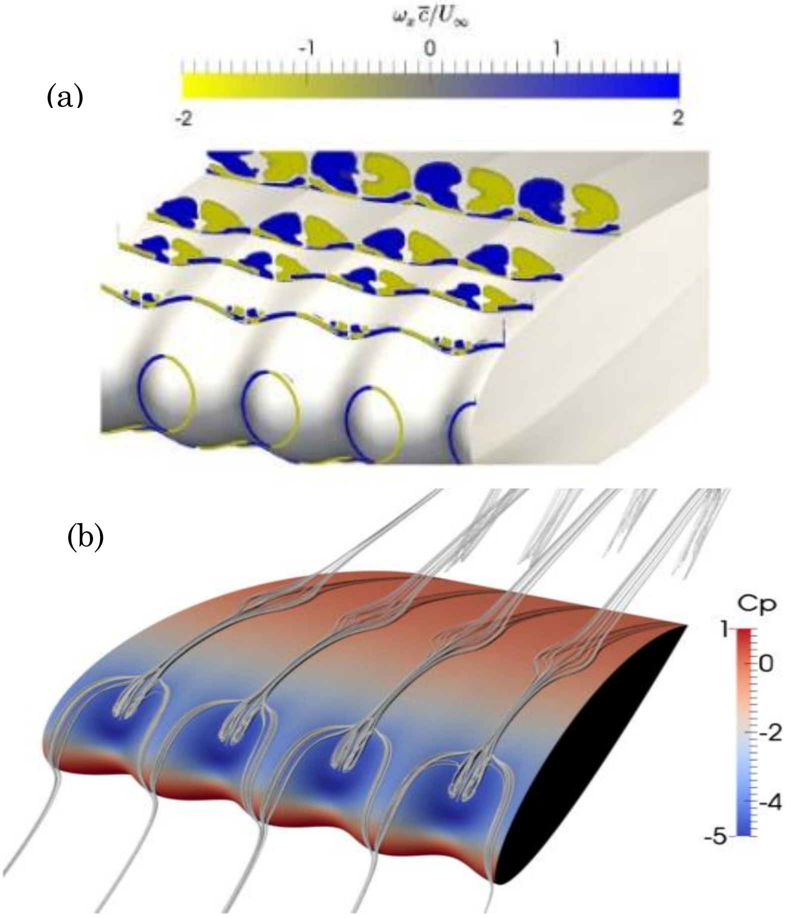

Figure 2-23: Colour slices of (a) streamwise vorticity averaged by time average, (b) streamlines with average time showing the secondary flow for pressure coefficient. [18].

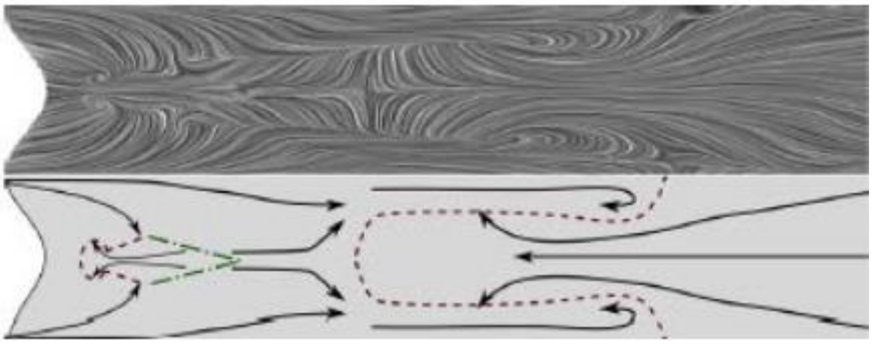

Figure 2-24: Time-averaged wall shear stress (top) and schematic of the flow direction (bottom), with indications of separation (dashed line) and reattachment (dot-dashed line) [12].

The important information for an effective leading edge design [114, 124]. The findings of initial studies show that a certain fraction α of the hydrodynamic wavelength needs to exceed the serration amplitudes.

$$A > (\alpha_{\text{frac}} . U_{\infty})/f_0 \tag{2-6}$$

Where α was found to vary between 0.4 and 0.5. A limited lower frequency f_0 can be defined according to Equation 2-6 [124]. Polacsek et al. [114] proposed defining the wavelength of serration with regard to the spanwise correlation of the length scale of the turbulence and the wave numbers of convection. They justified this suggestion by obtaining effects of de-correlation: if there is sufficient difference in chord among two points and they are fully correlated. This boundary condition appears to be fulfilled if the half wavelength is equal to the length of the spanwise correlation, which is mainly equal to the turbulence length scale of $\Lambda = 6$ mm. The serration amplitude should be set to the highest values with respect to aerodynamic stability constraints in order to achieve the highest noise reduction effects [128].

Chong et al. [129] presented sound results measured in an aeroacoustic facility with no turbulence grid installed into the nozzle. With low turbulence intensity, the leading-edge interaction noise was not the main noise source. The emitted noise from a straight leading edge aerofoil was mostly created from the trailing-edge, as confirmed by the SPL contour color map shown in Figure 2-25(a) (left). Some familiar features affecting the instability tonal noise generated by a laminar aerofoil were discernible: (1) the velocity scaling laws $U^{1.5}$ and $U^{0.8}$ for the broadband-hump and separate tones, respectively; and (2) the ladder-structure of the main tone frequencies that initially follow the $U^{0.8}$ scaling would suddenly jump to another parallel curve with the same $U^{0.8}$ dependence. The radiation of the aerofoil trailing-edge instability tonal noise is only efficient when a laminar separation bubble amplifies the T-S wave. The instability tonal noise radiation measured here clearly indicates the presence of a laminar separation region, which is shown by the shaded regions near the suction side trailing edge of the surface flow visualisation in Figure 2-25(b). The instability tonal noise radiation determined here clearly shows the presence of a laminar separation area, shown in Figure 2-25(b) by the shaded areas near the suction side trailing-edge of the representation of the surface flow.

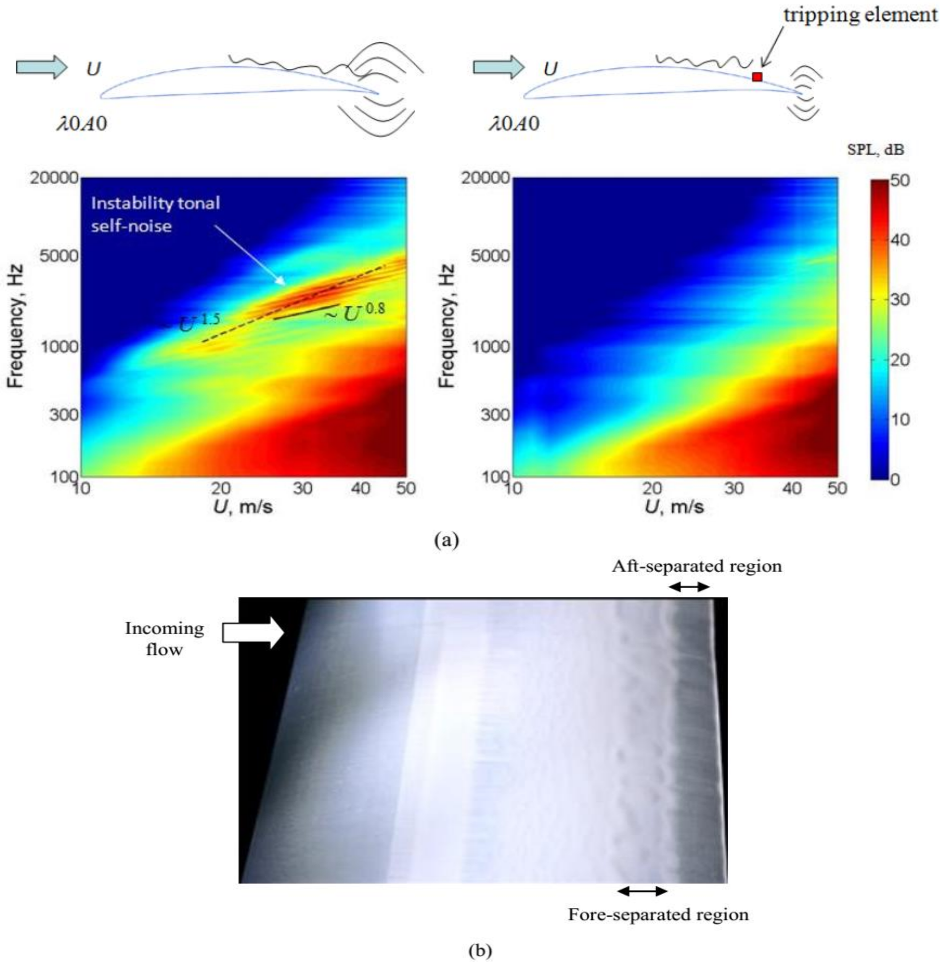

(a)

(b)

Figure 2-25: (a) Sound pressure level (dB) spectra schemed in the frequency and velocity domain for the baseline aerofoil (left), boundary layer tripping tape at $x/C = 0.88$ of the suction-side (right); (b) visualisation for the baseline at the suction-side. $U = 24$ m/s and 0° AoA [129].

Lacagnina et al. [130] presented the noise results measured in an experimental aeroacoustic study when no turbulence grid was installed into the nozzle. They showed that LE serrations are able to decrease the self-noise in a low frequency at negative AoA. The modification on the pressure side is a proof that the leading edge serrations are inducing the flow field at the trailing edge. This inflection can also be recovered in the velocity-spectra, as presented in Figure 2-27. Normalizing the Power Spectral Density (PSD) of the serrated LE aerofoil by the relevant one of the baseline case, it is clear how the suction side is significantly affected by the addition of the serrations, whereas the pressure side shows a significant reduction in the same frequency range where the noise reduction is observed.

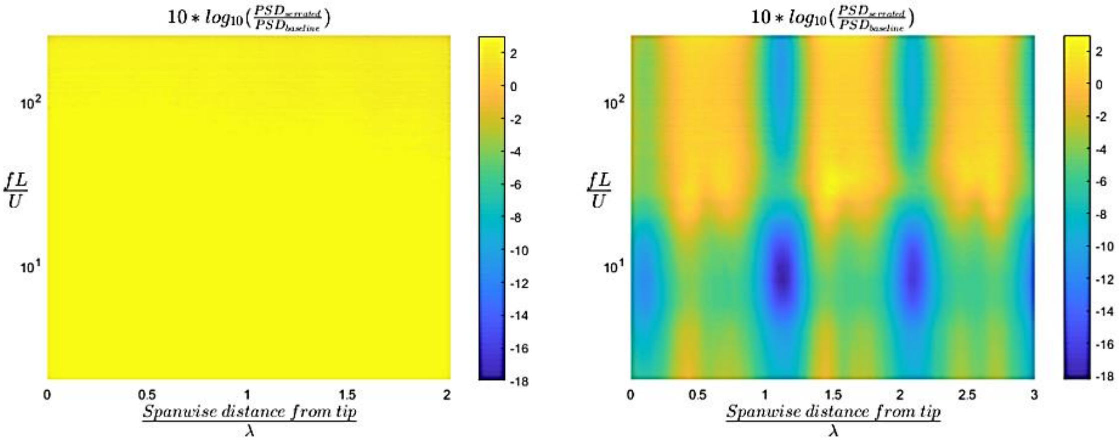

(a) Suction side

(b) Pressure side

Figure 2-27: PSD of the velocity streamwise along the span direction of the serrated aerofoil normalised by the PSD for straight leading edge at 40 m/s [130].

Chong et al. [125] carried out a study with four serration leading edges at low turbulence leading edge. These serration leading edges were studied for their effectiveness in suppressing of the instability tonal noise trailing-edge. The main reduction in aerofoil sound tends to associate with the serrated leading edge of the smallest wavelength and largest amplitude, while there is a noticeable noise rise at high frequency. Serrated leading edge produces strong streamwise vortices at the roots, which propagate downstream to the trailing edge, hence suppressing the separation area locally. Because of the large wavelength, and the vortices not being produced at the tip regions, the flow separation still exists close to the trailing edge. On the other hand, when the serrated leading edge is changed with the $\lambda/C = 0.1$ and a/C = 0.3, where extra streamwise vortices are produced per unit span, the separation area close to the trailing edge is almost totally suppressed, as seen in Figure 2-26.

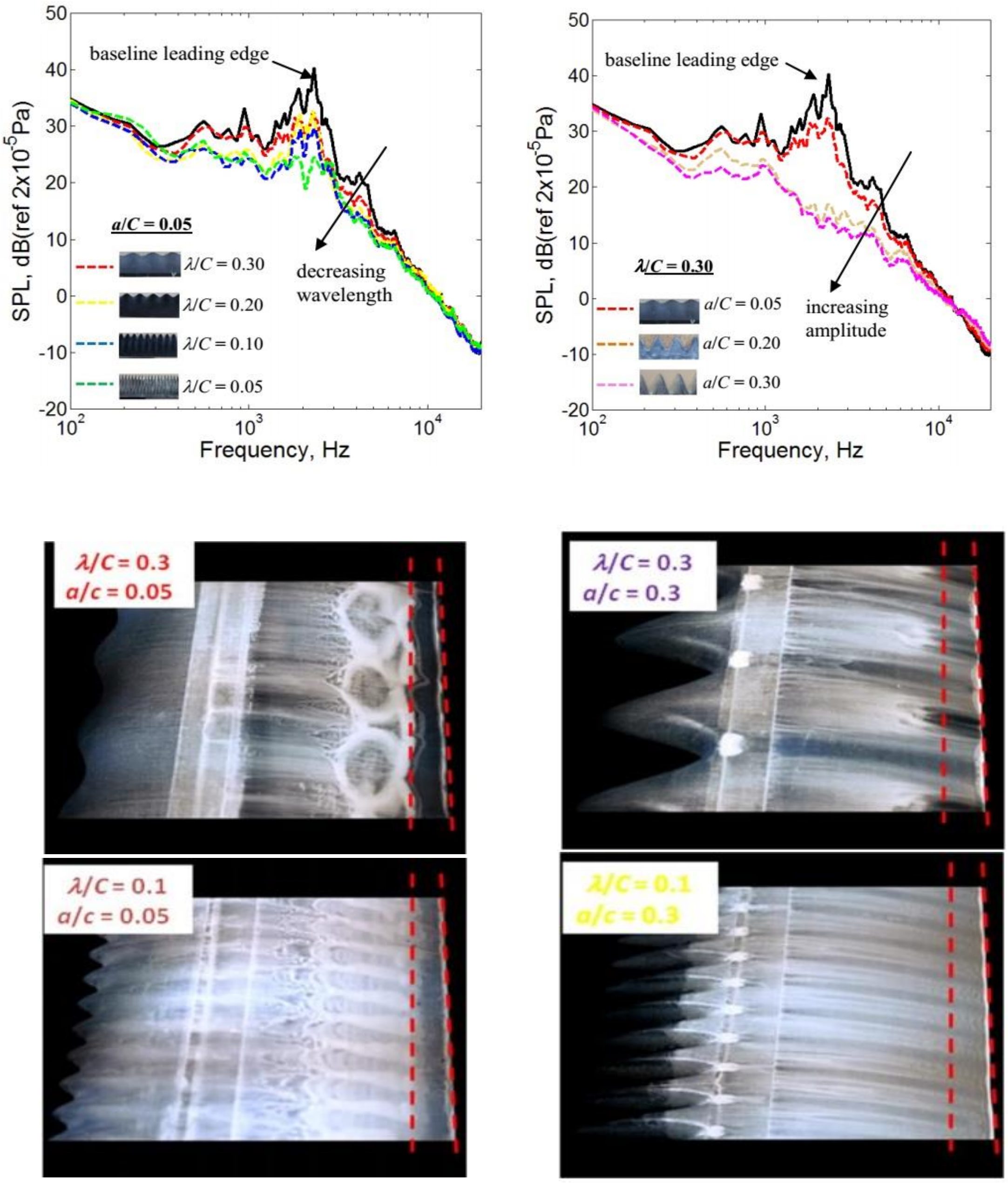

Figure 2-26: Sound pressure level, dB at $U = 32$ m/s, without grid, for the following serration leading edges. Difference in wavelength: $\lambda/C = 0.30$, 0.2, 0.1 and constant amplitude 0.05 ($a/C = 0.05$), and variation in amplitude: $a/C = 0.05$, 0.2 and 0.3 ($\lambda/C = 0.30$) (left). Surface oil flow visualisation for serrated leading edges of different wavelength and amplitude (right) [125].

Biedermann et al. [131] showed that the serration leading edge reduces broadband noise radiations as a result of aerofoil interaction at high turbulent intensity flow. The model was designed to measure the key effect of serrated leading edges as well as the interdependencies of flow and design parameters on the ability to reduce noise. The resulting velocity contours at different streamwise positions for the $A45\lambda26$ case are plotted in Figure 2-28. Increasing the streamwise location within the serration causes a shift of the main tip upwards to the suction side. The nearer the plane is to the serration troughs, the greater the effect of the serration on the fluid flow over the aerofoil. The results indicate that the region of high velocity tends to increase outwards. In the end, both the occurrence surface pressure variation and the scattered pressure are decreased, resulting in the broadband noise reduction. This might be the main noise reduction mechanism using serrations.

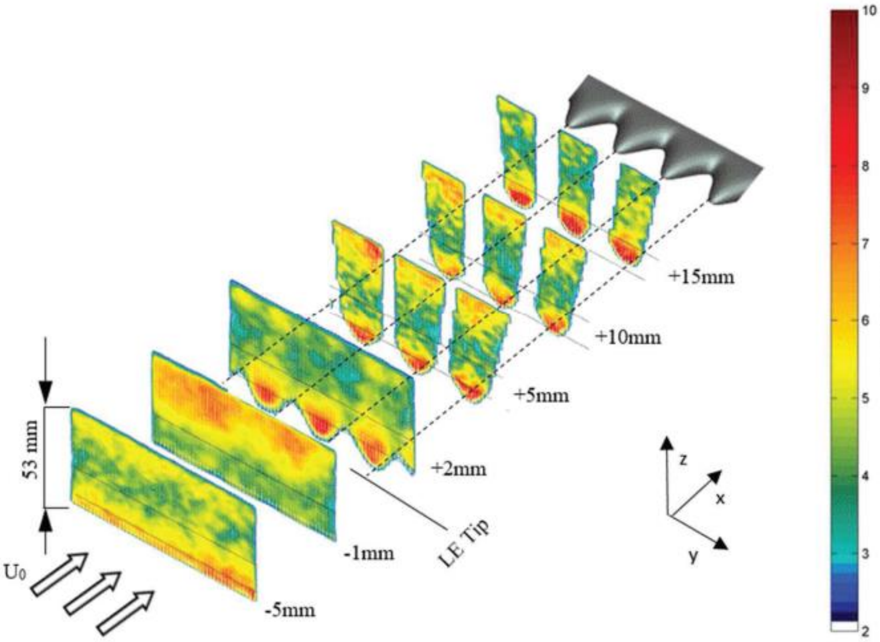

Figure 2-28: Vertical velocity distribution pattern [w] through various streamwise positions using the serrated leading edge of an ($A45\lambda26$). Re = 200000, Tu = 5.5%, and z/H = 0 [119].

Paruchuri [132] presented the influence of leading edge serrations on the fluid flow behaviour around the aerofoil using of PIV measurements. The normal axial flow component shows similar behaviour to the axial flow, as shown in Figure 2-29, which illustrates a zoomed-in view in the district of the LE for the AoA of 2.8°. The deviation in flow around the tip can be seen to be significantly weaker than in the straight baseline leading edge. On the other hand, streamlines emerging from the valley are noted to be developing to greater deviation than for the straight case, suggesting strong mean gradients of velocity. These wide gradients of velocity could be a source of turbulence generation, and thus a source of increased noise.

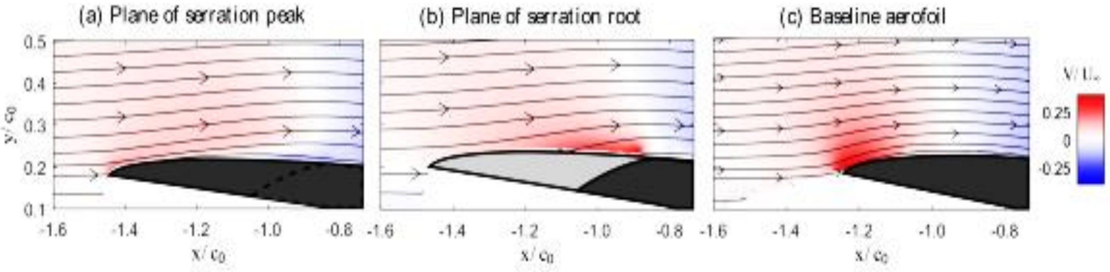

Figure 2-29: Mean vertical velocity contour at the LE of the baseline and serrated aerofoils at 2.8° [132].

Chen et al. [133] who indicated the mean (z) wall shear-stress distribution on the suction side of the aerofoil with and without serrated leading edge. A spanwise secondary flow from the tip to the root of the serration is noticeable, and the wall vorticity was directly proportional to the wall shear-stress in the 1-D flow close to the wall, which enables a contrast to the results of vorticity, as shown in Figure 2-30.

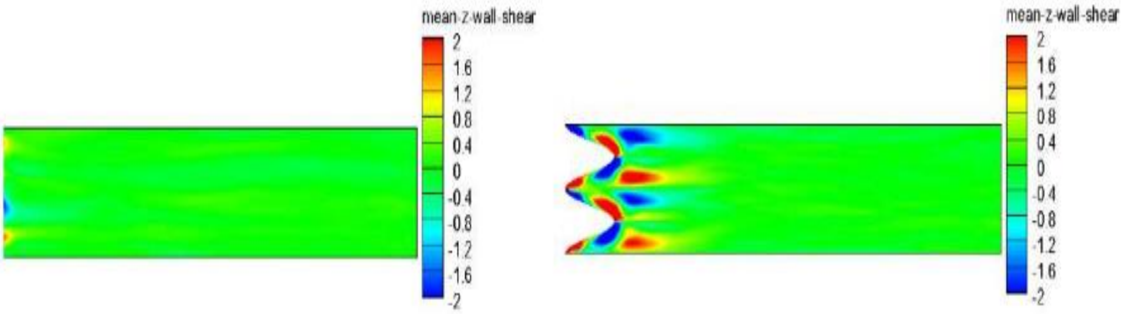

Figure 2-30: Numerical results of mean (z) wall shear-stress distribution above aerofoil suction side for NACA0012 aerofoil with straight leading edge (left) and serrated leading edge (right) [133].

2.6 Leading-edge blowing influence on aerodynamic and aeroacoustic aerofoils

A blowing technique was also tested to control the separate flow. In order to develop periodic perturbations in the boundary layer, small jets are mounted on the leading edge of the aerofoils. The idea is to make streamwise vortices using transverse steady and oscillating flow jets to increase cross-stream mixing and to cause stall suppression at adverse pressure levels. Leading edge blowing is a flow control system recently studied in order to reduce blade vortex interaction [134]. Helicopter rotors are the most common example of such interaction. The tip vortex generated by a blade convects to a subsequent rotor downstream. , whereby the interaction between the tip vortex and the advancing rotor blade results in unsteady blade forces. When the vortex and the blade are parallel, the worst case of this interaction takes place. The noise radiated by this type of interaction directly refers to the distance between the aerofoil and the vortex. Weiland cited a simplified 2D model of noise radiation as:

$$p(x,t^*) \approx \frac{\Gamma LB}{\rho_\infty d^2} \tag{2-7}$$

where, Γ is the incident vortex strength, the lift of the blade L is the lift by the unit length, B is the length of the interaction (i.e. the length over which it influences an aerofoil), ρ_∞ is the density of the fluid locally, and d is the distance of the aerofoil from the vortex [134].

Since the emitted noise is inversely proportional to the offset distance square, increasing the offset distance reduces the noise generated. The leading edge blowing includes a continuous jet fluid in the opposite direction to the input fluid, which has two different effects on the blade vortex interaction. For vertical structures approaching the blade directly according to the leading edge, the jet breaks the incoming structures into smaller and less coherent vortices. Smaller vortices have less strength, exerting less force on the aerofoil, thereby reducing the amount of radiated noise. However, most incoming fluid structures do not directly reach the leading edge. In these cases, leading edge blowing deflects the structure from the blade, thus increasing the offset distance [134], as shown in Figure 2-31.

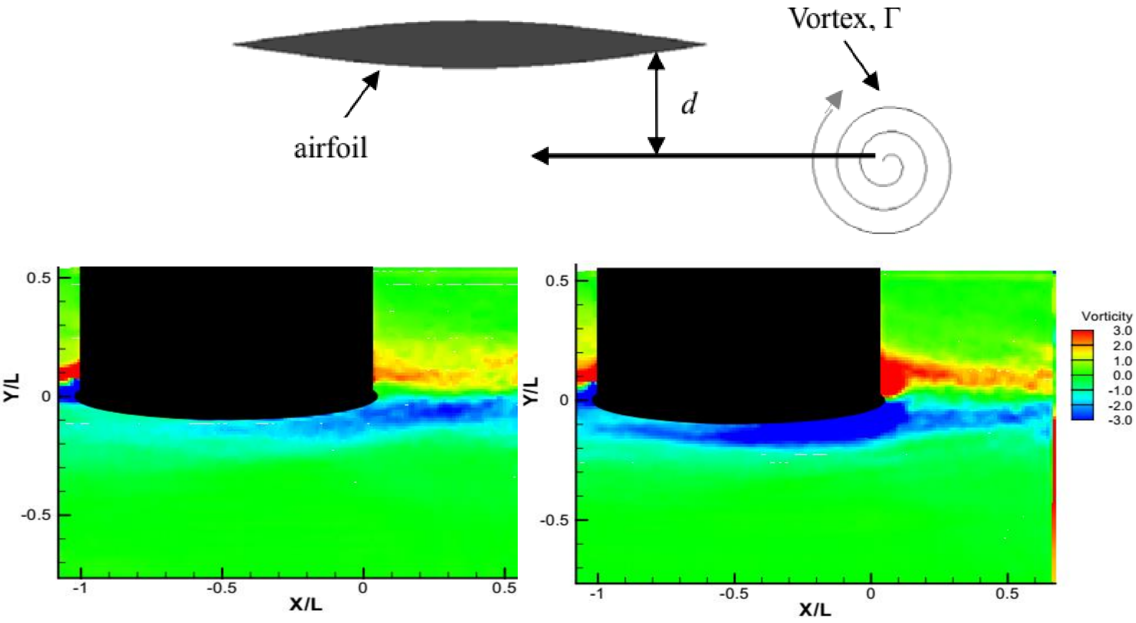

Figure 2-31: Vortex interaction for the parallel blade (top), and average time mean vorticity field with and without blowing leading edge (bottom) [134].

This method was tested by Weiland et al. in a 2D water test using cylinder wake shed to provide force for a symmetrical aerofoil. Changing the cylinder diameter varied the forcing frequency on the blade. Four jet mass flow rates were tested against the 8.4 and 5.8 Hz shedding frequencies. At the highest blow rate, the 8,4 Hz forcing frequency reported a reduction of 26 dB. On the other hand, the frequency was near to the system’s first natural frequency, so reductions were more dramatic. A reduction by 12 dB for a maximum blow rate was observed at a 5.8 Hz forcing frequency [134]. Originally, this flow control technique was designed to reduce the effects of the blade vortex interaction. It had not previously been applied to the situation of a 3D wake shed from a rotor. Weiland et al.’s work focused on the treatment of large, coherent vertical structures at very low frequencies. The technique has not been tested at the higher frequencies shed from a rotor. During these experiments, the speeds of the rotor yielded blade frequencies ranging from 50 Hz to 240 Hz, which were several times larger than those tested by Weiland et al. In addition, the flow field created by a rotor does have fundamental differences from that created by a cylinder in crossflow.

Furthermore, the flow field produced by a rotor has fundamental differences from that created by a crossflow cylinder. This study investigates the extent to which this technique works in the most complicated rotor wake flow.

Malovrh and Gandhi [135] showed that a 14.4 dB reduction is achieved in BVI noise by increasing the vortex stand-off from zero to half chord length (for example, with the blade penetrating the vortex). They also showed that changing the missing distance of the convecting vortex resulted in a smaller reduction, as long as the vortex was penetrated by the aerofoil. Ideas to increase the missing distance include active trailing edge flaps to affect the vortex path, and consequently the missing distance. Figure 2-32 explains the variation in maximum BVI noise levels with simultaneous differences in the two parameters. If the vortex centre is kept constant and its length is slowly decreased (moving down lines parallel to the Y-axis), which is equivalent to decreasing the blade area caused by the interacting vortex at the fringes of the vortex, the noise levels of BVI are seen to decrease.

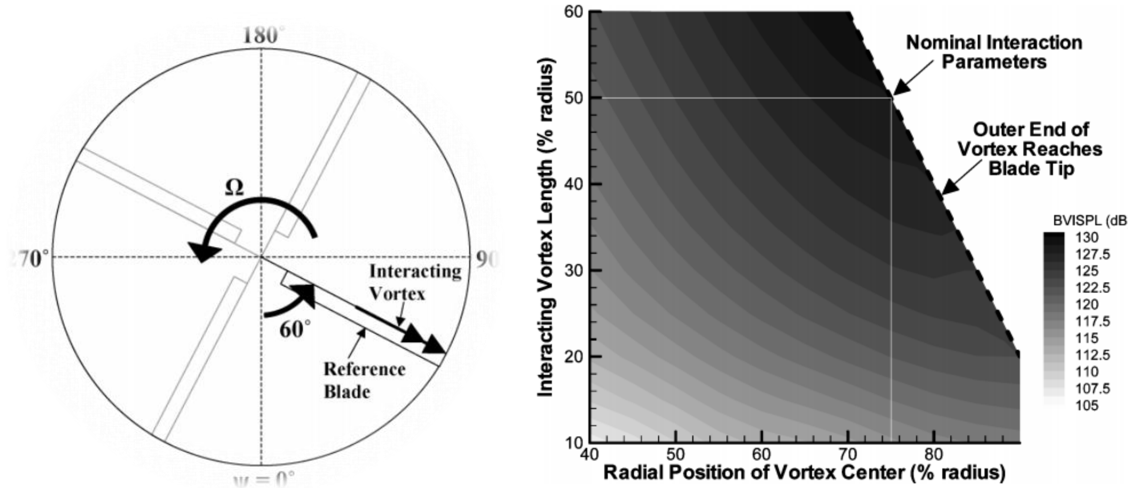

Figure 2-32: Vortex interaction geometry-baseline blade(left),and maximum SPL against the spanwise position of center interacting (right) [135].

While Howe [81] identified potential sources of broadband noise, Slomski tried to determine the cause of discrete tones seen in recent navy hydrofoil circulation control tests [136]. Early analyses revealed that the tones followed traditional scaling of the Strouhal numbers by lip thickness l and slot jet speed. Using LES, Slomski confirmed that the tones were actually attributed to a vortex shedding from the slot lip. He also simulated the influence of various lip modifications on the far-field acoustic spectra. The lower surface of the lip was reduced, but the tone was not completely eliminated. A sawtooth-patterned lip successfully eliminated the tone by breaking the noise producing vortices, as shown in Figure 2-33. Studying the separation control of an incompressible and compressible flow with pulsed jets, Slomski tested an aerofoil NACA-4412 section with a leading-edge flap.

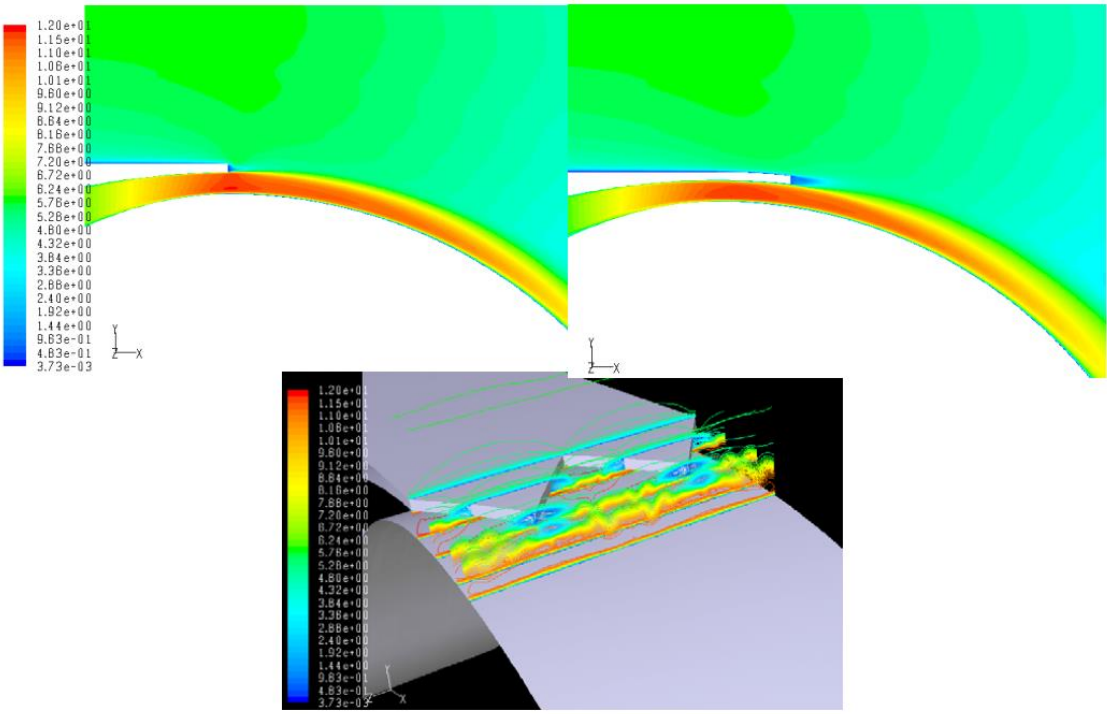

Figure 2-33: Colour maps of the mean velocity magnitude in the jet at the mid-span (left), and streamwise through one of the apexes of the sawtooth (right). At the bottom are colour maps of mean velocity along the serrated trailing edge in spanwise crossflow planes [136].

The leading edge flap was prepared with flow control actuators, each consisting of a cross-flow jet with 90° and 45° angles of pitch and screw. High velocity flow control valves were used individually to control the pulsed flow to each jet. The leading edge had three jet nozzles, but only two were used. An open and close valve cycle was used to manipulate a computer function generator, driving a power supply for the solenoid valve. The valve controller permitted pulse rates of up to 500 Hz and volume flow rates of more than 20 slugs per minute per jet. A constant average air mass flow was provided to the jet with a closed loop servo valve. Slomski's data showed that maximum lift improvements occur with a jet-pulse Strouhal number of about 0.6 [136]. On the other hand, McManus and Magill [137] found that the pulsed jets caused a lift increase of up to 50% and $\alpha \leq 10°$ for the baseline case, with the efficiency being found to decrease as the Mach number increased. The best results were obtained when the AoA was the same as the of CL_{max}, as shown in Figure 2-34.

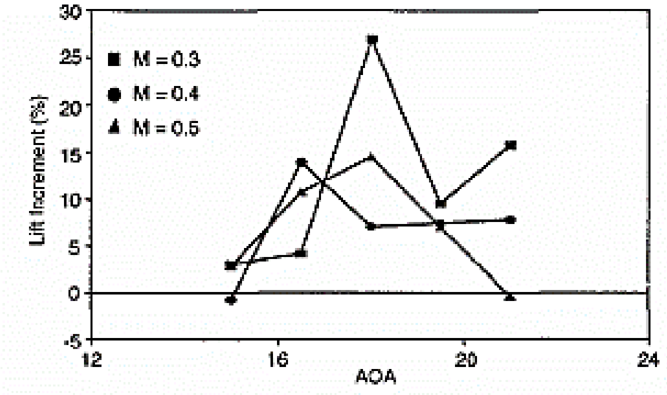

Figure 2-34: Lift improvement with pulsed-jet separation control [137].

Seifert et al. [68] investigated oscillatory blowing on an NACA0015 aerofoil trailing edge flap. They activated jets mounted on the upper surface above the flap hinge in a 2D slot. The aerofoil was placed at a 20° AoA, as shown in Figure 2-35. The authors concluded that there was no impact of steady blowing on lift or drag, but modulated blowing caused an increase in the lift and reduced the drag by half. The dynamic blowing and suction of synthetic jet actuators can be used effectively. Synthetic jet actuators based on piezoelectric equipment are the most effective at the device resonance frequency, and are limited by the cavity's natural frequency. These actuators have been shown to be useful in the laboratory, but may not be as effective in practice.

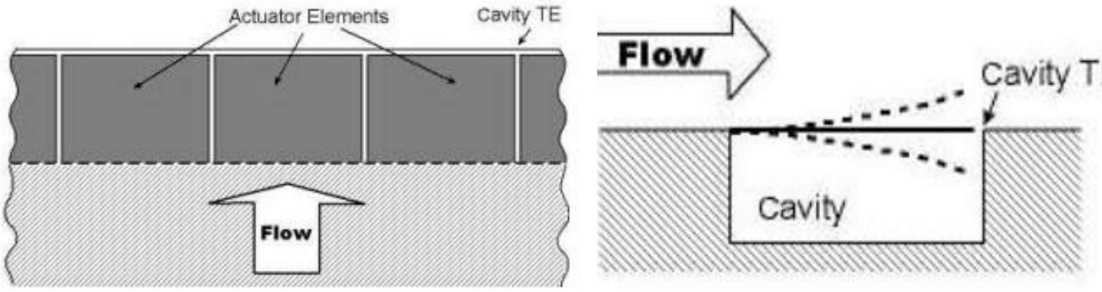

Figure 2-35: The application of ten surface mounted Piezo “benders” on the aerofoil for separation control [68].

The actuator designed by Rao et al. [138] is essentially a small positive displacement machine. The same team designed a similar device and tested an aerofoil NACA0015 with a ringed leading edge containing six reciprocal compressors, operated by two DC motors. These compressors and pistons produced a synthetic jet on the aerofoil’s leading edge (zero mean flux). They found that the flow separation control was shown at AoA and freestream speeds of up to 25° and 45 m/s, respectively. These actuators may have overcome some of the problems found with other designs, but they are complex machines that require high speed linear oscillatory motions as well as complex mechanical components.

Williams and Howe [139] continued to study circulation control for a rotary airplane with investigation into a 20 percent thick elliptical circulation control aerofoil with a 5 percent camber. The upper surface blowing slot was at the normalised chordwise position of $x/C = 0.973$, and the ratio between the chord and height of the slot was $h/C = 0.00128$. The aerofoil was designed with zero AoA for maximum efficiency, and a lift coefficient from 1.0 to 2.0. Within this desired lift coefficient range, the aerofoil generated a higher lift-to-drag ratio than other high-lift systems. The authors also added a trailing edge flap to the aerofoil to determine the feasibility of a circulation flow control wing for a fixed wing airplane. They determined that in the absence of an impractical distance from the Coanda surface, free-floating flap reduced lift growth; they proposed an alternative retractable flap.

Abramson [140] conducted the first Navy double-slot aerofoil circulation control tests between 1986 and 1987, although the results were not reported until 2004. The objective of the experiments was to determine whether the inclusion of a lower opposite blowing slot could expand the aerofoil's operating lift range without interfering with the flow of the curved wall jet. Tests were performed on an aerofoil with a 1 percent camber and 17 percent thick elliptical circulation control. An upper slot, placed at $x/C = 0.969$, and a lower blowing slot, placed at $x/C = 0.97$, were used to separate air supply plenums, which were individually tested. The experiments elicited that the presence of the lower slot did not inhibit upper blowing performance (and vice versa), and the blowing of the lower slot was successful in doubling the aerofoil lift range, as shown in Figure 2-36.

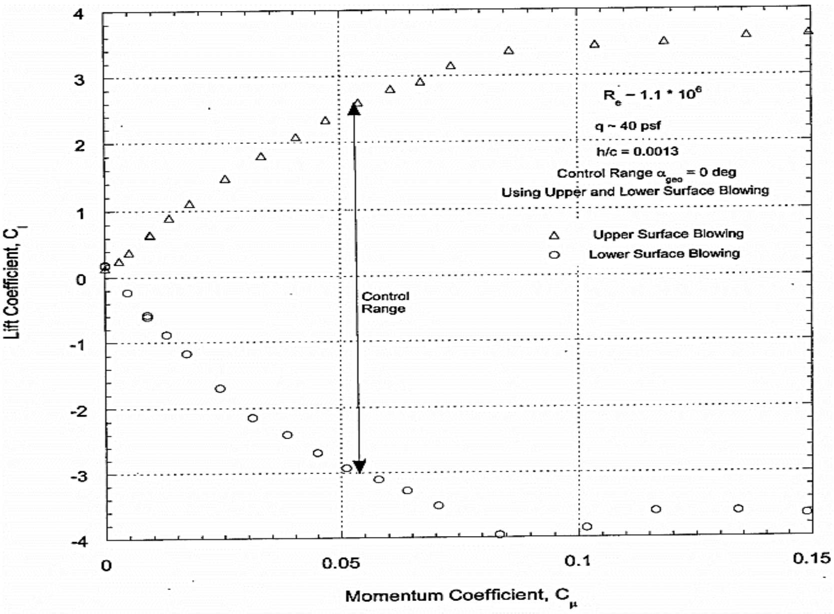

Figure 2-36: Aerofoil control range at fixed AoA [140].

Kobayashi and Fujisawa [141] deployed an experimental device consisting of a flat plate that allowed a plane wall jet flowing over it to become completely turbulent and similar, followed by cambered or concave plates of various radii. The ratio of the slot-height (measured on the flat plate) to the curvature radius varied from 3.2×10^{-3} to 8×10^{-3}. Hot wire anemometry was used to measure speed, and Stanton tubes to measure wall shear stress. The tests were carried out at slot Reynolds numbers from 1.7×10^4 to 2.6×10^4. Speed and distance from the surface were normalised with U_m and $y_m = 2$ (also known as jet half-width) in a mean tangential velocity profile of all types of surfaces.

The underlying flow physics related to active flow control utilising a low Reynolds number and 3D aerofoils at high attack angle were revised with novel test data for a low-AR aerofoil with leading-edge empowering attached on a pitch–plunge instrument in an unsteady wind tunnel. The flows of unsteady and transient created by leading-edge actuation (Figure 2-37) were investigated with both short-duration and continuous pulse of actuation. the main scope was limited to fluid-dynamical and control issues, and some information was omitted for brevity. The study implemented examination strategies for closed-loop flow and flight control utilising actuation of leading-edge whirls [142].

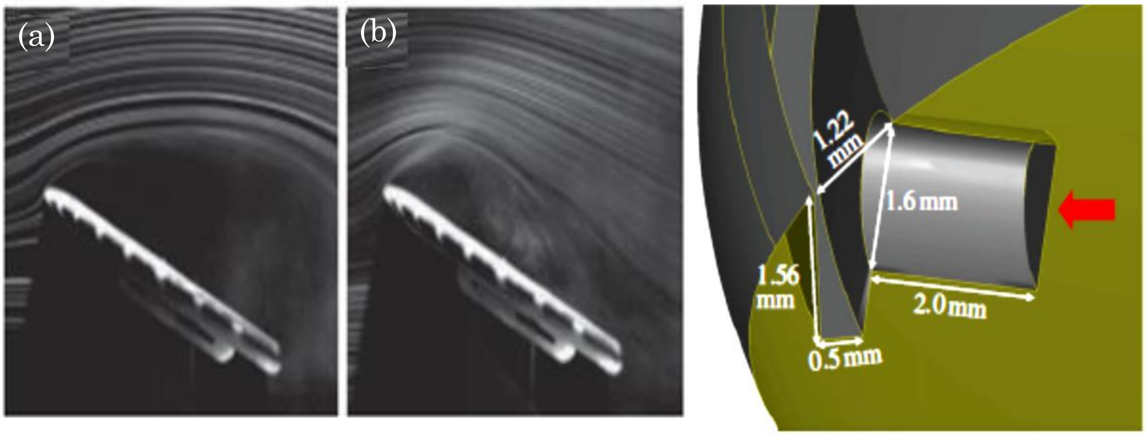

Figure 2-37: Visualization of the (a) baseline and (b) actuated in the mid-span flow over the aerofoil at $\alpha = 20°$, $U = 5$ m/s, $Uj/U = 2$ (left), and the semicircular aerofoil involved leading-edge actuators [142].

Jonathan et al. [143] investigated a non-circulation controlled wing with an active leading edge slot circulation control data for a case study of a 10:1 aspect ratio elliptical aerofoil (Figure 2-38) with a chord length and a span of 11.8 and 31.5 inches, implanted into the Closed Loop Wind Tunnel of West Virginia University, experiencing fluctuating wind rapidity (80, 100, and 120 ft/s), attack angle (0-16°), and coefficients of blowing alternating from 0.0006 to 0.0127, reliant on the pressure of the internal plenum. A trend was established concerning the effect of the circulation control exit jet on the stall features of the wing. They observed that when the circulation control is in utilisation on the 10:1 elliptical aerofoil, the stall angle drops from 8° to 6°, while creating up to a 46% escalation in the coefficient of lift [143].

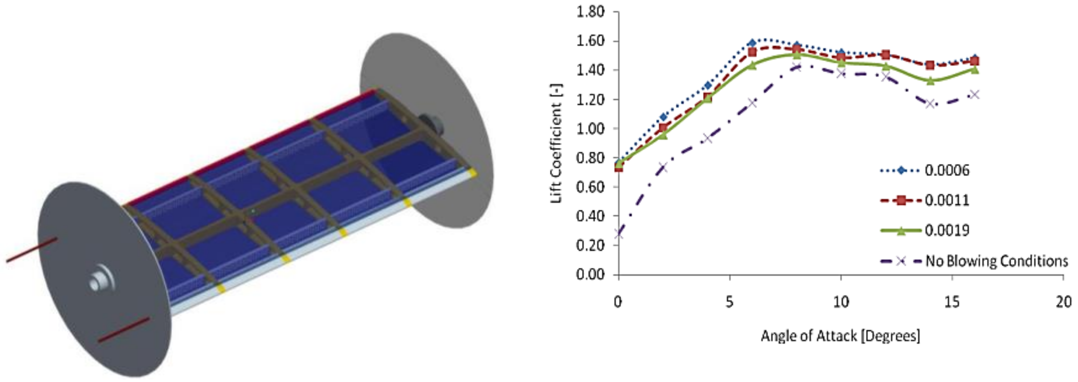

Figure 2-38: Aerofoil and slot design and lift coefficient against AoA [143].

Outcomes of experimental investigations on the influences of steady leading edge blowing on the flow of supersonic above an open cavity have been reported (Figure 2-39). Three patterns of spanwise-aligned rectangular slits were utilised to supply air into the boundary layer at the leading edge of the cavity. Varying data on surface pressure were attained to evaluate the efficiency of each control pattern at dropping the loads of pressure in the cavity. The velocity field was calculated for only the most effective design, as determined from the pressure information. Also, these evaluations were implemented to inspect the influences of the leading edge blowing on the stream, and involved both cross-stream oriented and streamwise planes, as shown in Figure 2-39. The study focused on clarification of the criteria utilised to choose particular designs picked for study of the velocity field [144].

Wolf et al. [145] investigated the broadband noise that ascends from the interface of the aerofoil trailing edge with the turbulent boundary layers, and the tonal noise that ascends from vortex shedding produced by trailing-edge bluntness and laminar boundary layers. The authors introduced some aspects of generation and propagation of trailing-edge noise that were not addressed (or which were not totally observed) in previous literature.

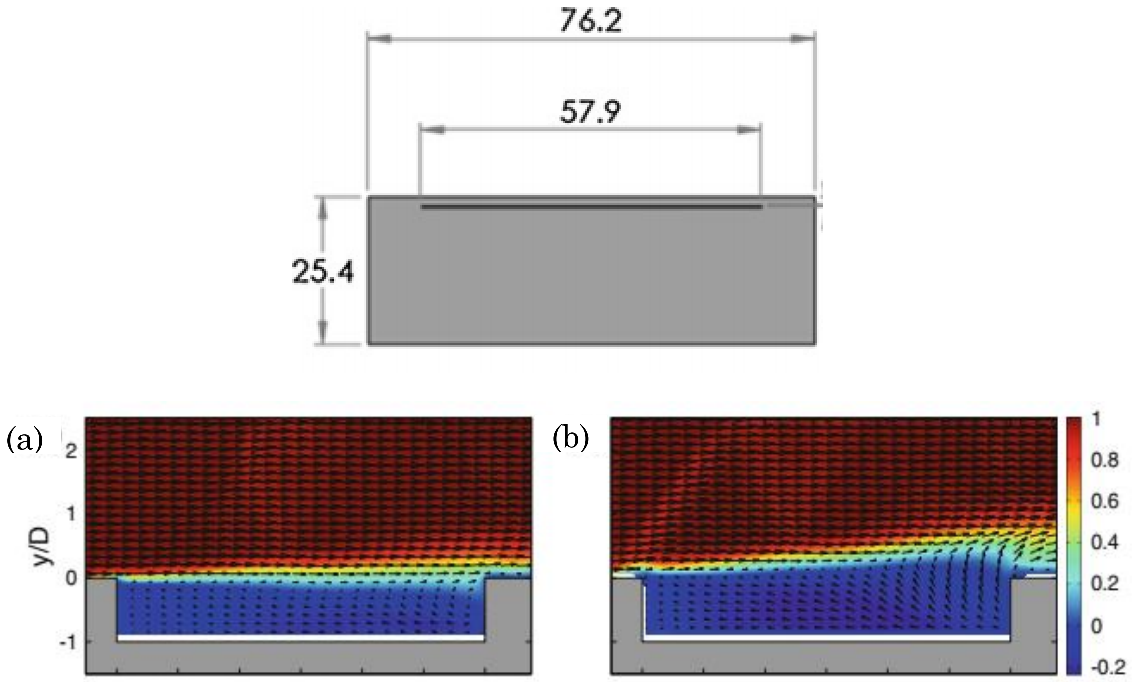

Figure 2-39: Top view of leading edge blocks that display slot settings for streamwise mean velocity fields, (a) baseline configuration; (b) slot blowing configuration [144].

The influences of convection of mean flow on sound directivity and the role of quadrupoles and dipoles for little and adequate Mach numbers for diverse frequency ranges were presented. For otherwise similar flow formations, the influences of stumbling the boundary layers only along the drag side of the aerofoil, or lengthwise along both sides simultaneously were evaluated, and the occurrence of total noise was explored. The turbulent aerodynamic streams investigated offer growth to noise causes at a wide range of frequencies and 3D measures, as shown in Figure 2-40. The study used the numerical method of LES for the flow simulations, in order to capture the most active scales related with noise creation at a reasonable computational rate (compared to DNS). Compressible LES was applied for an NACA0012 aerofoil with rounded trailing edge for four flow patterns. The FWH acoustic analogy formulation was utilised for acoustic predictions, including convective influences. The integrations of surface and volume of quadrupole and dipole source terms acting in the FWH formula were achieved utilising the 3D convective wideband multilevel adaptive fast multipole method (FMM) to decrease the simulation cost of the evaluation of aeroacoustic integrals in the FWH design. The NACA0012 aerofoil sample was selected due to the large computational and experimental statistics set existing in the literature.

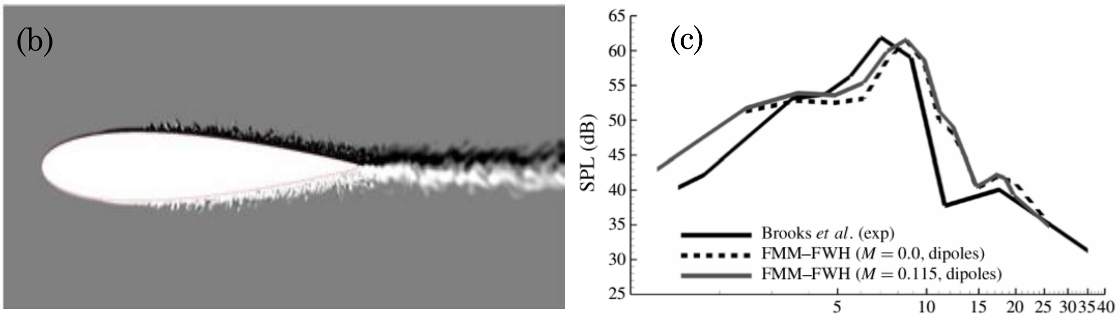

Figure 2-40: (a) Diagram of the boundary layer tripping at 0°, (b) colour map of the spanwise vorticity along aerofoil surface and wake area and view of the mean flow streamlines along trailing edge area, (c) SPL at observer position x = C, y = $7.9C$ and mid-span [145].

2.7 Thesis objectives and scope

The main part of this thesis comprises an aeroacoustic and aerodynamic study of the influence parameters such as Reynolds number, turbulence intensity, blow rates Q', spanwise air hole spacing λ', serration amplitude, and wavelength, as well as the AoA on the emitted leading edge broadband noise of a NACA65(12)-10 aerofoil. Turbulence intensity is an essential parameter, as turbulence is the main cause of leading edge noise. Thus, extensive preliminary hot wire measurements were carried out to provide certain levels of turbulence using a turbulent grid in the wind tunnel nozzle. In addition, the Turbulence Spectrum was analysed to obtain knowledge of turbulence isotropy, which is the initial condition of the aeroacoustic experiment.

The flow profiles of the nozzle outlet were recorded using hot wire anemometry and Pitot Tube measurements, to determine how a mounted aerofoil influences the free jet, and to define the conditions under which it is carried out. Four serrated leading edges with different amplitudes and wavelengths were analysed, and two straight blowing leading edges, by varying several aerodynamic parameters. Additive analyses of the flow features in “leading edge and within the interstices of the blowing are expected to provide useful information to link the aerodynamic effect of the straight and serration blowing to the acoustic effects of noise reduction. Furthermore, the quantitative results are compared for approaches using serrated, unserrated, and straight leading edge forms with blowing, to demonstrate whether the serration effects on an aerofoil can be mimicked by leading edge blowing. Finally, the aerodynamic and aeroacoustic performances of aerofoil with hybrid serrated-blowing leading edge was studied for the same influence of parameters, to explore innovative advanced designs that offer superior noise reduction in comparison with conventional leading edge serrations.

Chapter 3 : Experimental Facility and Methodology

3.1 Introduction

This chapter discusses the experimental equipment that used in aerodynamic and acoustic measurement.

Brunel University's open-jet wind tunnel facility was used to carry out acoustic investigations. The aerodynamic measurements were performed in an open-circuit suction-type wind tunnel. Flow measurements were performed on the straight, serrated aerofoils and these with blowing aerofoil leading edges through single hot wire anemometry. Note that flow measurements were only performed in a constant condition.

3.2 Aerofoil Design

NACA65(12)-10 aerofoil is used in this experiment to investigate the aerodynamic characteristics and aeroacoustic performance of serrated aerofoils and blowing leading edges. This aerofoil was chosen in the EU-funded FLOCON project as a representative aerofoil for aero engines, which was also used in an empiric-statistical aeroacoustic study [146]. This specific aerofoil has been used in various experimental and numerical investigations at Brunel University London and elsewhere.

The aerofoil is characterised by a high-cambered profile and its asymmetrical shape. Figure 3-1 shows the cross-sectional view of the model, including the dimensionless coordinates and characteristic lines. The chord line is defined as the straight line connecting the leading edge and the trailing edge. An angle of attack of zero is given when the chord line and the incoming flow are aligned. The asymmetric shape of the model leads to the presence of lift forces at zero AoA. The camber of this wing section is defined by the mean line and the thickness distribution. The numbering system for this NACA aerofoil is based on the aerofoil geometry. The The 6 is the series designation and denotes a high maximum lift coefficient and very low drag over a range of operating conditions. The aim of the geometrical shape of the 6-series is to maximise the region over which the airflow remains laminar. However, the drag coefficient is designated to be high outside of the optimum range of operating conditions for this aerofoil, and the 6-series generally shows a poor stall behaviour. This aerofoil is known for high-speed application and is suitable for use in fan blades. The second digit *5* denotes the chordwise position of minimum pressure in tenths of the chord behind the leading edge at zero lift. In the designation the lift coefficient in a frictionless flow CL_f is given by the numbers in the parentheses. In this case the number of $CL_f = 1.2$ is in direct relation to the camber of the aerofoil. The last two digits indicate the aerofoil thickness with a value of 10 percent of the chord [147, 148]. In the current study, manufacturing of the aerofoil model was enabled by the Selective Laser Sintering (SLS) method. Design of the aerofoil model was done with the CAD software NX9.0.

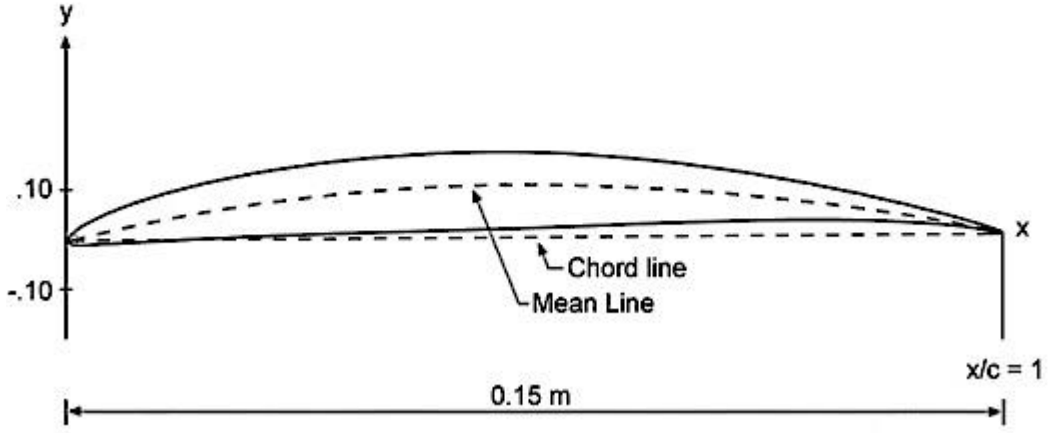

Figure 3-1: Schematic of NACA65(12)-10 aerofoil.

The effect of angle of attack (α) on the aerofoil is aerodynamic and aeroacoustic performances is investigated. It is of interest and great importance to practical applications. Angle of attack (α) the geometrical angle between the centreline at 0° and the actual aerofoil centreline. The geometrical angle of attack is limited to the range of $-10° \leq \alpha \leq +10°$ due to the restrictions of the nozzle dimensions and experimental setup (Figure 3-2).

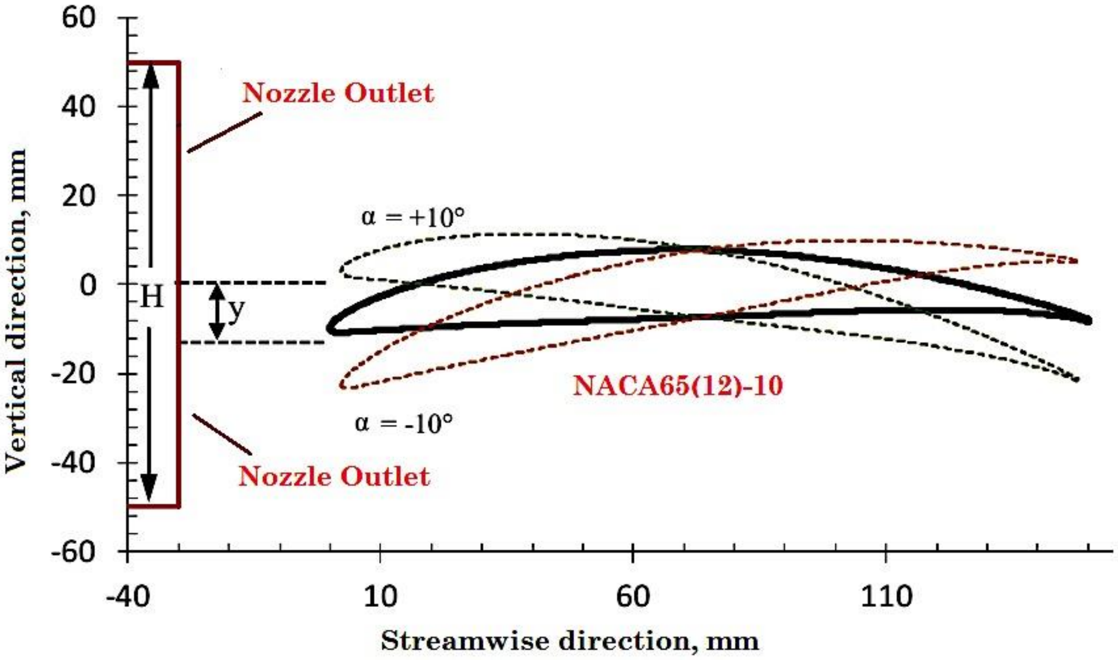

Figure 3-2: Geometrical Angle of attack -10° ≤ $\alpha \leq$ +10°, aerofoil location and nozzle exit in experimental setup are shown.

Figure 3-3 presents the NACA65(12)-10 model installed in the open-jet wind tunnel test section. The aerofoil is 0.495 m span and 0.15 m chord. A potential influence of this shift can be disregarded because the aerofoil is still in the core of the free jet and thus does not affect the noise generation mechanism. The aerofoils are held using clamps into side plates, and are mounted on rotating discs in order to facilitate the change in angle of attack.

This aerofoil is expected to generate higher level of leading edge noise due to its lower leading edge tip angle is taken to ensure that the surface roughness of the aerofoil will not contribute in extraneous noise radiation other than the leading and trailing edge noise. By treating the rapid prototyped and polished aerofoil and its edges with matt black paint and primer filler, the aforementioned extraneous noise radiation can be avoided.

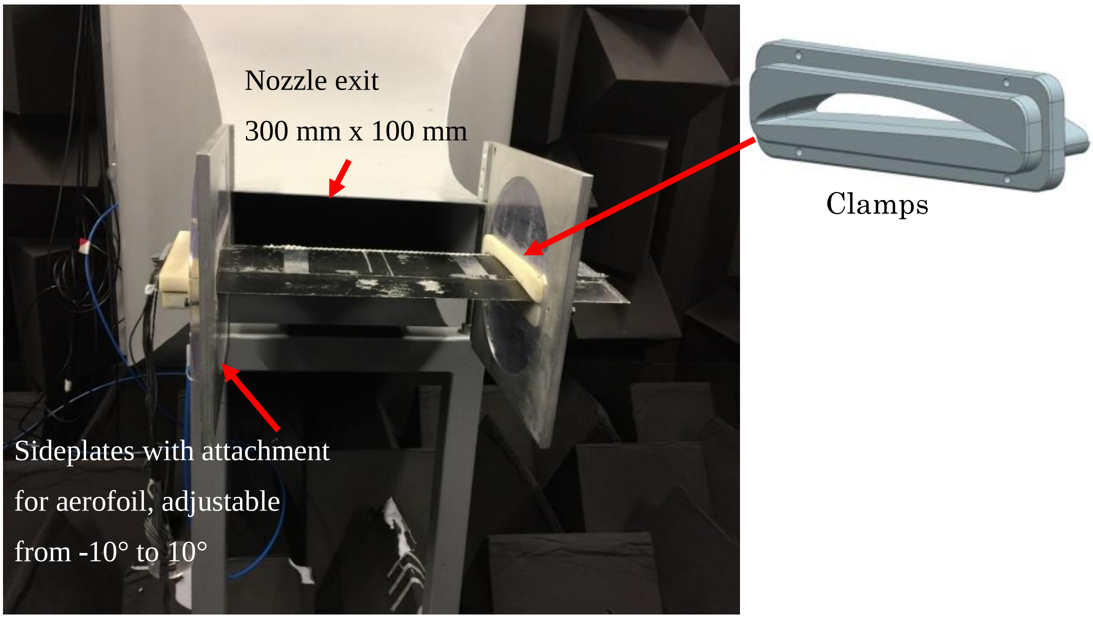

Figure 3-3: Aerofoil fitted on the rotating discs in the open-jet wind tunnel test section.

3.3 Leading Edge Design

The NACA65(12)-10 aerofoil has a section between the leading edge x/C= 0.0, and x/C= 0.33 which can be removed and replaced by various leading edge profiles. Note that x is the streamwise direction, and C is the aerofoil chord. In this study, three types of leading edge profiles were manufactured: the first type is instrumented with orifices at the leading edge, to allow mini-jet propulsion into the incoming flow; the second type is with varies serration profiles, and the third is a baseline leading edge.

3.3.1 Straight blowing leading edge

For the blowing leading edge, jet was supplied by a plenum from inside the aerofoil body, which contains several turning valves that help guide the flow from the air supply pipe to the orifices, as demonstrated in Figure 3-4. The injection of mass airflow is facilitated through the multiple orifices at the front edge. Each of these orifices has a diameter of 2 mm. Two concentrations of the orifices were facilitated by the spanwise spacing ($\lambda' = 5$ and 10 mm). The aerofoil was connected to an external air supply, and the flow rate could be adjusted via a digital valve. The controller and air supply were located outside the anechoic chamber to isolate the valve and other superfluous noise.

The level of leading edge blowing is quantified by the volumetric flow rate through each orifices Q', which is approximately equal to Q/n, where Q is the total volumetric flow rate into the aerofoil, and n is the number of orifices at the leading edge. Clearly this approximation does not take into account of the pressure loss through the internal ducting. Nevertheless, the loss is quite minor, therefore the current approximation should not deviate from the actual value significantly.

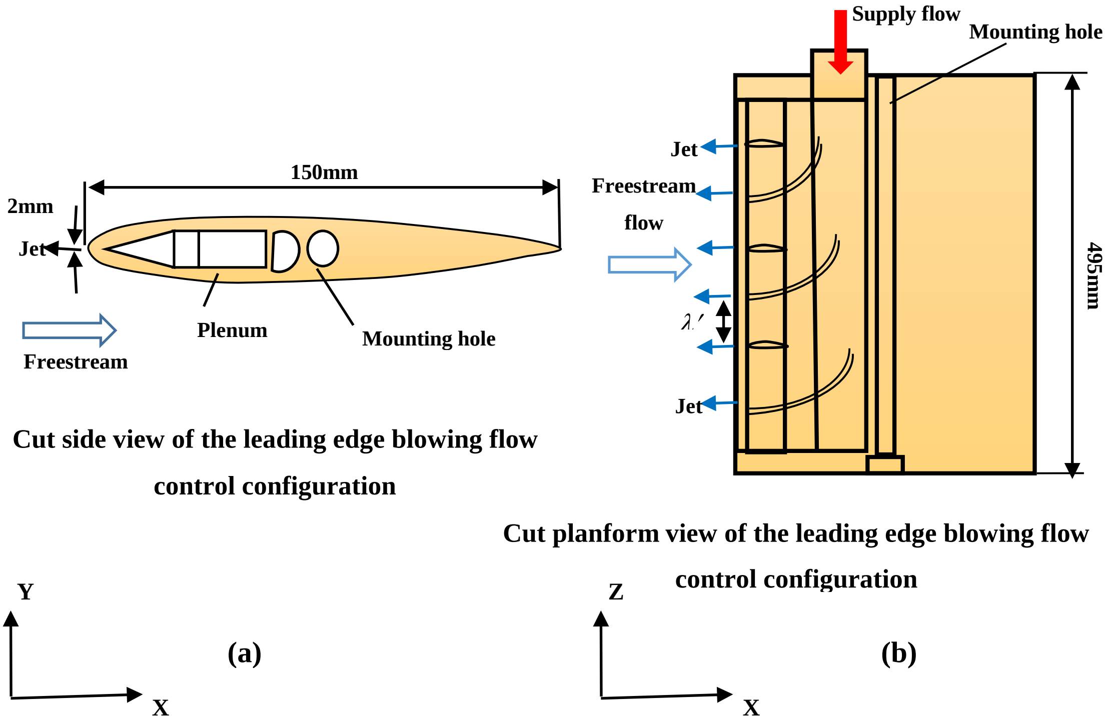

Figure 3-4: Blowing leading edge geometry. (a) Shows the cut side view, (b) shows the cut planform view.exit in experimental setup.

3.3.2 Serrated leading edges

The design of the leading edge serrations can be described by a sinusoidal curve , which can be described by serration amplitude A and the wavelength λ. This study adopted the design principle of keeping the same wetted area between the serrated leading edge and the baseline straight leading edge. This means that the serration peak will extend upstream of the baseline leading edge by $A/2$, while the remaining $A/2$ is cut into the aerofoil main body. This is reflected in Figure 3-5, which shows the 3D model of the aerofoil, including the attachable leading edge design. Within the scope of the current study two amplitudes (*A* = 15 and 30 mm) and two wavelengths (λ = 5 and 10 mm) were investigated. *A* summary of the geometrical details is provided in Table 3-1.

Table 3-1: Geometrical parameters of the leading edge serrations.

Model	***A***	***λ***	***A/*C**	***λ/*C**
-	mm	mm	-	-
Baseline	-	-	-	-
***A*15 *λ*5**	15	5	0.1	0.033
***A*30 *λ*5**	30	5	0.2	0.033
***A*15 *λ*10**	15	10	0.1	0.066
***A*30 *λ*10**	30	10	0.2	0.066

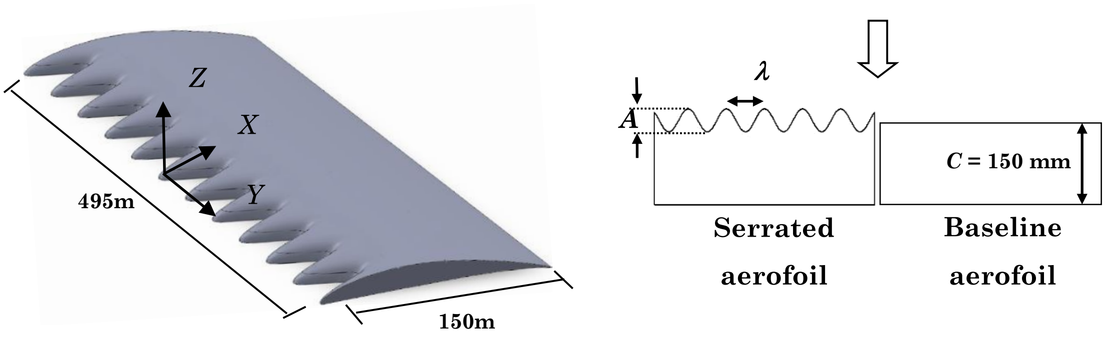

(a) (b)

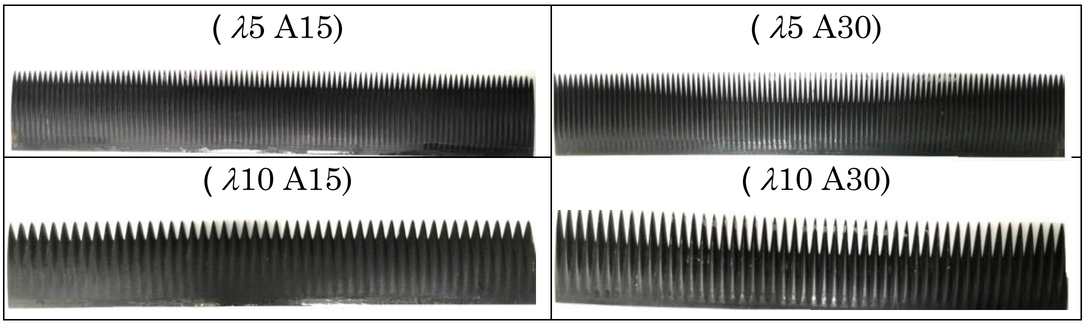

Figure 3-5: (a) isometric drawing of the NACA 65(12)-10 aerofoil model with serrated leading edge, and (b) comparison of drawings between serrated and baseline aerofoils.

3.3.3 Hybrid leading edge (serrated blowing)

This model is instrumented with orifices at the leading edge on the serration roots and peaks respectively. Similarly, the jet is supplied by a plenum from inside the aerofoil body, which contains several turning vanes and ducting system that help guide the flow from the air supply pipe to the slot, as demonstrated in Figure 3-6. The injection of mass airflow is then facilitated through the multiple orifices at the leading edge. Each of these orifices has the same hole area. The aerofoil was connected to the external air supply, whose flow rate can be adjusted via a digital valve. The controller and air supply were located outside the anechoic chamber to isolate the valve and the superfluous noise, as in the previous model described in section 3.3.1 (straight blowing leading edge).

The tolerances of the notches have been kept quite tight, which allows the bodies to join by just pressing them together without the need for additional support. On the other hand, a small gap between the two joined bodies was closed by the use of smooth surface tape. To ensure a high quality surface finish for the aerofoil, the leading edge and the main body were polished with fine grade sandpaper. The roughness of the surface was further reduced when the manufactured bodies were treated with a few layers of primer filler, and finished by spraying them with black matte paint.

The purpose of this investigation is to provide an informational basis on how a serration blowing applied to an existing aerofoil could reduce the generated broadband noise from the leading edge. This requires a constant maximum chord length for practical application because in the majority of cases an increase of the chord length of an already existing aerofoil is not possible.However, a reduced surface in the case of serration results in a reduction of the lifting surface and leads to a loss of aerodynamic efficiently when compared directly to the baseline.

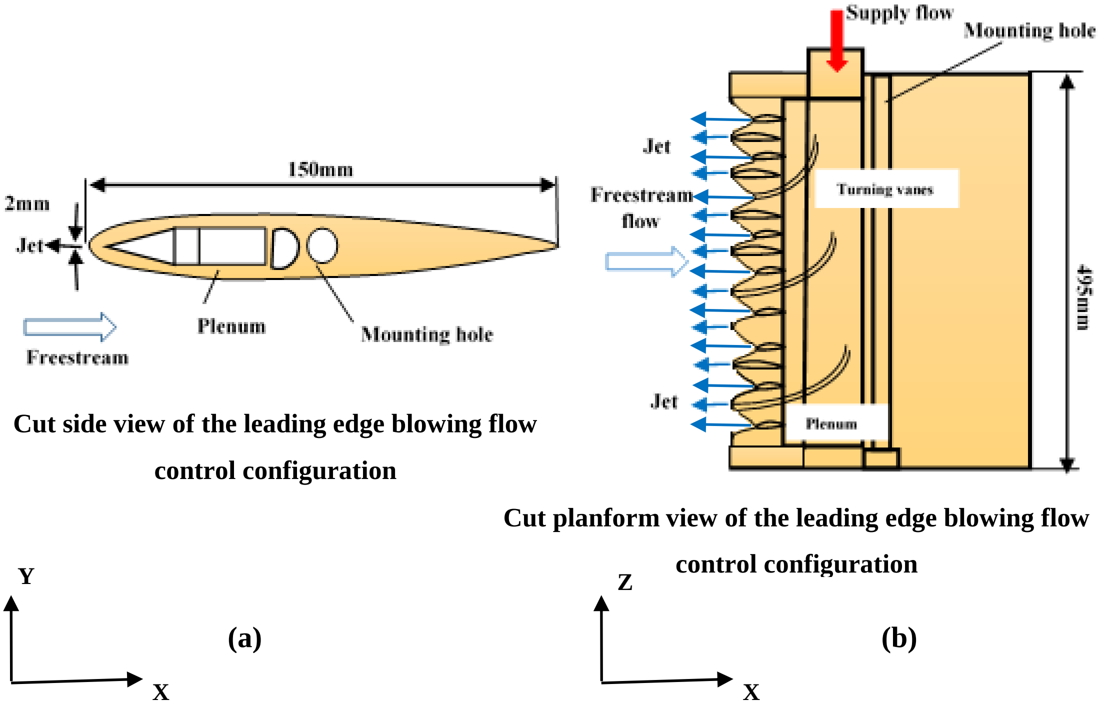

Cut side view of the leading edge blowing flow control configuration

Cut planform view of the leading edge blowing flow control configuration

Figure 3-6: Serrated blowing leading edge geometry. (a) Shows the cut side view, (b) shows the cut planform view.

3.4 Aeroacoustic facilities

3.4.1 Brunel London Anechoic Wind Tunnel Facility

Brunel University's research facility for aeroacoustics is designed for studies of aerofoil noise, mainly in the low to moderate pressure loading configurations. It is a blower type wind tunnel that is capable of producing a maximum mass flow rate of around 3.0 kg/s.

A nozzle with an Area Ratio (AR) of 25:1 was manufactured and installed. The nozzle inlet is 86.7 cm × 86.7 cm, where the outlet dimension is 10 cm × 30 cm.

With the given configuration, the jet can achieve a maximum velocity of about 80 m/s. The nozzle and the test section are placed within a semi-anechoic chamber, with the dimensions of 400 cm (width) × 500 cm (length) × 340 cm (height).

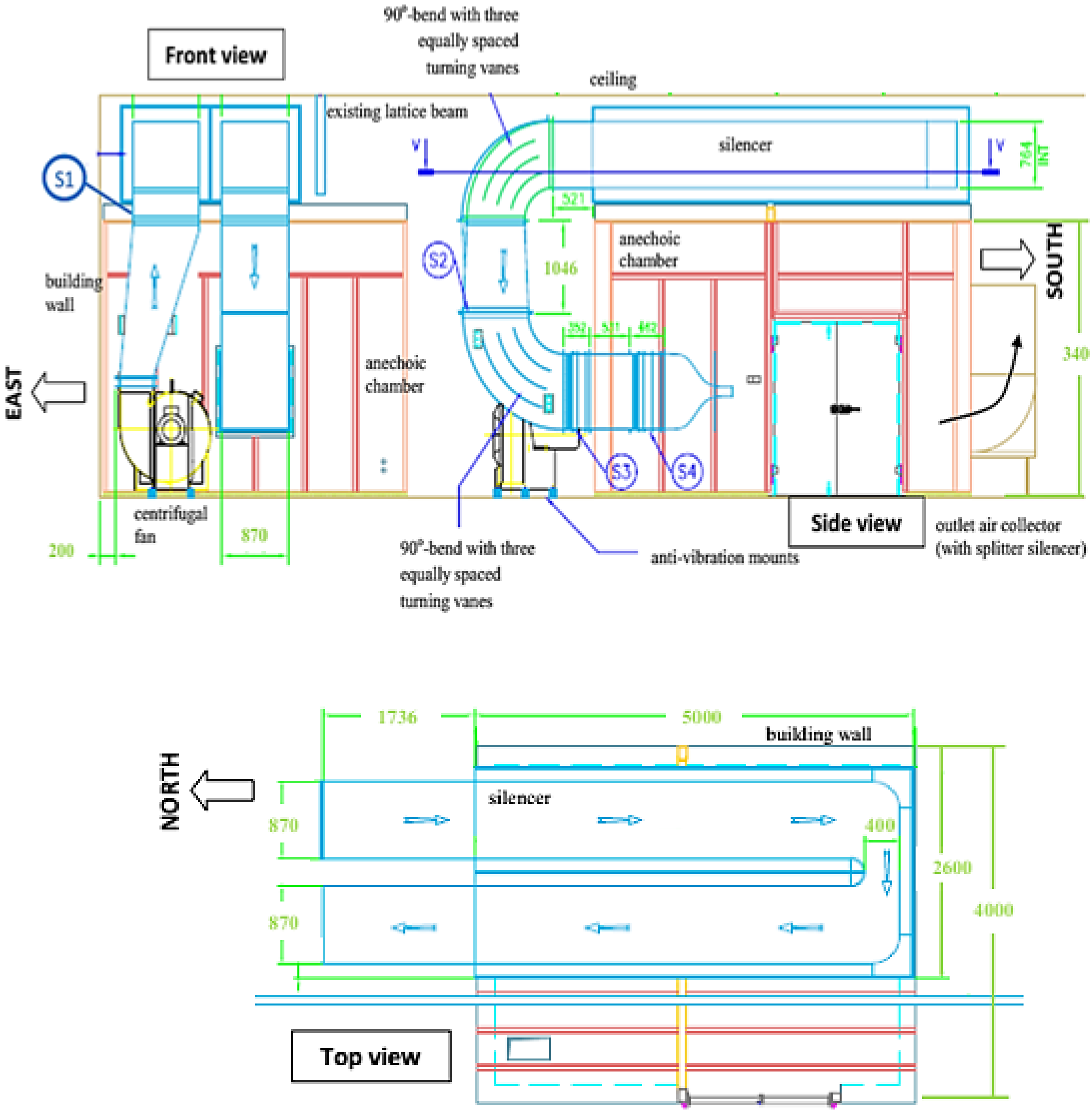

Figure 3-7: Front, side, and top views of the aeroacoustic Brunel wind tunnel facilities [149].

The aeroacoustic wind tunnel's front, plan, and side views are shown in Figure 3-7. A 30 kW AC-powered centrifugal fan was located on the north side, to propel air vertically (via an offset diffuser).

In order to achieve the maximum mass flow rate of 3.0 kg/s, the pressure increase generated by the fan is in the order of 8kPa, after taking into account the cumulative static pressure loss of the components of the wind tunnel. From there, the air extends to a 90 degree bend duct (AR=1) and enters a silencer, which is located at the top of the anechoic chamber. The air in the silencer flows towards the south side before turning 180 degrees at the far end and going through the north side in the opposite direction. The air exits the silencer after reaching the north end and is turned towards the floor by a 90-degree bend duct. At that point, the air expands slightly before turning again by 90 degrees in the anti-clockwise direction, with a constant area duct, entering from the northside into the anechoic chamber. The air is accelerated in the nozzle and discharges inside the anechoic chamber after passing a series of flow conditioning devices (honeycombs and woven mesh screens). The free jet's potential core has a typical range between 0.1% and 0.3% turbulence intensity.

The expanded jet reaches the attenuator of the acoustically lined outlet, bends vertically upward through a splitter-type silencer, and exits the anechoic chamber.

The electrical inverter digitally adjusts the current input into the centrifugal fan, thereby accurately controlling the nozzle's mass flow rate (the exit jet speed). Four anti-vibration mounts isolate the centrifugal fan from any possible vibration transmission into the anechoic chamber, and a flexible vinyl tube connects the centrifugal fan with the wind tunnel duct; both of these measures have been proven to be very effective in the vibration dampe.

The silencer is chosen in the form of a 2-pass plenum chamber, all of whose interior surfaces are lined with a basalt wool dissipative liner of 150 mm thickness, with a 4 mm thick facing cloth (Thermal 650 E-glass Needlemat) to inhibit flow delamination.

The basalt wool liners are held together by perforated metal frames. The silencer's outer wall is made of 1.8 cm thick plywood. The acoustic material selection meets the specification needs of low flow resistivity and high density. In addition, woven wire screens and/or honeycombs are located in positions S1 to S4, as illustrated in Figure 3-7, to provide sufficient flow straightening, and turblence conditioning.

A nozzle with AR=25 has been numerically verified to be free from pre-mature boundary layer seperation, as demonstrated in Figure 3-8. This nozzle is used in the current study.

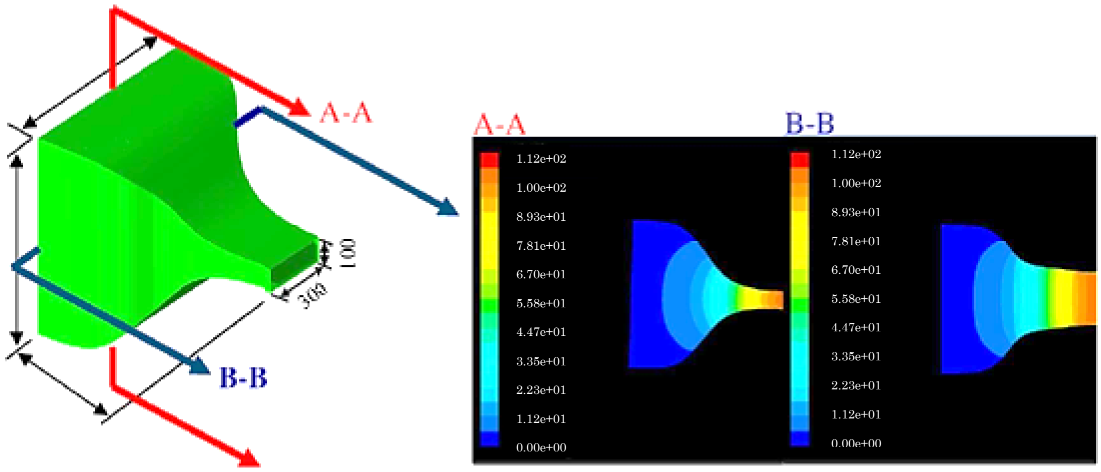

Figure 3-8: Left: 3D nozzle isometric view. Right: Numerical flow field results inside the nozzle, showing velocity contours on planes A–A and B–B [150].

3.5 Microphone Polar array and Acoustic Measurements Metric

To measure far-field noise radiation, an array of 8 G.R.A.S 0.5-inch microphones was located 1.2 meters from the leading edge of the aerofoil along a circular arc, as shown in Figure 3-9. The microphone signals were acquired at 44 kHz for 20 seconds by a 16-bit National Instrument Analogue-Digital card PXI 1042, and the noise spectra were calculated with a window size of 1024 data points corresponding to a frequency resolution of 48.83 Hz and a BT product of about 500, which is sufficient to ensure negligible variance in the spectral estimate [150]. The acoustic pressure at the microphone locations was recorded at the mean flow velocities (U_∞) of 20-60 m/s respectively. Acoustic pressure spectra and directivity patterns can be calculated in an azimuthal range of 60 degrees ($50^o \leq \theta \leq 110^o$, with $\theta = 0^o$ along the jet axis). In the current analysis, sound power level (PWL) and overall sound power level (OAPWL) can be calculated from the microphone array assuming a cylindrical spreading of sound waves from the aerofoil leading edge.

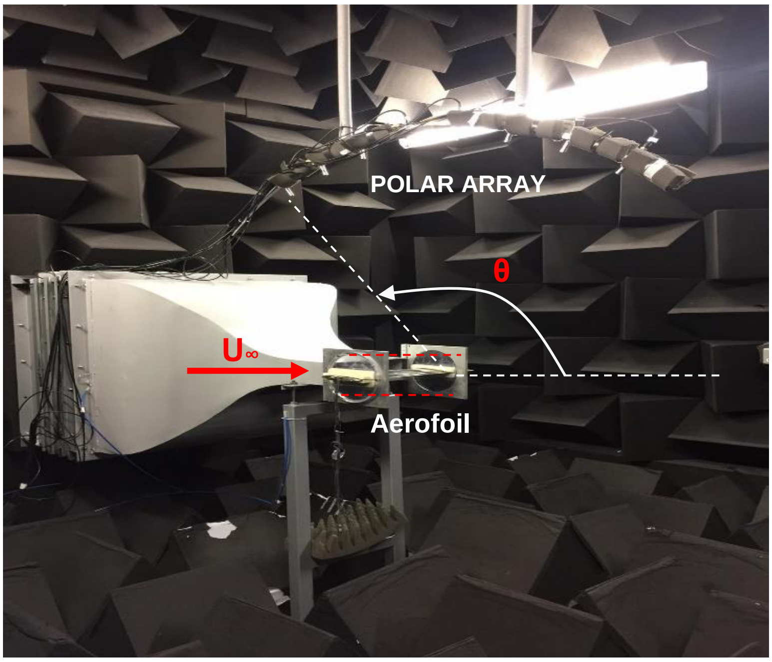

Figure 3-9: Nozzle, aerofoil model and polar array in the large anechoic chamber.

In this thesis, the noise radiation is investigated in terms of the Sound Power Level spectrum (PWL), as defined in Equation 3-1, and measured between 50° and 110° radiation angles (see Figure 3-9).

$$P_{xx}(f) = 2\pi \int W_{xx}(f, \theta_i) . \Delta\theta \,/\rho c0 \quad \text{, where} \quad i=1, \ldots, N \tag{3-1}$$

$$PWL(f) = 10 \log_{10}(\frac{P_{xx}(f)}{P_0}) \quad , 50° < \theta < 110° \tag{3-2}$$

Where $P_{xx}(f)$ is the integrated sound power between the 50° and 110°radiation angles, $P_0 = 10^{-12}\ W/Hz$ is the reference of sound power level of air, $W_{xx}(f, \theta_i)$ is the acoustic pressure PSD, measured at microphone i , N is a number of microphones, a polar angle $\Delta\theta$, θ (rad) between adjacent radiation angles of the microphone.

Aerofoil noise can also be defined by a specific flow rate as the overall sound power level (OAPWL):

$$OAPWL = 10\log_{10}\left(\left[\int_f P_{xx}(f)df\right]/P_0\right) \tag{3-3}$$

Brüel & Kjaer used 4231 pistonphone is used to calibrate and the far field microphones.

3.6 Fluid Dynamic Measurements

3.6.1 Hot-wire anemometry (HWA) and system configuration

Hot-wire anemometry (HWA) is a technique primarily used to measure velocity fluctuations. It is based on the convective heat transfer from a heated wire placed in a fluid flow, whereby the input voltage variation as a result of the charge in flow velocity is the basis for turbulence measurement. Consequently, any change in the fluid flow condition which affects the heat transfer from the heated element can be described with HWA. One advantage of the hot wire probe is the small size of the wire element compared to other instrument, so that the disturbance of the measured flow can be kept as small as possible. Very accurate results can be achieved in carefully controlled experiments. Furthermore, the technique allows the measurement of fine-scale and high-frequency velocity fluctuations. The signal-to-noise ratio of HWA is very good, since it can have very low noise levels [151]. In this study a Dantec Dynamics Type 54N80 multichannel constant temperature anemometer (CTA) was used to measure the velocity fluctuations. while keeping the current constant (CCA). The four-resistor electrical circuit in this anemometer, part of a Wheatstone bridge configuration, can detect very small changes in temperature variations. The hot-wire probe is connected to a CTA, as shown in Figure 3-10, where changes in voltage of the hot wire can be measured accurately. The signal passes a low-pass filter before it is digitised by an A/D board.

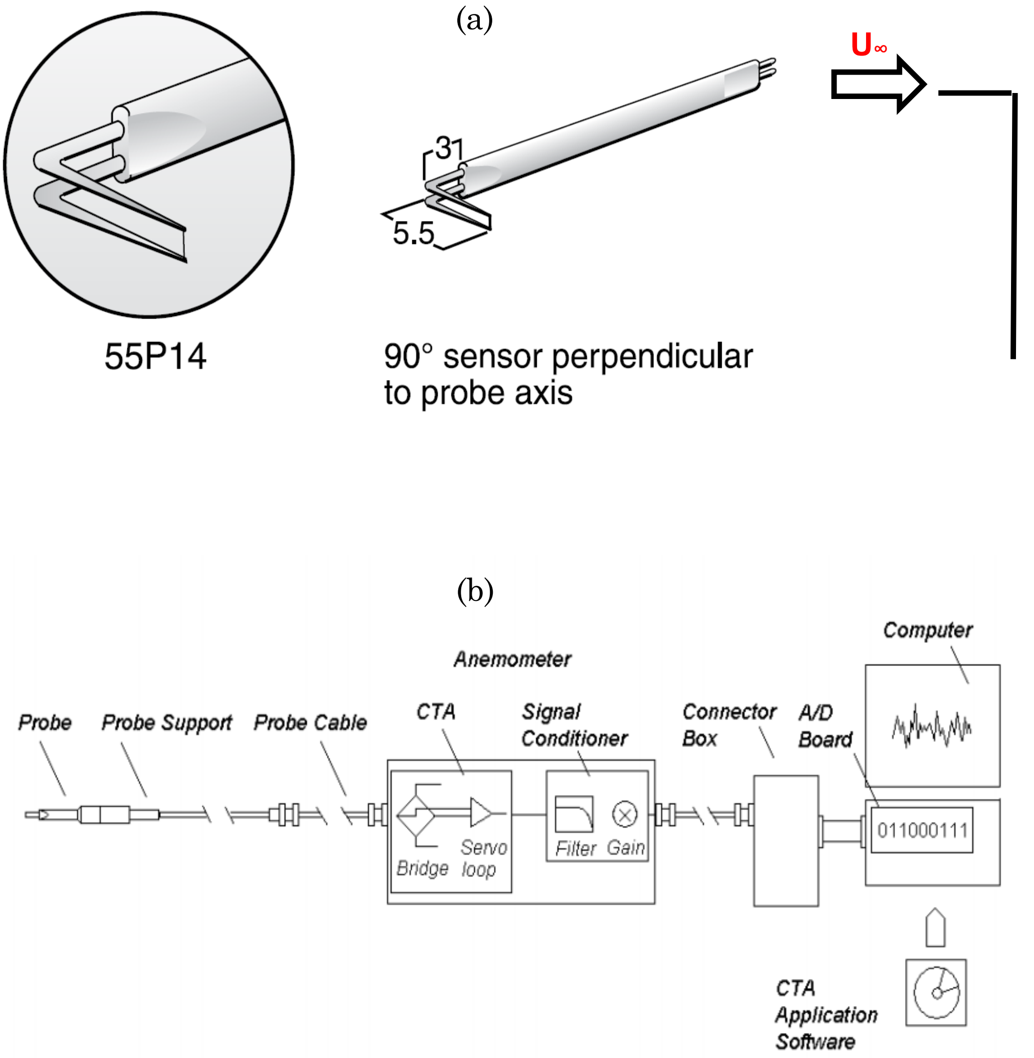

Figure 3-10: (a) Appropriate hot wire exposure to measure incoming flow and miniature wire probe, perpendicular (55P14) [152]. (b) Hot wire anemometer measuring chain [153].

The constant temperature anemometer must be carefully calibrated to ensure high-quality data is obtained. For this purpose, the CTA was manually calibrated to compensate for the cumulative resistances for the probe lead support and cable. Determining the sensor's working temperature was done by defining the overheat ratio, and hence the relation between the warm and cold resistor. In addition, using the square wave test, the bridge was dynamically balanced. Bridge balancing serves the aim of optimising the sensor/ anemometer circuit bandwidth [153].

In this project, a 55P14 probe by the Dantec Dynamics was used to measure the jet profile and freestream turbulence intensity. The probe consists of a miniature wire with very high frequency response. The 1.25 mm long tungsten wire, of 5 µm diameter, is directly welded to the hot-wire prongs. The probe body consists of a ceramic tube with a diameter of 1.9 mm.

The CTA has a built-in signal conditioner with a low-pass filter to remove electronic noise and prevent aliasing. A high-pass filter is not needed, because it would only remove the low frequency fluctuations (DC-part) prior to spectral analysis [154]. Furthermore, the offset and gain of the CTA is carefully adjusted to optimise the input range for the A/D board (0-5 V) and to achieve a high resolution. The analogue signal is digitised by a 12-bit A/D card after running through an eight channel BNC connector board. The application software ThermalPro by TSI is used both for the probe calibration and data acquisition. Data analysis is carried out with MathWorks MATLAB and Microsoft Excel. The data acquisition is defined by the sampling rate (SR) of 20 kHz and the number of samples (N) of 256,000, which together determine the sampling time (T = N/SR) of 13.1 seconds. For spectral analysis the sampling rate must be at least two times higher than the highest occurring fluctuation frequency in the flow (equation 3-4).

$$SR \geq 2 \times f_{max} \quad [Nyquist\ criteria] \tag{3-4}$$

3.6.1.1 Anemometer setup

The total resistance of the setup includes the lead, probe support, and cable resistance, as well as the hot wire sensor.

$$R_{tot,0} = \sum R_{lead}, R_{support}\,, R_{cable}, R_{sensor,0} \tag{3-5}$$

The subscribe “0” denotes the resistance at the refernce temperature. To balance the resistance of the measurement chain, a zero-resistance shorting probe was inserted into the probe holder.

After balance, Now the indicated resistance will show the resistance of the sensor at the actual room temperature.

One important step before starting the experiment is the adjustment of the CTA. A high temperature across the sensor element results in high frequency response, signal-to-noise ratio, and velocity sensitivity. The operating temperature of the sensor is defined by the overheat ratio (a) according to equation 3-6.

$$a = \frac{R_w - R_{20}}{R_{20}} \tag{3-6}$$

Where R_w is the sensor resistance at operating temperature T_w and R_{20} is its resistance at ambient (calibration) temperature T_0. The overall temperature can be calculated using equation 3-7:

$$T_w - T_0 = \frac{a}{\alpha_{20}} \tag{3-7}$$

Where α_{20} is the sensor temperature coefficient of resistance at T_0. Manufacturer will specify the sensor resistance at 20°C (R_{20}), and the sensor temperature coefficient (TCR) α_{20}. For a chosen wire temperature of 300°C, this leads to an overheat ratio of 1.8 [155].

3.6.1.2 Velocity calibration and data conversion

Calibration of the hot-wire probe system is necessary to establish a relation between the CTA output (E) and the flow velocity (u). The probe is exposed to a set of known velocities in the range of 0-65 m/s, and the corresponding values of the voltages are noted. The flow speed is calculated using a pitot-static tube, which is placed close to the hot-wire, to measure the dynamic pressure. Additionally, the flow temperature was measured using a digital thermometer. The first step to convert the data records from voltages into velocities for the scheduled hot-wire experiments is the application of a 4th-order polynomial curve fit (equation 3-8) (Figure 3-11).

Where C_0 to C_4 are calibration constants and u is the flow velocity. One of the most important sources of error in measuring velocity using hot-wire anemometry is the change in the hot-wire calibration due to changes in the ambient temperature. Consequently, the temperature is noted at the beginning and the end, both for the calibration and the experiment [156]. In order to minimise this error, an accurate correction method is necessary.

Bruun [151] documented a technique in which the output voltage E_w is corrected to a reference temperature T_r:

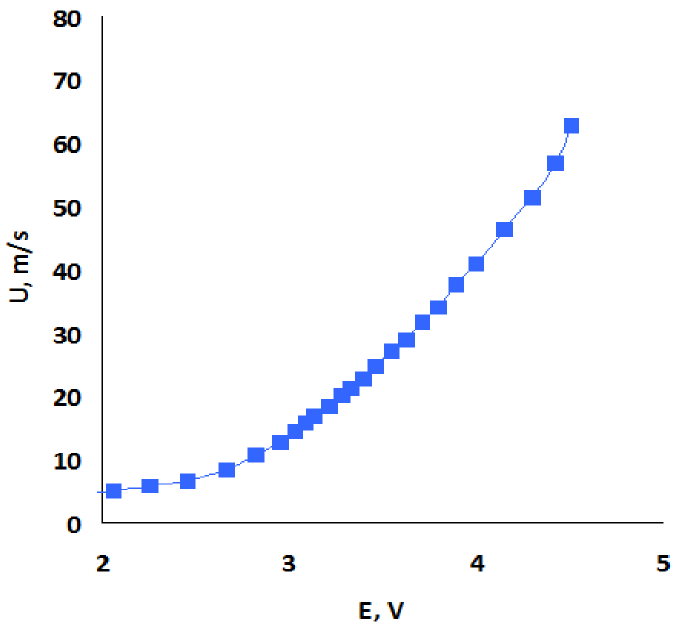

Figure 3-11: Boundary layer probe calibration polynomial regression of 4th order.

$$u = C_0 + C_1E + C_2E^2 + C_3E^3 + C_4E^4 \tag{3-8}$$

$$E_{w,r} = E_w \times \left[\frac{T_w - T_r}{T_w - T_a}\right]^{1/2} \tag{3-9}$$

Where T_w is the wire temperature, T_a is the ambient temperature, and T_r the reference temperature (which is equal to the calibration temperature). This correction is only valid for small temperature changes (up to two or three degrees), as otherwise the changes in fluid properties would lead to an over-correction.

3.6.1.3 Traversing system

Since automatic probe movement is part of the experimental procedure, a three-axes traverse system is used for the hot-wire measurements. The traverse mechanism is connected to the central unit box and can be controlled by the ThermalPro software. The accuracy of the movement is within ±0.01 mm. It should be noted that the traverse does not disturb the flow at the probe position (Figure 3-12).

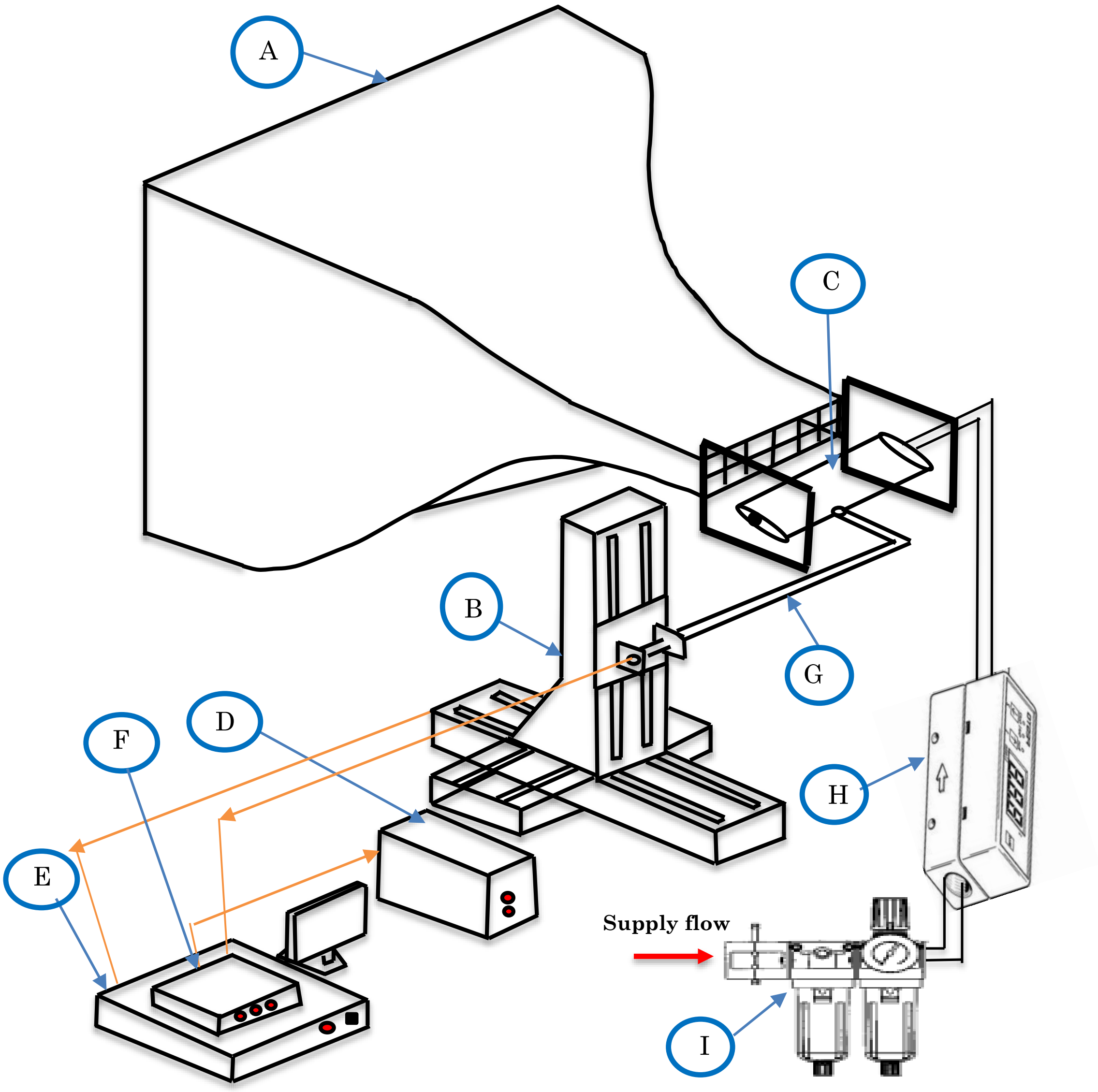

Figure 3-12: Schematic diagram of the experimental setup traversing system. (A) Wind tunnel, (B) Three-axis Isel® traverse mounted in front of the nozzle exit to measure the x, y, and z planes, (C) Test section& model, (D) PC, (E) Traverse control system, (F) CTA, (G) Mobile probe, (H) Digital valve flow sensor, and (I) Pressure regulator.

3.7 Experimental Methodology

This section discusses the generation of turbulence by several bi-planar orthogonal square grids, and the characterisation of the freestream turblance as a result of the flow passing these grids.

3.7.1 Generation of turbulence

The broadband interaction noise radiation at the leading edge depends strongly on the level of turbulence intensity, and the integral length scale of the incoming flow turbulence. Turbulence grids are well-known for their ability to reduce or enhance turbulence and flow steadiness, depending on their geometry, such as the mesh length (M) and wire diameter (d). Description for the M and d can be refered to Figure 3-13. In order to choose a suitable grid design for this experiment, it is important to define the characteristic parameters describing the turbulence [157]:

$$Tu = \frac{1}{\sqrt{3}} \times \frac{|\bar{u}'|}{\bar{u}} = \sqrt{\frac{\overline{u'^2} + \overline{v'^2} + \overline{w'^2}}{3(\overline{u^2} + \overline{v^2} + \overline{w^2})}} \qquad (3\text{-}10)$$

Where the $\overline{u'^2}, \overline{v'^2}$ and $\overline{w'^2}$ are the mean sequre velocity flactuations, and $\bar{u}', \bar{v}'$ and $\overline{w'}$ are the mean velocities. If the velocity fluctuation is equal in all three directions, with $\overline{u'^2} = \overline{v'^2} = \overline{w'^2}$, the turbulence can be described as isotropic, which is equal to the standard deviation of the flow velocity (equation 3-12) in relation to the mean flow velocity (equation 3.11).

$$u_m = \frac{1}{N}\sum_{i=1}^{N} u_i \qquad (3\text{-}11)$$

$$u_{rms} = (\frac{1}{N-1}\sum_{i=1}^{N}(u_i - u_m)^2)^{0.5} \qquad (3\text{-}12)$$

$$Tu_{isotrop} = \frac{u_{rms}}{u_m} \qquad (3\text{-}13)$$

In this experiment, a bi-planar square orthogonal grid with square section bars is used. By adopting the suggested mesh-to-diameter ratio of about 5, the combination of M = 72 mm and d = 17 mm is used in the current study. The grid is placed inside the nozzle after the large curvature point. The grid adjustment to the nozzle yields W (width) = 361 mm and H (height) = 208 mm in total dimension (Figure 3-13). A one-dimensional hot-wire probe was placed 30 mm downstream of the nozzle exit, which corresponds to the leading edge tip of the aerofoil when installed, to calculate the turbulence intensity (Tu), which gives a value of 4.5%. To determine the level of turbulence isotropic generated by the grid, the velocity power spectral density measured by the hot wire is compared with Von Karman one-dimensional turbulence model in accordance with Eq. 3-10:

$$\phi_{uu}^{VK}(\omega) = \frac{\overline{u'^2}\times\Lambda_{uu}}{\pi\times U_\infty}\times\frac{1}{\left[1+\left(\frac{K_x}{K_e}\right)^2\right]^{-5/6}}, \quad \begin{cases} K_x = \dfrac{\omega}{U_\infty}; when\ \omega = 2\pi f \\ K_e = \dfrac{\sqrt{\pi}\times\Gamma(^5/_6)}{\Lambda_{uu}\times\Gamma(^1/_3)} \end{cases} \tag{3-14}$$

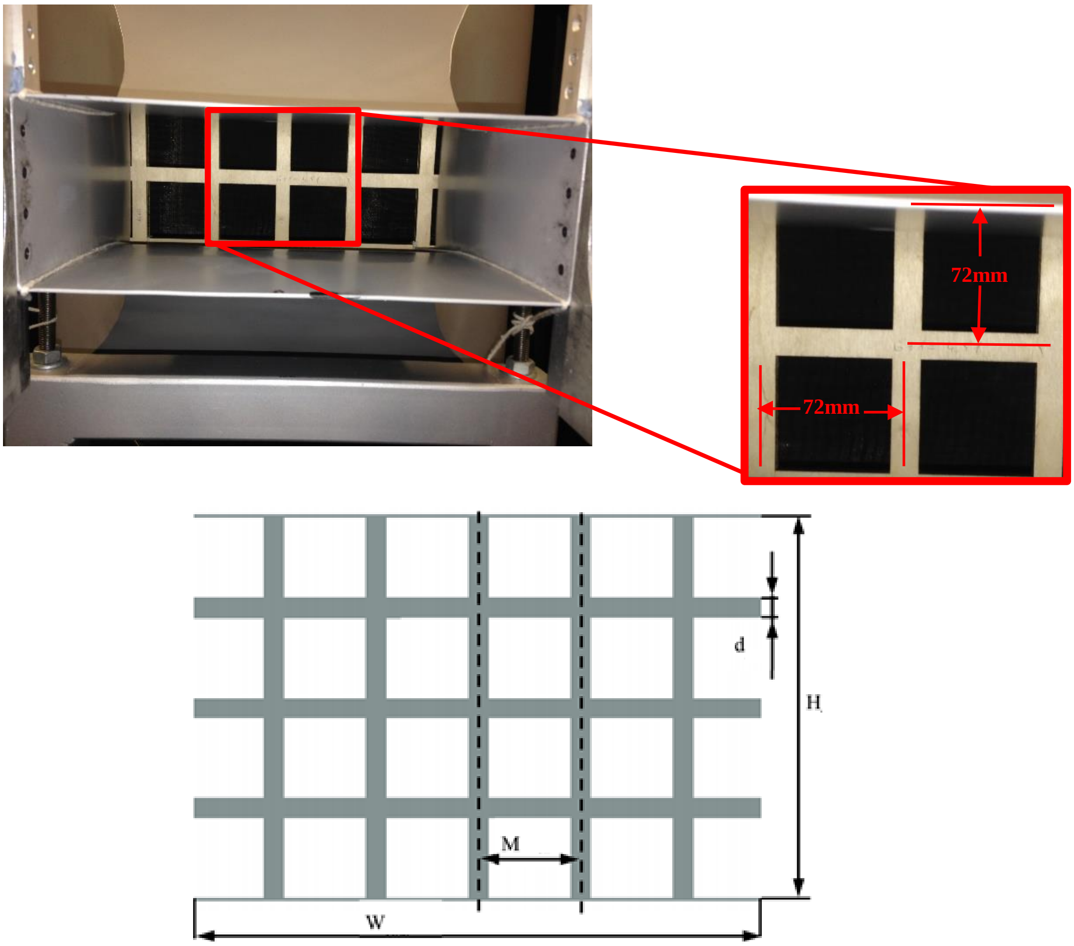

Figure 3-13: Characteristic parameters of the turbulence grid.

Where $\overline{u'^2}$ is the mean square velocity fluctuation, Λuu is the integral length scale, U_∞ is the mean velocity, K_e is the reduced wavenumber, K_x is the stream-wise wavenumber, and ω is the angular frequency. In the comparison presented in Figure 3-14 between the theoretical spectrum with the measured quantities, some discrepancies can be observed at the lower frequency region, where the measured values exhibit slightly larger spectra level. However, the overall measured streamwise fluctuating velocity spectra shows good agreement between the medium and high frequency range. The -5/3 Kolmogorov decay rate can also be seen in the measured spectra. This suggests that the turbulence generated in the present study is reasonably isotropic [158].

The flow range for the aeroacoustics test was $20 \le U_\infty \le 60$ m/s. In order to reduce the statistical spread and uncertainty, all measurements were repeated and averaged.

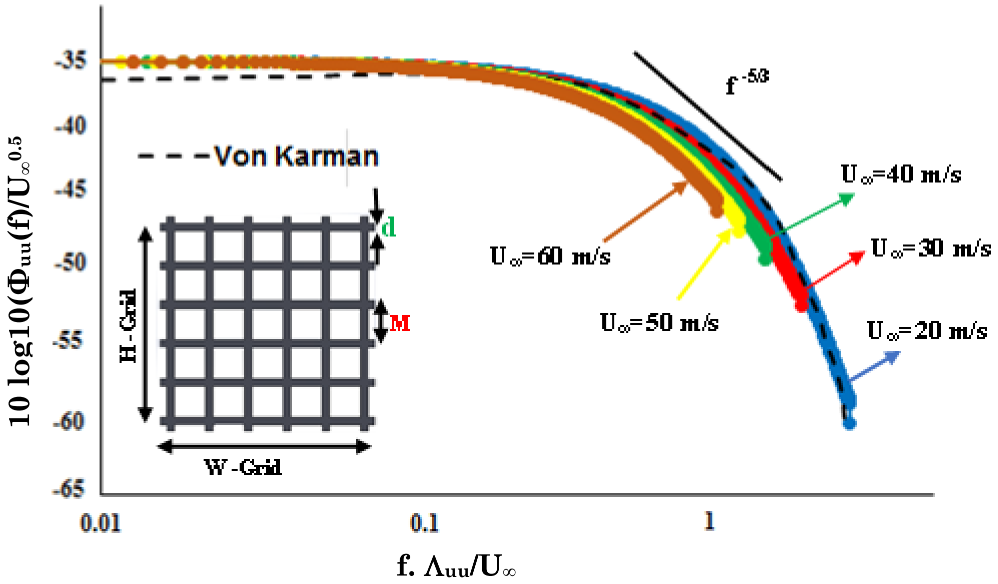

Figure 3-14: Grid producing Tu=4.5%, U_∞ = 20-60 m/s. Velocity power-density spectra against scaled frequency by the eddy integral length.

3.8 Aerodynamic Measurement Facilities

Aerodynamic measurements of a two-dimensional NACA65(12)-10 wing section were conducted to characterise the aerodynamic performance of the aerofoil with different leading edges. Lift and drag forces are measured under various angles of attack, and the corresponding non-dimensional values coefficients are calculated.

3.8.1 Wind tunnel open circuit

The aerodynamic measurements were conducted in the Aerodynamic Laboratory at Brunel University. The wind tunnel is an open circuit, suction-type wind tunnel, with a closed test section of 50 (height) x 50 (width) cm. The air enters the wind tunnel through a nozzle with an area ratio of 3:1, which is equipped with several mesh and honeycomb screens, to reduce the turbulence intensity of the free stream, and to create a high-quality flow with a turbulence intensity of about 0.2 to 0.3%. An axial fan (99 cm, 8 blades, 32.5°) powered by a 7.5 kW motor produces a maximum free stream velocity of 35 m/s, located at the exit of the diffuser. On each side of the test section there are three interchangeable acrylic glass windows to allow installation of different configurations. A three-component balance by Plint & Partners LTD [159] was used to measure the aerodynamic forces produced by the aerofoil inside the wind tunnel (Figure 3-15).

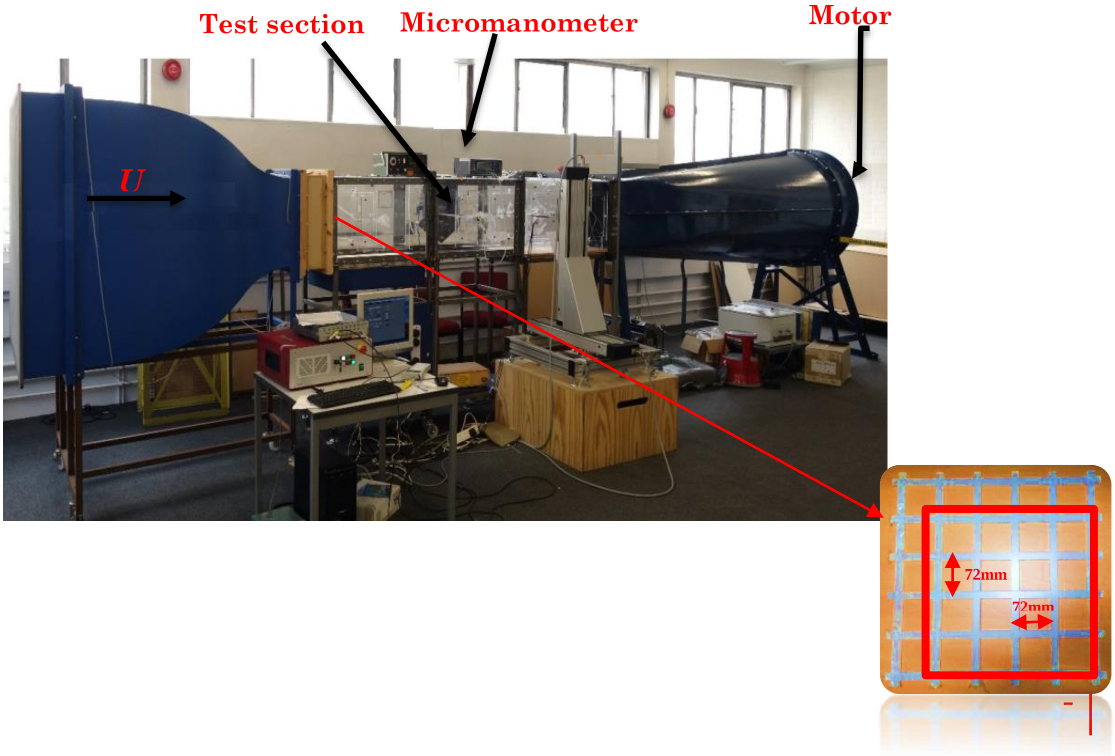

Figure 3-15: Wind tunnel open circuit at Brunel University London.

3.8.2 Three-component balance

A three-component balance by Plint & Partners LTD was used to measure the aerodynamic forces produced by the aerofoil inside the wind tunnel (Figure 3-16). The balance consists of a force plate and an aluminium mounting plate which is secured to the wind tunnel working section. The force plate is able to rotate about the horizontal axis. The aerofoil model is inserted with a 12 mm diameter mounting stem in the model support of the force plate. This support is free to rotate for adjustment of the angle of attack, while its position may be locked by means of the incidence clamp. The forces acting on the force plate are transmitted by flexible cables to strain gauge load cells, which measure the lift and the drag forces. The drag cable lies horizontally and passes through the centre of the force plate stem, while the two lift cables act vertically and are positioned equidistant from the model support. The accuracy of the readings is found to be ±0.05 N. The three-component balance is calibrated prior to the measurements to ensure accuracy of the readings. Calibration is carried out by removing it from the wind tunnel and installing it in a mounting frame. Zero readings of the load cells are checked before any load is applied. The cells are adjusted by setting the adjusting screw until the display shows a value of zero. The calibration procedure involves the application of known forces using dead weights. It is important that the force balance is completely levelled both vertically and horizontally during the calibration procedure. Any deviations given from the forces are corrected by adjusting the cable tensions until similar readings for both load components, aft and fore, are achieved. Three calibrations are made to check the linearity of the relationship between load and cell output.

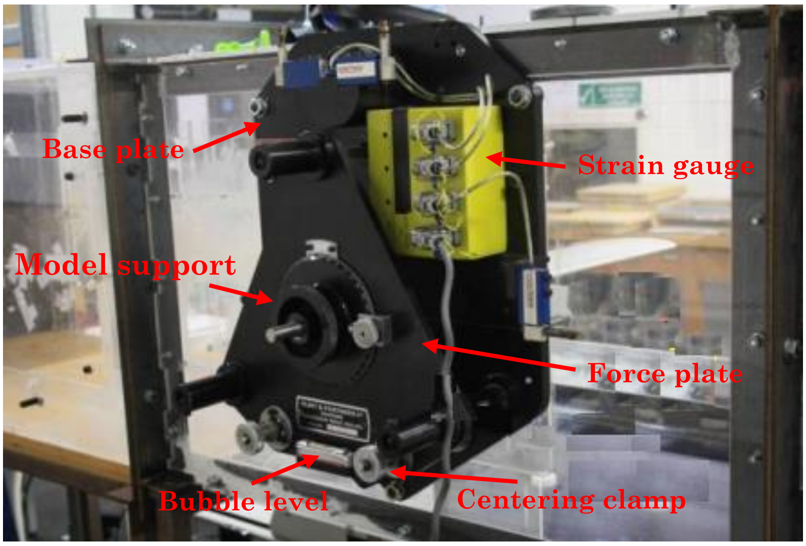

Figure 3-16: Three force balance system used for the lift and drag measurements.

3.8.3 Experimental procedures

A standard pitot-static tube was used to measure the total pressure p_t and the static pressure p_s of the freestream in the test section. To ensure the measurement of the correct freestream velocity, dynamic pressure calibrations are made without the aerofoil model, because the model's static pressure field would influence the pressure sensed by the static ports. During acquisition of the data, the pitot-static tube is placed with an acceptable distance in front of the model (~80 mm). To calculate the velocity, the pressures from the two orifices of the pitot-static tube are connected across a Furness Controls Limited FCO510 micromanometer. The indicated dynamic pressure is in direct relation to the flow speed. A scheme of the set-up is displayed in Figure 3-17.

The free stream velocity u can be calculated from Bernoulli's incompressible equation $p_t=p_s+(1/2\ \rho \times u^2)$ after computing the density ρ from the equation of state ($p=\rho RT$).

$$u=\sqrt{\frac{2(p_t-p_s)R_{specific}.T}{p}} \tag{3-15}$$

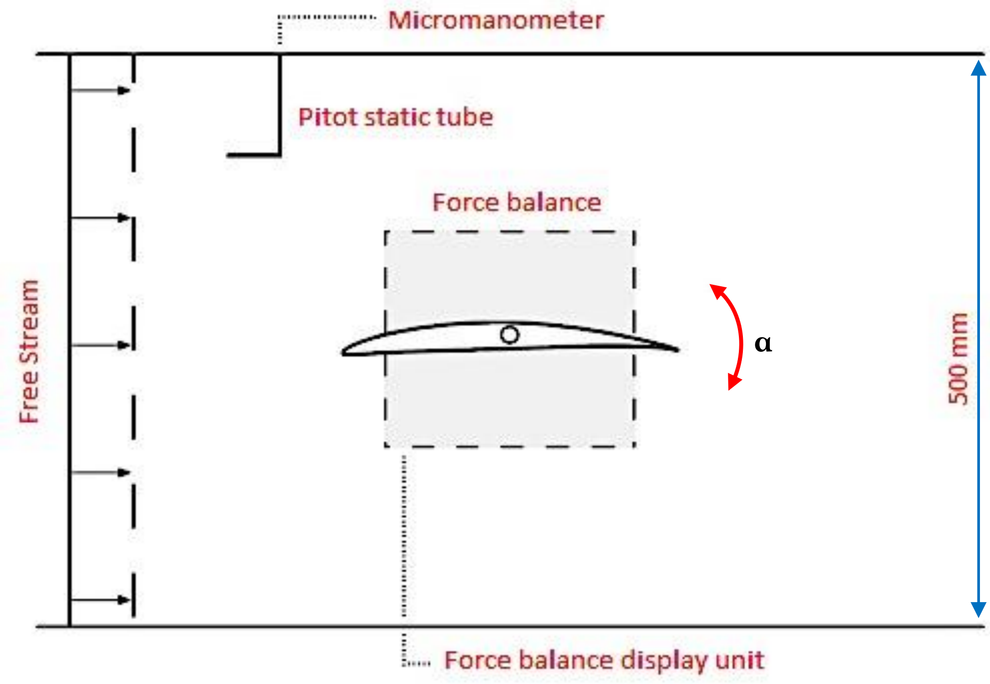

Figure 3-17: Experimental setup in the working section of the wind tunnel.

Where p_t is the total pressure, p_s is the static pressure, and T is the absolute temperature in the test section. The universal gas constant for dry air $R_{specific}$ is 287.058 J/(kg K), and p is the atmospheric pressure.

The pitot-static tube with hemispherical tip has some inherent error. To achieve the highest accuracy, the yaw angle with incoming flow direction should be less than 3°.

Freestream velocity represents an influencing parameter on the lift and drag curves, and all measurements are taken at 25 m/s. The velocity is varied through different power input to change the RPM of the motor.

The corresponding chord-based Reynolds number is ~2.5 x 10^5 according to equation 3-16.

$$Re_c = \frac{\rho \times u \times C}{\eta} \tag{3-16}$$

Where C is the chord length of the aerofoil (m) and η is the dynamic fluid viscosity (18.24 x 10^{-6} kg/m.s at ambient temperature of 20° C).

All tests were undertaken at angles of attack α ranging from -15° to 15° degrees, at 25 m/s. The rotating dial mechanism of the mounting plate is used to adjust the angle over this range with an estimated uncertainty of ±0.2 degrees. Force readings displayed on the display unit are noted for every leading edge configuration and each angle of attack. In order to verify the results and to check the accuracy of the measurements, three sets of measurements are taken for each cases across the entire α range. Prior to every measurement set, readings for ambient room temperature as well as atmospheric pressure are noted for use in the subsequent data processing. Furthermore, the values corresponding to the zero readings of lift and drag at the start and end of each measurement series are noted.

Lift and drag forces from the three-component balance are directly obtained in Newtons, and they need to be corrected to determine the actual lift and drag forces using the following equations:

$$L = (A_u - a_0) + (F_u - f_0) \tag{3-17}$$

$$D = (D_u - d_0) \tag{3-18}$$

Where L is the actual lift force, A_u is the lift force aft load cell, a_0 is the zero reading (wind off) aft load cell, F_u is the lift force fore load cell, f_0 is the zero reading (wind off) fore load cell, D is the actual drag force, D_u is the uncorrected (measured) drag force from the drag load cell (which includes both parasite and lift-induced drag), and d_0 is the zero reading (wind off) drag load cell. The lift coefficient C_L is defined as

$$C_L = \frac{L}{1/2\rho \times u^2 \times S} \tag{3-19}$$

Where S is the planform area of the aerofoil. Similarly, the drag coefficient is defined as

$$C_D = \frac{D}{1/2\rho \times u^2 \times S} \tag{3-20}$$

Since the flow conditions in a wind tunnel are not the same as in an unbounded airstream, the lift and drag coefficients have to be corrected. The wind tunnel test section is finite in size, and produces changes in flow patterns. This blockage effect leads to lift increments, as well as an increment in drag [160]. Determination of the reliable aerodynamic coefficients of an aerofoil needs to be corrected using the solid-blockage correction, as well as a correction factor for the wake blockage. The total blockage error can be estimated by the following equations:

$$C_D = C_{Du} \times (1 - 3\varepsilon_{sb} - 2\varepsilon_{wb}) \tag{3-21}$$

$$\varepsilon_{sb} = \frac{\pi^2}{3} \times \frac{\lambda_2}{4} \times \frac{t^2}{h^2} = 0.822 \times \lambda_2 \times \frac{t^2}{h^2} \tag{3-22}$$

Where C_{du} is the uncorrected drag coefficient, which can be calculated from the force balance measurements. ε_{sb} is the solid-blockage correction factor, t is the aerofoil thickness (m), and h is the wind tunnel test section height (m). The body shape factor λ_2 is a function of the fineness ratio $\frac{C}{t}$ and thickness ratio $\frac{t}{C}$. It can be estimated with sufficient accuracy by interpolation [161]. For a NACA65-0xx aerofoil, a value of 4.1 is suggested (with $\lambda_2 \times t^2 = 1/4\, \Lambda \times C^2$, where Λ can be determined for any base profile from the relationis introduced by Allen [162].

$$\varepsilon_{wb} = \frac{\Delta U_h}{u} = \frac{C}{2 \times h} \times C_{du} \tag{3-24}$$

For the factor in equation 3-24, ε_{wb} is the wake blockage correction, ΔU_h is the induced horizontal velocity from the wake blockage (m/s), and u is the uncorrected freestream velocity (m/s).

The presence of the ceiling and floor prevents the normal curvature of the flow, thus the aerofoil appears to have more camber relative to the straightened flow. Accordingly, the aerofoil in a closed section would appear to have has more lift and momentum than it would have in an open freestream. Therefore it has to be corrected according to equation 3-24.

$$C_L = C_{Lu} \times (1 - \sigma - 2\varepsilon) \begin{cases} \sigma = \dfrac{\pi^2}{48} \times \left(\dfrac{C}{h}\right)^2 \\ \varepsilon = \varepsilon_{sb} + \varepsilon_{wb} \end{cases} \tag{3-25}$$

3.9 Leading Edge Blowing Configurations

The jet was supplied by a plenum from inside the blade body, which contains several turning valves that help guide the flow from the air supply to the slot, as demonstrated in Figure 3-12. The injection of mass flow is then facilitated through the multiple orifices at the front edge. Each of these orifices has a diameter of 2 mm. Two concentrations of the orifices were facilitated by spanwise spacing of the orifices λ'. The aerofoil was connected to the external air supply, and the flow rate can be adjusted via a digital valve flow sensor (SFAB-600U-HQ10-2SA-M12), with rotatable knob to adjust the flow rate. The controller and air supply were located outside the acoustic chamber to isolate the valve and the superfluous noise. The flow was fed into the aerofoil through a system of 6 mm diameter tube. In the current study, the level of leading edge blowing is quantified by the volumetric flow rate through each orifices Q', which is approximately equal to Q/n, where Q is the total volumetric flow rate into the aerofoil, and n is the number of orifices at the leading edge. This simple relationship between Q' and Q is based on the assumption that there is negligible pressure loss inside the ducting system.

3.10 Characterisation of Jet Profile

3.10.1 Straight blowing leading edge

One of the important hypothesis made in this study relates to the analogy between spanwise spacing of the orifices λ' and the spanwise wavelenght of the serration, λ. Additionally, another hypothesis describes the correlation between the volumetric blow rate of air jet Q' from each orifice, and the serration amplitude A.

As mentioned earlier, two spanwise spacing values were chosen for the orifices, λ'= 5 and 10 mm. The test matrix also consists of different volumetric flow rates for each orifice: Q' = 1.0, 2.0, 2.5, and 3.0 liter/min. An example of the spreading of jet from these orifices under quiescent conditions is shown in Figure 3-19. Each velocity profile represents the averaged values of three air jets situated adjacent to each other. The velocity distributions generally exhibit a Gaussian-liked profile. The jet array at the aerofoil's leading edge serves as the primary mechanism designed in the current study to interact with the incoming flow, thereby achieving control in the flow and aeroacoustic behaviours.

The velocity profiles were also analysed in the horizontal plane via the jet axis. Figure 3-19 shows the velocity profile development in the streamwise direction. The jet is found to decay along the axis and is spreading.

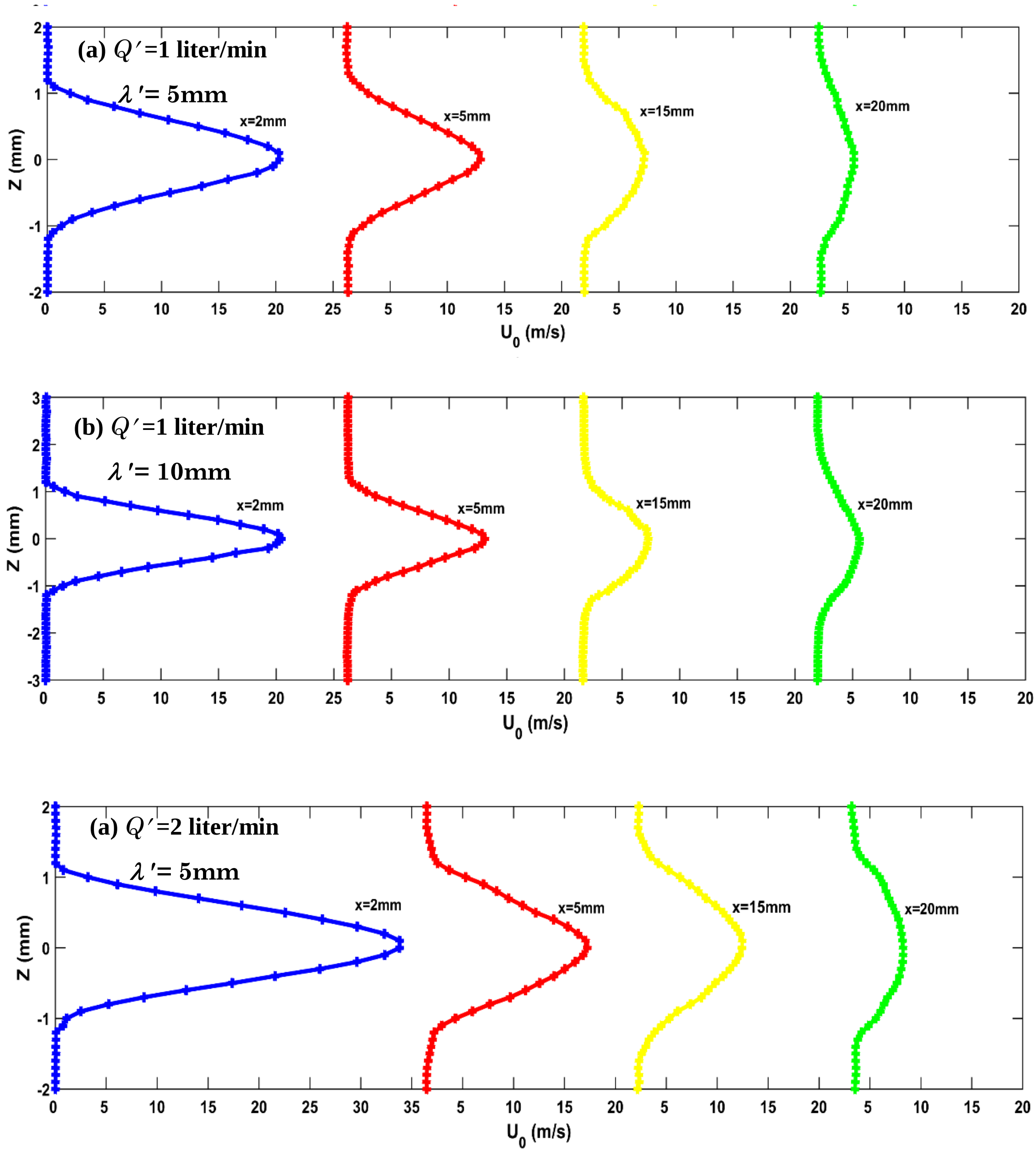

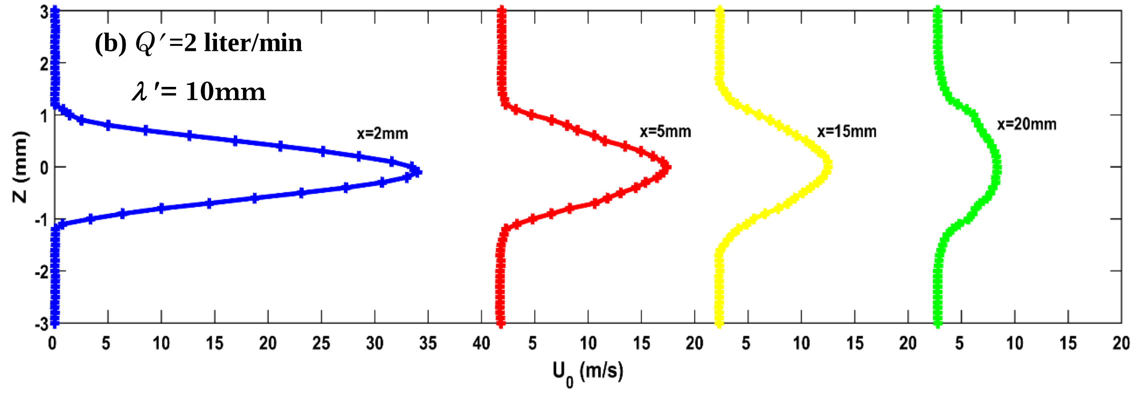
(b) Q'=2 liter/min
λ'= 10mm
x=2mm
x=5mm
x=15mm
x=20mm
Z (mm)
3
2
1
0
-1
-2
-3
0 5 10 15 20 25 30 35 40 5 10 15 20 5 10 15 20 5 10 15 20
U_0 (m/s)

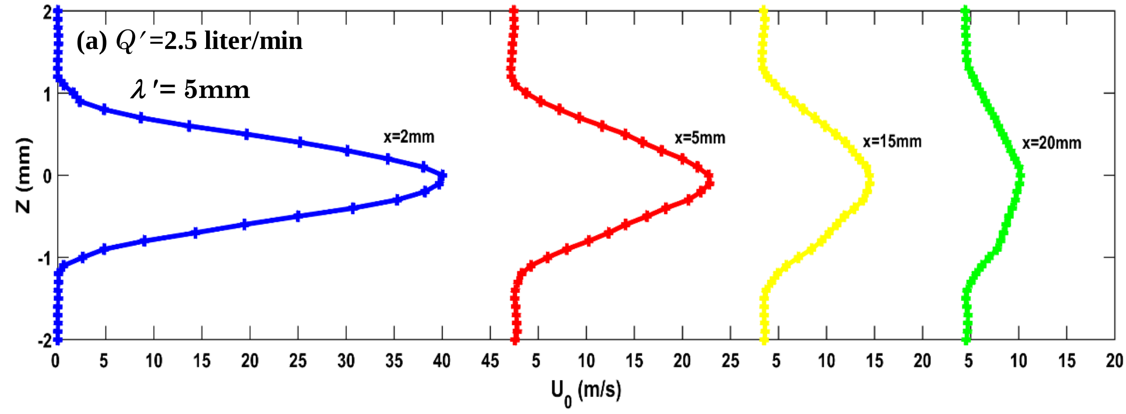
(a) Q'=2.5 liter/min
λ'= 5mm
x=2mm
x=5mm
x=15mm
x=20mm
Z (mm)
2
1
0
-1
-2
0 5 10 15 20 25 30 35 40 45 5 10 15 20 25 5 10 15 20 5 10 15 20
U_0 (m/s)

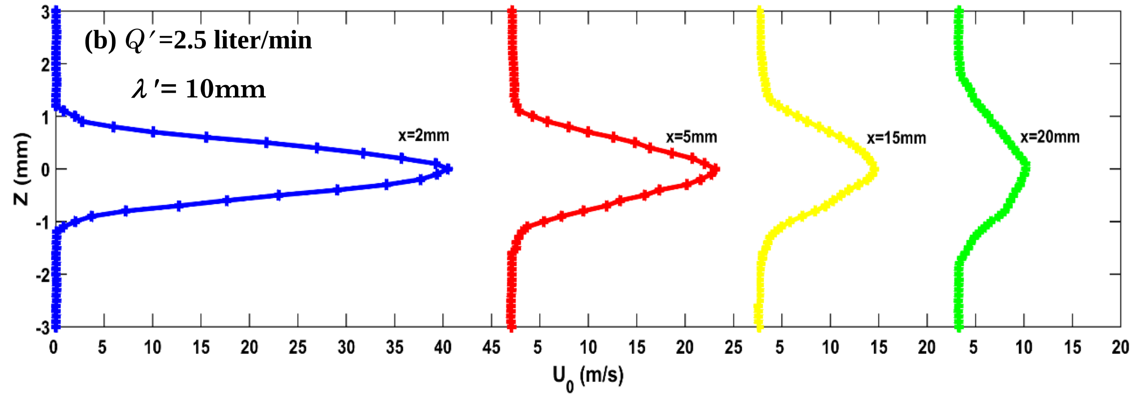
(b) Q'=2.5 liter/min
λ'= 10mm
x=2mm
x=5mm
x=15mm
x=20mm
Z (mm)
3
2
1
0
-1
-2
-3
0 5 10 15 20 25 30 35 40 45 5 10 15 20 25 5 10 15 20 5 10 15 20
U_0 (m/s)

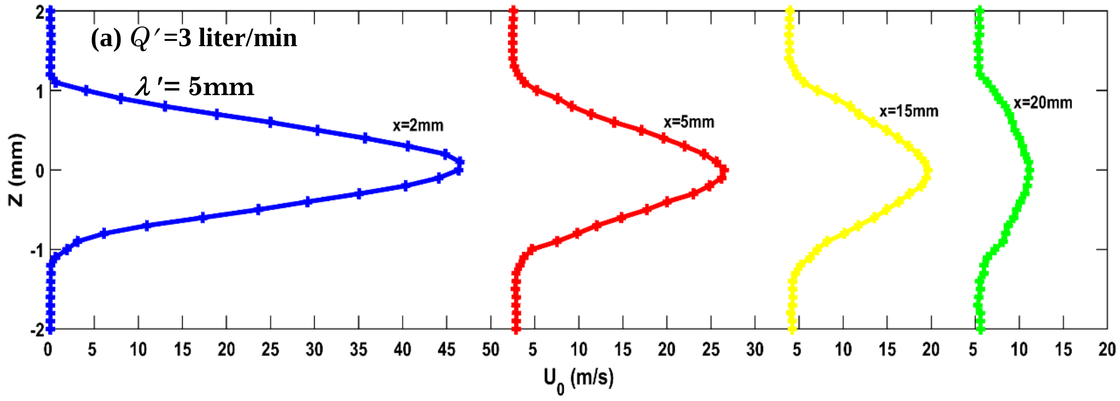
(a) Q'=3 liter/min
λ'= 5mm
x=2mm
x=5mm
x=15mm
x=20mm
Z (mm)
2
1
0
-1
-2
0 5 10 15 20 25 30 35 40 45 50 5 10 15 20 25 30 5 10 15 20 5 10 15 20
U_0 (m/s)

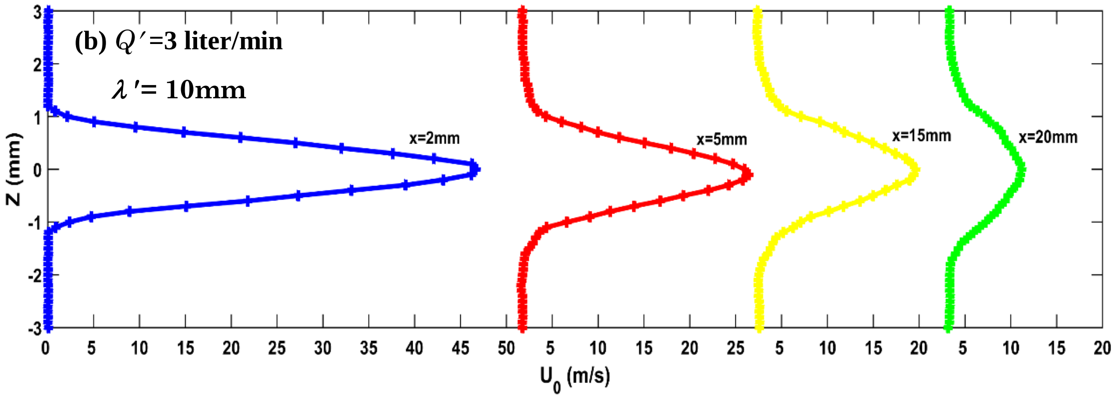

Figure 3-18: Velocity profiles of the blowing for leading edge jet at various streamwise locations for (a) λ' = 5 and (b) λ' = 10 mm with Q' = 1, 2, 2.5 and 3 litre/min.

The maximum velocity at the centre of the jet, $U_{0\max}$, for various streamwise locations at different blow rates are shown in Figure 3-20. It was found that $U_{0\max}$ as a function of the Q' and X is unaffected Y the spanwise spacing of the orifices. From the figure, it can be seen that the variation of the $U_{0\max}$ at the closest to the jet exit (e.g. X=2mm) would exhibit the most sensitive and behaves linearly to the Q'. On the other hand, at the furthest streamwise distance (e.g. X=20mm), the $U_{0\max}$ is almost the same value across the entire range of Q'.

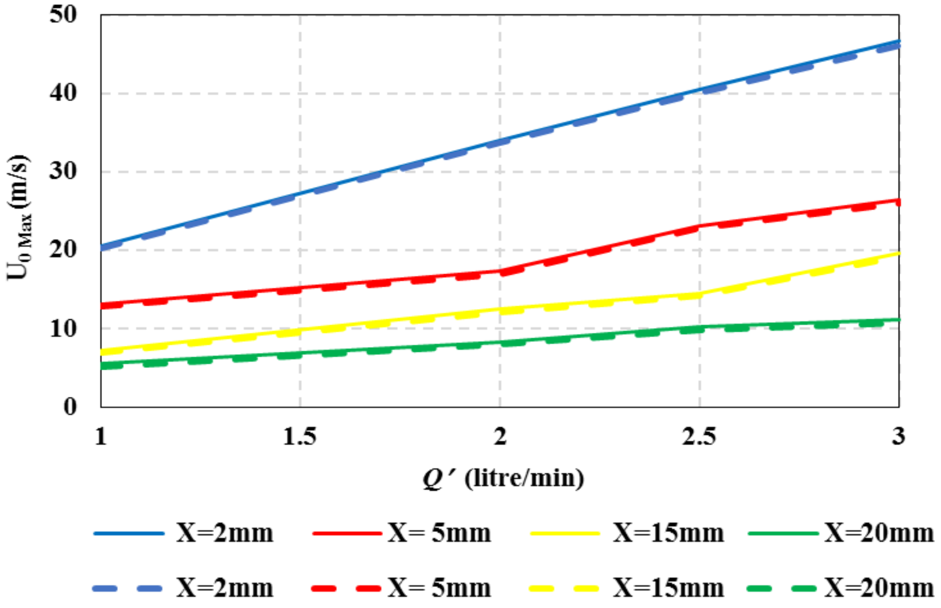

Figure 3-19: Correlation of the $U_{0\max}$ at different streamwise distances for different blow rates from 1-3 litre/min for λ'= 5 (solidline) and 10 mm (dashline).

3.10.2 Serrated blowing leading edge

Figure 3-21 represents the jet velocity profiles produced of quiescent condition at several X-axis positions for the case of serrated blowing the leading edge. Note that the velocity profiles shown in Figure 3-21 correspound to the orifices located at the root of the serration. It was generrally observed that velocity profiles produced by the orifices at the serration tip would have the same characteristic as those produced by a stright blowing leading edge, which had been discussed in the sub-section earlier.

For the jet profiles produced at the serration root, it is clear that they are much thicker due to their early formation compared to use a straight blowing leading edge, as well as at the serration tip. It is expected that, as the jet is still developing within the gap of the serration, it would somehow interact with the serration surface and affect its growth. Indeed, this is manifested in Figure 3-22 for the distribution of $U_{0\mathrm{max}}$ against Q' at different streamwise locations (X=2, 5, 15, and 20mm). The linearity that was exhibited earlier in Figure 3-20 for the straight blowing leading edge no longer exists. Rather, the curves in Figure 3-22 are mostly non-linear, although the decrease in the absolute value for the $U_{0\mathrm{max}}$ is also noted.

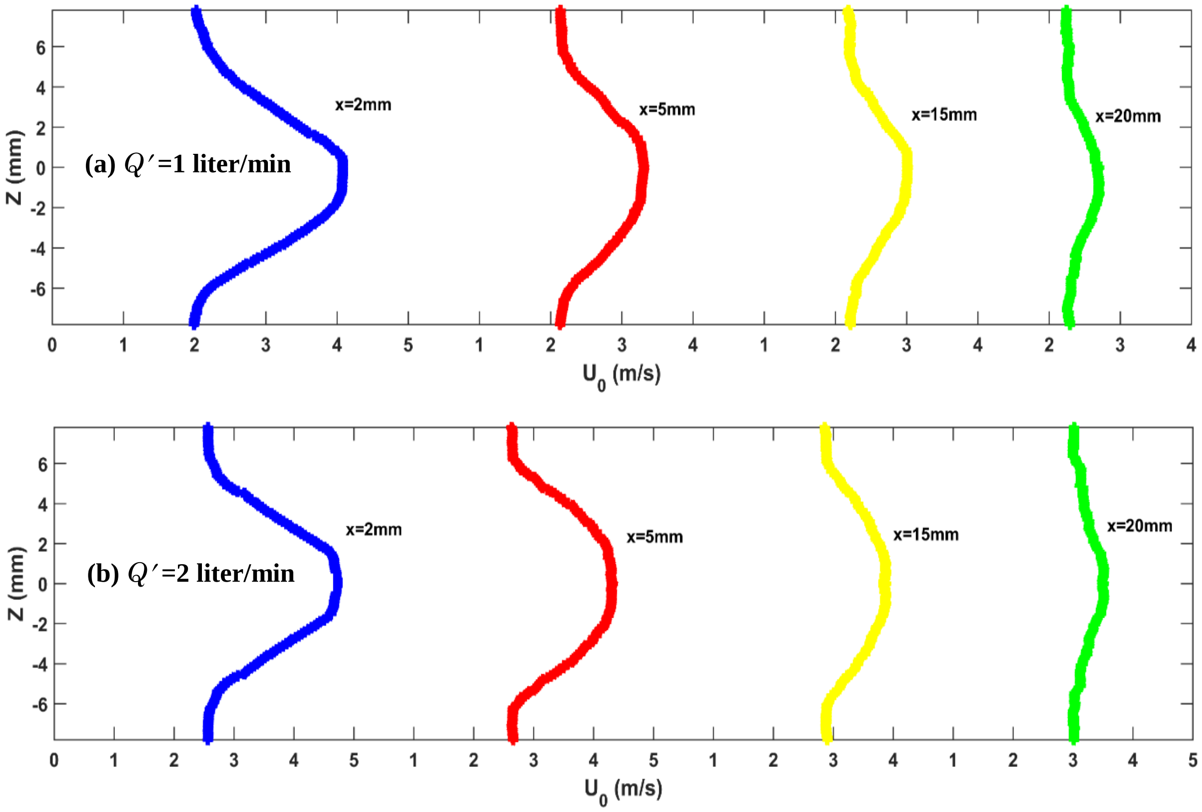

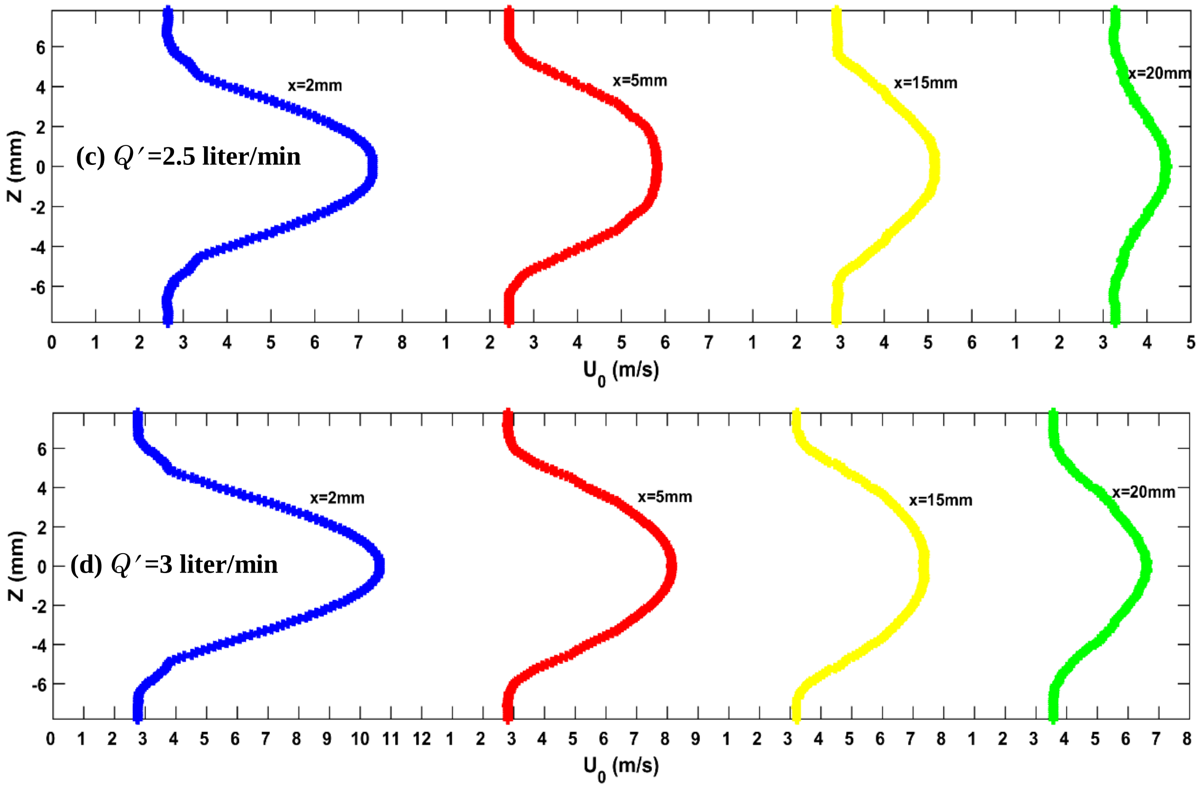

Figure 3-20: Blowing velocity profiles for serrated leading edge jet at various streamwise locations for λ = 45, and A = 30 mm, with Q'= 1, 2, 2.5, and 3 litre/min.

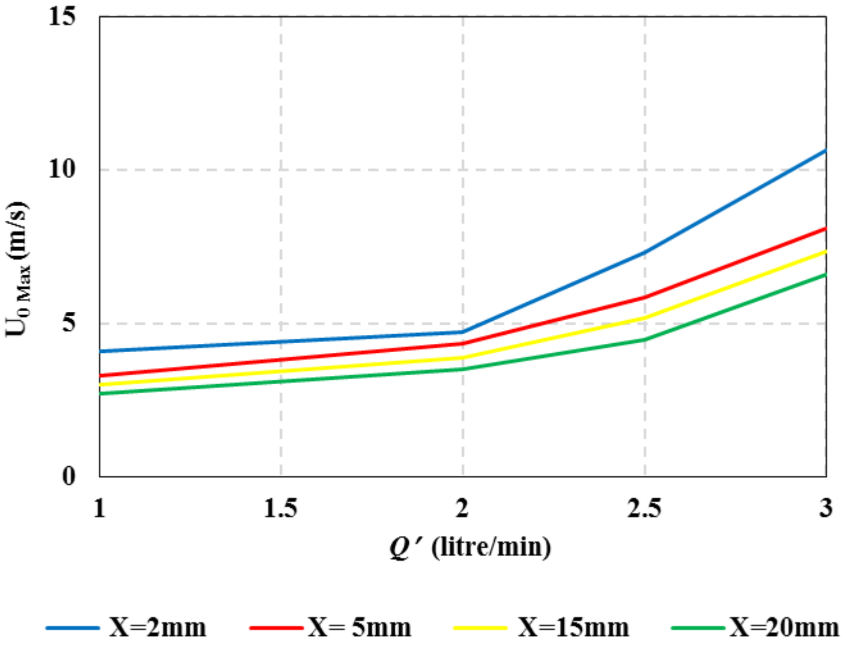

Figure 3-22: Correlation of the $U_{0\max}$ at different streamwise distances for different blow rates from 1-3 litre/min for hybrid device λ =45mm and A=30mm.

Chapter 4 : Aeroacoustic of Straight Blowing and Serrated Leading Edges

4.1 Introduction

Today the aviation industry is facing major challenges with respect to noise pollution. To overcome the challenges, there is a great initiative by the government to reduce the aviation noise. As a result, many airplane and aero-engine manufacturers prioritise their efforts for the reduction of the airplane and turbomachinary noise.

Of particular interest is the turbomachinary noise which is related to the hydrodynamic interaction between the incoming turbulent flow and the leading edge of fan blades. This mechanism is, perhaps, the most relevant at the rotor-stator stage of the aero-engine, where the wake generated from the upstream rotor impinges on the downstream stator (or the outlet-guided-vanes OGV) to radiate the broadband interaction noise. The analytical work by describes the turbulent–leading edge interaction noise, ϕ, is described as a function of angular frequency ω, as[10,130]:

$$\phi(\omega) = \frac{2b}{\pi c}\left(\frac{2\Lambda_{uu}}{3\pi R}\right) Tu^2 \rho_0^2 U_0^4 \left[\frac{\Gamma(1/3)}{\Gamma(5/6)}\right]^2 \frac{\widehat{K}_x^2}{\left(1+\widehat{K}_x^2\right)^{\frac{7}{3}}}\, exp\left(\frac{-\omega \cdot d}{2U_0}\right) \tag{4-1}$$

where Λ_{uu} is the longitudinal integral length scale of the turbulence, Tu is the turbulence intensity, U_o is the velocity, R is the observer distance, b is the aerofoil semi-span, d is the aerofoil thickness, Γ ( ) is the gamma function and $\widehat{K}_x = \frac{k_x}{k_e}$ is the normalised longitudinal wavenumber where $k_x = \frac{\omega}{U_0}$ and $k_e = \frac{\sqrt{\pi}}{L} . \frac{\Gamma(\frac{5}{6})}{\Gamma(\frac{1}{3})}$. the normalised longitudinal wavenumber. From this expression, apart from the aerofoil geometry and physical configuration, the level of the interaction noise can be governed by the external factors in flow, such as the longitudinal turbulence length scale and the turbulence intensity.

Inspired by the ability of owls to hunt in acoustic stealth, there is now a great interest to reproduce the shape of owl wings: first, the leading edge (or primary feathers, on owl wings) are serrated; second, the trailing feathers on the back end of the wing are tattered; and third, the rest of the owl wings are covered in velvety feathers. It is believed that the leading edge serrations are responsible for the reduction of the leading edge noise.

The chapter discusses above concerns the aeroacoustic performances of aerofoils with serrated leading edge to act as a simple and effective passive flow control device. A research question also arises of whether the underpinning physical mechanisms in the application of serrated leading edge can be replicated by a completely different flow control approach. Active flow control has the advantages of being versatile when the flow condition changes considerably over a short period of time, and incurring less parasite drag when implemented into the aerofoil system. The analytical solution of Amiet [10] shows a relationship between the level of leading edge noise radiation and the incoming flow turbulence intensity and integral length scale. Therefore, one avenue to reduce the leading edge noise is to weaken the fluid-structure interaction. Leading edge blowing is an attractive method to achieve this objective, because the injection of mass flow from the leading edge (against the incoming flow) could potentially decrease the turbulence intensity, and hence the level of noise radiation. Depending on the blow rate of the leading edge jet, once mixed with the incoming flow it can be entrained and propagated as streamwise vortices in the downstream direction, along the aerofoil surface. These streamwise vortices, generated indirectly as a result of the leading edge blowing, could bear a certain level of similarity to those produced by a serrated leading edge.

The aerofoil noise theory, injection of mass flow from the leading edge (against the incoming flow) could potentially be an effective mechanism for lowering turbulence intensity, thus the level of turbulence–leading edge interaction noise radiation. The mass flow can be entrained and propagated in the downstream direction in the aerofoil surface following the injection of air from the leading edge and combined with the incoming flow. These streamwise vortices, which were indirectly created by the blowing (serrated) of the leading edge, could also be effective in suppressing the separation of boundary layers, thus increasing tonal noise instability. Leading edge blowing, an active flow control method, can lead to the same mechanisms as a serrated leading edge created to improve the aerodynamic and aeroacoustic performances of aerofoil.

Therefore, the objective of this chapter is to present the experimental aeroacoustic results for an aerofoil subjected to both a serrated leading edge, and an unserrated, straight leading edge, with blowing. Comparisons of the results achieved by the approaches in serrated and straight blowing leading edges will be made quantitatively, to demonstrate whether the serration effects on an aerofoil can be mimicked by leading edge blowing.

4.2 Generation of Turbulence in the Freestream

One of the important parameters to characterise of the flow is the intensity of turbulence (Tu), which is instrumental in many flow phenomena. The rotor-stator interaction and turbulent wake-convection in turbomachinery can achieve Tu of up to 20 percent, which is why it is of major interest to generate the Tu accurately in experimental wind tunnel installations. The very low turbulence intensity of the aerodynamically well-designed wind tunnels is between 0.1 and 0.3 percent. Elevated freestream turbulence generation can be achieved by the biplanar bars with cylindrical wire screens, placing at the inlet of the nozzle as already discussed in chapter 3.

4.3 Analysis of the Acoustics Results

This section introduces the results of a detailed experimental investigation into the efficiency of the straight blowing and serrated leading edges on aerofoils to reduce the leading edge interaction noise and trailing edge instability noise.

The intensity of the turbulence are $Tu = 4.5$ percent (with grid), and $Tu = 0.2$ percent (without grid). The effect of the geometric angle of attack from $-10° \leq \alpha \leq +10°$ will also be investigated. The relationships between ($A \leftrightarrow Q'$) and ($\lambda \leftrightarrow \lambda'$) will be explored for the same conditions as a described in Figure 3-4 and Figure 3-5.

4.3.1 High Turbulence Intensities

4.3.1.1 Effect of Amplitude and Wavelength

This section discusses the acoustic spectra for the different serration wavelengths (λ) and amplitudes (A), and for a turbulent inflow with a turbulence intensity of 4.5%. Figure 4-1 a-f shows the sound power level PWL spectra against the non-dimensional frequency $f\,'(= f.C/U_\infty)$, at open jet velocities from 20 m/s to 60 m/s at combinations of two serration amplitudes (15, 30 mm) and two serration wavelengths (5, 10 mm). The introduction of the serration leading edge is clearly beneficial, with a significant reduction in the turbulent broadband noise, up to 9 dB in some cases. Interestingly, whilst the level of broadband noise reduction increases with A between 15 and 30 mm when λ is constant, as demonstrated in the ΔPWL spectra (ΔPWL is the difference in PWL between the acoustic spectral generated by the baseline and treated (serration) leading edges. A positive +ΔPWL denotes noise reduction by the treated aerofoil, and -ΔPWL means noise reduction), further increase of A actually becomes more prominent. For example, no large difference in noise reduction can be achieved at $\lambda5A30$ and $\lambda10A15$.

It is also clear that the elevated freestream turbulence intensity has triggered a bypass transition on the aerofoil surface, as there is no evidence of instability tonal noise in the acoustic spectrum. First, the comparison is made against the serrated leading edges only. As demonstrated in Figure 4-1 (b, d, f), it can be observed that the most effective serration configuration for the turbulence–leading edge broadband noise reduction is the one with the smallest serration wavelength λ and largest serration amplitude A, although there is also noise increase at high frequency. The level of noise reduction is more sensitive to the serration amplitude A than the serration wavelength λ. Indeed, the use of leading edge serration has been demonstrated throughout the current measurement campaign to be so effective that significant broadband noise reduction across a wide range of frequency, angle of attack and velocity can be achieved by $\lambda5A15$, $\lambda10A15$, $\lambda5A30$, and $\lambda10A30$ respectively as demonstrated in Figure 4-2.

Figure 4-2 also shows the effect of the angle of attack on the ΔPWL. This sensitivity to angle of attack for conventional serration edge aerofoils is well documented in the literature [11]. The minor changes in ΔPWL are observed at $\lambda 10A15$ with increasing the angle of attack observed and large change in the 'effective' angle of attack from -10° to 10° at $\lambda 5A15$, $\lambda 5A30$, and $\lambda 10A30$ respectively. The level of broadband noise reduction and the corresponding frequency bandwidth starts to increase. At the same time, the increase of the high frequency noise becomes more prominent. This trend continues as the angle of attack increases. Overall, the serration becomes highly effective as the angle of attack is increased towards the negative value after identification of different flow behavior features linked to a variable incidence are found. The best reduction noise actually happens at -10° degree angle of attack. To explain this, three schematics were drawn alongside. The noise reduction level is generally observed to be the most sensitive to serration amplitude A. Throughout the range of the angles of attack tested here. At negative angle of attack AoA, the stagnation point is close to the suction surface where the main flow is deflected upwards, which then pass to the valleys of the serration. In this situation, the main flow impinges the leading edge where the serration can exert its "turbulence filtering" effect to reduce the interaction noise. The incoming turbulent eddies by displacing the leading edge stagnation point of the aerofoil. The large positive angle of attack case where the stagnation point is near to the pressure surface, though there are still certain extents of main flow passing through the serration valley. At zero degree the main flow affects the leading edge and the stagnation point close to the leading edge. The overall sound power level (OAPWL) is measured for all serrated leading edge cases, as well as the baseline $\lambda 0A0$, to study the overall effect.

The OAPWL is achieved by integrating the mean-square acoustic pressure, the upper and lower limits of frequencies 20000 and 50 Hz, respectively. Here the level of OAPWL reduction is denoted by (ΔOAPWL), which is defined as OAPWL (baseline) - OAPWL(λxAy), where x = 5 and 10 mm, and y = 15 and 30 mm. Figure 4-3 illustrates the different (ΔOAPWL) achieved by all cases of the serrated leading edges. Similarly, a positive (ΔOAPWL) represents noise reduction, and a negative one represents noise increase.

As a result, as illustrated in Figure 4-3, the OAPWL changes continuously with different serration amplitude (A). Defining of the OAPWL reduction (i.e. ΔOAPWL > 0) would most likely result in stagnation at low serration wavelength (λ). According to this trend and the low noise reduction capability of low amplitudes, the low amplitude of interest for the Design of Experiment is set to A = 15 mm. The influence of the serration wavelength (λ) shows a more continuous tendency than the serration amplitude (A) much weaker. In specific, the influence of this factor on the response variable in the mid to high amplitudes can be represented by the selected experimental design (Figure 4-2). This hypothesis is also supported by the ΔOAPWL, as shown in Figure 4-4.

It can only reach a maximum ΔOAPWL of about 3.35 dB at 20 m/s. However, this is as a result the fact that high frequency noise rise is absence for this specific serration design. This is because the OAPWL in this case also consists of the contribution of sound increases at high frequency. Consequently, it can be shown that the noise performance of the serrations tends to decrease with an increase in U_∞. The serration ($\lambda 5A30$) has been found to reach the best performance, with ΔOAPWL decreasing from 3.35 dB at 20 m/s to 1.4 dB at 60 m/s. The ΔOAPWL results also highlight a new observation in case of the sound reduction. It can be shown that, although the serration $\lambda 5A30$ has generated the largest level of noise reduction in terms of PWL at low frequency, up till now does not produce any noise rise at high frequencies. The main flow impinges the leading edge when the flow deflected upwards and pass through valleys serration.

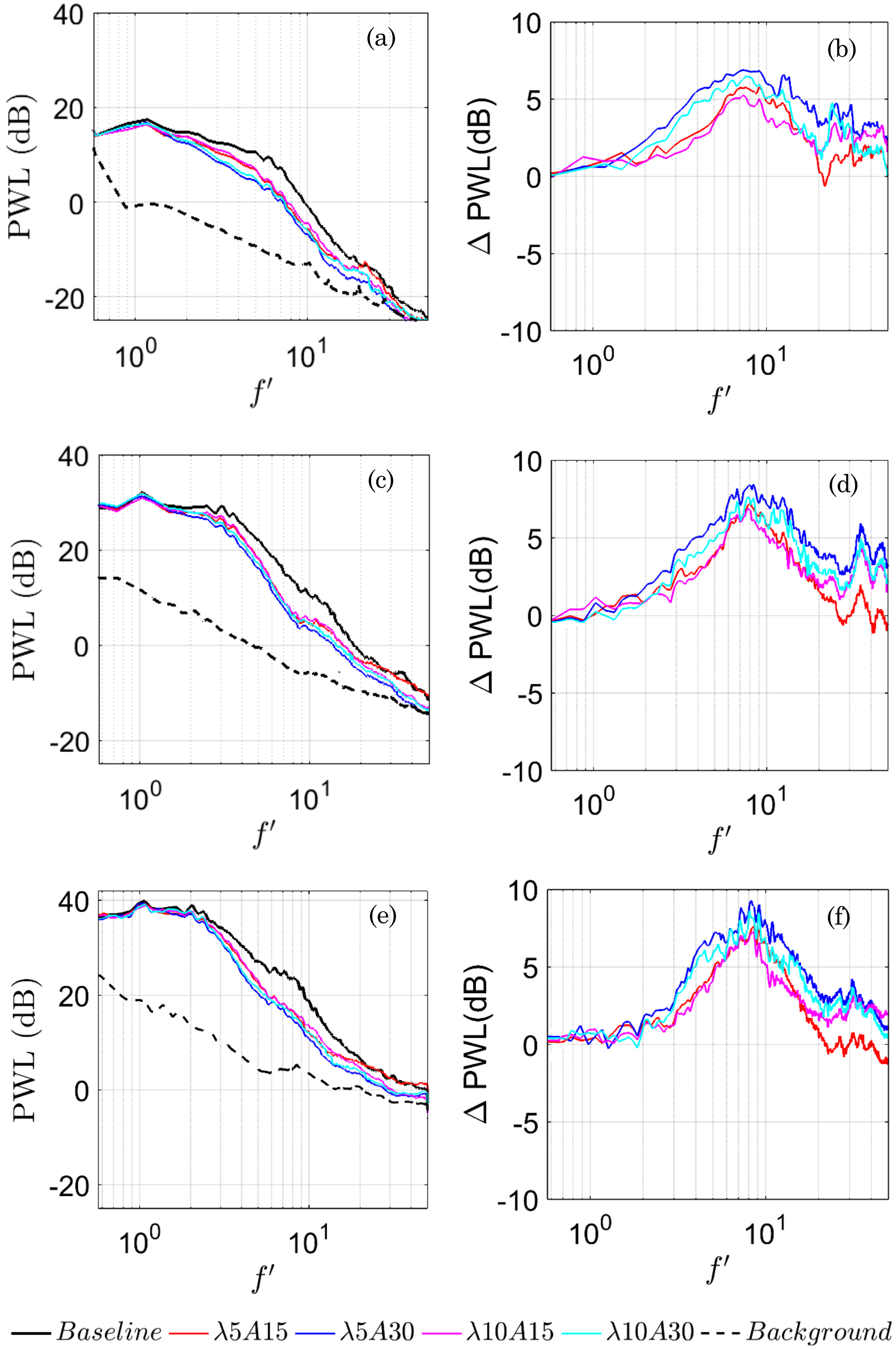

Figure 4-1: Comparison of PWL and ΔPWL as a function of normalised frequency f' at (a, b) U_∞ = 20 m/s (c, d) U_∞ = 40 m/s and (e, f) U_∞ = 60 m/s for various serrated amplitudes (A) and wavelengths (λ), $\alpha = 0°$, and Tu = 4.5%.

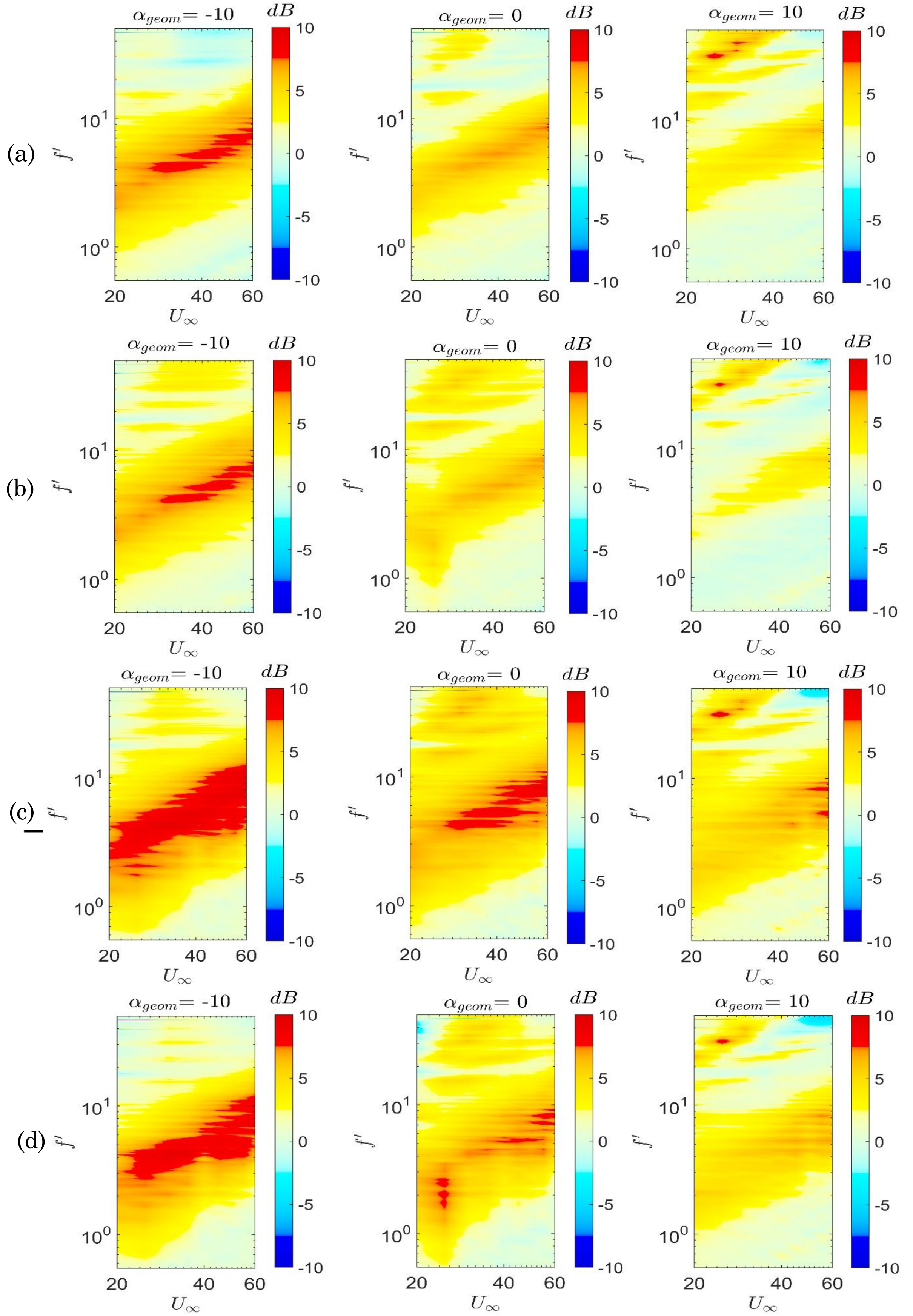

Figure 4-2: Comparison of ΔPWL as a function of normalised frequency f' and U_∞ produced by the serrated leading edges of (a) $\lambda5A15$, (b) $\lambda10A15$, (c) $\lambda5A30$, and (d) $\lambda10A30$. Note that all cases without grid at (α = -10°, 0° and10°) and Tu = 4.5%.

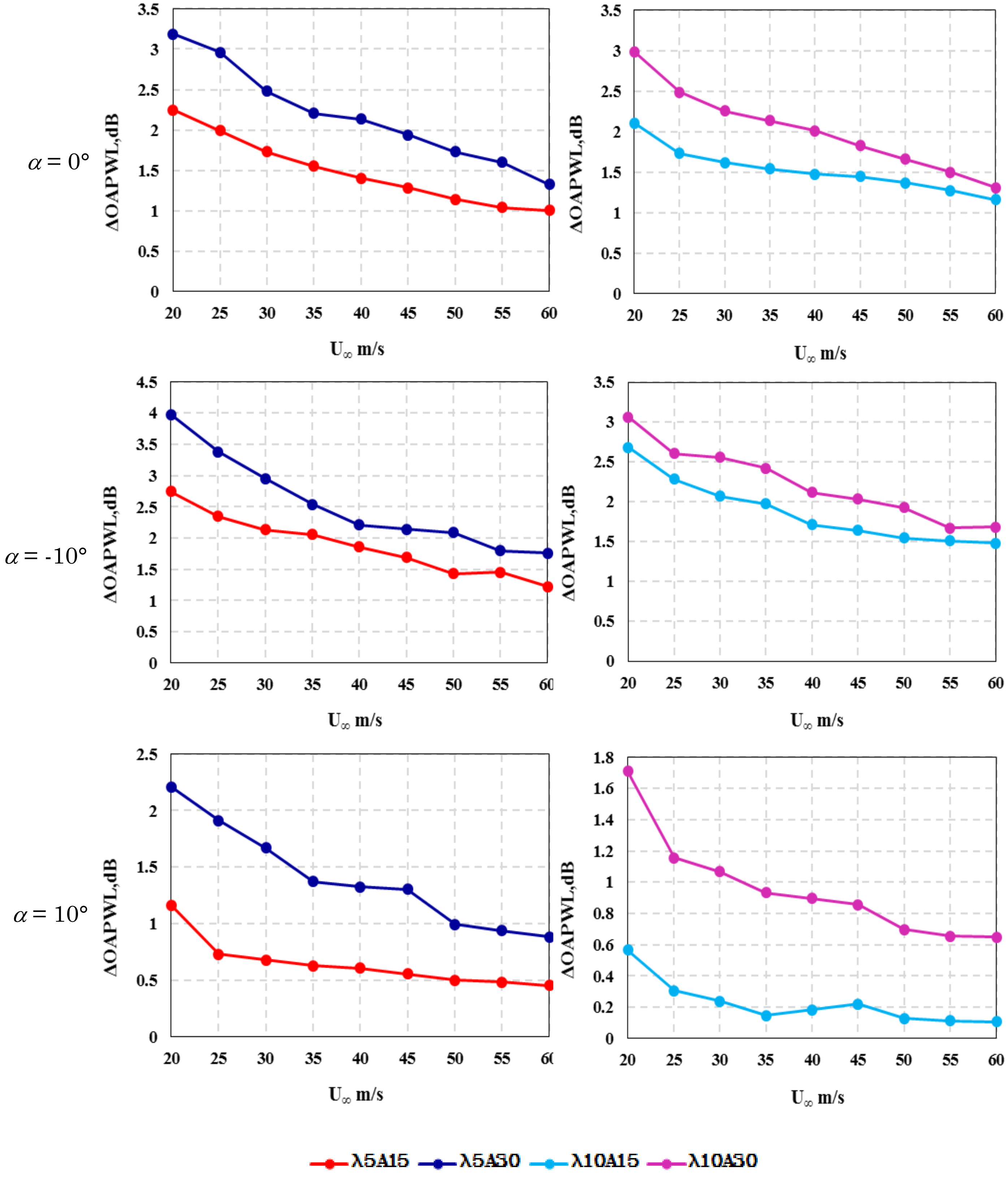

Figure 4-3: Variation of ΔOAPWL for different A and λ at U_∞ = 20-60 m/s by the serrated leading edges. Note that all cases with grid at (α = 0°, 10° and -10°) and Tu = 4.5%.

4.3.1.2 Effect of Blowing rate (Q')

The aeroacoustics results presented in this section relate to the turbulence–leading edge interaction noise due to the presence of elevated turbulence intensity (4.5%) at the freestream subjected to the leading edge blowing. Figure 4-4 compares the sound power level PWL produced by the baseline aerofoil (i.e. $\lambda' = 0$, $Q' = 0$ liter/min) against the blowing leading edge when $\lambda' = 5$, 10 mm and $0.5 \leq Q' \leq 4.5$. Here, λ' represents the spanwise spacing of the blow holes, and Q' represents the volume flow rate. ΔPWL represents the difference in noise spectra between the baseline and blowing leading edges, as a function of non-dimensional frequency ($f.C/U_\infty$). A positive value of ΔPWL denotes noise reduction, and vice versa. The range of jet velocity is $20 \leq U_\infty \leq 60$ m/s, and the angle of attack is set at zero degree. The background noise of the wind tunnel, when far field noise radiation pertaining to the bare jet is measured, is significantly lower than when the aerofoil is present. This confirms the high signal-to-noise ratio of the aeroacoustics results presented in the current study.

In the Figure 4-4, when $U_\infty = 20$ m/s, the PWL spectra produced by the baseline aerofoil is examined, the broadband characteristic as a result of the turbulence interaction is clearly discernible at the low to mid-frequency regions. It is also assumed that the increased freestream turbulence intensity caused a bypass transition on the surface of the aerofoil, as there is no trace of the instability tonal noise in the spectra because these cases happen at high turblent intensity. The introduction of the blowing leading edge is clearly beneficial, with a significant reduction in the turbulent broadband noise (up to 9 dB in some cases). Interestingly, whilst the level of broadband noise reduction increases with Q' between 0.5 and 1 liter/min, as demonstrated in the ΔPWL spectra, further increase of Q' actually becomes detrimental. For example, noise reduction is negligible at $Q' \geq 3.0$ liter/min. Thus emphasise that there exists an optimal value of the blow rate (i.e. ~ 1 liter/min) in relation to the cancellation of incoming freestream turbulence and reduction of the interaction broadband noise. However, based on the available data set, it can be tentatively observed that the criterion of $Q' = 1$ liter/min for an effective reduction of the interaction broadband noise does not apply for higher freestream velocity (e.g. U_∞ = 60 m/s) (see in Figure 4-6).

It should also be mentioned that self-noise produced by the air jets from the leading edge orifices contributes to high frequency noise, typically at $f' > 10$. Although not desirable, this unwanted noise source is outside the frequency range of interest which is within the out of maximum hearing range. Moreover, it becomes less of an issue at higher freestream velocity, because of the increased level of overall aerofoil noise radiation.

Figure 4-5 follows the same format as Figure 4-4. At first glance, the overall trend on the aeroacoustics performance remains relatively the same, thus giving an impression that the effect of Q' to the turbulent broadband noise reduction is more dominant than that by the λ'. However, a closer examination reveals that λ' can also be a significant influencing parameter in the aeroacoustic performance.

The effect of spanwise air hole spacing λ' of aerofoil on leading edge interaction noise is investigated. The sound power level has been plotted against non-dimensional frequency ($f.C / U_\infty$) in Figure 4-5 for varying blow rates from 0.5 to 4.5 liter/min at fixed angle of attack ($\alpha = 0°$), for a jet velocity of 40 m/s. Figure 4-4 clearly shows that the sound power level decreases with increasing blow rate, further supplemented by a smaller value of λ'.

The noise experimental data presented so far could allow us to investigate the mechanism of an optimized serration to further reduce broadband noise.

Figure 4-6 shows the PWL spectra produced by baseline (Q'= 0 liter/min) and blow rates from 0.5 to 4.5 liter/min at angle of attack ($\alpha = 0°$), at U_∞ = 60 m/s. It can be seen that, the PWL spectra in the baseline caseare not very sensitive to the change in Q'. In contrast, the PWL produced by the blowing leading edge increases with Q' up to 1 dB (against the level at Q' = 0) for $3 < f' < 73$ (for two different spanwise air holes, with spacing λ' 5&10mm). Between Q' = 0.5 and 4.5 liter/min, the level of the broadband noise reduction is very low.

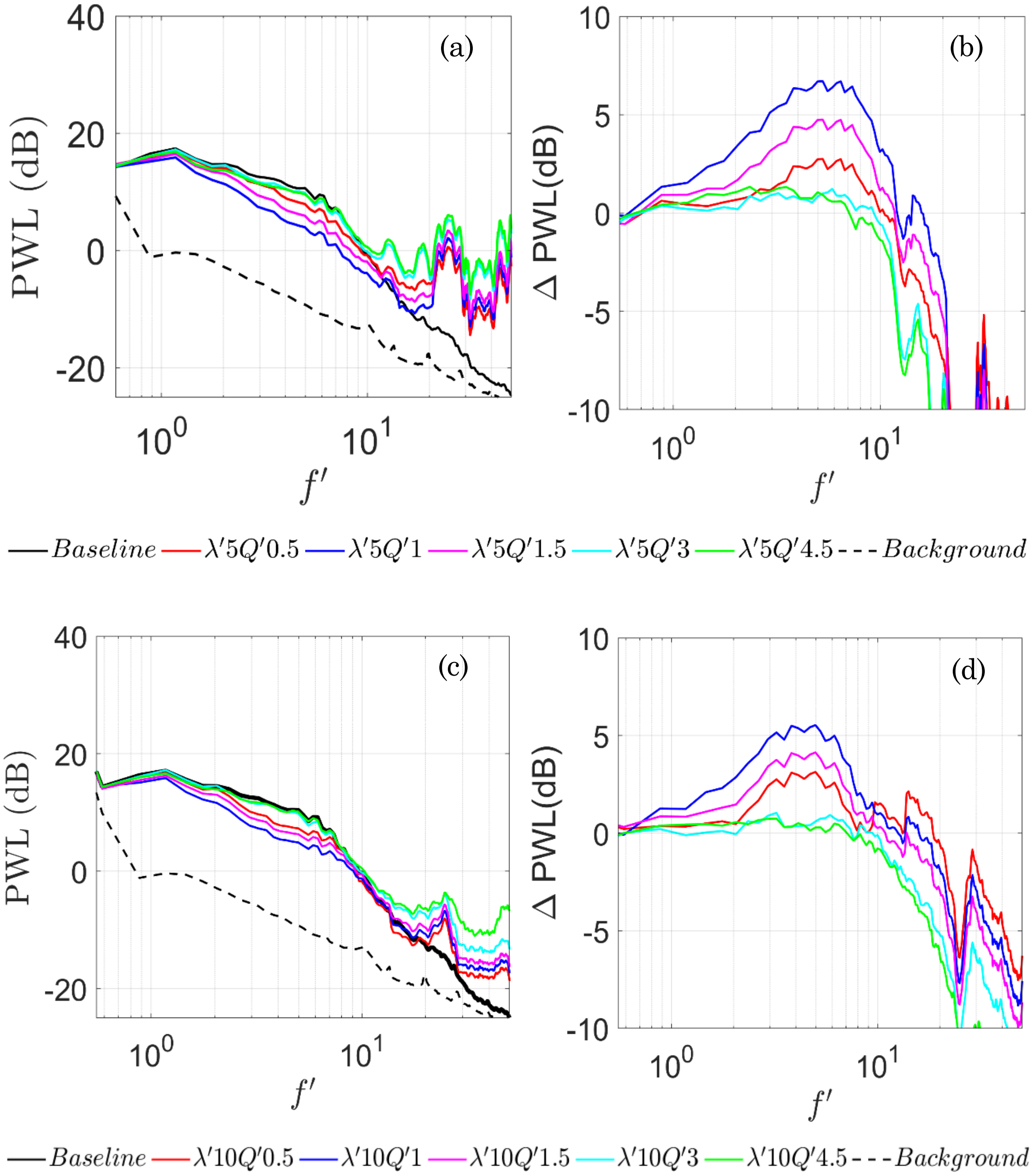

Figure 4-4: Comparison of PWL and ΔPWL as a function of normalised frequency f' at (a, b) λ' = 5 mm and (c, d) λ' = 10 mm when U_∞ = 20 m/s, α = 0°, and Tu = 4.5%.

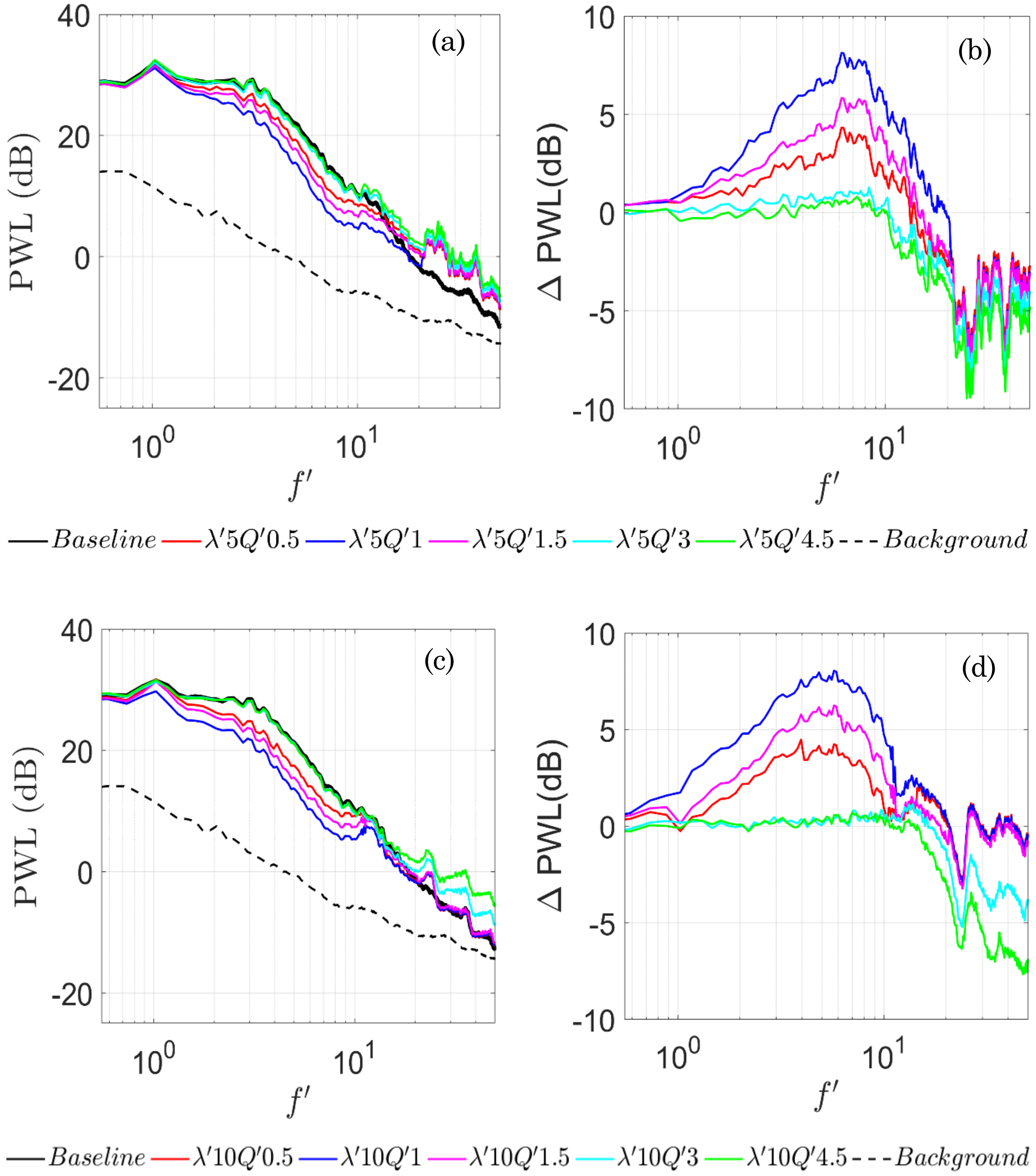

Figure 4-5: Comparison of PWL and ΔPWL as a function of normalised frequency f' at (a, b) λ'= 5 mm and (c, d) λ'= 10 mm when U_∞ = 40 m/s, α = 0°, and Tu = 4.5%.

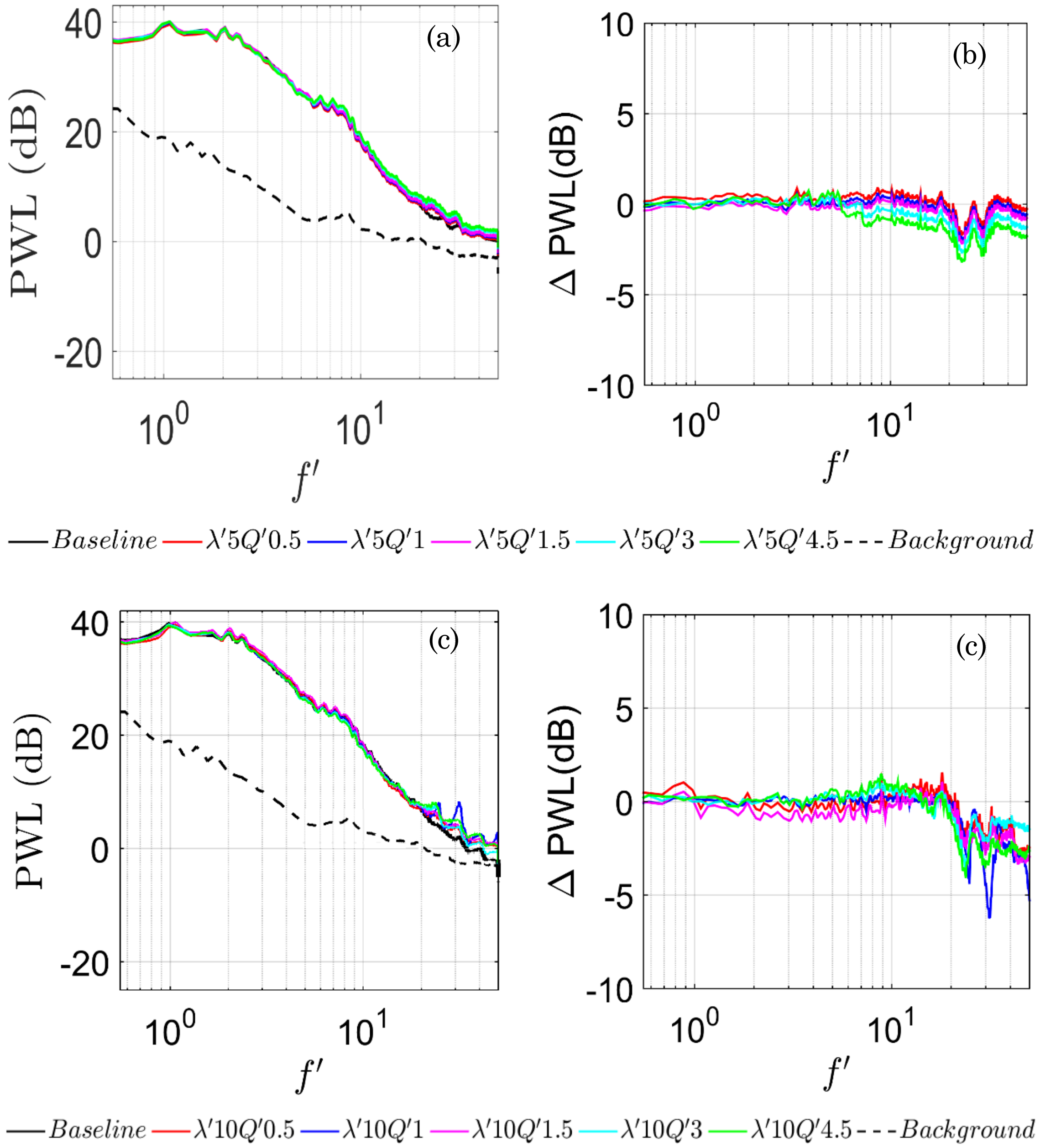

Figure 4-6: Comparison of PWL and ΔPWL as a function of normalised frequency f' at (a, b) λ'= 5 mm and (c, d) λ'= 10 mm when U_∞ = 60 m/s, α = 0°, and Tu = 4.5%.

There may be hints from the noise experimental data that enable us to determine the mechanism of further broadband noise reduction through an appropriately optimized spanwise air hole λ'. To this end, blowing types $\lambda'5$ and $\lambda'10$ were selected to study their correlation with maximum $\Delta\mathrm{PWL}_{\mathrm{max}}$ level (for blow rate (Q'=1 liter/min case) at U_∞ = 20 and 40 m/s. The results are shown in Figure 4-7, indicating that the mechanism underpinning the further broadband noise reduction by the $\lambda'5$ $Q'1$ leading edge is likely to be associated with the increase volume of constant air treatment to the inflow turbulence.

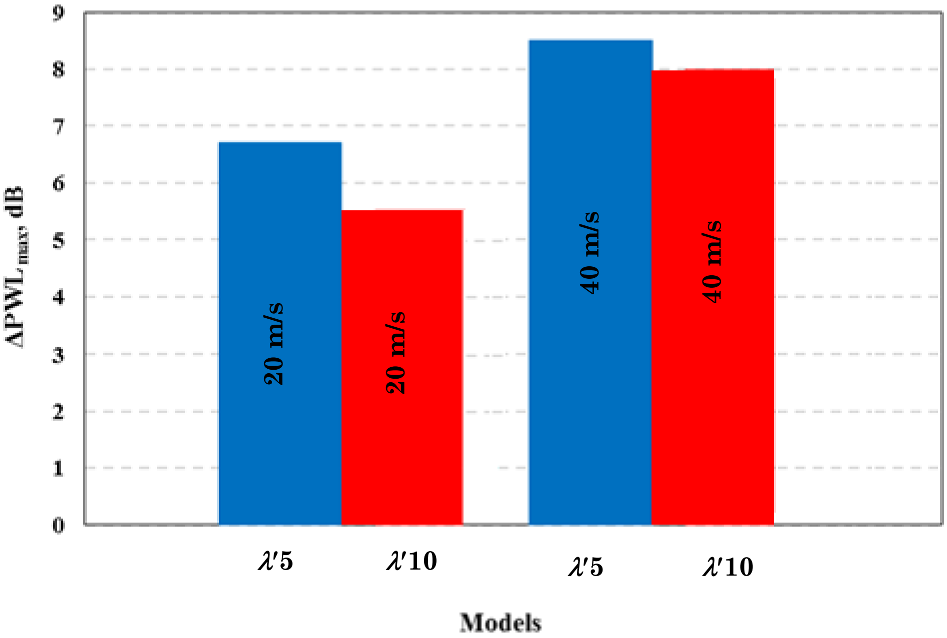

Figure 4-7: Correlation of the ΔPWLmax, (dB) across the models' blowing leading edges (blue bars, 5mm) and (red bars, 10mm) when Q' = 4.5 litre/min. Note that the angle of attack for all cases is set at α = 0° and Tu = 4.5%.

Figure 4-8 shows the contour plots of ΔPWL as a function of f' and U_∞ for the two types of λ' (5 and 10 mm), both of which are subjected to $0.5 \leq Q' \leq 4.5$ liter/min. Although noise reduction generally occurs at a similar frequency range between the two λ' cases, the one with a smaller λ' (5 mm) is found to be more superior and has a wider range of effective freestream velocity. The results depicted in Figure 4-8 largely correspond to the ΔPWL trend in Figures 4-4, 4-5, and 4-6. The highest level of broadband noise reduction over a large frequency bandwidth can be reached with the optimum blowing leading edge (smallest spanwise air hole λ'). It should be noted that in some cases noise increases, especially above the non-dimensional frequency 11 can be observed. The results also suggest that the Q' = 4.5 liter/min case can not achieve noise radiation at the entire velocity range, but improves only with minor effects for lower frequency, as shown in Figure 4-8(g-h). It should be noted that noise increase at higher frequencies can be observed in all cases.

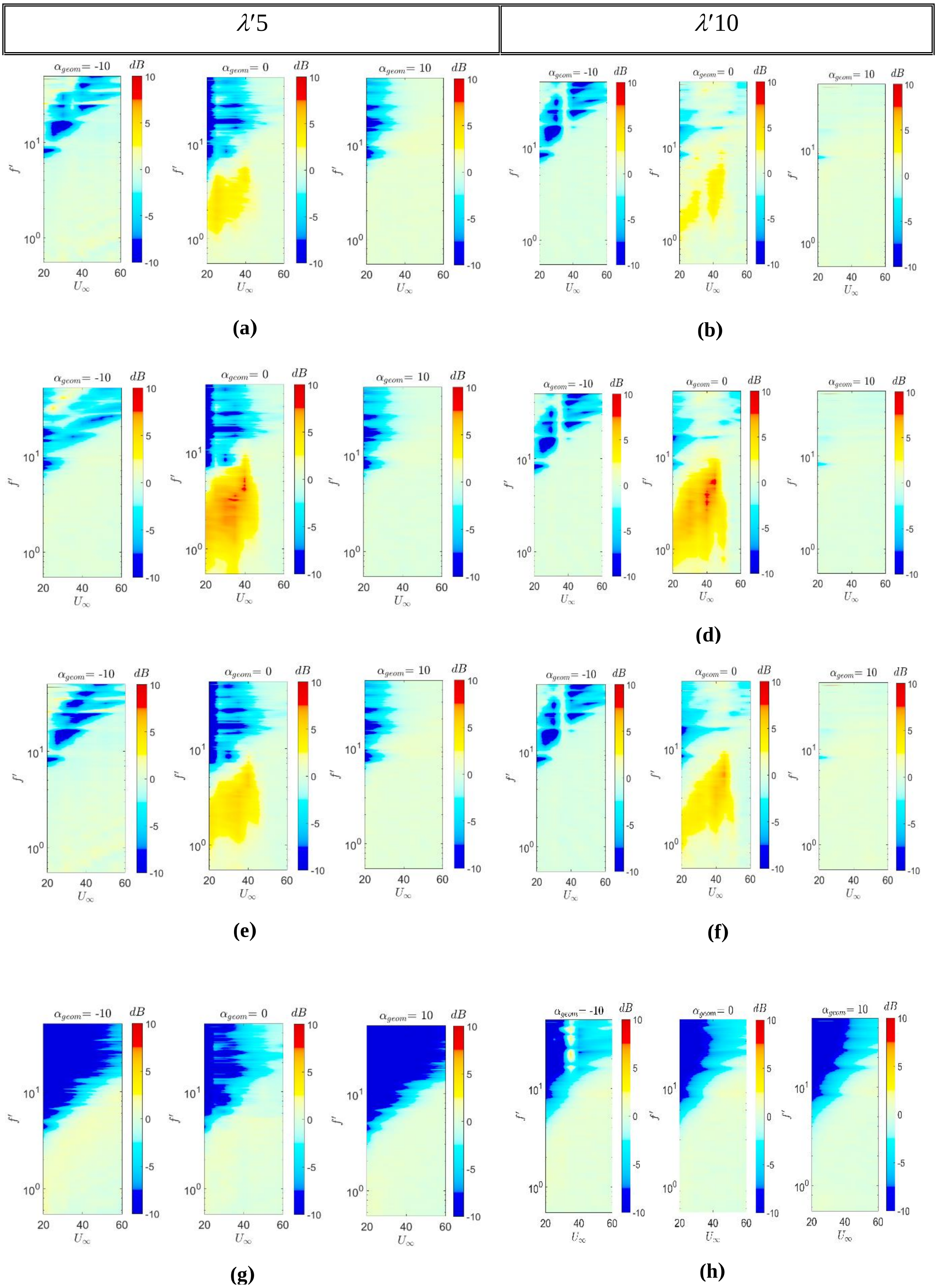

(a) **(b)** **(d)** **(e)** **(f)** **(g)** **(h)**

Figure 4-8: Comparison of ΔPWL for λ´5 (left) and λ´10 (right) as a function of normalised frequency f ′and U_∞ at (α = 0°, 10°, -10°) when Tu = 4.5%, under Q´= 0.5 (a,b), Q´= 1 (c,d), Q´= 1.5 (e,f) litre/min and Q´= 4.5 (g,h) litre/min.

Figure 4-9 shows the ΔOAPWL (difference in OAPWL produced by a baseline and straight blowing leading edges) at $20 \leq U_\infty \leq 60$ m/s for three different blow rates (Q') 0.5, 1.0 and 1.5 liter/min, and a turbulence intensity of 4.5%. The figure suggests the existence of an optimum spanwise air hole λ' and Q' at which maximum noise reductions occur. It is particularly well defined for the smaller $\lambda'5Q'1$, where noise reductions are the greatest. Interestingly, the one with $\lambda' = 5$ mm initially excels at the lower velocity range. After reaching a critical velocity, the ΔOAPWL decays at a faster rate than the $\lambda' = 10$ mm case against the freestream velocity. Coupled with a larger value for the critical velocity, the one with $\lambda' = 10$ mm actually performs better at higher freestream velocity. Another way to examine the ΔOAPWL is shown in Figure 4-10 for a contour maps. The ΔOAPWL bar charts also demonstrate the superior noise reduction performance with a small spanwise air hole space and lower blow rate leading edge. When comparing the two models of spanwise air hole space of $\lambda' = 5$ mm and 10 mm in the ΔOAPWL, the results also suggest that the $Q' = 0.5$ - 4.5 cases are not necessarily the optimum choice. This might be due to the tendency of high frequency noise increase for small spanwise space holes.

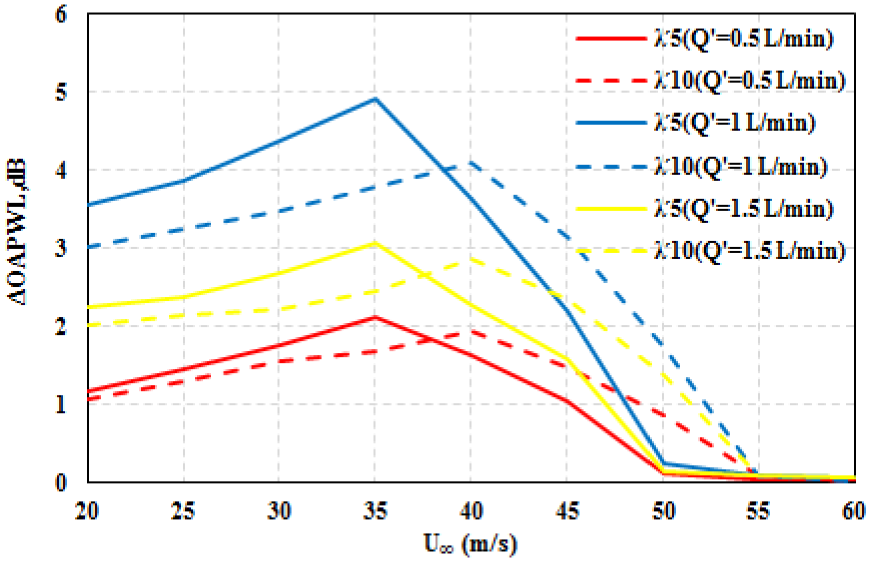

Figure 4-9: Variation of ΔOAPWL for different Q' and λ' at U_∞ = 20-60 m/s, $\alpha = 0°$ and Tu = 4.5%.

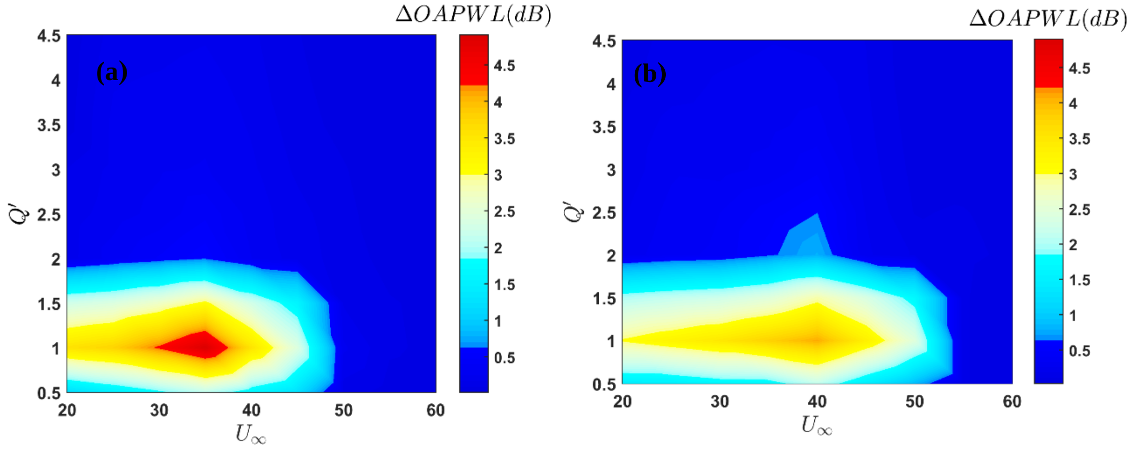

Figure 4-10: Contour maps of ΔOAPWL, dB (noise reduction in the turbulence–leading edge interaction) with velocity for various Q' values produced by the blowing leading edges at (a) $\lambda' = 5$ mm and (b) $\lambda' = 10$ mm, and Tu = 4.5%.

4.3.1.3 Effect of Angle of Attack (AOA)

Figure 4-8 in the perviouse section only demonsturates the ΔPWL for each blowing cases. On the other hand, it does not show the PWL individually to exhibit the broadband interaction noise for each AoA. Consequently, the PWL and ΔPWL are compared the characterics are discussed. Noise radiation by the aerofoil baseline as well as the straight blowing leading edge were measured at various angles of attack. The experimental configuration refers to that already described in Section 3.4. The aerofoil's geometric angle was altered from -10 ° $\le \alpha \le$ +10 °. The turbulence intensity measured between the exit of the nozzle and the leading edge of the aerofoil was Tu = 4.5 percent. Generally speaking, the radiated noise with and without blowing for the straight leading edge does not change much with the angle of attack, with increasing velocity from 20 to 60 m/s, compared with background noise. The PWL radiated noise reaches a maximum value at 10° in the case of a baseline leading edge, and decreases with increasing angle without blowing when Q' = 0 liter/min from positive to negative angle, as shown in Figure 4-11 and reach to maximum noise reduction at -10° angles of attack blacklines.

The related noise emission can be seen in Figure 4-11, after identification of different flow behavior. The noise level increases slightly with increasing angles of attack when the boundary layer is expected to be attached from 0° until 10°.

Further increase cause a short PWL increase, followed by a big reduction with increased blow rates from 0.5-1.5 liter/min when α =0°. A region of angles at 0° defines the best sound reduction capability. In addition, high flow speeds provide the maximum sound reduction when the velocity is 40 m/s, after which the noise reduction decreases to minimum values, as shown in Figures 4-12, 4-13, 4-14, 4-15, 4-16, and 4-17.

In the following discussion, the two parameters that could be used to define a blowing leading edge are the blowing rate Q' and spanwise distance orifice λ'. It has been seen that the leading edge blowing that can achieve the most reduction in the noise level is the $\lambda'5Q'1$ type. In this section, this blowing rate and spanwise of the air hole spacing is chosen to investigate the influence when the aerofoil is subjected to different AoA. Noise measurements were taken with the aerofoil located in the freestream flow at AoA ranging between 10^o and -10^o incresed by 10^o for a velocity from 20 to 60 m/s. Figure 4-14 and Figure 4-15 of ΔPWL between a baseline and straight blowing (Q'=1 liter/min) aerofoil are the optimal reduction level noise compares with other cases, as a function of velocity and frequency. As the angle of attack is increased, changes are observed up to $\alpha = 10^o$ due to the relatively low effective angle of attack. At $\alpha = 10^o$ and $^-10^o$, the level of broadband noise reduction, as well as their frequency bandwidth decrease, and at the same time the increase in high frequency noise becomes more prominent as shown in Figures from 4-12 until the Figure 4-17 and Figures A1 to A4 as shown in Appendix A.

A straight blowing leading edge has been presented to produce good performance in the noise reduction. On the other hand, some disadvantages have also been noticed, most notably the drawbacks in high-frequency noise increases. The next measure is to change the velocity to alleviate the problem of high-frequency noise increase.

It can be seen that for the blowing leading edges of Q'=3.5, and 4.5, increasing Q' at a particular inclination angle of attack will be produced slight changes in the high-frequency noise rise as shown in Appendix A.

Figures A1 to A4 appearance the effect of (AoA) angle of attack on the interaction level noise of the baseline and staight blowing leading edges, which in two cases is negligible. This insensitivity to AoA for conventional straight edge aerofoils is well documented in the literature. Viewing the same insensitivity for leading demonstrates that the mechanism of noise generation at the leading can be similar in both cases and that noise reductions are as a result of interference through the leading edge.

As mentioned before Figure 4-14 & Figure 4-15 shows some important characteristics. The first important feature to note is the region for non-dimensional frequencies from 2 to 12. In this region, the spectral levels are different in amplitude by about 2-3.6 dB between the different cases with the lowest levels shown at 0°, matched flow speed case and the highest levels are seen at 10°, when Q' = 1 liter/min.

The measurements of the far-field noise on the Q' = 1.5 liter/min at flow speeds of 20, 40 and 60m/s were made for three angles of attack from -10° through 10° in increments of 10°. There is a slight decrease in the radiated noise as the angle of attack is increased from -10° to 10° for both spanwise spacing hole λ'= 5 and 10 mm. Figure 4-16 shows that the radiated noise only decreases by 1-3 dB as the angle of attack is decreased from 10° to 0° at 40 m/s when λ'= 5. Figure A1 and A3 (e-f), shows a similar result as shown in Figure A3 and A4 in Appendix A. There is only about a 1-1.3 dB increase in the radiated noise as the angle of attack is increased from 0 to -10° at high frequency Clair [13]. These results are shown for blowing rate of 3.5 liter/min and 4.5 liter/min. The overall shape of the spectra between the two different blowing rates appears to be similar suggesting that the spectra can be scaled on the flow velocity. This scaling will be discussed in detail in a pervious part.

Figure 4-2 in the perviouse section only demonsturates the ∆PWL for each blowing cases. However, it does not appearance the PWL separately to show the broadband interaction noise for each AoA. As a result, will compare the PWL and ∆PWL and discuss the characterics.

The angle of attack has been significantly varied, typically from 0° to -10°. No noticeable difference of noise level has been observed, as shown in Figure

A5 and Figure A6 for the serrated leading edge $\lambda5A15$, and $\lambda5A30$. Only the additional vortex noise mechanism on the aerofoil is found to strongly depend on the angle of attack: the larger the incidence is, the smaller the reduction noise at high frequency for the lower velocity, as observed in the Figure A5a in Appendix A. To summarize, the present measurements show that, at least in the range of parameters investigated, turbulence-interaction noise of an aerofoil is almost independent of the angle of attack. Additionally, it weakly depends on the wavelength serration leading edge. the velocity has a significant impact on the leading edge noise and some significant noise reduction at 60 m/s, increasing with frequency.

Figure A7 and Figure A8 shows the PWL and ΔPWL produced by $\lambda10A15$, and $\lambda10A30$, respectively, at α = 0°, 10° and -10 and U_∞ = 20-60 m/s in Appendix A. It can be seen that for the serrated $\lambda10A30$, the PWL spectra are not very sensitive to the change in α. By contrast, the PWL produced by the $\lambda10A15$ serrated leading edge increases from 1-1.5 dB (against the level at α = -10°) for $10 < f' < 20$. The PWL comparing $\lambda10A15$, and $\lambda10A30$, as a function of U_∞, are shown in Figure. Figures A5 to A8 shows the ΔPWL spectra generated by $\lambda5A15$, $\lambda5A30$, $\lambda10A15$, and $\lambda10A30$, respectively, α = 0°, 10° and -10° and U_∞ = 20-60 m/s. The ΔPWL spectra are sensitive to the change in angle of attack α. In addition, the ΔPWL produced by the $\lambda5A30$ serrated leading edge is the maximum increases with an up to 9.5 dB when f'=11 at negative angle of attack =-10°. Only minor modifications in ΔPWL are observed from α = -10°, 0° in Appendix A. At the same time, the increase of the high frequency noise becomes more prominent. This trend continues as a increases. Overall, the serration becomes more effective as the angle of attack is increased from positive to negative angles of attack.

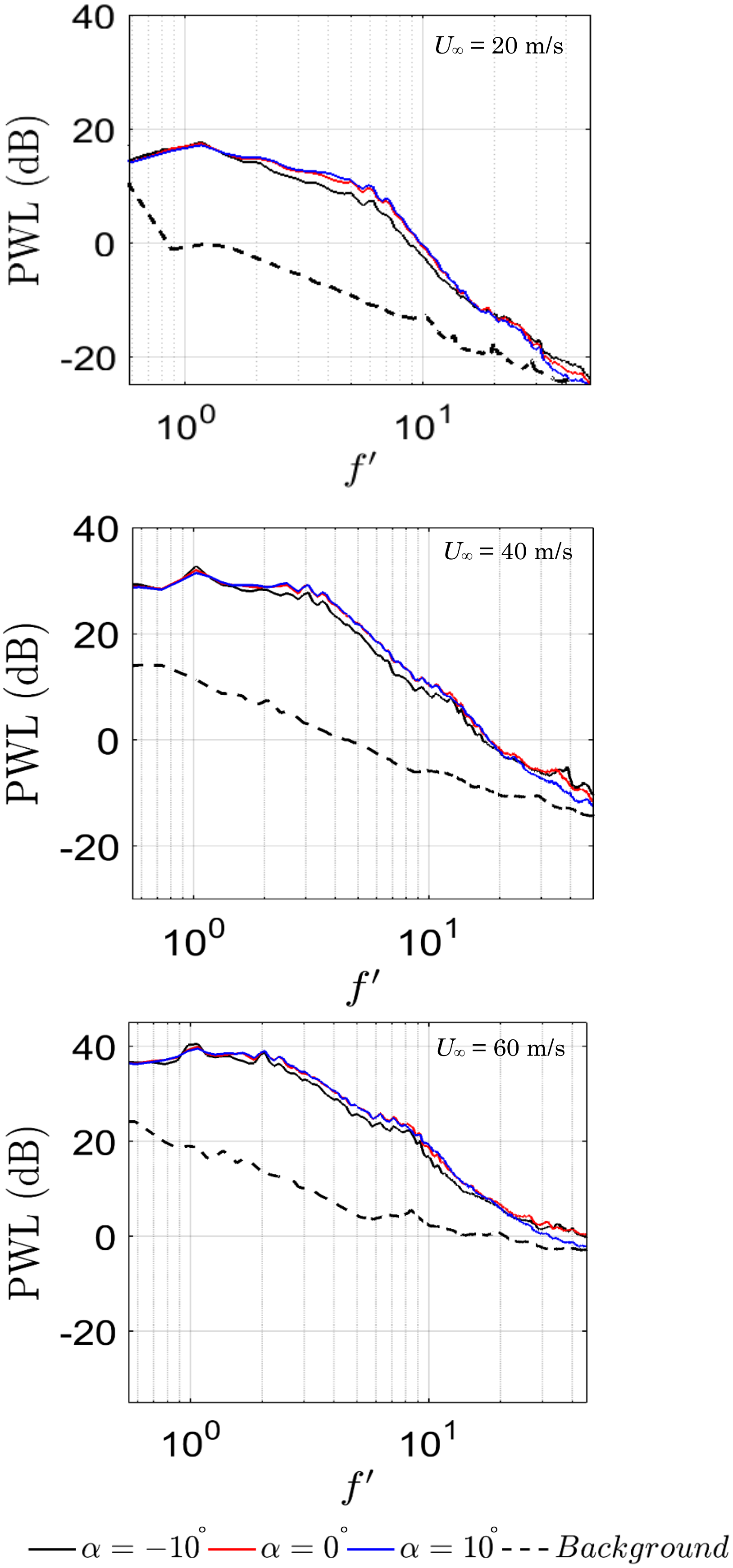

Figure 4-11: Comparison of PWL as a function of normalised frequency f' at U_∞ = 20-60 m/s when Q' = 0 litre/min and Tu = 4.5%.

λ'= 5 mm

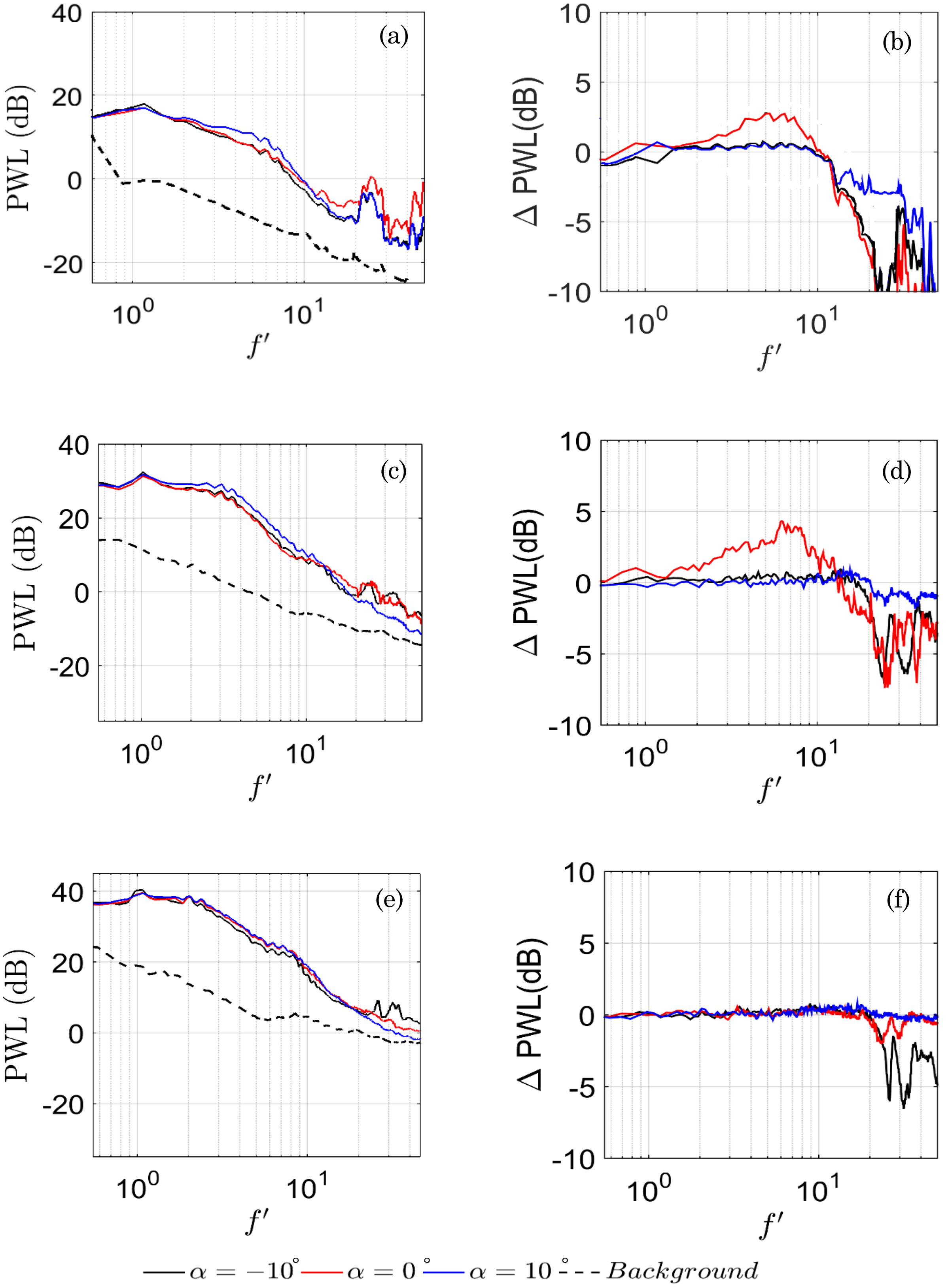

Figure 4-12: Comparison of PWL and ΔPWL as a function of normalised frequency f' at (a, b) U_∞ = 20 m/s, (c, d) U_∞ = 40 m/s and (e, f) U_∞ = 60 m/s when Q' = 0.5 litre/min and Tu = 4.5%.

$\lambda' = 10$ mm

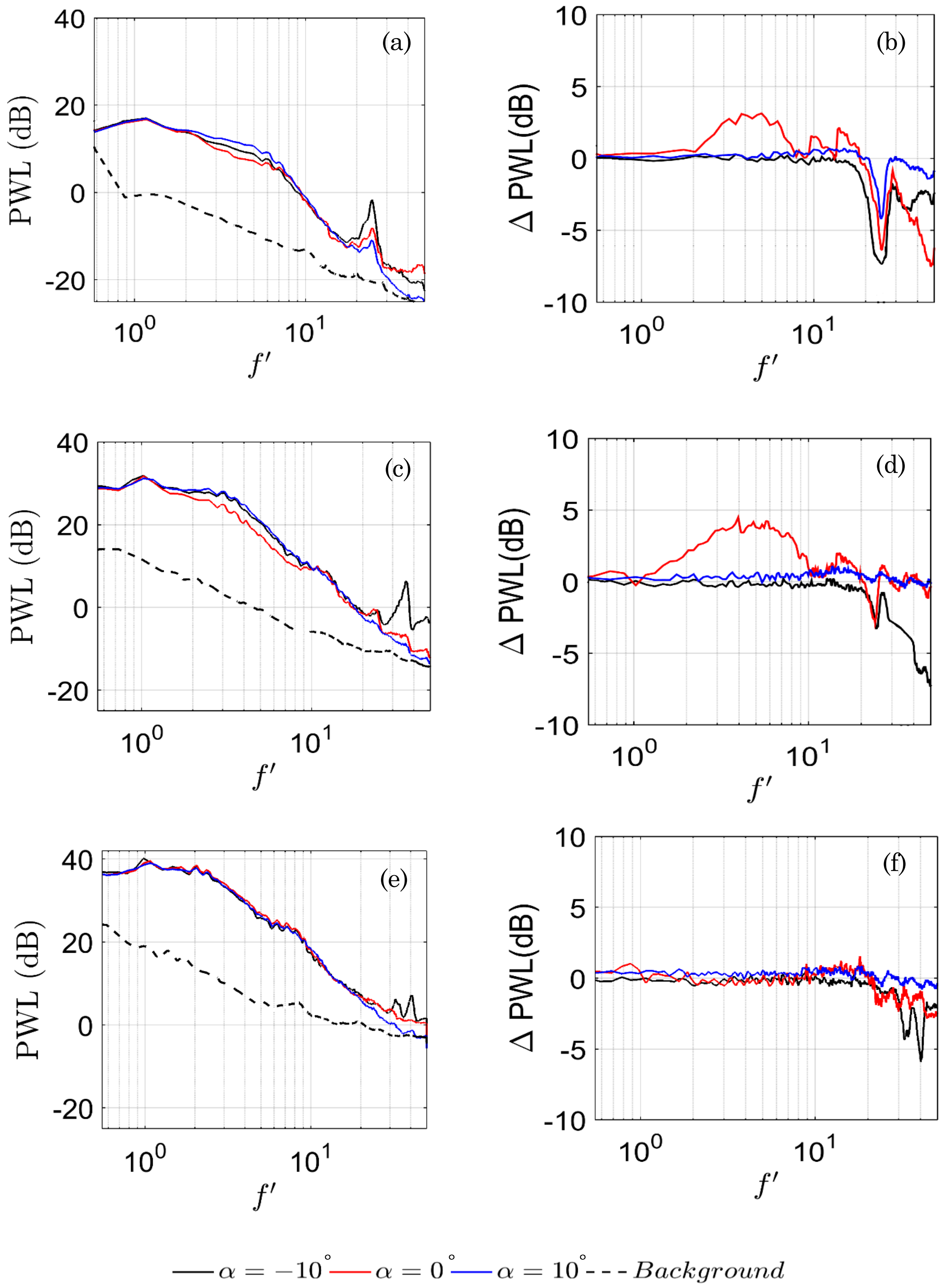

Figure 4-13: Comparison of PWL and ΔPWL as a function of normalised frequency f' at (a, b) $U_\infty = 20$ m/s, (c, d) $U_\infty = 40$ m/s and (e, f) $U_\infty = 60$ m/s when $Q' = 0.5$ litre/min and $Tu = 4.5\%$.

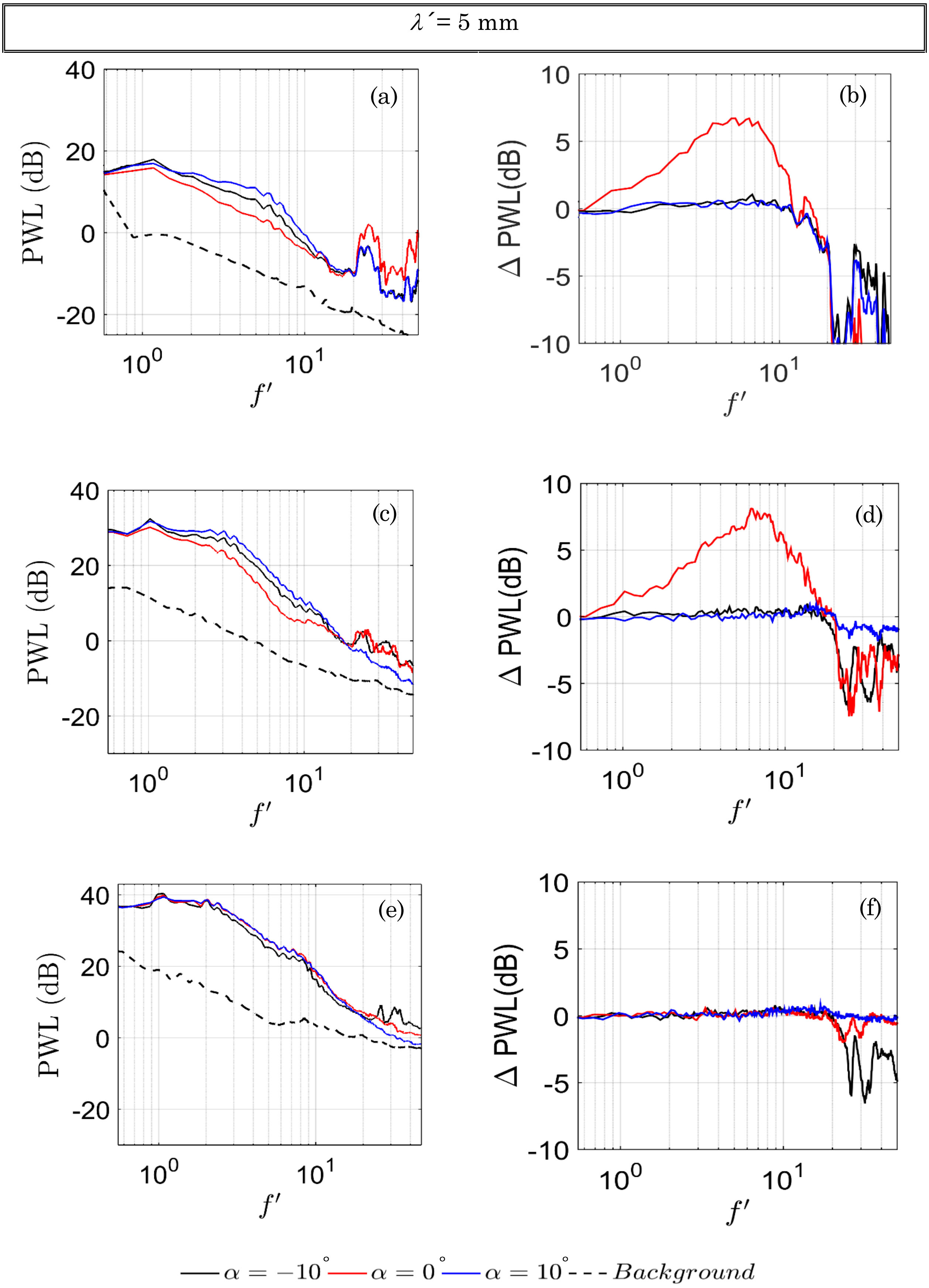

Figure 4-14: Comparison of PWL and ΔPWL as a function of normalised frequency f' at (a, b) U_∞ = 20 m/s, (c, d) U_∞ = 40 m/s and (e, f) U_∞ = 60 m/s when Q' = 1 litre/min and Tu = 4.5%.

λ' = 10 mm

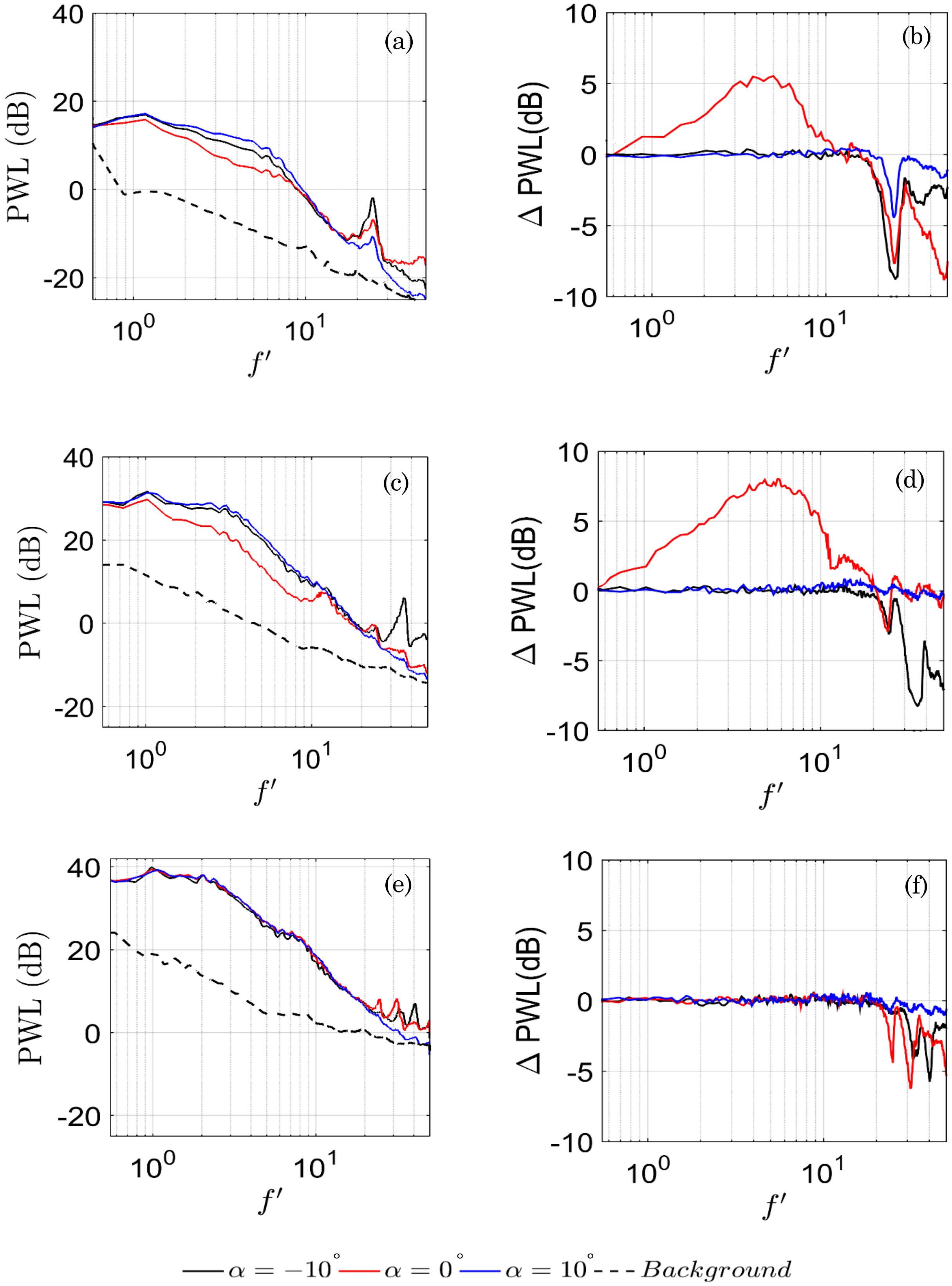

Figure 4-15: Comparison of PWL and ΔPWL as a function of normalised frequency f' at (a, b) U_∞ = 20 m/s, (c, d) U_∞ = 40 m/s and (e, f) U_∞ = 60 m/s when Q' = 1 litre/min and Tu = 4.5%.

$\lambda' = 5$ mm

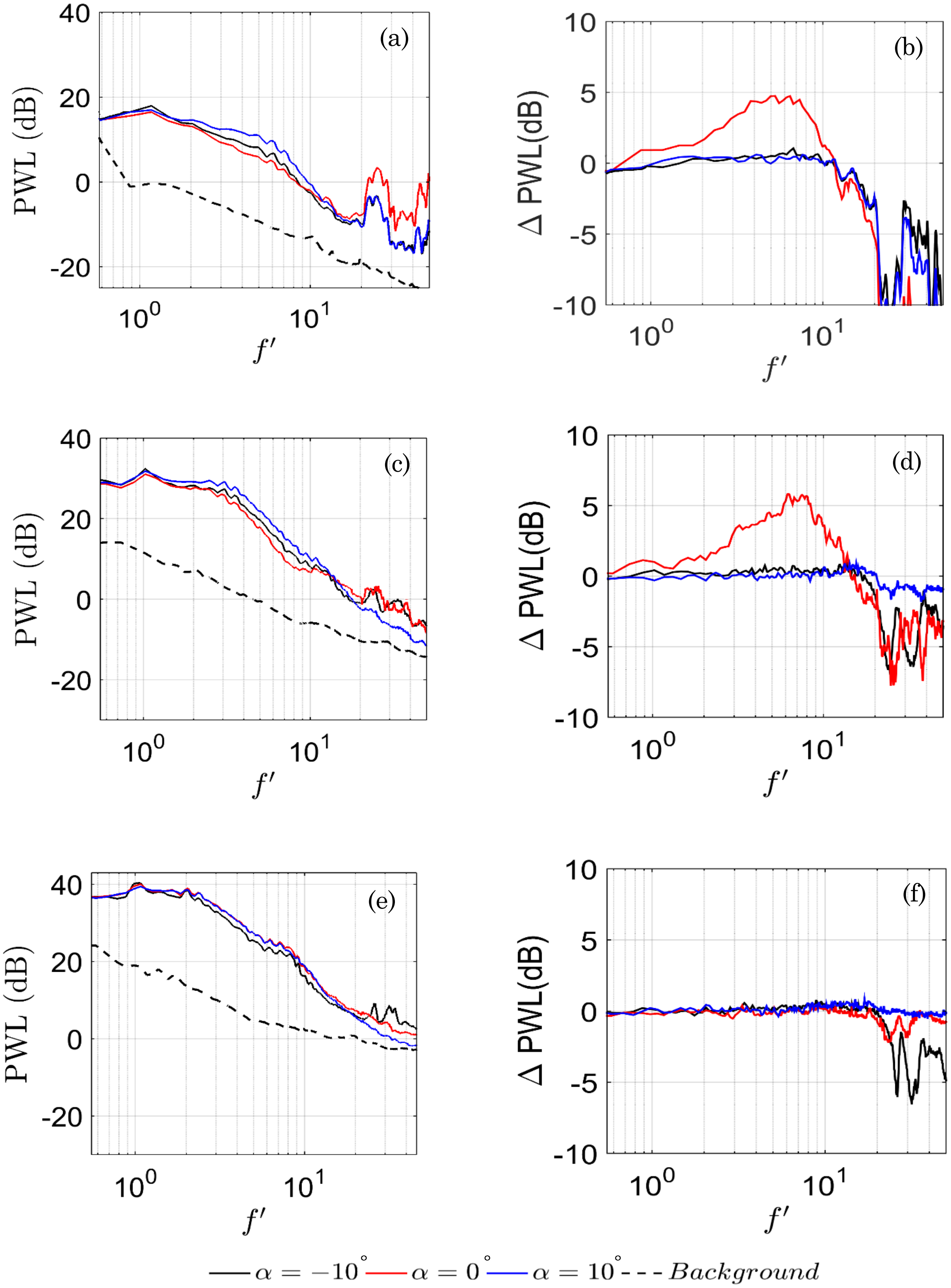

Figure 4-16: Comparison of PWL and ΔPWL as a function of normalised frequency f' at (a, b) U_∞ = 20 m/s, (c, d) U_∞ = 40 m/s and (e, f) U_∞ = 60 m/s when Q' = 1.5 litre/min and Tu = 4.5%.

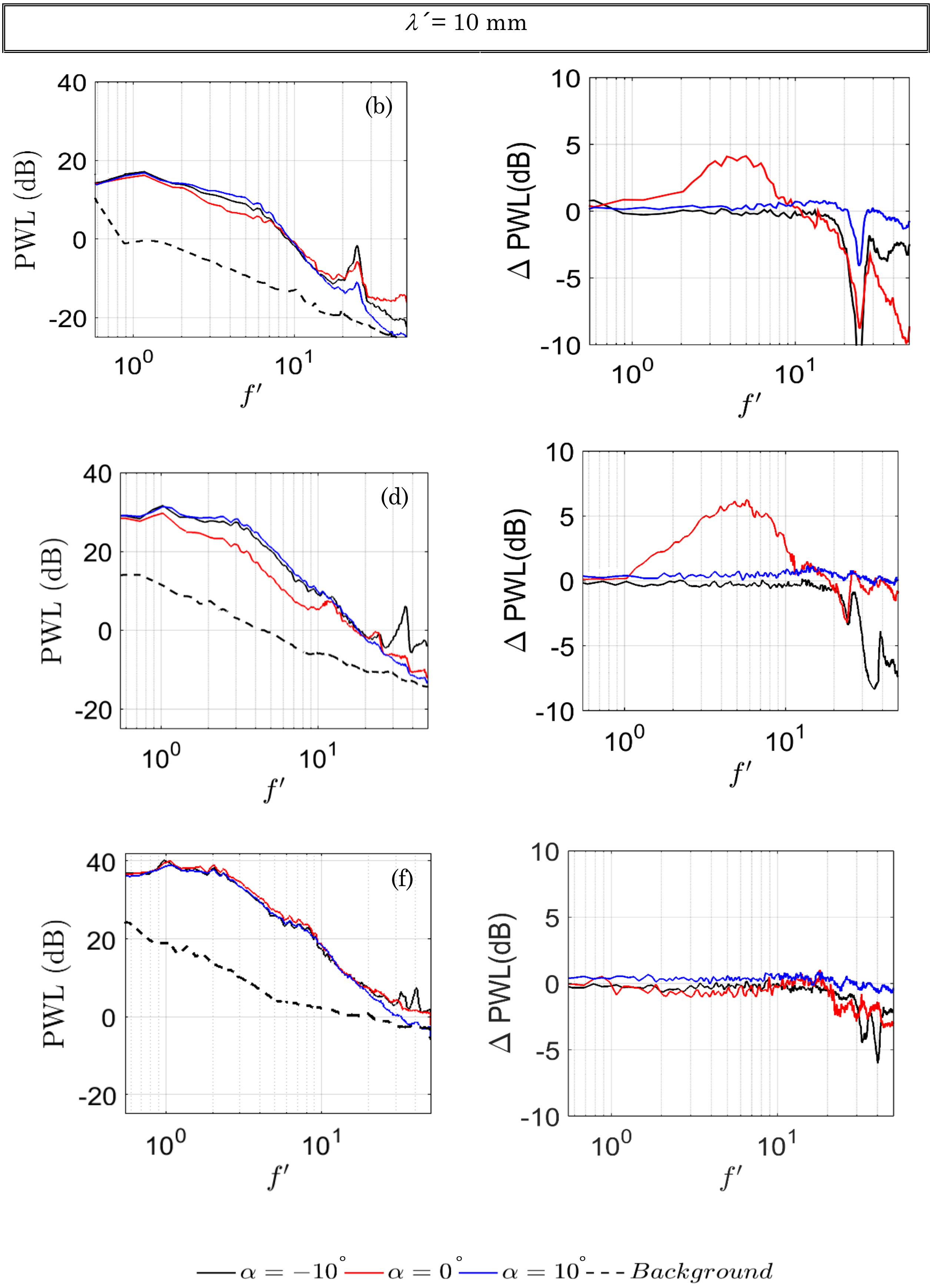

Figure 4-17: Comparison of PWL and ΔPWL as a function of normalised frequency f' at (a, b) U_∞ = 20 m/s, (c, d) U_∞ = 40 m/s and (e, f) U_∞ = 60 m/s when Q' = 1.5 litre/min and Tu = 4.5%.

4.3.1.4 Correlation between the ($A \leftrightarrow Q'$) and ($\lambda \leftrightarrow \lambda'$)

Facilitating different blowing volume flow rates on the straight leading edges could produce very interesting noise performances. It is generally found that the noise reduction by leading edge blowing can indeed be achieved, but over a rather narrow range of blowing rate Q'. Below or above the optimal range of Q', no significant noise reduction can be observed across the frequency. One-on-one direct comparison between each paring of (λ and A – serrated leading edge) and (λ' and Q' – leading edge blowing) against their performances in the PWL and ΔPWL. Noise performances by the $\lambda5A15$ and $\lambda10A15$ serrated leading edge are compared against $\lambda'5Q'1$ and $\lambda'10Q'1$ at $U_\infty = 25$ m/s, which is shown in Figure 4-26a,b. It clearly identifies strong similarities in the noise reduction trend at $f' < 10$. Above this frequency, however, jet noise from the air holes becomes dominant and overtakes the aerofoil noise. As a result, the negative value of ΔPWL (i.e. noise increase) has been produced by the leading edge blowing.

It is interesting to note that the effective margin of the leading edge blowing volume flow rate is the same for Q' from the most optimised value would produce a large difference in the noise performance when $\lambda' = 5$ mm. The concept of the leading edge blowing is to minimise the interaction of an incoming turbulent flow with the leading edge of the aerofoil. Through blowing, the leading edge jet continuously opposes (and possibly dissipates) the incoming turbulent eddies by either displacing the leading edge stagnation point of the aerofoil, or creating a buffer zone over the region around the aerofoil leading edge. It seems that one or possibly both of these mechanisms could be very sensitive to the blowing volume flow rate.

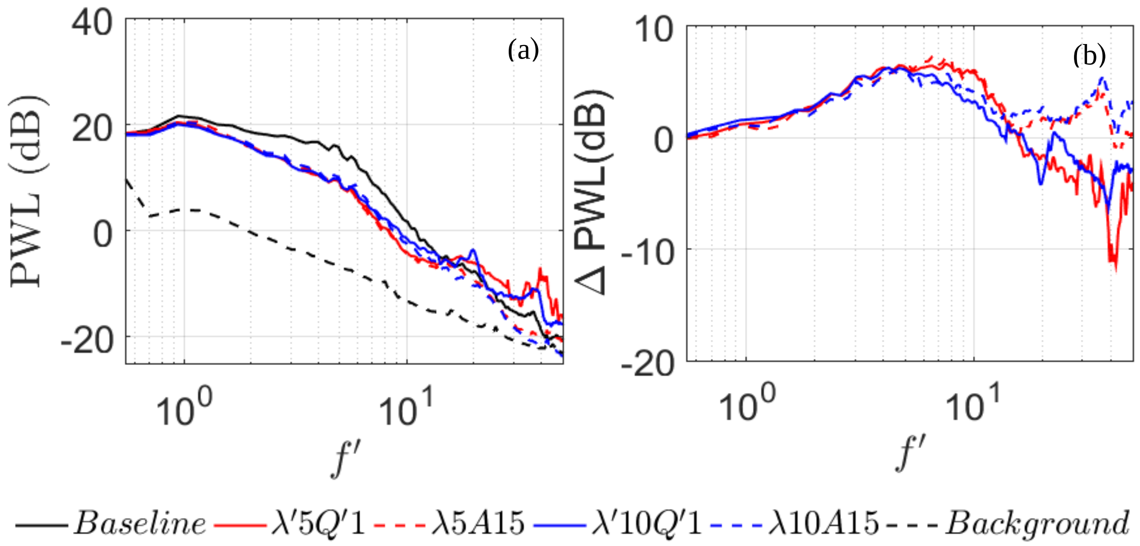

Figure 4-18: Comparison of (a) PWL and (b) ΔPWL, as a function of normalised frequency f', produced by serrated leading edges (broken lines red & blue, $\lambda 5A15$ and $\lambda 10A15$), and blowing leading edges (solid lines red & blue, $\lambda' 5Q' 1$ and $\lambda' 10Q' 1$) at U_∞ = 25 m/s and Tu = 4.5%. Note that the angle of attack for all cases is set at $\alpha = 0°$.

4.3.2 Low Turbulence Intensities

When the freestream turbulence intensity is low, the aeroacoustic response of an aerofoil will be predominantly at the trailing edge. More specifically, without mechanism of bypass transition, and at low Reynolds number, the Tollmien-Schlichting instability waves will form and propagate downstream towards the trailing edge. If a separation bubble forms near the trailing edge, the incoming instability waves will interact with the separation bubble to cause an inviscid amplification, which is significant enough to scatter a broadband-hump into the far field. Due to a relatively high boundary layer receptivity to disturbances, including acoustical disturbance, at the upstream part of the aerofoil, the scattered broadband-hump feeds back to the inception point of the original Tollmien-Schlichting waves. This combination of hydrodynamic and acoustical disturbances forms a loop and phase completion of 2nπ, where n is an integer. A selection of integers n will resonate the broadband-hump to cause superposition of multiple, sharp tones. There are several familiar features concerning the laminar tonal noise instability, including the existence for the broadband-hump and discrete tones of the velocity, and the "ladder" structure. The result shows that the transition from the bypass boundary layer on the aerofoils surfaces was not triggered by the low intensity of freestream turbulence.

4.3.2.1 Effect of Amplitude and Wavelength

Tonal noise generation is believed to be initiated by Tollmien-Schlichting instabilities in a laminar boundary layer, which become amplified at the aerofoil trailing edge or at a point nearby. In this context, leading edge serrations can be responsible for the suppression of the tonal noise generation at the trailing edge or the reduction of trailing edge broadband noise. As already mentioned the generation of tonal noise at the aerofoil trailing edge occurs only in case of a low turbulent inflow. The leading edge interaction noise and self-noise trailing edge influence of the serrated leading edge can be determined by individual measures of overall radiation noise (i.e. LE, TE, and background noise), the amount of self-noise (without turbulent grid), and background noise spectra (without aerofoil) alone.

This section studies the difference between the leading edge noise and self-noise, in addition to assessing the influence of serrated leading edge on the trailing edge self-noise. And presents the results of noise measured in an acoustic facility at low turbulence without grid, mounted in the nozzle. The low turbulence intensity during the freestream makes sure that noise interaction from the leading edge is not the main source of noise.

Figure 4-27 illustrates the total emitted sound power level spectra for the baseline versus non-dimensional frequencies ($f.C/U_\infty$) at the freestream velocities from 20 to 30 m/s. The figure also presents the PWL spectra created by $\lambda5A15$, $\lambda10A15$, $\lambda5A30$, and $\lambda10A30$. The baseline leading edge is $\lambda0A0$. A clear trend that can be seen in the figure is that when λ decreases, the PWL level decreases at the same and value of *A*. Several discrete tones are generally preserved for these serrated cases, even if the frequency of the tone remains unchanged. Consequently, instability tonal noise radiation would be less effective, as shown in the lower PWL spectra in Figure 4-27a. As a summary of the influence of wavelength λ on instability tonal noise, the tonal noise level can be further reduced by a smaller λ. This is because a smaller serration can be produced more streamwise vortices for each unit span that would cover a larger area of the separated area close to the trailing edge, thus weakening the amplification process necessary to maintain the radiation of instability tonal noise. The influence of serrated amplitude A on tonal noise radiation is investigated now. It is apparent from the figure that the radiated noise is more sensitive to amplitude A, and the reduction level of the tonal noise instability can be significantly improved by the increase of A. The $\lambda 5A30$ case can completely suppress the tonal noise instability up to 35 dB at $U_\infty =$ 20 m/s. In order to cause a complete loss of tonal acoustic instability characteristics (multiple discrete tones and tonal broadband-hump), the amplitude (A) should be at least 30 mm (or A/C = 0.2).

In the acoustic spectra there is a large difference between the baseline and serrated leading edges of $\lambda 5A15$ and $\lambda 5A30$. This is because the serrated leading edge of the $\lambda 5A30$ is expected to provide stronger streamwise vortices that can penetrate into the back separated area near the trailing edge. The flow structures can also be created with the serrated leading edge $\lambda 10A15$, which suppresses a larger part of a separated area near to the trailing edge, as manifested by the slightly improved tonal noise reducation.

The results thus far for the $\lambda 5A15$, $\lambda 10A15$, $\lambda 5A30$, and $\lambda 10A30$ serrated leading edges allow us to determine that small λ and large A are the requirements for effective reduction of instability tonal noise.

The mechanism is that the laminar separation area near the trailing edge is suppressed by generating more high streamwise vortices.

It is necessary to note that some high-frequency ($f' > 10$) noise increases occur when amplitude (A) increases, enabling identification of the exact noise source, where it could be estimated that the high-frequency noise incresae is the result of leakage noise through the large serration gaps.

Figure 4-28a-d shows the ΔPWL colormap (as a function of velocity and frequency). Many familiar features of the instability of tonal noise created by a laminar aerofoil are discernible. In this case, the noise reduction involves the elimination of instability tonal noise and is significantly higher level than the reduction of broadband noise. Therefore, noise reduction jumps from 10 dB in the low A to 35 dB in the high A serrations.

As a summary, larger amplitudes are more effective for sound reduction. The wavelength appearances are best at intermediate values, and the sound reduction capability decreases at low values.

Figure 4-28c presents the ΔPWL for the different angle of attack (α) cases between the baseline ($\lambda0A0$) and serrated ($\lambda5A30$), depending on U_∞ and f'. Due to the relatively good change in the effective angle of attack, the slight changes in the ΔPWL are noted from 0° to 10°. The level of the noise reduction and the corresponding frequency range start to decrease as the AoA increase, especially when wavelength increases from 5 to 10 mm with constant amplitude at 15 mm, as seen in Figure 4-28a,b. The serration is generally less effective when the angle of attack is increased. This could be fact that boundart layer separation changes considerably whenthe pressure gradients vary. To study the overall influence, the OAPWL is calculated for all serrated leading edge cases, including the baseline case $\lambda0A0$. Various ΔOAPWL values produced by all of the serrated leading edges are shown in Figure 4-29. The sensitivity of the noise performance to A can be shown to decrease gradually as λ decreases. The most significant noise reduction is still the serration $\lambda5A30$, where a maximum ΔOAPWL of around 24 dB is achieved at U_∞ =20 m/s. However, another serration $\lambda10A30$, at the same U_∞, can also achieve good level of ΔOAPWL of around 21 dB. The ΔOAPWL results also highlight that the performance of the serrations tend to decrease with increasing U_∞.

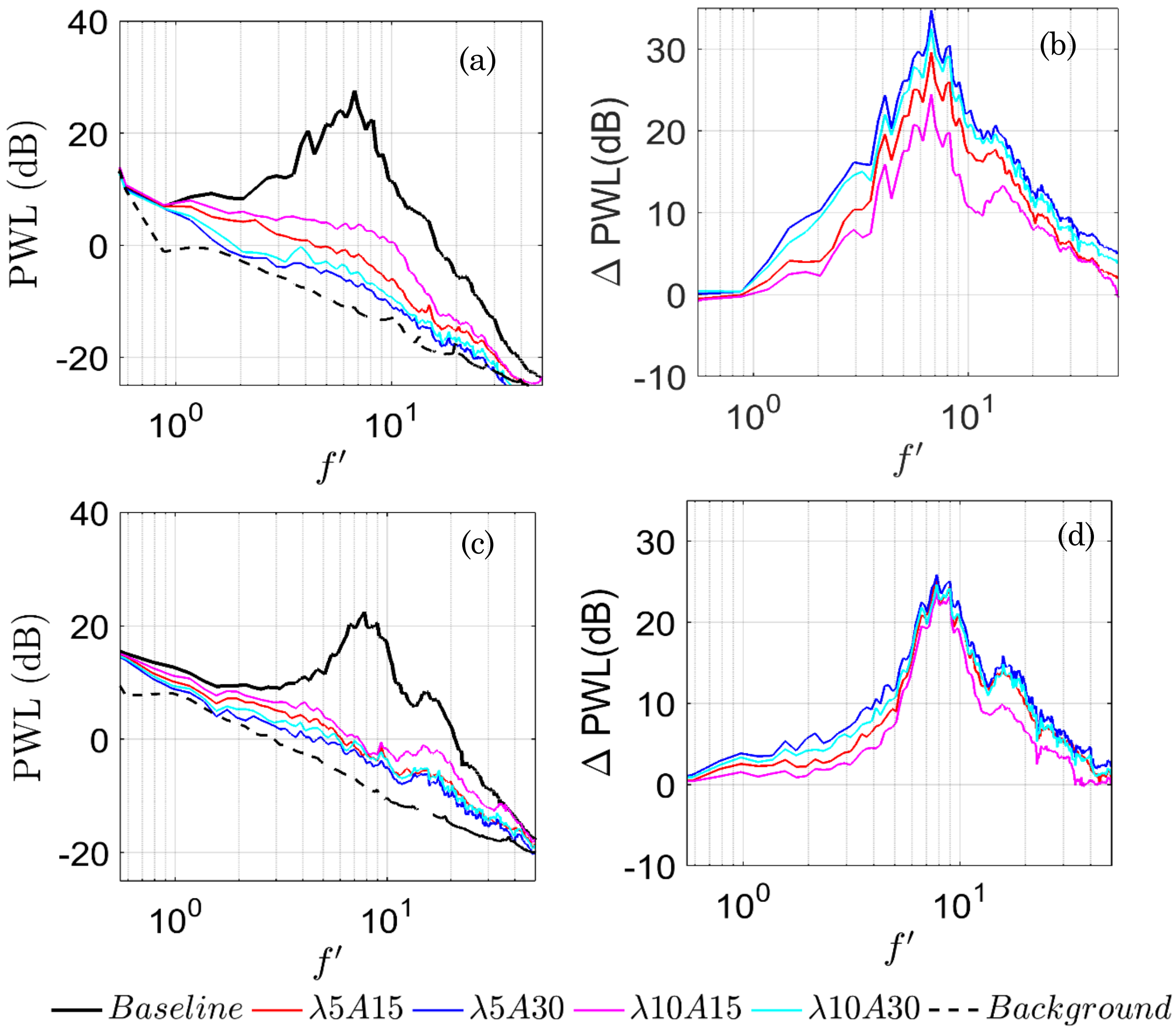

Figure 4-19: Comparison of PWL and ΔPWL as a function of normalised frequency f' at (a, b) $U_\infty = 20$ m/s and (c, d) $U_\infty = 30$ m/s and for various serrated amplitudes (A) and wavelengths (λ), $\alpha = 0°$, and $Tu = 0.2\%$.

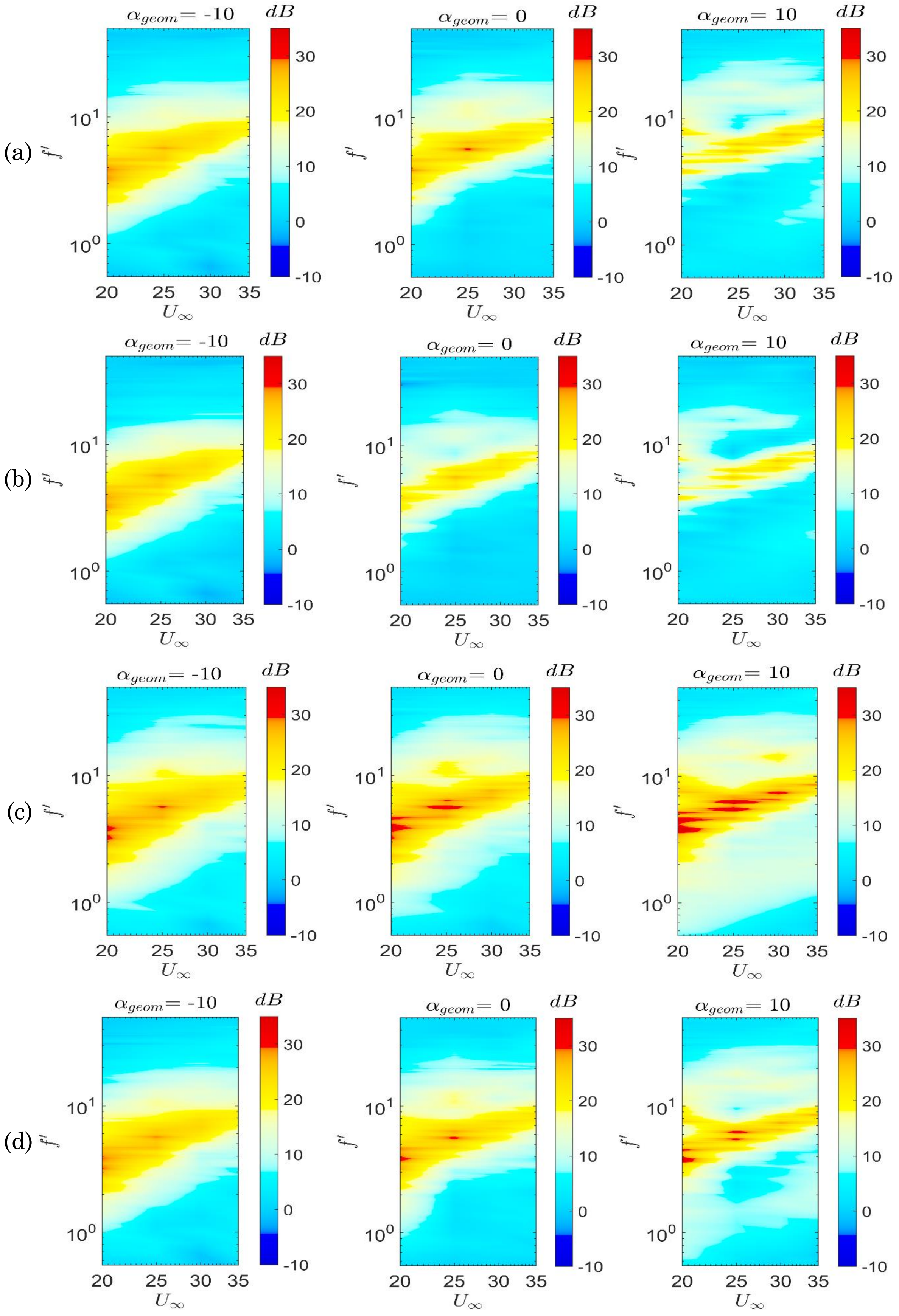

Figure 4-20: Comparison of ΔPWL as a function of normalised frequency f' and U_∞ produced by the serrated leading edges of (a) $\lambda 5A15$, (b) $\lambda 10A15$, (c) $\lambda 5A30$, and (d) $\lambda 10A30$. Note that all cases without grid at (α = -10°, 0°, and 10°) and Tu = 0.2%.

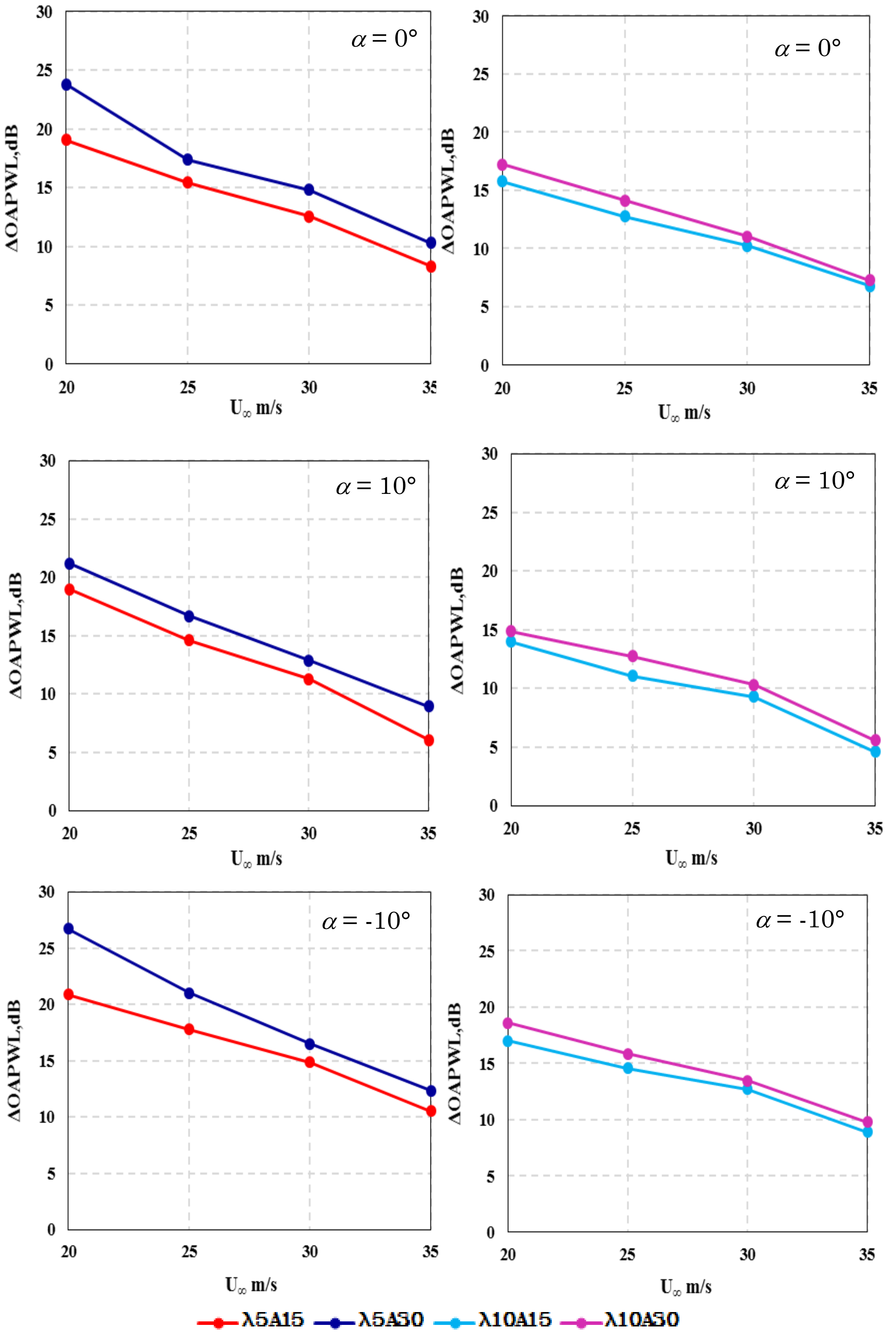

Figure 4-21: Variation of ΔOAPWL for different A and λ at U_∞ = 20-35 m/s by the serrated leading edges. Note that all cases without grid at (α = 0°) and Tu = 0.2%.

4.3.2.2 Effect of Blowing Rate (Q')

The laminar instability tonal noise could also be suppressed by the leading edge blowing. Figure 4-30 presents several acoustic spectra pertaining to both the baseline and blowing leading edges (λ' = 5 & 10 mm, Q' = 1, 2, 2.5, 3, 3.5, 4, 4.5 liter/min) at U_∞ = 20 m/s and α = 10°. It should be noted that the α described here refers to the geometrical angle of attack, under an open jet configuration. Similarly, the features of broadband-hump and discrete tones are easily discernible from the figure, which are markedly different with the leading edge turbulent broadband noise spectra presented in Section 4.3.1.2. The application of leading edge blowing in a manner similar to the previous turbulence–leading edge interaction study also results in the reduction of laminar instability noise level, albeit with a more straightforward relationship between ΔPWL and Q'. Based on the results in Figure 4-30 and Figure 4-31, it is clear that the largest level of instability tonal noise reduction requires the combination of the largest Q' and smallest λ'. Results for the models' blowing leading edges with two different values of λ' (= 5 and 10mm) are plotted in Figure 4-32. In this figure, two blowing types were selected, including the correlation between the $\Delta \mathrm{PWL}_{\max}$ level and the λ'5 and λ'10, respectively (for the blow rate (Q'=4.5 liter/min) only) at U_∞ = 20 & 30 m/s. One important point is that the total number of spanwise hole on the leading edge can affect the level of trailing edge noise reduction. Reductions in the overall tonal noise of up to 18.5 dB can be achieved by the λ' =5mm, which is significantly larger than that λ' =10mm about 5dB at 30 m/s. This effect is certainly due to the greater number of streamwise vortices generated by the small λ' where enhanced suppression of the separated boundary layer happens.

Next, Figure 4-33 shows the effect of leading edge blowing (Q' = 1, 2.5, 3.5 and 4.5 liter/min) across a range of freestream velocities U_∞ = 20–35 m/s and geometrical angles of attack (α = -10°, 0°, and 10°) at two spanwise air hole λ' of 5 and 10 mm. It should be noted that the straight blowing leading edge for these cases is close to the optimum spanwise air hole λ' identified in Figures 4-24. It can be seen that the level of ΔPWL is rather small across the

f' and U_∞ for $\alpha = -10°$ and $0°$, reflecting the ineffectiveness of the leading edge blowing at these geometrical angles of attack. However, at $\alpha = 10°$, the leading edge blowing is seen to be very effective across a large range of freestream velocity.

The NACA 65(12)-10 is designed as a laminar aerofoil where separation bubble tends to form at the suction side trailing edge first. In previous study on the same type of aerofoil [120], such separation bubbles were suppressed effectively by serrated leading edge with a large serration amplitude and small wavelength, thus resulting in a significant reduction of the instability tonal noise. It is reasonable to conjecture that the reduction of instability tonal noise by the leading edge blowing demonstrated in Figure 4-33 is associated with the flow entrainment. The generated air jet from the leading edge orifices is in the opposite direction to the incoming freestream jet, which creates a localised vorticity field, possibly via the Kelvin-Helmholtz inviscid instability mechanism. The vortex structures are then entrained back to the aerofoil surface, before continuing to propagate downstream towards the trailing edge. These vortex structures, generated by the interaction of the opposing jets described earlier, are similar in characteristics to those generated by the vortex generator, which is known for it capability of suppressing separated boundary layer. In accordance with the geometry of the NACA 65(12)-10, the landing of the vortical structures on the aerofoil suction surface after the flow entrainment is most effective at a positive angle of attack. This conjecture remains to be verified as a future study, but currently it seems to be a plausible explanation to describe the sensitivity of the aerofoil's angle of attack to the instability tonal noise control by leading edge blowing.

ΔOAPWL plots for combination of $\lambda'$and Q' at U_∞ = 20, 25, 30 and 35 m/s are shown in Figure 4-34. In Figure 4-34a,b, the comparison of ΔOAPWL versus the freestream velocities from 20 to 35 m/s are plotted against blowing leading edge on low turbulence intensity for a fixed spanwise air hole λ' for seven different blow rates Q' from 1-4.5 liter/min. Two important results can be found in this figure. The first arises from the noise reduction spectra, which shows that the level increases with the blow rate value. The second is that the identification of an optimum spanwise air hole λ' =5 mm is practically independent of flow speed, thus confirming this optimum value's generality. Results presented in Figure 4-34 a,b can also be demonstrated as contour maps, which is shown in Figure 4-35 a,b, respectively.

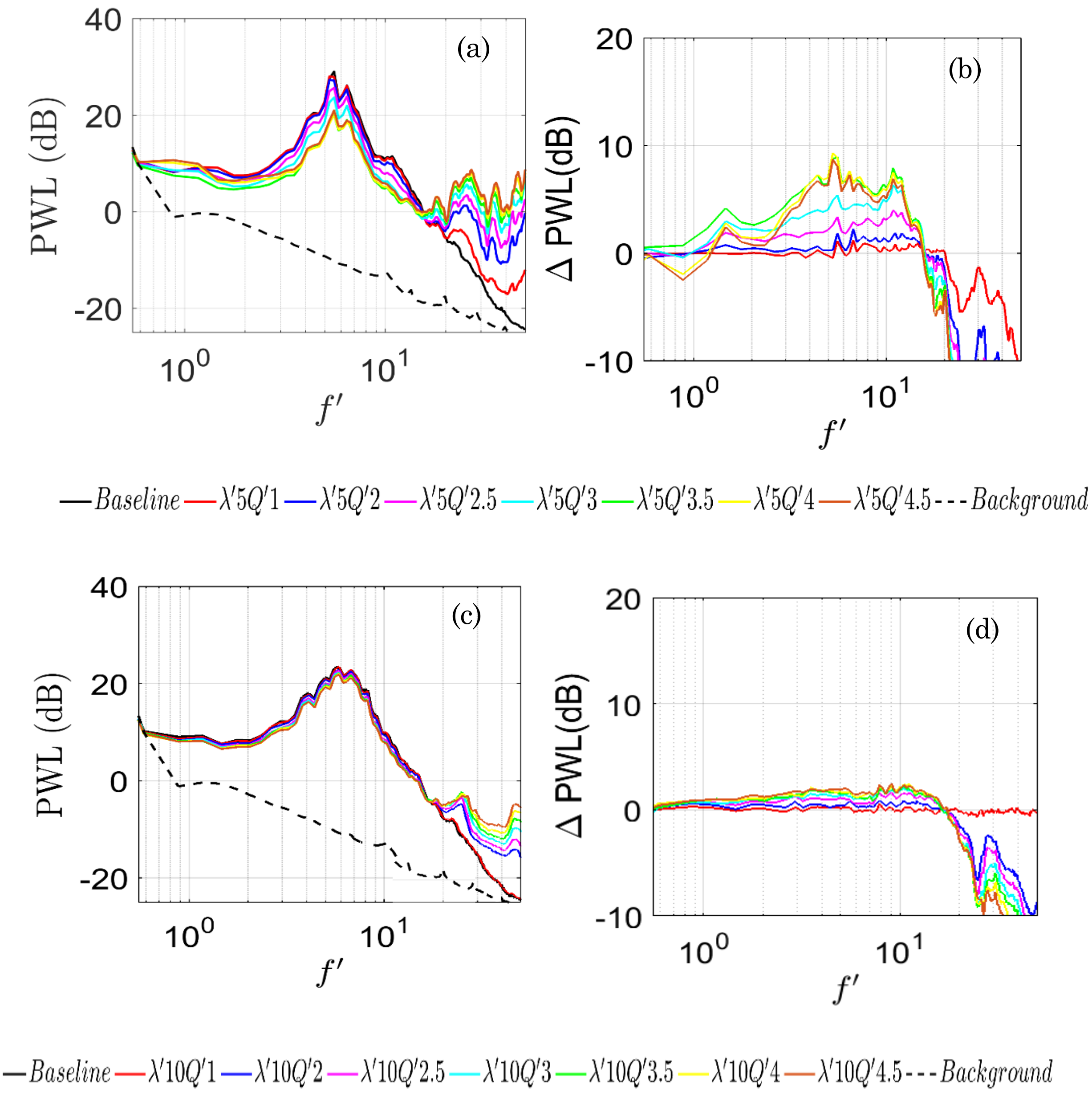

Figure 4-22: Comparison of PWL and ΔPWL as a function of normalised frequency f' at (a, b) λ'= 5 mm and (c, d) λ'= 10 mm when $U_\infty = 20$ m/s, $\alpha = 10°$, and $Tu = 0.2\%$.

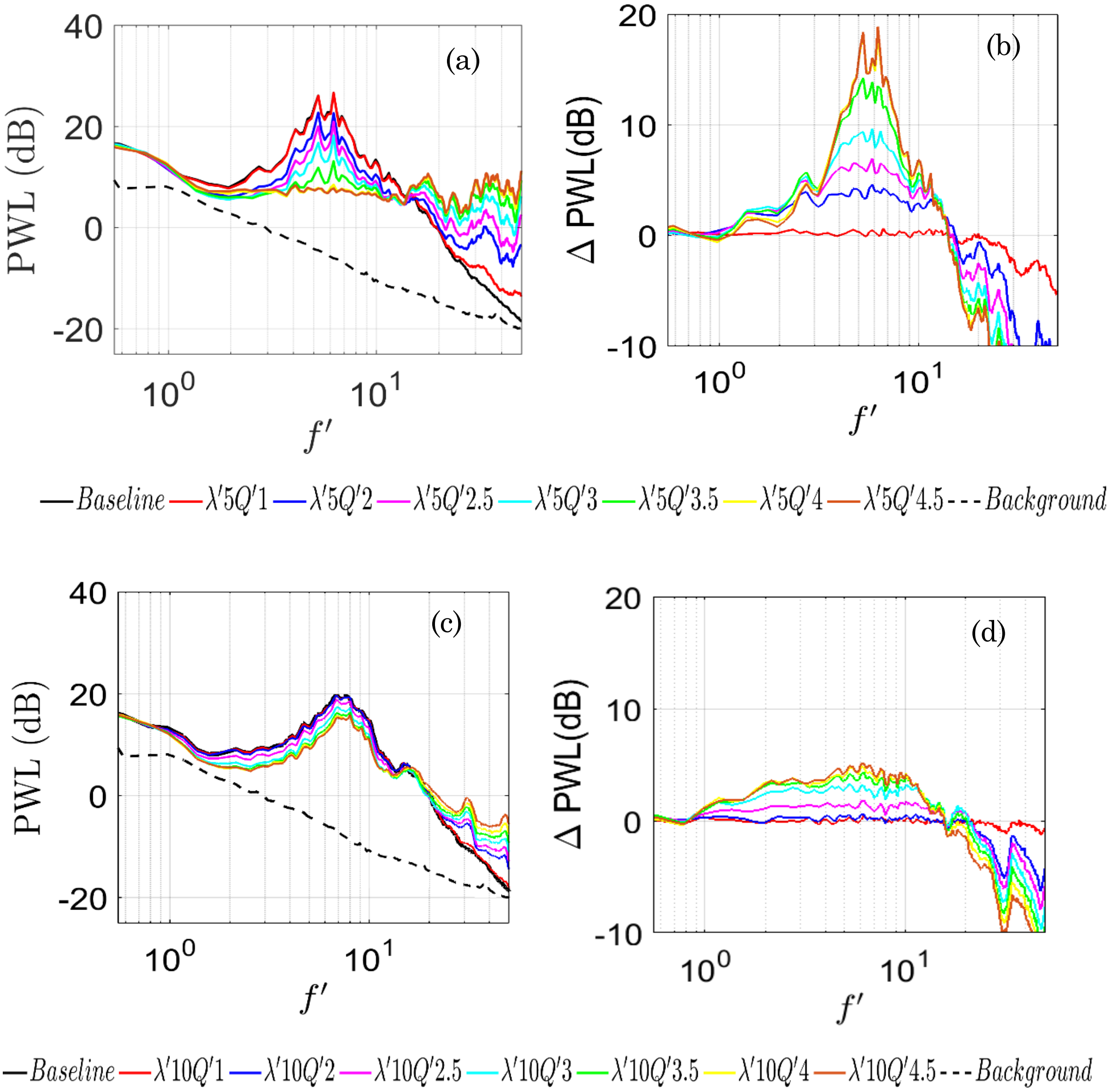

Figure 4-23: Comparison of PWL and ΔPWL as a function of normalised frequency f' at (a, b) λ'= 5 mm and (c, d) λ'= 10 mm when U_∞ = 30 m/s, α = 10°, and Tu = 0.2%.

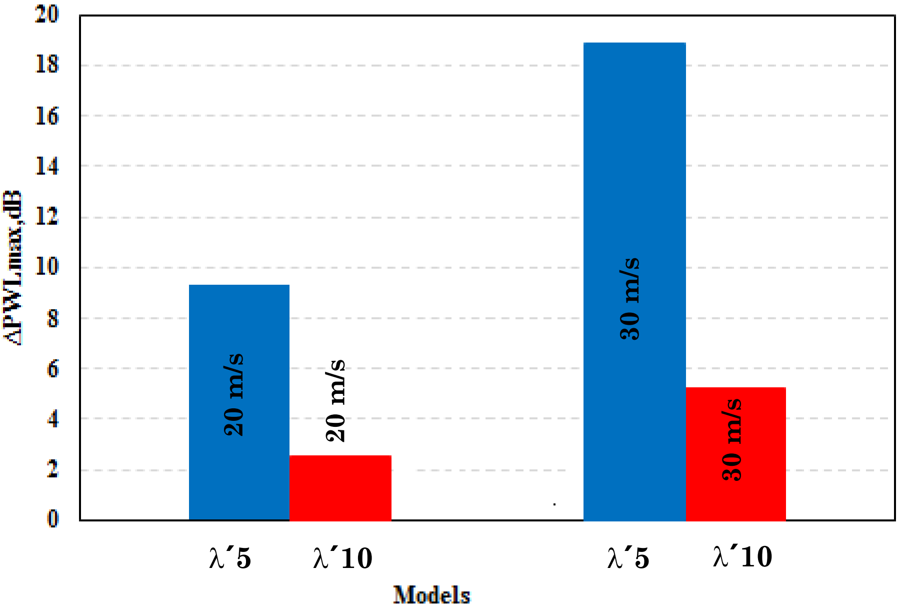

Figure 4-24: Correlation of the ΔPWLmax, dB across the models blowing leading edges (blue bars, 5mm) and (red bars, 10mm) when Q'=4.5 litre/min. Note that the angle of attack for all cases is set at $\alpha = 10^{o}$ and Tu=0.2%.

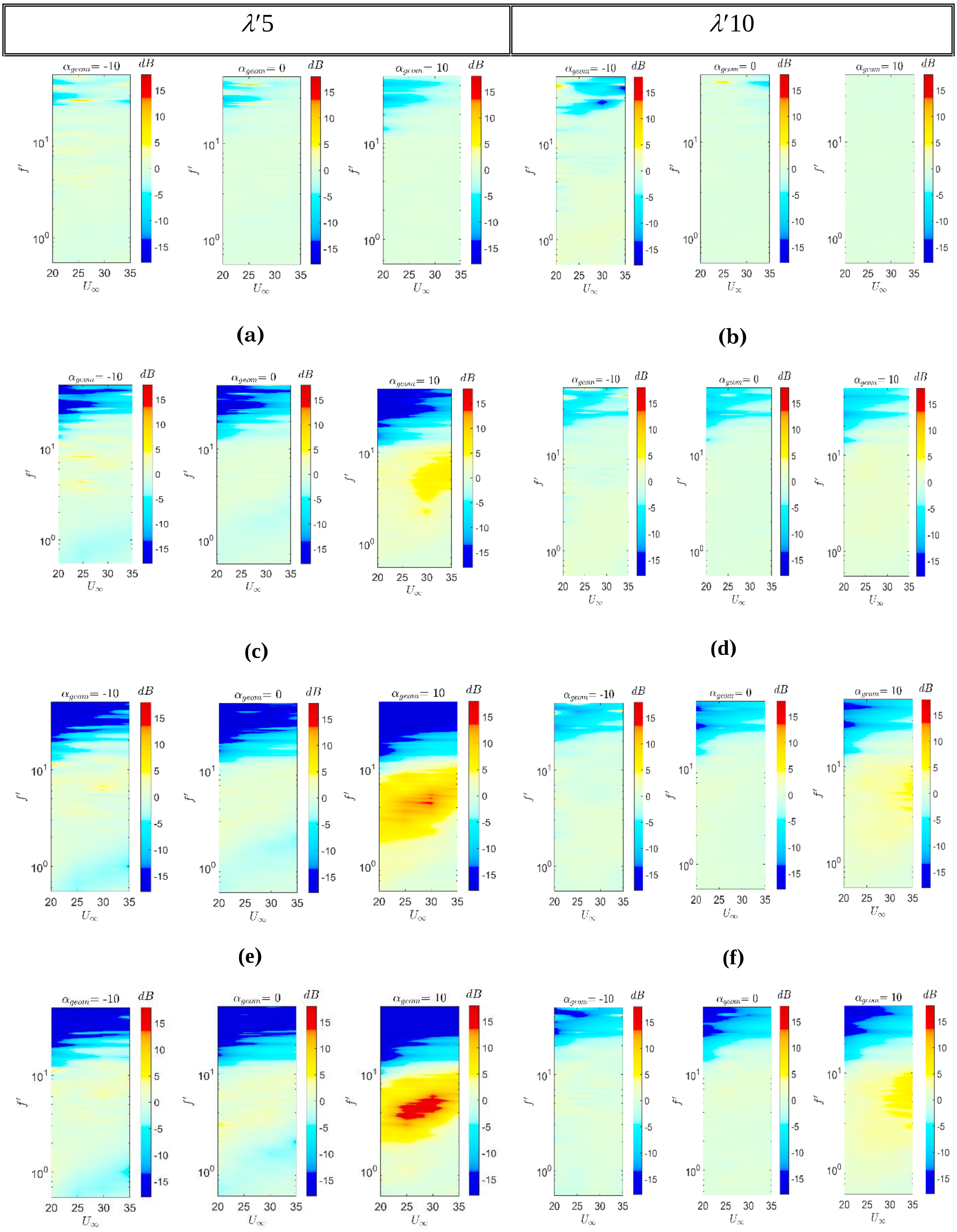

(a) **(b)**

(c) **(d)**

(e) **(f)**

(g) **(h)**

Figure 4-25: Comparison of ΔPWL for $\lambda' = 5$ mm (left) and $\lambda' = 10$ mm (right) as a function of normalised frequency f' and $\lambda' = 10$ mm when U_∞, at ($\alpha = 0°, 10°$, and -10° when $Tu = 0.2\%$, under Q'=1 litre/min (a,b)), Q'=2.5 litre/min (c,d), Q'=3.5 litre/min (e,f), and Q'=4.5 litre/min (g,h).

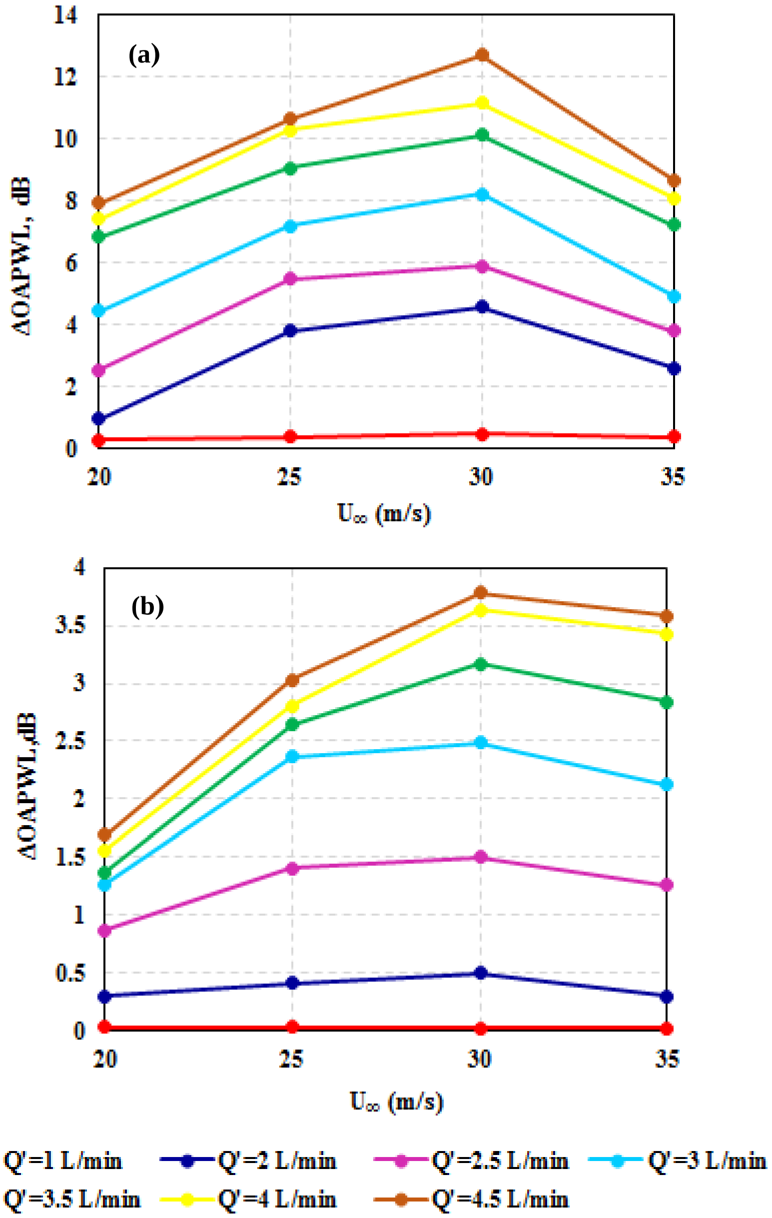

Figure 4-26: Comparison of ΔOAPWL blowing leading with velocity for various Q' when (a) $\lambda'5$ and (b) $\lambda'10$ at U_∞ = 20-35 m/s. Note that all cases are set at α = 10° and Tu = 0.2%.

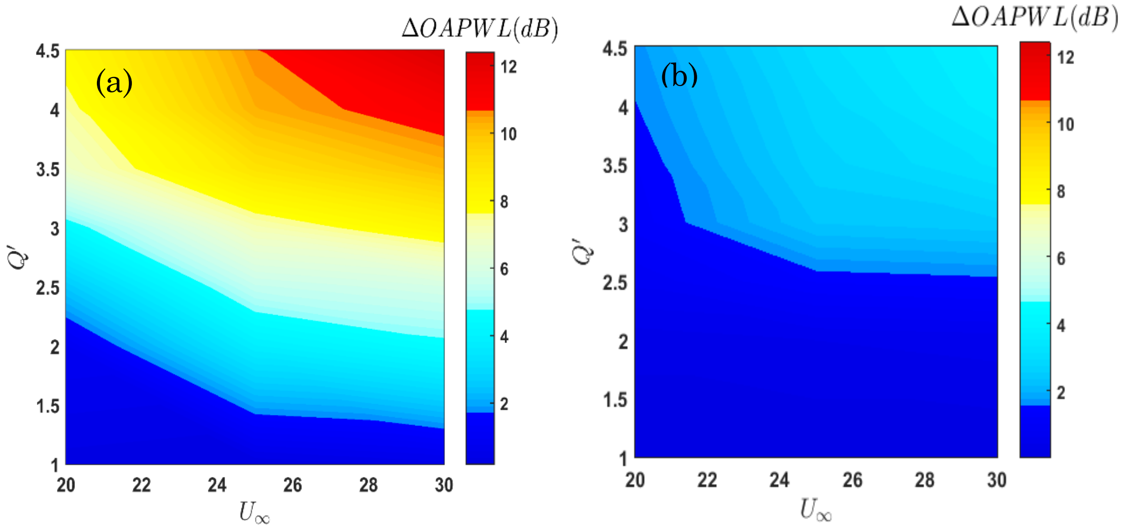

Figure 4-27: Contour maps of ΔOAPWL, dB with velocity for various Q' values produced by the blowing leading edges at (a) $\lambda' = 5$ mm and (b) $\lambda' = 10$ mm without grid set at $\alpha = 10°$ and $Tu = 0.2\%$.

4.3.2.3 Effect angle of attack (AOA)

Figure 4-25 in the previous section only demonstrates the ΔPWL for each blowing cases. However, it does not show the PWL individually to exhibit the instability tonal characteristics for each angles of attack. Therefore, this section will compare the PWL spectra and discuss their characteristics. Figure B1 in Appendix B illustrates the influence of angle of attack on the interaction noise of the baseline, the variation of the interaction noise in sound power level versus non dimensionless frequency $(f.C/U_\infty)$ at a jet velocity of 20-35 m/s, and different angle of attack ($\alpha = -10°$, 0° and 10°), indicate that the PWL spectra are sensitive to the change in α. The PWL sound power level reduces when the angle of attack (α) decreases from 0° to -10° lower dimensionless frequency, from 2 to 5 for the baseline cases, when $Q' = 0$ liter/min. On the other hand, the PWL values will be generally reduced by up to 12 dB at $f' \geq 5$ when (α) decreases from 10° to -10°. On the other hand, the PWL will decrease with increasing velocity, and the variation for the PWL for different angle of attack will decrease. Furthermore, the PWL spectra produced by the $\lambda' = 5$ and 10 mm straight blowing leading edge increases with reduced α up to 15.5 dB at $f' \geq 7$, and up to 4 dB at $0.5 \geq f' \geq 2$ when Q'

= 1 liter/min, as shown in Figure B2a,b Appendix B. Simultaneously, the variation of the interaction noise in sound power level versus non-dimensionless frequency decreases with increased spanwise air hole from λ'= 5 mm to 10 mm, and reduces with increasing jet velocity of 20-30 m/s. Only minor changes in the PWL are observed from α = 0° and 10° due to the relative change in the effective angle of direction for the flow from holes on the leading edge against incoming flow for cases 5 and 10 mm spanwise air hole, however, the variation of the interaction noise in sound power level decreases with increased λ', as illustrated in Figures B2 to B3. From Figures B2 to B7 in Appendix B, it is evident that the influence of angle of attack on low turbulence–aerofoil interaction noise is effective. Additionally, these results are consistent with the findings of Devenport et al. [160], in which the angle of attack influence is keen when the incoming flow is laminar, although the tone frequencies remain unchanged. There are two distinctive features of the noise spectra broadband-hump and several discreet tones, which are equally spaced. Another significant feature is that as the angle of attack increases, the amplitudes of the discrete tones are amplified.

$\lambda' = 5$ mm

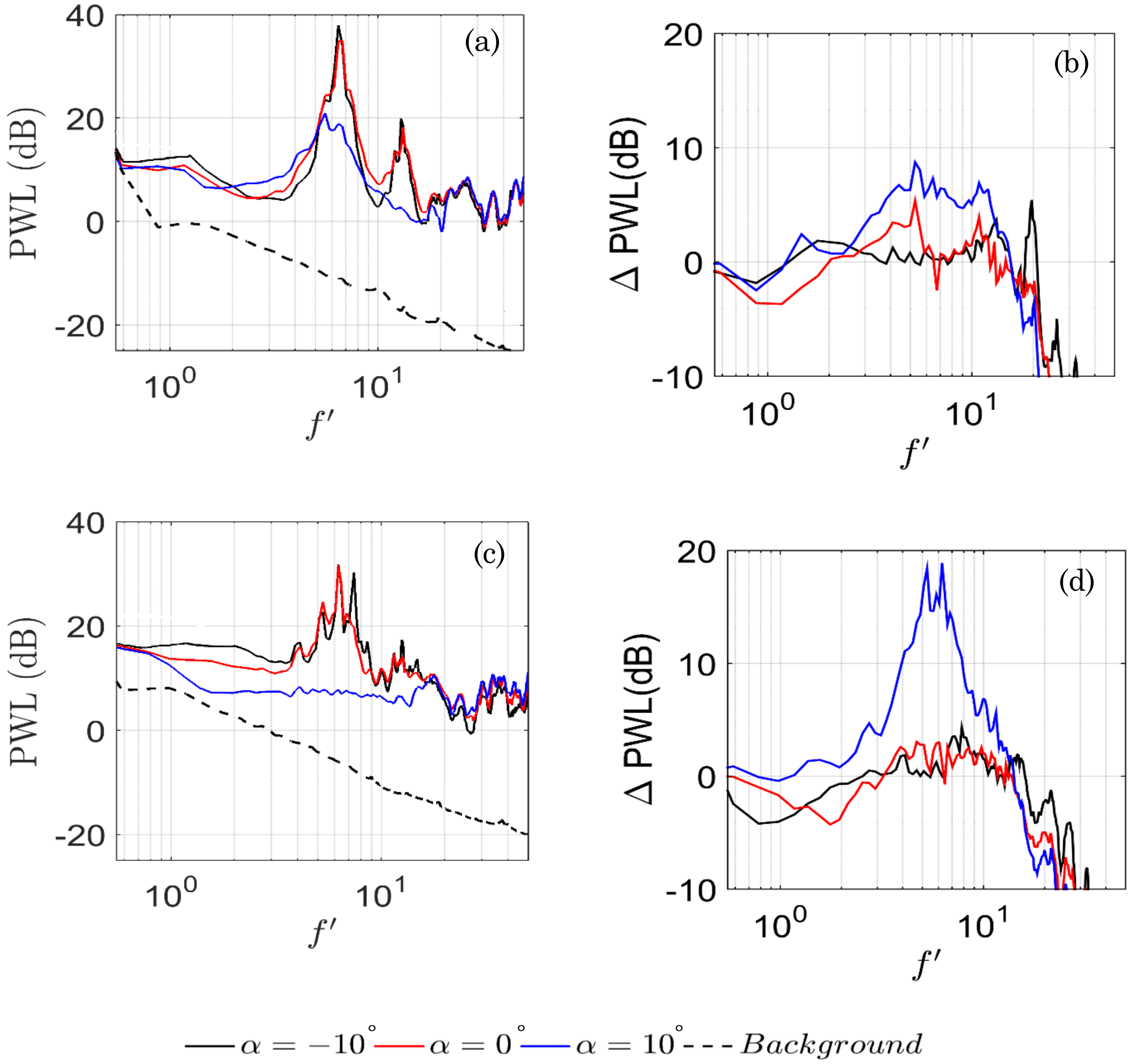

Figure 4-28: Comparison of PWL and ΔPWL as a function of normalised frequency f' at (a, b) U_∞ = 20 m/s, and (c, d) U_∞ = 30 m/s when Q' = 4.5 litre/min and Tu = 0.2%.

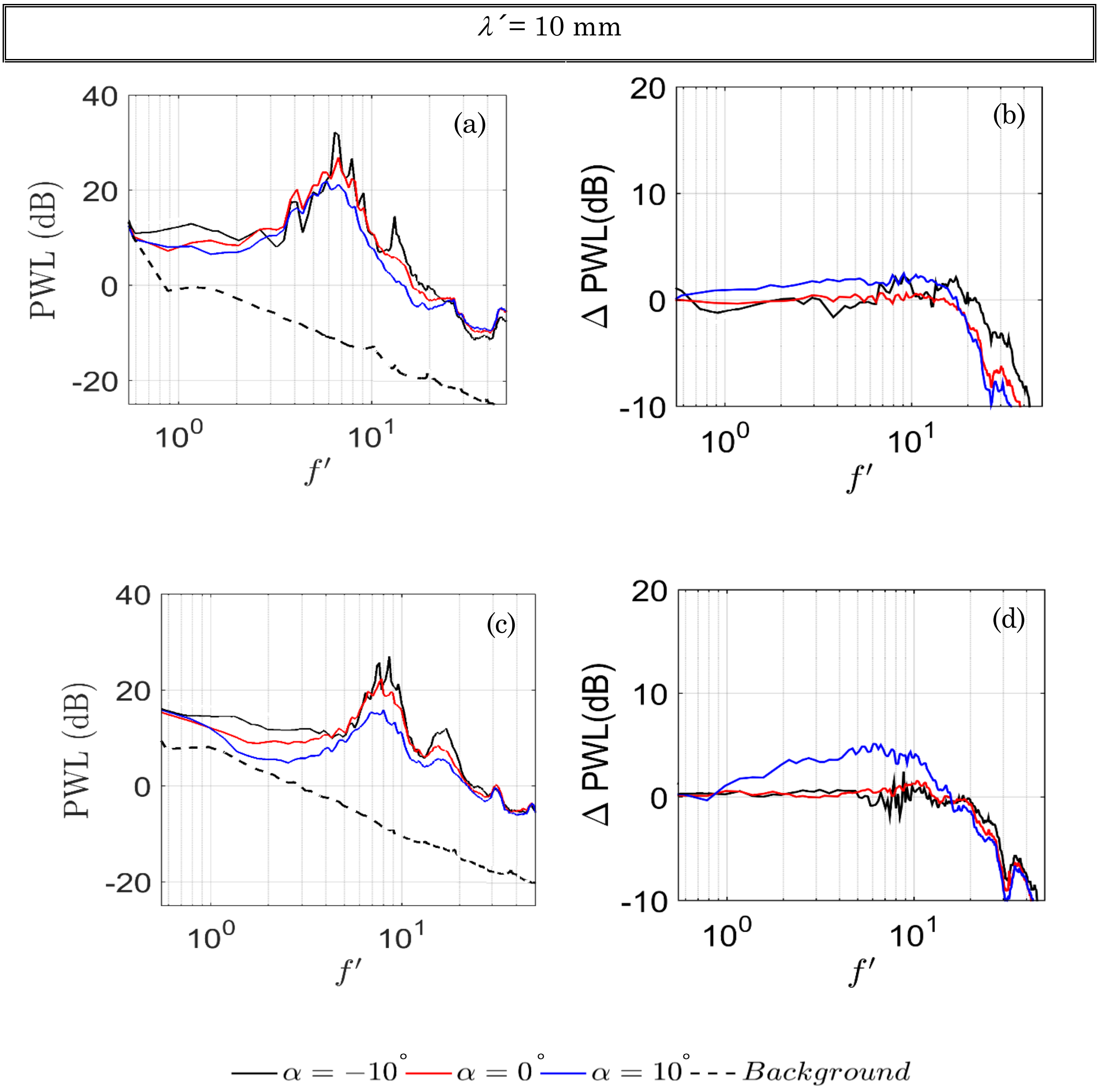

Figure 4-29: Comparison of PWL and ΔPWL as a function of normalised frequency f' at (a, b) $U_\infty = 20$ m/s, and (c, d) $U_\infty = 30$ m/s when $Q' = 4.5$ litre/min and $Tu = 0.2\%$.

As mentioned earlier, the objective of this research is to investigate the impact of leading edge serrations in decreasing the self-noise produced at the trailing edge. In order to do so, acoustic measurements were first performed to assess the different noise radiated by a serrated and baseline leading edges aerofoil, having as serration parameters *(λ5A15, λ10A15, λ5A30,* and *λ10A30)*. Figures B8, B9, B10, and B11 in Appendix B show the self-noise sound power levels produced by the four types aerofoils leading edegs at an angle of attack of 0° degrees, for different velocity from 20 m/s, 30 m/s and 35 m/s in contour Figure 4-25. To show and quantify the impact of the leading edge serration, the (ΔPWL) at different velocities are presented in that figure. The noise reduction due to the serrated leading edge levels around 5 and 8 dB at 0° and the maximum collapses perfectly when scaled versus a non-dimensional fequency.

At the velocity from 20-35 m/s the range of nondimensional frequency corresponds to about (0.5 - 60) Hz. The influence of the angle of attack *(α)* is represented in figure 4-25. Insignificant noise reduction can be acheived at high positive angles of attack, whereas they become noticeable around 0° angle of attack remarkable and condition at negative angles -10°. Additionally, the highest is the negative angle -10°, which the maximum noise reductions happen consistent with previous empirical studies [154, 155].

Figures from B8 to B11 in Appendix *B* compare the PWL spectra of four serration leading edges ($\lambda 5A15$, $\lambda 10A15$, $\lambda 5A30$, and $\lambda 10A30$) with the baseline aerofoil. Enhanced noise reduction is shown when A is increased.

The dependency of the radiated noise with and without serrated leading edge shows a great impact on the angle of attack, with increased noise reduction with decreasing (α) from 10° to -10°, especially at lower velocity when U_∞ = 20 m/s, with only a slight effect on the angle of attack when increasing the amplitude from 15 to 30 mm, as shown in Figures B8 to B11 Appendix *B*. For the baseline leading edge, the radiated sound is at its maximum value at negative degrees, and reaches a lowest value of ten degrees. The radiated noise decreases with increasing angle. The serrated leading edge has deviant behaviour. Multiple discrete tone frequencies stay the same, indicating that the serration leading edges produce flow structures. However, the absolute variation of the PWL in dependency of the angle of attack is defined by values ≤ 15.5 dB.

The analysis starts with certain acoustic spectra for the angle of attack α = -10°, 0°, and 10°, as shown in Figure B8a-d and Figure B9a-d Appendix *B*. There are some points to be noted in interpreting this analysis. There are two distinct characteristics in the noise spectra: a broadband-hump and some equally spaced discrete tones embedded therein, consistent with previous empirical studies [163, 164]. Another important feature is that as the angle of attack increases, the amplitudes of the discrete tones are amplified. The influence of low frequency leading edge noise becomes more prominent from 20 m/s onwards. The predicted tonal noise is presented in Figure B10a-d and Figure B11 Appendix *B*. Comparisons are good for both the acoustic intensity as well as the tone's main central frequency among the measured and predicted far-field spectra. The range of angle of attack (-10° and 0°) investigated here is likely to yield a larger range of effective angle of attack. This implies that the noise performance of the serration leading edge will be sensitive to the angle of attack. The nature of this separation is currently unclear although there is evidence of a small separation bubble near to the leading edge at small angles of attack.

Chapter 5 : Aerodynamic Forces Produced by Straight Blowing and Serrated Leading Edges

5.1 Introduction

This chapter describes the lift and drag forces in a non-dimensionalised form, as a function of the angle of attack. These results provide a quantitative measure to determine the aerodynamic performance of optimal straight blowing and serrated configuration for the NACA 65(12)-10. Experiments are performed to reveal the effects of serration amplitude and wavelength for the serrated leading edge, as well as, the spanwise air hole space λ', and blowing flow rate Q' for straight blowing leading edge. The research was performed with the aerofoil presented in Sections 3.3.1 and 3.3.2 at a velocity of 25 m/s. In order to be more effective in the prediction of the dimensionless parameters, the amplitude to chord length ratio (A/C), the wavelength to chord length (λ/C) ratio and the spanwise air hole spacing λ' were employed to highlight the trends. The momentum exchange as a result of mixing between the streamwise vortices and the boundary layer is regarded as one of the main enhancement mechanisms to prevent/delay stall and improve the post-stall performance. The streamwise vortices in the form of counter-rotating pairs are predominantly generated at the troughs of the serration as a direct consequence of the serration geometry10. Skillen et al. [18] highlighted that secondary flow can be induced by the spanwise pressure gradient where near-wall low-momentum fluid is transported away from the serration peak towards the trough. Conversely, high-momentum fluid from the freestream is drawn to re-energise the boundary layer downstream of the serration peaks. Hansen et al.[17] focus on the evolution of vorticity near the serration troughs, where they observed that the external pressure force transforms the initial vorticity near the leading edge into pairs of counter-rotating streamwise vortices via a three-dimensional process (stretching, tilting and diffusion).

The discussion above concerns the aerodynamic performances of aerofoils with serrated leading edge to act as a simple and effective passive flow control device. A question worth exploring is whether the underpinning physical mechanisms, respectively, can be replicated by a completely different flow control approach. More specifically, active flow control has the advantages of being versatile when the flow condition can change considerably over a short period of time, and producing little parasite drag when implemented into the wing system. Leading edge blowing is an attractive method to achieve this objective because the injection of mass flow from the leading edge (against the incoming flow) could potentially decrease the turbulence intensity, hence produce the lift enhancement and drag reduction. Depends on the blow rate of the leading edge jet, once mixed with the incoming flow it can be entrained and propagated as the streamwise vortices in the downstream direction along the aerofoil surface. These streamwise vortices generated indirectly as a result of the leading edge blowing could bear a certain level of similarity as the one produced by a serrated leading edge.

In Figure 5-1, the stall angle of attack increases for turbulent flows was significant in comparison to the corresponding laminar flow. At $\alpha = 8°$, the aerofoil begins to stall for low turbulent intensity and the max lift coefficient begins to increase with increasing Tu and stall will be increased to 9° when $Tu = 4.5\%$.This already known behaviour is attributed to the ability of turbulent boundary layers to overcome larger adverse pressure gradients, retarding flow separation with a lift curve slope of 2π was estimated in the linear region, i.e., between $-2° \leq \alpha \leq 5°$. The lift curve slope for the baseline decreases the lift curve slope $(dCL/d\alpha)$ to 0.096 for low turbulent intensity. This tendency is in agreement with the earlier publication of Johari et al. [15], who measured $(dCL/d\alpha)$, for NACA 65-1012. This tendency is consistent with earlier recorded data.

Figure 5-1 compares the CL created by the straight baseline leading edge aerofoil. CL expected by the Chonge, el al [125], which is also included. Both the experimental results match very well, and both display a lift curve slope is around 0.1 per degree (at the pre-stall region).

The results indicate that the rise in turbulence intensity delayed the stall AoA and improved the lift and drag coefficients. At the smaller turbulence intensity of 0.2%, the lift coefficient is improved by increasing the AoA to the stall angle (9^o). The lift coefficient fell quickly after the stall angle. Figure 5-2 also demonstrates that the increase in the turbulent intensity allows the stall angle to happen at the higher AoA and also improves the peak lift coefficient. This is perhaps due to the rise in turbulent kinetic energy generated at the boundary layer with the greater energy on the aerofoil that delayed the separation flow.

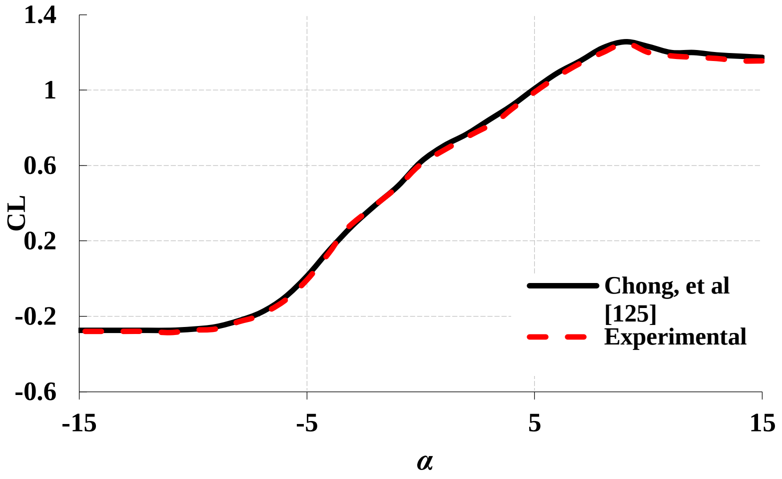

Figure 5-1: Comparison of lift coefficient CL , as a function of angles of attack (α), produced by straight baseline leading edge when $Tu = 0.2$ % at $U_\infty = 15$ m/s.

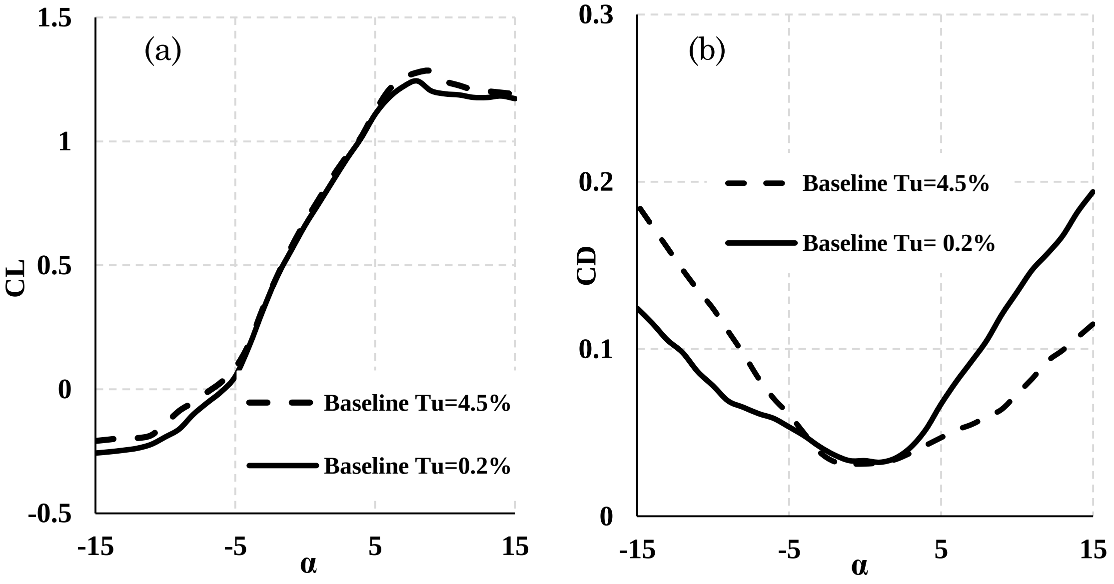

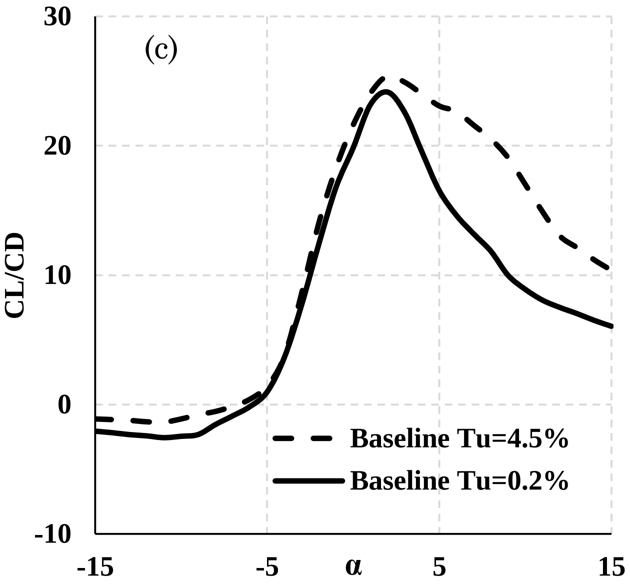

Figure 5-2: Comparison of lift coefficient CL , CD (a-b) and (c) CL/CD, as a function of angles of attack (α), produced by straight baseline leading edge when Tu = 0.2 % and 4.5% at U_∞ = 25 m/s.

The performance is significantly lower compared to the baseline leading edge. The lift-to-drag ratio given by CL/CD is an indicator providing information about the aerodynamic efficiency (Figure 5-2). Results are presented for Baseline cases with low *Tu* =0.2 % and high *Tu*=4.5 %. The data confirms the previous observations that small and high turbulent intensity lead to superior aerodynamic performance while *Tu* of intermediate (or larger) achieve higher lift coefficients. Furthermore, it can be seen that the turbulent intensity shows nearly the same performance with slightly higher peak values (25.39) than the low turbulent intensity aerofoil. The aerofoil shows a reduction in $(CL/CD)_{Max}$ of 11.50%.

5.2 High Turbulence Intensities (*Tu* = 4.5%)

In this section, the results of the aerodynamic experiments including the lift and drag coefficients for the NACA65(12)-10 aerofoil produced at high inflow turbulence are presented and discussed. Using active and passive treatments to aerofoil not only can cause a noise reduction, but also significantly change the aerodynamic behaviour of the aerofoil. The objective of this experiment is to identify the effects of serration and straight blowing at leading edges compared to the baseline case.

5.2.1 Effect of Serrations and Angle of Attack (AoA)

The NACA65 (12)-10 aerofoil model has a chord and span of C = 150 mm S = 495 mm, respectively. The aerofoil model is composed of the main body, with a length of 100 mm, and an interchangeable leading edge of 50 mm. The geometrical modification only affects the leading edge region, and the remainder of the aerofoil is unchanged. This study adopts the design principle of keeping the same wetted area between the serrated leading edge and the baseline straight leading edge. This means that the serration peak will extend upstream of the baseline leading edge by A/2, while the remaining A/2 is cut into the aerofoil main body. The current study investigated two amplitudes (A = 15 and 30 mm) and two wavelengths (λ = 5 and 10 mm). A summary of the geometrical details is provided in Table 5-1. Figure 5-3 presents results of the lift coefficients for the aerofoil with leading edge serrations over the AoA range of -15° to 15°. Results are presented for serrations with different amplitudes of A/C = 0.1 and 0.2 (A = 15 and 30mm), with wavelength of λ = 5mm and λ = 10mm.

Table 5-1: The serration leading edge effect on aerodynamic performance for NACA 65(10)12, corresponding to the turbulence intensities of Tu = 4.5%.

Configuration	**Stall angle (*α*)**	***A(mm)***	***λ(mm)***	***A/C***	***λ/C***	**CL(max)**	**ΔCL(max)**
Baseline	8	-	-	-	-	1.24	reference
λ5*A*15	12	15	5	0.1	0.033	1.25	0.007
λ5*A*30	7	30	5	0.2	0.033	1.07	-0.170
λ10*A*15	13	15	10	0.1	0.066	1.28	0.034
λ10*A*30	10	30	10	0.2	0.066	1.23	-0.008

The aim of this comparison is to provide information on how the serration amplitudes affect the lift coefficient in the designated angle of attack range. The comparison with baseline aerofoil requires a constant surface area S of the aerofoil. According to equation 3-20, the same wetted wing area (see Table 5-1) would normally lead to a higher CL, subjected to the use of serration amplitude. Lift coefficients pertaining to the baseline straight leading edge case are plotted in the figure for comparison. It can be seen that for the baseline case the corresponding lift curve largely follows the classical thin aerofoil theory, where a lift curve slope of 2π is evident at $-6^{o} \leq \alpha \leq 8^{o}$. At $\alpha > 8^{o}$, the aerofoil starts to stall and the lift coefficient begins to drop. On the other hand, at $\alpha < -6^{o}$ the lift coefficients do not vary much at increasingly negative angle of attack.

Generally, it can be observed that a smaller serration wavelength (i.e. $\lambda = 5$ mm), regardless of the serration amplitude, can preserve the lift curve slope at $-6^{o} \leq \alpha \leq 8^{o}$. For a larger serration wavelength, such as the $\lambda = 10$ mm case, a smaller lift curve slope is produced by the serrated aerofoil. With regard to the effect of the serration amplitude, it can be concluded that a smaller serration amplitude (i.e. $A = 15$ mm) is superior than a larger one ($A = 30$ mm) in two aspects: the stall angle achieved by the slightly smaller amplitude serration is considerably larger; and the values of the lift coefficient at the post-stall regime also larger.

Figure 5-4 shows the comparison of the drag coefficients produced by the different serrated leading edges and the baseline leading edge. For the baseline straight leading edge, the variation of the drag coefficient almost exhibits a symmetrical pattern across the angle of attack, with the lowest drag coefficient achieved at $\alpha = 0^{o}$. The same symmetrical leading edge, but increasingly deviates when the serration wavelength becomes larger ($\lambda = 10$ mm). For the low-wavelength serrated leading edge ($\lambda = 5$ mm), both the serration-amplitudes ($A = 15$ and 30 mm) are lower than the baseline leading edge at $\alpha < 0^{o}$. The lowest drag coefficient across the negative angle of attack is when the serration amplitude is also the lowest. However, for the positive angle of attack ($\alpha > 0^{o}$), complete reverse pattern happens. The serrated leading edge seemingly attains a larger rate of increase of the drag coefficient with respect to the angle of attack than the baseline straight leading edge. Furthermore, for the serrated leading edge, the one with the smaller serration-amplitude actually produces the largest drag coefficient. Referring to Figure 5-4b, when the serration-wavelength is increased to λ = 10 mm, at a different picture can be observed. At $\alpha < 0^o$, whilst the larger serration-amplitude (A = 30 mm) produces the similar level of drag coefficient as the baseline-straight leading edge, the lower-amplitude one (A = 15 mm) produces higher drag coefficient. Interestingly, at $\alpha > 0^o$, the drag coefficient produced by high the serrated leading edges is actually lower than the baseline straight leading edge. The one that produces the lower drag coefficient is actually the A = 15 mm, in contrary to the case when the serration wavelength is small i.e. $\lambda 5A15$ vs $\lambda 10A15$.

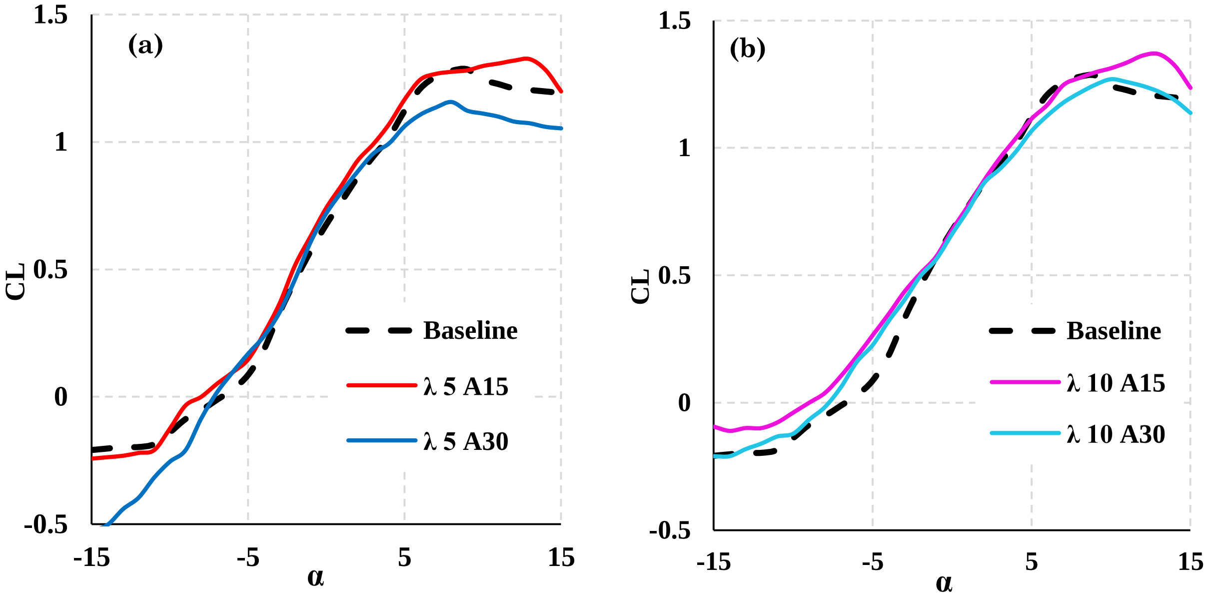

Figure 5-3: Comparison of lift coefficient CL, as a function of angles of attack (α), produced by serrated leading edge when $\lambda = 5$ &10 mm and $A = 15$ &30 mm at $U_\infty = 25$ m/s and $Tu = 4.5\%$.

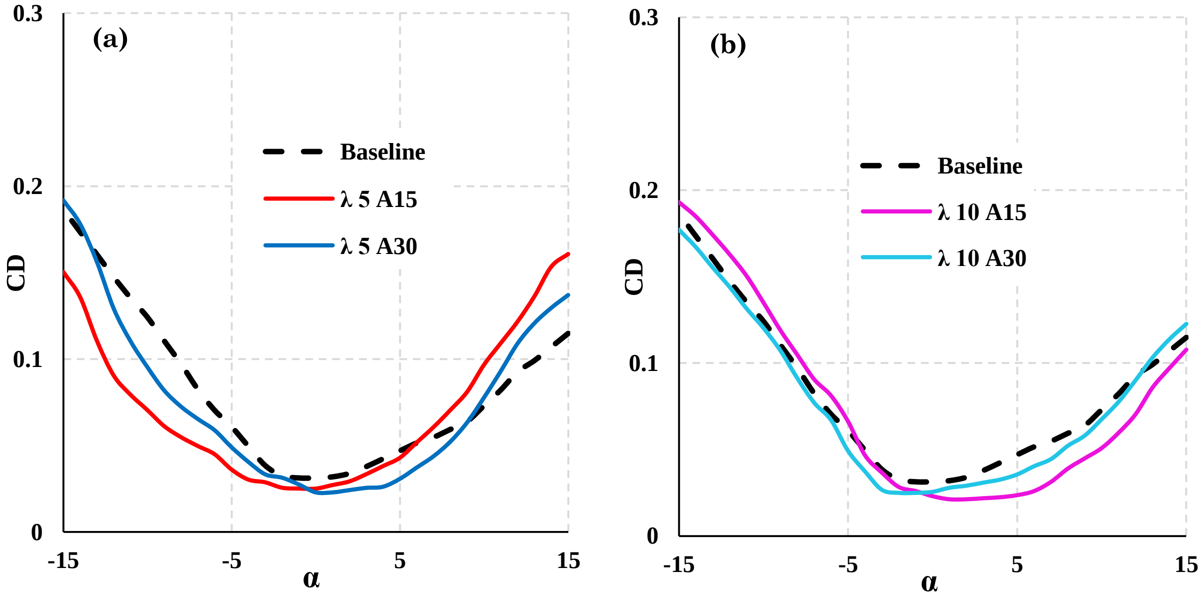

Figure 5-4: Comparison of drag coefficient CD, as a function of angles of attack (α), produced by serrated leading edge when $\lambda = 5$ &10 mm and $A = 15$ &30 mm at $U_\infty = 25$ m/s and $Tu = 4.5\%$.

5.2.2 Effect of Blowing Rates (Q')

This section presents the CL and CD for different types of blowing leading edges at a range of angles of attack ($-15^o \leq \alpha \leq 15^o$). The freestream velocity was maintained at 25 m/s. Note that the planform area remains constant during the calculation for the CL and CD, irrespective of whether it is a baseline or a blowing leading edge. Figure 5-5 compares the CL distributions for various combinations of λ ′ and Q ′, also subjected to high (4.5%) freestream turbulence intensity. For the leading edge blowing, using a lower blow rate (Q ′) and a larger spanwise spacing of the orifice (λ ′), is observed to achieve higher level of lift coefficient, most notably at the post-stall regime. The stall angles also increased, which can be seen in Table 5-2. However, it is interesting to note that the lift curve slope for the leading edge blowing follow the 2π gradient quite accurately when the freestream turbulence intensity is high. In summary, the ability of the leading edge blowing to suppress boundary layer separation at high angle of attack is demonstrated, when the comparison of low Q ′ and large λ ′ is implemented.

The results show individual post-stall characteristics for each LE and indicate a clear tendency in slope characteristics. The maximum CL coefficients vary with various patterns. It can be seen that larger blow rate decrease the slope up to 18% and lower the maximum CL up to 22%. While the low blow rate Q ′= 1 liter/min experience a sharp stall, large blow rate (Q ′) show a significant decrease in the maximum stall angle ($\text{AoA}_{\text{STALL}}$) and have smoother stall characteristics and unsteady post-stall. The straight blowing leading edge λ ′ = 10mm impacts the curve progression by the maximum CL on the same stall angle CL increase with increase the spanwise spacing of the orifice (λ ′) can be seen in Figure 5-5.

Figure 5-6a&b shows the CD counterpart for various combinations of λ ′and Q ′ subjected to high (~4.5%) freestream turbulence intensities. Similarly, lower drag tends to associate with low Q ′ and large λ ′ for the leading edge blowing in both the pre-stall and post-stall regimes. A summary of the geometrical details is provided in Table 5-2. All curves have roughly the same point of interception at $\alpha = 0^{\circ}$ with CD ≈ 0.03.

At the high turbulent intensity, the blowing rate configurations, following the lift performance, undergo great changes in drag behaviour when compared to baseline configuration. At negative angle of attack, the blowing rate Q' configuration approaches extraordinary lower drag values. The configuration $\lambda'5Q'4$ decreases drag in 0.131 drag when compared to baseline case and it keeps this change up to $\alpha = -15^{\circ}$. In addition, the straight blowing configurations $\lambda'10Q'4$ and $\lambda'10Q'3$ stay with lower drag when compared to the baseline aerofoil in the pre stall range of angle of attack whereas the configuration $\lambda'10Q'1$ and $\lambda'10Q'2$ have the lower values up to 0.03 at $\alpha = 7^{\circ}$.

Table 5-2: The straight blowing leading edge effect on aerodynamic performance for NACA 65(10)12, corresponding to the turbulence intensities of Tu 4.5%.

Configuration	**Stall angle(α)**	**Q'(liter/min)**	**λ'(mm)**	**CL(max)**	**ΔCL(max)**
Baseline	9	-	-	1.28	reference
$\lambda'5Q'1$	13	1	5	1.29	0.058
$\lambda'5Q'2$	12	2	5	1.25	-0.032
$\lambda'5Q'2.5$	11	2.5	5	1.18	-0.104
$\lambda'5Q'3$	10	3	5	1.17	-0.110
$\lambda'5Q'3.5$	9	3.5	5	1.15	-0.138
$\lambda'5Q'4$	8	4	5	1.11	-0.176
$\lambda'5Q'4.5$	7	4.5	5	1.07	-0.216
$\lambda'10Q'1$	13	1	10	1.34	0.053
$\lambda'10Q'2$	12	2	10	1.31	0.021
$\lambda'10\ Q'2.5$	11	2.5	10	1.27	-0.015
$\lambda'10Q'3$	10	3	10	1.23	-0.051
$\lambda'10Q'3.5$	9	3.5	10	1.19	-0.095
$\lambda'10Q'4$	8	4	10	1.13	-0.160
$\lambda'10\ Q'4.5$	8	4.5	10	1.06	-0.226

The increase of the drag coefficient at the post-stall area is noticeable for the blowing leading edge and serrated leading edge, which could be a result of the strong streamwise vortices produced by both the passive and active mechanisms.

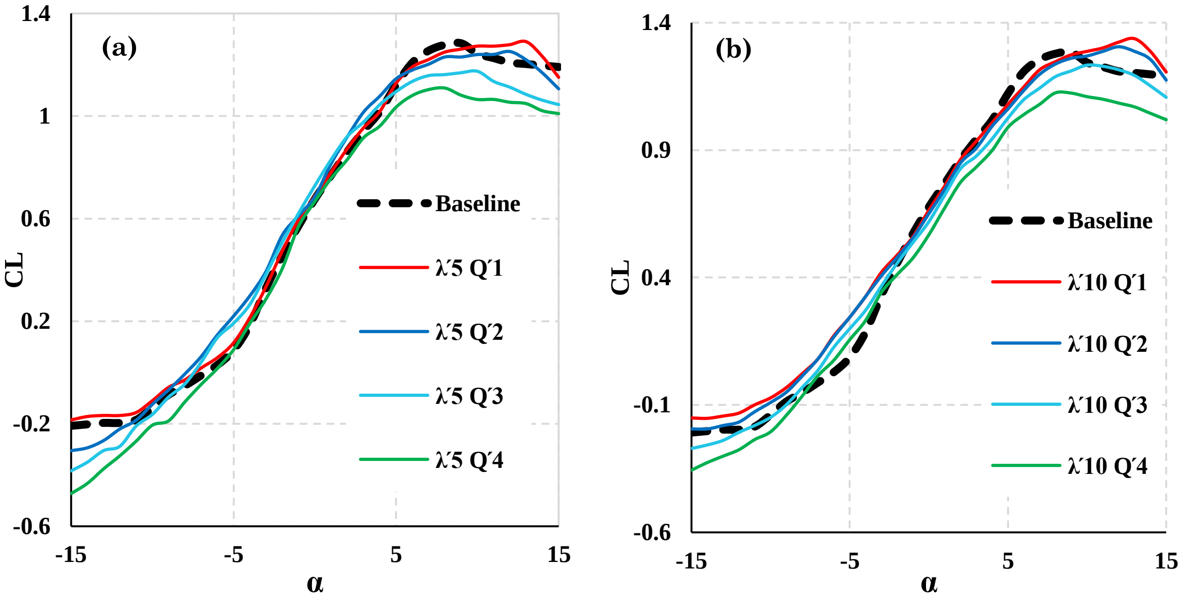

Figure 5-5: Lift coefficient curve at the case of U_∞ = 25 m/s, as a function of angles of attack (α), corresponding to λ', produced by leading edges blowing (a) λ' = 5mm and (b) λ' = 10mm in the range of 1-4 liter/min when Tu = 4.5%.

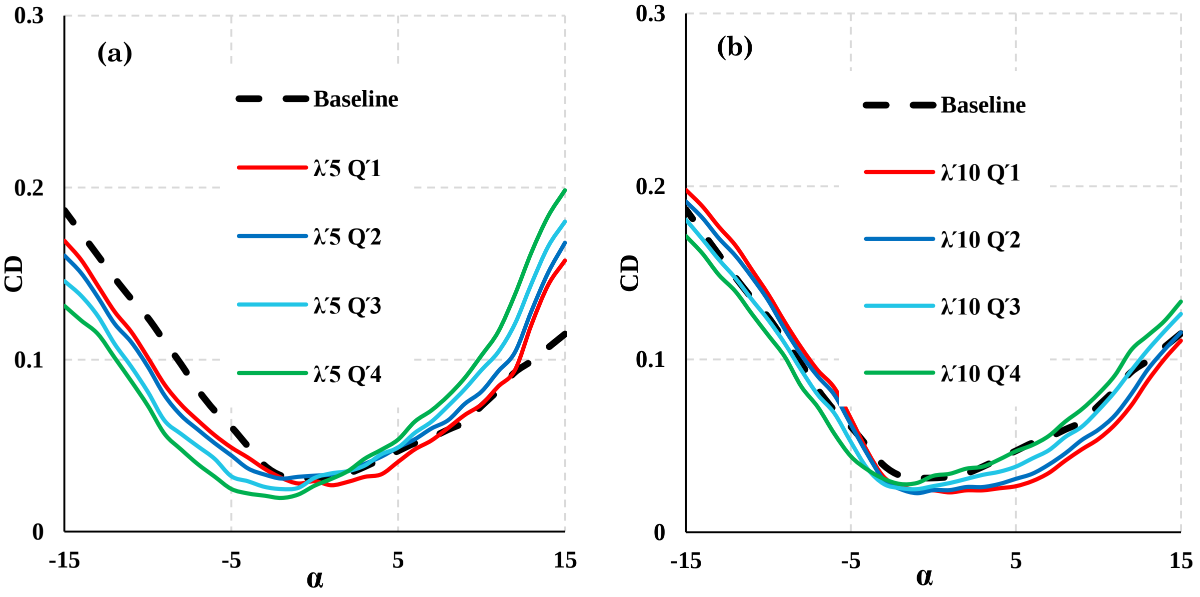

Figure 5-6: Drag coefficient curve at the case of U_∞ = 25 m/s, as a function of angles of attack (α), corresponding to λ', produced by leading edges blowing (a) λ' = 5mm and (b) λ' = 10mm in the range of 1-4 liter/min when Tu = 4.5%.

Figure 5-5 presents the performance indicators, explained by the maximum lift coefficient, with the blowing rates of 1-4.5 liter/min for the serrated and straight blowing leading edges configurations. These plots indicate that the best wavelength to amplitude for the serrated aerofoil is $\lambda 10A15$. The plot also highlights that the largest spanwise air hole spacing and smallest blow rate configuration, would produce the superior performance ($\lambda'10Q'1$). As will be shown later, whether the incoming flow is of low or high turbulence intensity, both achieve higher lift coefficients for the $\lambda'10Q'1$ combination. On the other hand, it is interesting to note that the CL distribution by the leading edge blowing follows more accurately from laminar when the freestream turbulence intensity is high.

Figure 5-7 shows the blow rate (Q' effect in performance in terms of ΔCL ($CL_{\text{stright blowing}} - CL_{\text{Baseline}}$). On the other hand, an increase in performance occurs by decreasing the spanwise spacing of the orifice (λ').

Figures 5-7a&b clarify the blowing leading edge design space as well as its dependency on blow rate and spanwise air hole spacing. When comparing the aerofoils with different blowing rates it becomes immediately seeming that, as previous works have suggested, the spanwise spacing distance λ' has a significant influence on the lift characteristics of the aerofoil. An important feature in this set of results shown below in Figure 5-7 is the influence of blowing rates at large λ'. Whereas at the lowest λ' the performance increased with a decrease in Q', by using a large λ' the performance enhanced from the lowest to the medium blowing rates (1.5-3.5) liter/min, then reduced at the largest Q'. Since this degradation in performance was observed at only one of the λ', the result indicate there is a connection between λ' and Q' and the two cannot be separately analysed. Considering the aerofoils at the largest λ', one can note that the maximum lift produced by the aerofoils decreased by 5%, 9%, 16% , and 22% for the largest, compared with a decrease of 11%, 13%, 17% and 21% for the lowest, medium and lowest blowing rates at the lowest spanwise spacing distance. The lower λ' aerofoils also perform improved over the whole range of AoA. Whilst the maximum lift coefficient is similar to the low λ' aerofoils at 2-2.5 liter/min, the range over which this increasing happens is between $-1^{o} < \alpha < -9^{o}$ compared to $-2^{o} < \alpha < -13^{o}$ at the higher spanwise spacing distance. The gain in lift in the post-stall regions is also lower, at a maximum of ΔCL for the aerofoil at the higher λ' happens is at 1 liter/min. positive angle of attack (i.e. 10^{o} - 15^{o}), trend to be at lower Q'(i.e. between 1 and 2 liter/min). The ΔCL trends to be better when the spacing is larger, especially for the positive angle of attack this is in line with the serrated leading edge case.

The stall characteristics of the large λ' are however softer than the shorter λ' aerofoils. At the largest and medium blowing rates the loss of lift is of 22% and 5% respectively whereas at the smallest blowing rate, the aerofoil stall in the traditional way lower but rather kept a increasing in lift coefficient of approximately more than 5%.

Combining the results of CL and CD against α for the blowing leading edge aerofoil, the following observations can be made:

At low level of Q', the jet leaving the orifices at the straight leading edge will be entrained back to land on the aerofoil suction surface.These-entrained jets will form streamwise vortices and propagate all the way down to the trailing edge. If there is a separation bubble, the streamwise vortices generated by the jet will help to suppress it. As a result, the CL performance will be improved, as well as the stall angle. These streamwise vortices by themselves do not contribute in the generation of CD too significantly.

At high level of Q', the jet leaving the orifices at the straight leading edge will not be entrained back. Rather, they will continue to oppose the incoming flow until fully dissipated. During the process, leading edge stagnation point could be altered, thereby producing a new flow circulation around the aerofoil. Although it remains a conjecture, it is reasonable to believe that the change in circulation reduces the pressure leading on the aerofoil surface and violated the classic thin aerofoil theory. Therefore at high level of the Q' the deviations of CL and CD from those produced by a baseline aerofoil become significant.

.

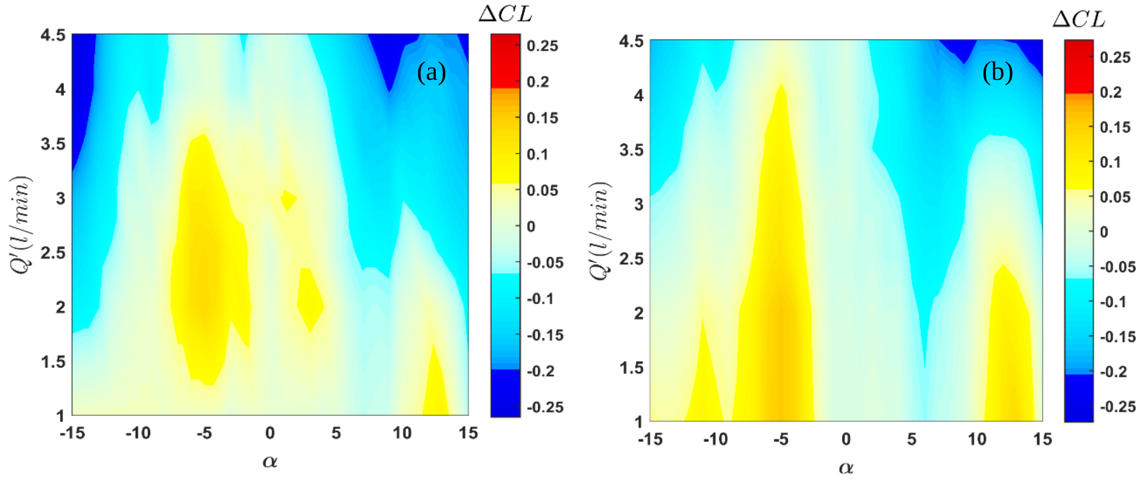

Figure 5-7: Contour maps of ΔCL at different angle of attack (α) at the case of U_∞ = 25 m/s, corresponding to Tu = 45%, produced by leading edges blowing (a) λ' = 5mm and (b) λ' = 10mm for a range of 1-4.5 liter/min.

5.2.3 Correlation between the (A↔Q') and (λ↔λ′)

Within the active and passive flow control parametric range investigated thus far,blow rate ranges described above, it is possible to individually match some of the lift coefficient curves produced by the leading edge blowing to those produced by the serrated aerofoil, as shown in Figure 5-8. An important trend is discernible: with an increase of serration amplitude from A = 15 mm to 30 mm, regardless of the serration wavelength, the same lift coefficient curves can be re-produced by straight leading edge with $\Delta Q' \approx$ 2-3 liter/min. Another similar trend can be seen between the serration wavelength λ and hole spacing λ'. It can be observed that, in order to match the same lift coefficient curves, a doubling of the serration wavelength from λ = 5 mm to 10 mm also corresponds to a doubling of the λ'. The two trends described above as demonstrated in Figure 5-8,suggest the existence of similar mechanism between the serration amplitude/wavelength and blowing rate/air hole spanwise spacing in the lift generation, as well as the suppression of boundary layer stall at high angles of attack.

The observation above can be corroborated by the corresponding drag coefficients' CD values, as shown in Figure 5-9. Similar to their lift coefficient counterparts, each paring between the serrated and blowing leading edges for the drag coefficients across $-15^{o} \le \alpha \le 15^{o}$ is also well matched. All curves have roughly the same point of interception at $\alpha = 0^{o}$ with CD ≈ 0.03 because these are for unsymmetrical aerofoil. When subjected to an increase of either Q' or A for the leading edge, a decrease of CD is exhibited at $-15^{o} \le \alpha \le 0^{o}$, but an increase of CD at $0^{o} < \alpha \le 15^{o}$ compared to the baseline edge. The increase of the drag coefficient at the post-stall area is noticeable for the blowing leading edge and serrated leading edge, especially for lower λ and λ'. This could be a result of the strong streamwise vortices produced by both the passive and active mechanisms. Where the level of CD increases with lower value of λ and λ', as underpinned by the large number of vortices produced per unit span.

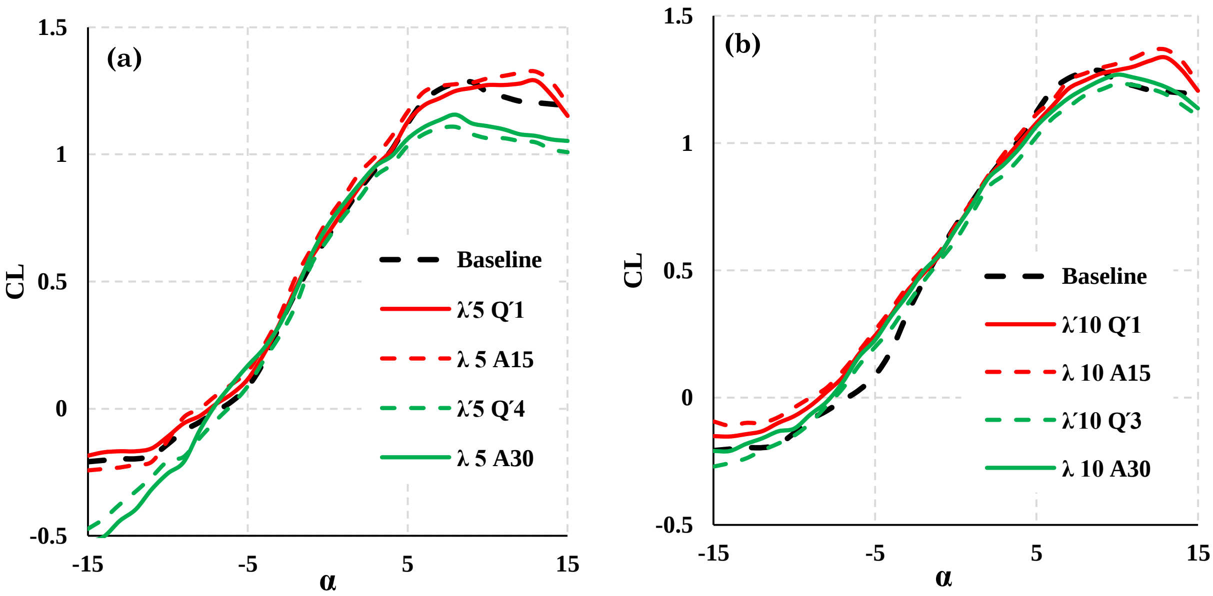

Figure 5-8: Comparison of lift coefficient CL, as a function of angles of attack (α), produced by serrated and blowing leading edges. $U_\infty = 25$ m/s, when Tu = 4.5%.

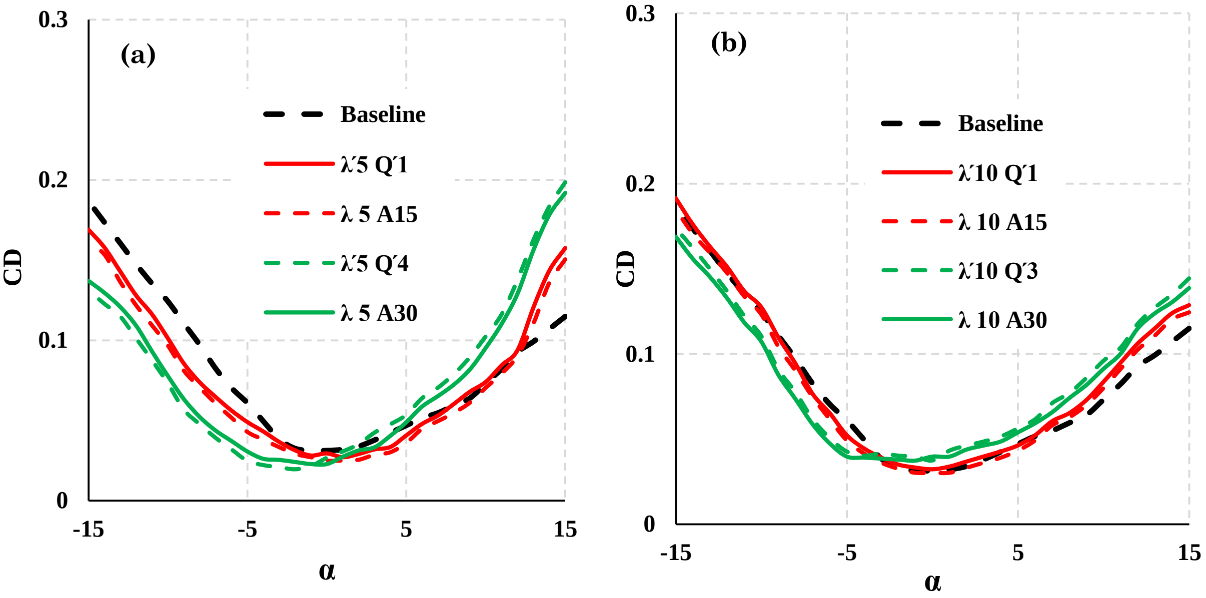

Figure 5-9: Comparison of drag coefficient CD, as a function of angles of attack (α), produced by serrated and blowing leading edges. U_∞ = 25 m/s. when Tu = 4.5%.

5.3 Low Turbulence Intensities

Earlier sections have highlighted the potential effectiveness of leading edge straight blowing and serrations leading edge aerofoils at high turbulent intensity. This section compares the influence of leading edge straight blowing serrations with baseline conditions. Therefore, the baseline leading edge acts as a reference case in this study, and the steady aerodynamic performance of aerofoils is studied experimentally at low turbulent intensity when Tu = 0.2%. The lift and drag forces were measured on the NACA65(12)-10 aerofoil with varying serration wavelengths (λ = 5mm & 10mm) and amplitudes (A = 15mm & 30mm), and also different air hole spanwise spacing ($\lambda'5$ & $\lambda'10$). The geometric angle of attack varies from -15 ° to 15 °.

5.3.1 Effect of Serrations and Angle of Attack (AoA)

This section shows the lift coefficients at low turbulent intensity, CL for several types of serration leading edges at different AOA. The aerodynamic results were achieved at a separate wind tunnel described previous in chapter

3. The freestream under investigation was U_∞ = 25 m/s, corresponding to to Reynolds number of $Re = 2.5 \times 10^5$ based on chord length C. Note that the same planform area has been used throughout the study of the lift coefficient, regardless it is a serrated leading edge or a baseline leading edge. Figure 5-10 compares the CL generated by Four serrated leading edge (A = 15 and 30 mm, all with λ = 5 and 10 mm) and the baseline leading edge aerofoil.

The lift coefficient generated by the serrated leading edge of A = 30mm, λ = 5 and 10 mm are significantly lower than those generated by the baseline case. In this case, the reason for the decrease in CL is probably to be caused by the significant loss of lift producing surfaces. The lift curve slope decrease to 0.088. The stall angle is improved, and the increase in lift coefficient with AoA at the post stall region is better than the baseline leading edge at low wavelengths. The lift performance enhance with A = 15mm and λ = 5 and 10 mm slightly better from pervious case, where the amplitude λ is lower. Interestingly, the improvement in aerodynamic efficiency is quite noticeable at the lowest serration amplitude of A = 15 and λ = 5.

In the case of such a serration amplitude λ = 5, the lift slope improves, and the stall angle is significantly bigger reaching to 13^o and the decrease in CL after the stall angle is smoother than the baseline case. As a consequence, this type of serration leading edge has higher efficiency in the post stall region.

Figure 5-10b compares the lift coefficient of other two serration leading edges with bigger wavelength (A = 15, and 30mm with λ = 10).

The results in Figure 5-9b show a good efficiency in lift data and slope curves relative to those in Figure 5-10a, stating that a bigger wavelength is another criteria for maintaining aerodynamic efficiency. Notably, the one with the lowest serration amplitude A = 15mm and λ = 10mm even generates a greater CL than the baseline case at an angle of attack of more than 13^o. The maximum lift coefficient for the serrated leading edge is also consistent with the baseline leading edge. Table 5-3 provides a summary of the baseline lift slopes and the serrated leading edges.

The Figure 5-3 and 5-10 show difference of lift coefficient against angle of attack at U_∞ = 25 m/s, the stall angle is delayed and the maximum lift coefficient by the increase the turbulence intensity; however, the rate of increase is not linear with the increase of turbulent intensity. The result displays that the increase in turbulent intensity improved the maximum lift coefficient.

The Figure 5-3 and 5-10 show the relation between the CL and the *Tu* at different angles of attack. Generally, it indications that lift coefficient rises as the turbulent intensity increases. The CL rises up to the stall and after the stall angle, the lift coefficient start to reduction, on the other hand, the decrement rate is not much higher than the slope of the baseline at the same condition.

The drag efficiency figure below illustrates a significant decrease in drag in the pre stall region. The aerofoil with the largest serration-wavelength the better one with an increase in drag of up to 8% at the negative angle of attack. Furthermore, there was negligible difference at lower angles from (0^{o} -11^{o}). On the other hand, the post stall-drag coefficient was increased with increasing angle of attack. In contrast to the pattern noted for lift, the aerofoil with a smaller wavelength conducted better than the aerofoil with the largest serration-wavelength $\lambda = 10$mm.

Previously, a maximum rise of 6% was observed, compared to a maximum rise of 9% in drag for the smallest wavelength. Also, while both models performed better than the baseline leading edge in the pre-stall, the lowest wavelength aerofoil maintained a decrease in drag up to 11% up to -9 ^{o}, while the other wavelength moved towards the baseline case.

The results for the drag characteristics of the aerofoil were similar to those for the smaller amplitude, with a rise in drag in the post stall region and a negligible change in the region between (0^{o} -12^{o}). Compared to the consequences of the larger amplitude, however, the performance was observed to be worse at positive angle of attack, with a maximum drag coefficient rise up to 0.22 at 15 ^{o} while lower amplitude up to 0.17 at the same degree. In the same way as the lift characteristics of this case, the rise in drag was reported over a wider range of AoA. Also, while the lower serration-amplitude showed the worse in post stall region performance, and around 11% enhancement in drag coefficient. It is apparent from the results of this research that the small amplitude, small wavelength aerofoil has superior lift and drag coefficients than the other serration leading-edge aerofoils. , which could be caused by strong streamwise vortices produced by both the passive mechanisms at lower turbulent intensity. As a result, the values of lift coefficient are greater at high turbulent intensity compared with lower turbulent intensity, and the value increases with increasing *Tu*. The influence of the turbulence intensity on the NACA65 (12)-10 aerofoil drag coefficient is illustrated in Figure 5-3. The result appearances that the rise in turbulence intensity induced a tiny rise in drag coefficient at 25 m/s. The relationship between the drag and the *Tu* at 25 m/s can be seen in Figure 5-4 and Figure 5-11. The CD also improves as the angle of attack rises. The results indicate that the increment level is low at the start, but after the stall, the increment level is steeper. This is mainly due to the sudden increase in the pressure drag force due to the separation of the flow.

Table 5-3: The serration leading edge effect on aerodynamic performance for NACA 65(10)12 without grid-generated turbulence intensity (0.2%).

Configuration	**Stall angle(α)**	***A(mm)***	**λ *(mm)***	***A/C***	**λ*/c***	**CL(max)**	**ΔCL(max)**
Baseline	8	-	-	-	-	1.24	reference
λ5A15	12	15	5	0.1	0.033	1.25	0.007
λ5A30	7	30	5	0.2	0.033	1.07	-0.170
λ10A15	13	15	10	0.1	0.066	1.28	0.035
λ10A30	10	30	10	0.2	0.066	1.24	-0.008

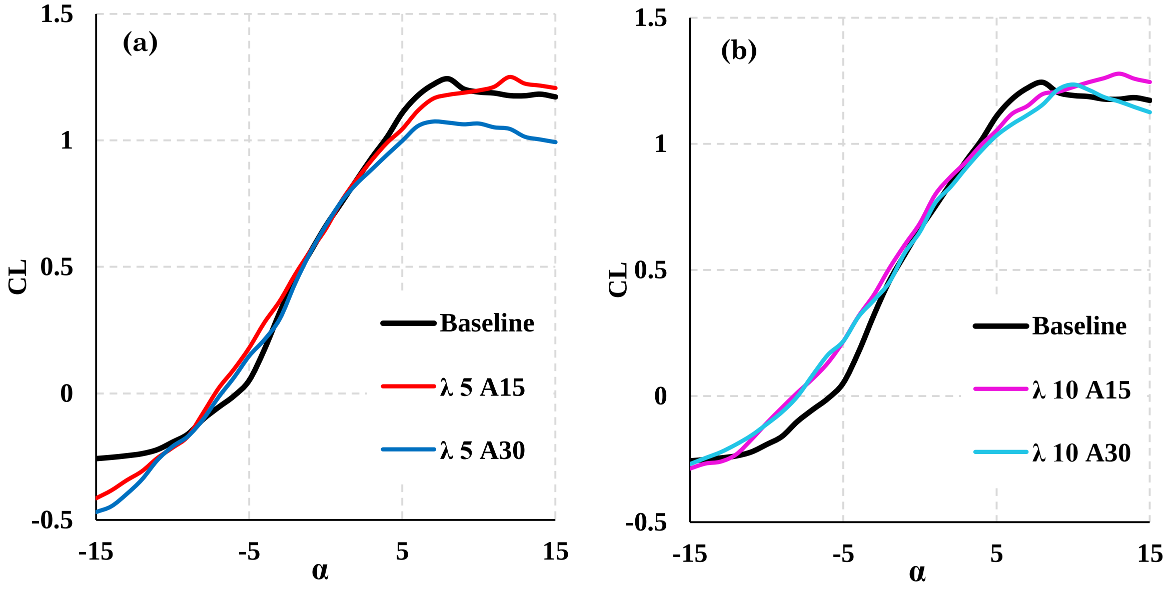

Figure 5-10: Comparison of lift coefficient CL, as a function of angles of attack (α), produced by serrated leading edge when λ = 5 &10 mm and A = 15 &30 mm at U_∞ = 25 m/s and Tu = 0.2%.

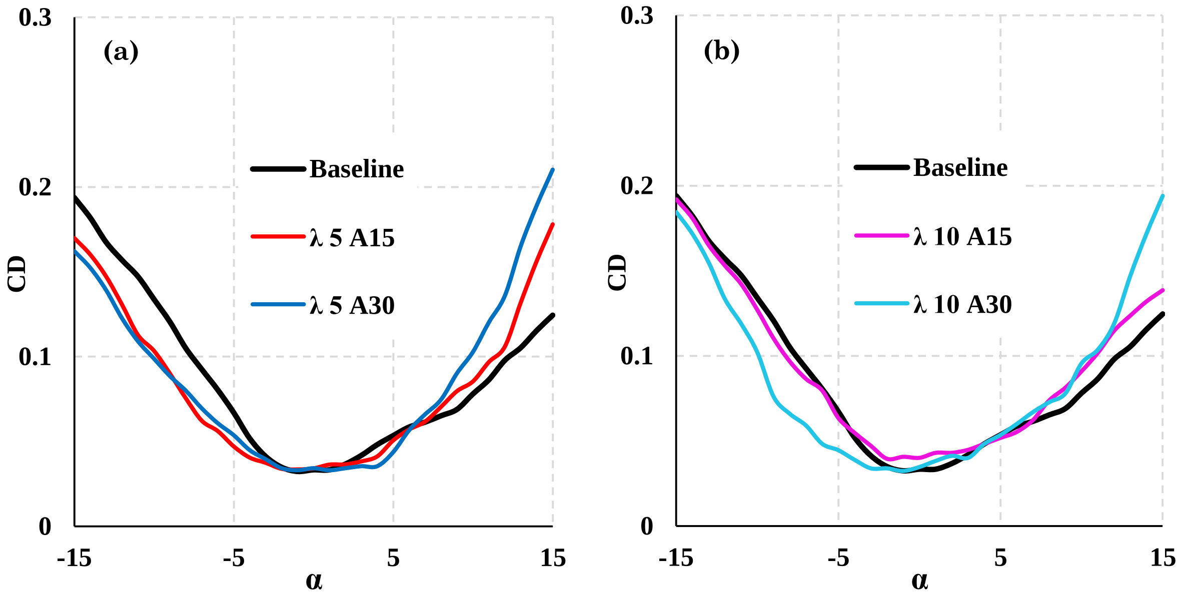

Figure 5-11: Comparison of drag coefficient CD, as a function of angles of attack (α), produced by serrated leading edge when λ = 5 &10 mm and A = 15 &30 mm at U_∞ = 25 m/s and Tu = 0.2%.

5.3.2 Effect of Blowing Rates (Q')

The leading edge is equipped with many holes, allowing jets to pass through the freestream flowing around the aerofoil, thus improving the lift force's energy. The main aim of flow control for fixed wing airplane is to improve the lifting force when big lifting forces or/and low velocities are needed, such as during take-off and landing. While a significant increase in lifting coefficients can be achieved using blowing leading edge, there is also decreased drag coefficient on the negative AoA, and an inherent increase in the drag coefficient on positive AoA of the aerofoil [130,165, 166].

Figure 5-12 shows the variation in lift when blowing flow was performed under steady conditions in an incompressible flow. It seems that a small rise in CL occurred in the pre stall region at $\alpha<6°$, for lower blowing leading edge. The small rise in lift is due to the lower pressure beginning at 10% of the cord with the lateral and downstream proximity of the leading edge jets. It is also important to note that, there is a negative pressure gradient immediately above of the blowing jets suggesting a small stagnation area. However, the suction peak around the leading edge is maintained and does not seem to be influenced by the pressure gradient.

In comparison with the current research, is observed negligible flow change at pre-stall angles of attack is observed, suppressed separation to a greater angle of attack, and witnessed lift improvement in the post-stall regime [34]. Specifically, when blowing was applied at $Q'=1$ liter/min, the peak CL was increased by 5% and stall was delayed by $\Delta\alpha=3°$. Lift post stall was increased by up to 10%.

Interestingly, as mass air flow rate was increased, a blowing rate at $Q'=3$ liter/min where $Q'>4$ liter/min blowing did not show significant variation from the $Q'=4$ liter/min just reduced the stall angle of attack up to 2° compares with baseline case results depicted in Figure 5-12 [34].

The following paragraph deals with the effect of spanwise spacing of the orifice (λ') on the characteristic values CL_{max} and angle of attack at peak lift coefficient as well as the slope characteristics and post stall behaviour. Figure 5-12a presents the results for $Q'= 1$, $Q'= 2$ $Q'= 3$ and $Q'= 4$ liter/min with a constant spanwise spacing of the orifice of λ' = 5mm. It can be clearly seen that the variation of blowing rate is an influencing factor for the aerodynamic performance. Higher blowing rates achieve an increase in lift coefficient up to 21% as well as a delay in stall. The slope $dCL/d\alpha$ is increased by 4%. Overall the performance is significantly higher compared to the baseline case. Figure 5-12b compares the leading edges Q'= 1, Q'= 2 Q'= 3 and Q'= 4 liter/min all with a spanwise spacing of the orifice of λ' = 10mm. The plots show a good agreement with the observed effect. Furthermore it can be seen that the effect caused by Q' is lowered with higher spanwise spacing of the orifice. While the influence of Q' on the CL is high at small through to peak distances, it increase with the application of larger λ'.

The lift coefficient values were plotted in Figure 5-12b as function of angle of attack for blowing and baseline configurations. At pre stall region, all blowing leading edge configurations follow the baseline curve from -3° to 2°. The blowing rates delay the increase in lift curve slope by one degree when compared to the baseline aerofoil. In addition, for higher angles of attack up to stall, the configurations Q'= 3, and Q'= 4 liter/min keep close and with similar tendency as the baseline case one, having lift values slightly lower.

In the cases of the blowing configuration Q'= 1, and Q'= 2 liter/min. it can be observed a large aerodynamic performance deterioration for higher values of angle of attack ($\alpha > 8°$) where the lift curve trends to increases significantly when compared to the baseline configuration. In terms of maximum CL and stall AoA. the configurations Q'= 3 liter/min reach similar values close to the baseline case. For Q'= 4 liter/min the CL_{max} is lower than other configurations with the lowest stall angle. At post stall region, all blowing leading edge configurations have a smother stall keeping the lift coefficients near CL_{max} at higher angles of attack expected when Q'= 1 liter/min with sharp post stall, differently from the abrupt stall that occurs for the baseline aerofoil indicating a leading edge stall.

The blowing leading edge geometries defined by blowing rate Q' and spanwise spacing of the orifice λ' affect the pre stall and post stall characteristics. By increasing the Q' at the same λ' a large increase in linearity is observed on lift curve at pre-stall regime where the configuration

Q'=1 liter/min presents significantly higher lift values than those for the baseline configuration. whereas the highest Q' configuration Q'=4 liter/min has similar performance to the baseline case up to stall. However, as consequence of a higher stall angle at lower and greater λ', the configurations Q'1 reach maximum lift coefficients with values of 1.256 (λ'5) and 1.31 (λ'10), respectively. In contrast with pre-stall conditions, an increase in λ' does not change the post stall characteristics keeping the same behaviour.

By increasing the blowing rate Q' for the same (λ'), significant variations on the lift curve on the post stall and pre stall region do not happen where the lower Q' has a little smoother post stall behaviour.

Figure 5-12 presents maximum lift coefficient, at the freestream velocity U_∞ = 25 m/s, aerodynamic deterioration caused by the straight blowing leading edge. The blowing rate configurations reach lower values than the baseline aerofoil except at Q'=1 liter/min for specific configuration λ'=5mm and Q'=1-2 liter/min when spanwise spacing of the orifice λ'=10mm. As result of the spanwise spacing of the orifice effects on blowing leading edge performance at stall conditions, the aerodynamic deterioration in maximum lift coefficient, caused by blowing leading edge aerofoils, increases with increasing in aerofoil spanwise spacing of the orifice. In addition, the blowing largest aerofoil establishes the stall angle near to baseline case. On the other hand, lowest blowing rate aerofoil has significant increase in stall angle for straight blowing leading edge configurations.

Figure 5-13 shows the blowing leading edge performance in terms of drag. At low AoA ($\alpha < 15°$). The bigger spanwise spacing of the orifice configurations (λ'10 Q'1 and λ'10 Q'2) have similar higher CD values than the baseline case. For the smaller spanwise spacing of the orifice configuration (λ'5) the drag coefficient at 13° lift reaches the highest value when compared to baseline case (ΔCD= 15%).

For intermediate angles of attack (7° < α < stall AoA), the blowing leading edge geometry influence on drag coefficient curves depends on how the configurations resist to beginning of the stall AoA. The configuration of λ'10 Q'1 anticipates at α =8° and thus reduce the extent of the drag bucket increasing drag at early AoA. On the other hand, the configurations λ'5 Q'3 and λ '5 Q '4 keep a parabolic rise in the drag curve up to 15° presenting higher drag values, and both configurations overcoming the drag values of the baseline case in positive angle of attack.

In terms of λ ' influence, an increase in spanwise spacing of the orifice at a fixed blowing rate (Q ') reduces the drag coefficient at maximum lift and anticipates the post stall resulting in a large increase in drag. Considering the blowing rate influence, except at negative angle of attack, the configurations λ '10 Q '3 and λ '10 Q '4 present near similar drag values showing a negligible blowing rate variation influence at negative angle of attack. For higher angles of attack at post stall region, the bigger blowing rate appearances higher drag values.

As discussed previously, presents lower values than the baseline case does at negative angles of attack and the case Q '=4 liter/min shows an early and expressive increase in drag because of the anticipation on the flow separation onset. From the previous plots compares with Figure 5-3, it can be inferred that turbulence intensity governs the location of angle of attack maximum CL while the integral length scale governs the gradient of the lift slope. An increase in turbulence intensity shows an increase in the maximum CL. The angle at which of maximum CL is higher at higher intensity, the lift slope is nearest to smooth. This shows that as Tu increases the time averaged aerofoil characteristics tend to become similar to steady condition. The decrease in lift slope is believed to be due to the unsettled boundary layer formed due to the high energy small turbulence eddies current within small length scale turbulent flows.

The lift results illustrate that the addition of turbulence delays stall, which would generally increase the lift coefficient, as was shown by 5-5 and 5-12. The low turbulence flow shows drop in lift, but at a lower α. Higher blowing rate values in the low Tu may describe why this case generally appearances a slightly higher lift coefficient for angles of attack up to 13°. Drag value in all cases is very similar until α is above -6° and 6°.

The low Tu case appearances a stall angle at 13°. This is followed by a jump in the drag coefficient at 7°. In contrast, the lift coefficient for the 4.5%

turbulence intensity doesn't start to reduce until an about 13°, and even then decreases slightly. Also, this is followed by a jump in CD at -7°.

Figure 5-14 illustrates the blow rate (*Q* ′ effect in performance in terms of ΔCL ($CL_{\text{straight blowing}}$ –CL_{Baseline}). The results show that the baseline aerofoil stall starts around 12° for *λ* ′5 and 13° *λ* ′10 and the difference of the lift coefficient decreases suddenly. Similarly to the ΔCL at high turbulent intensity, the difference between the pitching up and pitching down lift coefficient were then plotted in Figure below.

Figure 5-14a and 5-14b compare the difference between the baseline and the profile of with the large and smallest spanwise spacing of the orifice (*λ* ′). The maximum ΔCL for blowing leading edge cases up to 18% *λ* ′=10mm and 15% for *λ* ′=5mm all with α= -5° especially when *Q* ′=1 liter/min, the lift difference losses range $-0.002 \leq \Delta CL \leq -0.29$ when angle of attack between 11 and -15 on the same time ΔCL also reduced for the range $6 \leq \Delta CL \leq 15$ it reduced up to -0.23 compared with baseline case.

Table 5-4: The straight blowing leading edge effect on aerodynamic performance for NACA 65(10)12, corresponding to the turbulence intensities of *Tu* 0.2%.

Configuration	**Stall angle(*α*)**	***Q* ′*(liter/min)***	***λ* ′*(mm)***	**CL(max)**	**ΔCL(max)**
Baseline	8	-	-	1.24	reference
λ′5 Q′1	12	1	5	1.26	0.011
λ′5 Q′2	11	2	5	1.22	-0.028
λ′5 Q′2.5	10	2.5	5	1.18	-0.063
λ′5 Q′3	9	3	5	1.15	-0.095
λ′5 Q′3.5	8	3.5	5	1.11	-0.136
λ′5 Q′4	7	4	5	1.07	-0.176
λ′5 Q′4.5	6	4.5	5	1.01	-0.238
λ′10 Q′1	13	1	10	1.30	0.056
λ′10Q′2	12	2	10	1.26	0.021
λ′10 Q′2.5	11	2.5	10	1.21	-0.029
λ′10 Q′3	10	3	10	1.20	-0.036

Configuration	**Stall angle(α)**	***Q′(liter/min)***	***λ′(mm)***	**CL(max)**	**ΔCL(max)**
λ′10 Q′3.5	9	3.5	10	1.164158	-0.079
λ′10 Q′4	9	4	10	1.098925	-0.145
λ′10 Q′4.5	8	4.5	10	0.993548	-0.250

This performance is significantly worse than those obtained with the smallest spanwise spacing of the orifice (*λ′*=10mm) for the blowing range between 1-3 liter/min. The performance of the aerofoils enhanced with increase in spanwise spacing of the orifice at the negative angle of attack; furthermore, the improvement is less than 13% at the post stall region when the blowing rates *Q′*=1-3 liter/min. The profile with the smaller spanwise spacing of the orifice (*λ′*=5mm) exhibited a further enhancement in performance with ΔCL on the pre stall region. The effect of spanwise spacing of the orifice can also be considered to be insignificant for difference of the lift coefficient at the small *λ′* when α= 0°. From the results presented above compare with pervious results in the last section at high turbulent intensity, the ΔCL is significantly reduced for blowing rate profiles with increase *Tu* and practically nonexistent with large blowing rates. Thus, provided that the variation in angle of attack is very low compared to the low turbulent intensity, aerofoil operational characteristics with such leading edges over the whole working range of of angles of attack can be considered.

In summary, blowing leading edge with low blow rate is beneficial for aerodynamic lift, the delay in stall AoA can be noticed. The flow jet from the orifices will be backed to surface of the aerofoil these will be formed a separation bubble the jets will help to suppress it, therefore CL performance will be increased and the stall angle of attack will be enhanced. However, at high blow rate jet will be opposed the incoming flow until fully dissipated.

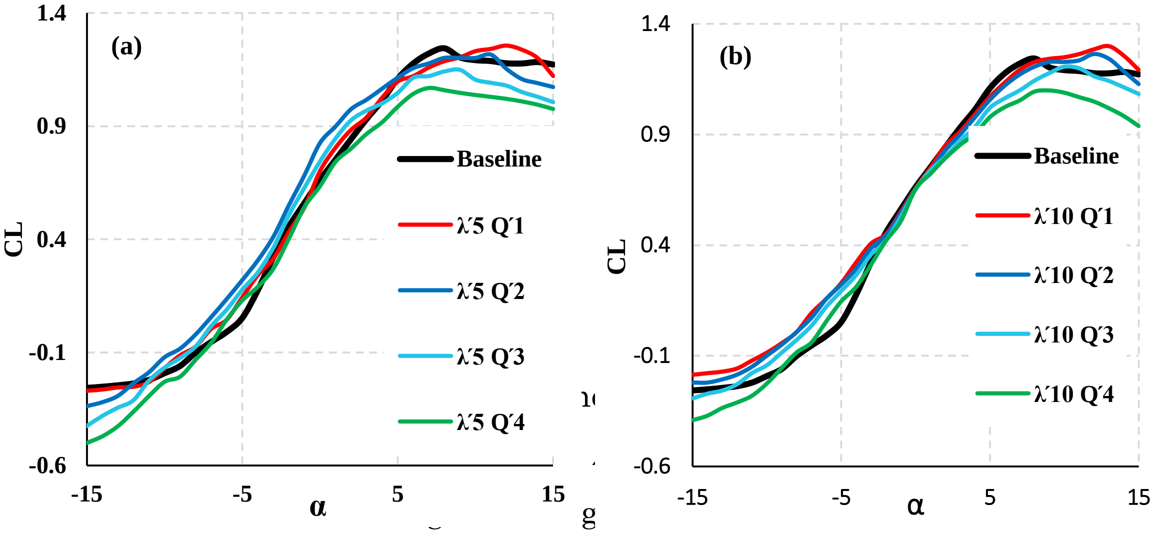

Figure 5-12: Lift coefficient curve at the case of U_∞ = 25 m/s, corresponding to Tu = 0.2%, when (a) λ' = 5 mm and (b) λ' = 10 mm, produced by leading edges blowing for a range of 1-4 liter/min.

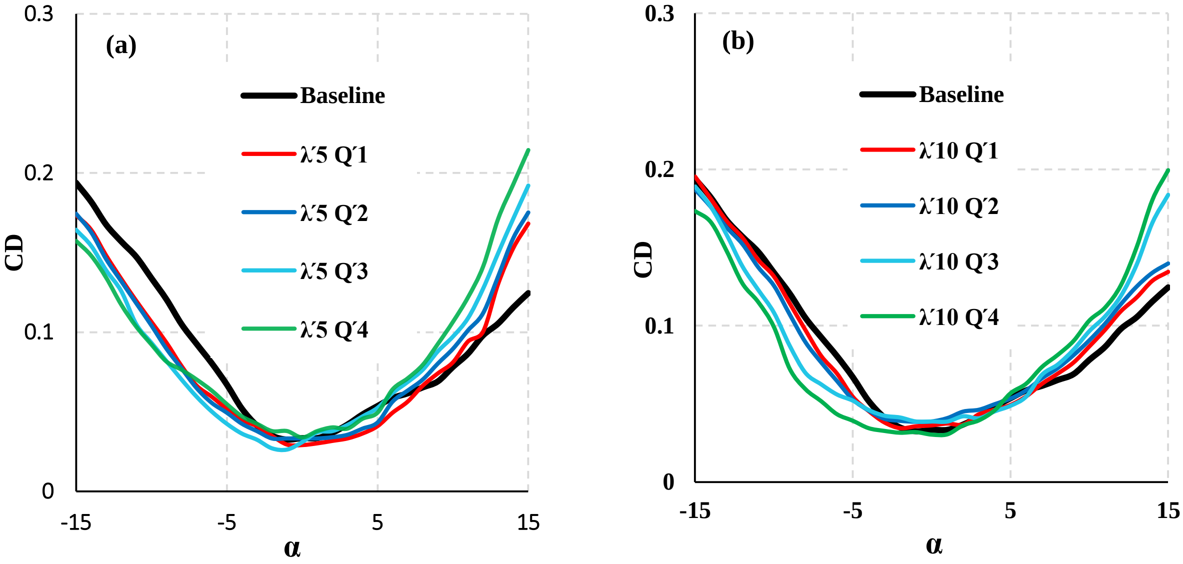

Figure 5-13: Drag coefficient curve at the case of U_∞ = 25 m/s, corresponding to Tu = 0.2%, when (a) λ' = 5 mm and (b) λ' = 10 mm, produced by leading edges blowing in the range of 1-4 liter/min.

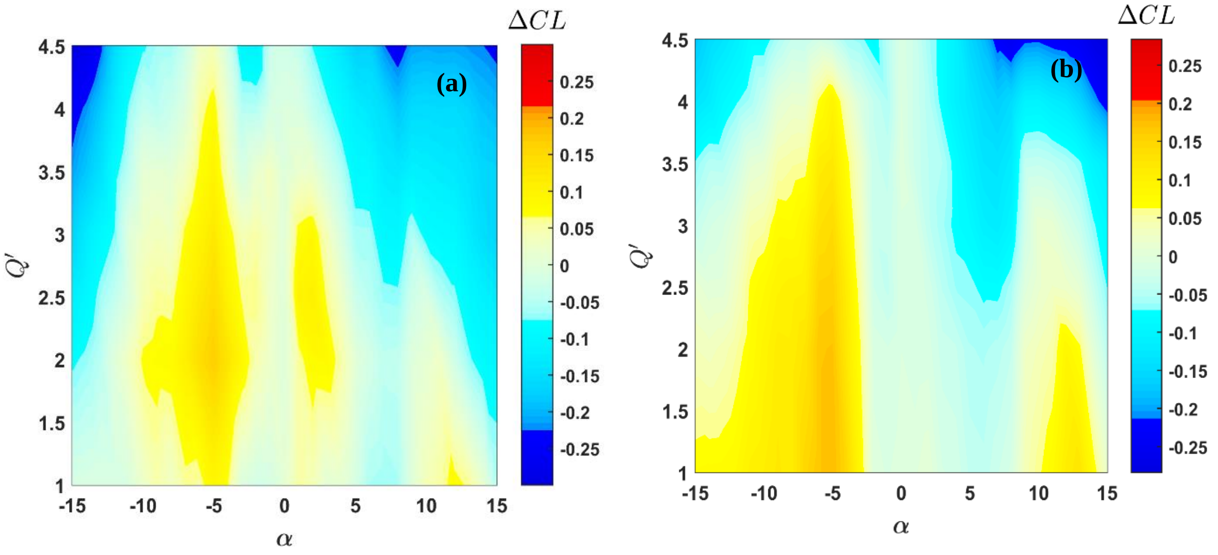

Figure 5-14: Contour maps of ΔCL at different angle of attack (α) at the case of U_∞ = 25 m/s, corresponding to Tu = 0.2%., produced by leading edges blowing in the range of 1-4 liter/min, when (a) λ' = 5 mm and (b) λ' = 10 mm.

5.3.3 Correlation between the (A↔Q') and (λ↔λ′)

In the following sections, the naming of each serrated and blowing leading edges is in accordance to the values of their serration wavelength λ = 5mm &10mm, and serration amplitude A = 15mm&30mm (also, blowing spanwise air holes (λ') = 5 mm and λ' = 10 mm) at low turbulent intensity.

For λ' = 5 mm and λ' = 10 mm, the volumetric blowing rates differ from $1 \leq Q' \leq 4$ liter/min. It is noted that a reduced blow rate can reach both a higher lift and a stall angle. The impact of the volumetric blowing rate on the lift coefficient is also influenced by the spanwise spacing of the air hole. For instance, $\lambda'5Q'1$ is discovered to fit the $\lambda5A15$ superior qualitatively, while the $\lambda'10Q'1$ would match the $\lambda10A15$.

On the other hand, it should be observed that the lift curve slopes produced are still very dissimilar. In the above-mentioned flow rate ranges, some of the lift coefficient curves generated by the serrated leading edge can be individually matched to those generated by the leading edge blowing aerofoil. The results show individual post-stall characteristics for each leading edge and indicate a clear tendency in slope characteristics. The reach similar value for the serrated and blowing leading edges. It can be seen that larger serration amplitudes have the same slope and the CL_{Max} up to 1.255 compares with higher blowing rate at 4 liter/min. While the large serration amplitude (A=30mm) with blowing rate at 3 liter/min when λ'=10mm experience a sharp stall and unsteady post-stall behaviour, small serration amplitudes and lower blowing rate show a significant increase in the maximum stall angle and have smoother stall characteristics. The serrated leading edge A = 15mm, λ = 5mm (smallest amplitude, intermediate wavelength) and $\lambda'5Q'1$ influences the curve progression by the stall angle up to 12°.

While the CL remains high (CL_{Max}=1.3) compared to the blowing leading edge at higher spanwise spacing of the orifice. Lift coefficients for wavelengths of λ= 10mm with amplitudes of A = 15mm and A = 30mm are shown in Figure 5-15b as functions of AoA. Compared to the baseline, the slope of both serration and blowing decrease by 13%. It can be seen that the stall of the aerofoil is delayed by 5 degrees. Overall it can be observed that both serration and blowing show the similar behaviour in slope characteristics.

The same lift coefficient curves can be re-generated by a straight blowing leading edge of Q' = 1 liter/min, with a rise in serration amplitude A = 15 mm to 30 mm. Another correlation between wavelengths λ and volumetric blowing rates Q' is present. It can be noted that a duplication of the serration wavelength from λ = 5 mm to 10 mm also equates to a doubling of the Q' in order to match the same lift coefficient curves.

The two developments mentioned above indicate the presence of comparable mechanisms in the lift generation between serration wavelength/amplitude and air hole spanwise spacing/blowing rates, as well as the suppression of boundary layer stall at high AoA as shown in Figure 5-15.

As illustrated in Figure 5-16, the observation below can be confirmed by the drag coefficient. Each intersection between the blowing and serrated leading edges for the drag coefficients across $-15^{o} \leq \alpha \leq 15^{o}$ also correspond very well, as do their lift coefficient counterparts. The interception level at $\alpha = 0^{o}$ with CD to 0.04, is approximately the same for all curves. There is a reduction in CD at $-15^{o} \leq \alpha \leq 0^{o}$, but an increase in CD at positive AoA compared to the standard one when exposed to an increase in either Q' or amplitude for the leading edge, especially when λ' is larger at 10mm, whereby the CD slightly decreases at positive AoA (0° ≤ α ≤ 5°). For the serrated and blowing leading edges, the increased drag coefficient at the post-stall region may be seen as the consequence of the strong streamwise vortices caused by passive as well as active mechanisms.

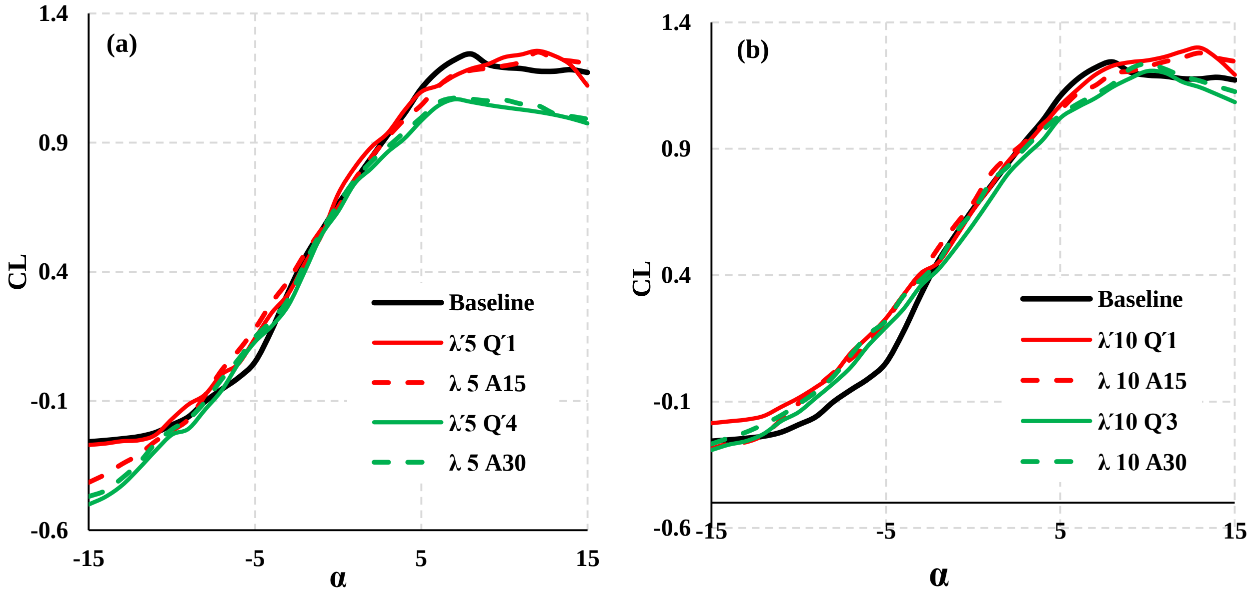

Figure 5-15: Comparison of lift coefficient CL, as a function of angles of attack (α), produced by serrated and blowing leading edges. U_∞ = 25 m/s. when Tu = 0.2%.

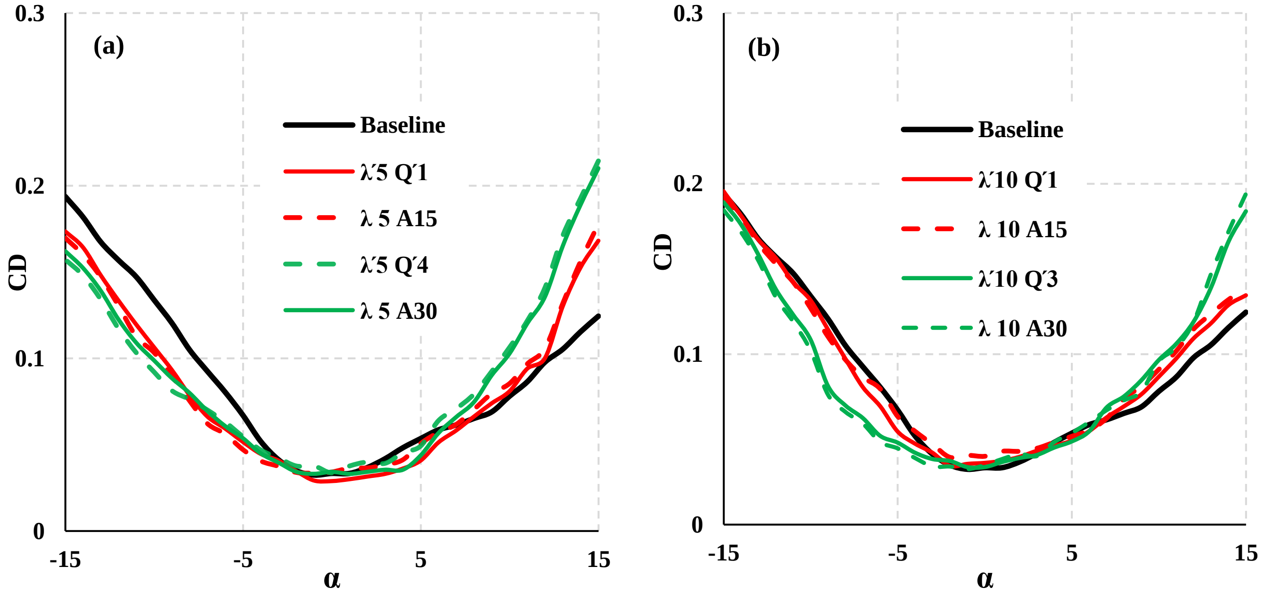

Figure 5-16: Comparison of drag coefficient CD, as a function of angles of attack (α), produced by serrated and blowing leading edges. U_∞ = 25 m/s. when Tu = 0.2%.

Chapter 6 : Hybrid Leading Edge

(Serrated-Blowing)

6.1 Introduction

Previously, aeroacoustic investigation reveals that the largest level of reduction in the turbulence–leading edge interaction noise is associated with a larger concentration of holes. There is also an optimal blow rate to tackle this particular noise source. For the instability tonal noise at the trailing edge, the most effective configuration is with the lowest possible blow rate. The most effective configuration for aerodynamic performance is leading edge blowing with low blow rate of orifices and serration, which inhibits the boundary layer separation at large angle of attack, increases the stall angle and lift coefficient, and reduces the drag coefficient. This chapter presents the results on the combined use of serrated *λ45A30* (passive control) and blowing leading edge (active control) for broadband interaction noise radiation at the leading edge, which depends strongly on the freestream level of turbulence intensity. Use of low freestream turbulence intensity (0.2%) would cause the aerofoil acoustic response to be predominantly at the trailing edge, particularly without the mechanism of bypass transition and with a low Reynolds number. Conversely, a high inflow turbulence would cause a predominantly acoustical radiation at the leading edge region. Small air holes implemented at the root and peak region of the serration would facilitate the injection of mass flow against the incoming flow. The noise performance of the so-called hybrid (serrated-blowing) leading edge is analysed in the following sections, focusing on trailing edge instability tonal noise and leading edge interaction broadband noise reduction.

There are two possible co-existence of noise reduction mechanisms, where one is associated with the serrations, and the other potentially arising from the mass flow injection.

6.2 Rationale for the Hybrid Concepts

Previously, the serrated leading edge has been proven to be a useful passive device for the reduction of the leading edge-interaction noise and trailing edge-instability tonal noise. The most dynamic part of the serrated leading edge remains at the root region, where leading-edge interaction remains to be still effective, and the trailing-edge will be subjected to the incoming streamwise vortices emanated from the serration roots.

Having a blowing leading edge as an active device, it is also demonstrated that the produced jets can oppose the inflow turbulence, and at the same time, roll back and form streamwise vortices to interact with the boundary layer near the trailing edge.

This chapter deals with a hybrid concept wher the jet orifice were placed at the root and tip regions of the serration. The premises of this configuration are:

1- Jet produced at the roots (as well as at the tips) can further reduce the level of interaction with the inflow turbulence.
2- Jet produced at the tips (and/or the roots) can increase the number of streamwise vortices, thereby enhance the level of suppression of separation bubble to achieve a greater level of instability tonal noise reduction.

6.3 Overview of the Model for the Hybrid Device

Chapter 3 summarises the geometrical parameters and drawings of hybrid configuration which is subjected to blow rates of Q'= 0.5-4.5 liter/min. Note that only one serrated configuration is used, which has λ =45 mm and A=30mm. The far field measurements of the aerofoil noise were conducted in the open jet wind tunnel at Brunel University. The range of jet velocities under investigation was between 20 m/s and 60 m/s, with a step size of 5 m/s, corresponding to Reynolds numbers based on C of 2 x 10^5 and 6 x 10^5 respectively. In this study, the aerofoil noise focuses on the AoA of $\alpha = 0°$.

6.4 Serration-Blowing Experimental Results

6.4.1 Acoustic Results

6.4.1.1 High turbulence intensities

Effect of hybrid device with different blowing rates (Q')

Since the serrated leading edge has a new configuration compared to the previous chapter, a comparison is first made against the straight leading edge case. Figure 6-1 shows that indeed this type of serration significant by reducing the interaction noise. In what follows, the effect of blowing in combination with the serration will be discussed.

Figure 6-2 shows the influence of a varying blow rates for $\lambda 45A30$. Such a hybrid configuration shows a reduction of the broadband peaks in the narrow band spectrum compared to the baseline case. Here, the baseline refer to the serration $\lambda 45A30$ without blowing, i.e. $Q' = 0$ liter/min when $Q' = 0.5$ liter/min to = 1.5 liter/min the results show that the hybrid can out perform the baseline ($\lambda 45A30$) across a broad frequency range, before producing a smaller difference between Q' = 3 and 4.5 liter/min. The advantage of the hybrid device becomes less prominent as the freestream velocity increases. It is also worth noting that noise increase generally happens at the high frequency region due to the extraneous jet noise. Summary of other effects such as the velocity and angles of attack is shown in Figure 6-3. It is important to note that the ΔPWL shown in Figure 6-3 is $\Delta\text{PWL}=\text{PWL}_{(\lambda 45A30)} - \text{PWL}_{(\text{hybrid})}$. Therefore, a positive ΔPWL denotes further noise reduction achieved by the hybrid device over the $\lambda 45A30$ serrated trailing edge, and vice versa. Again, it shows that Q' is only the optimum at intermediate value (i.e. $Q' = 1$ liter/min) to achieve further interaction noise reduction than the pure passive device of the serration. Further reduction of noise by hybrid device is also shown to be effective up to U_∞=40 m/s. In terms of the angle of attack, the hybrid device seems to be slightly more effective at negative angle of attack, although it is not sensitive to the level of Q'. Within the experimental space covered in the current study, the hybrid device is found to outperform the serrated leading edge counter-part by further 4dB maximum. The overall sound power level reduction represents a holistic take for the noise performance of the hybrid device.

Figure 6-4 shows the graph of ΔOAPWL against U_∞ at different Q'. The equivalent data can be shown more vividly as a contour map in Figure 6-5. The largest recorded ΔOAPWL (difference in OAPWL between $\lambda 45A30$ and hybrid devices is about 2.3 dB for Q'=1 liter/min and U_∞ = 35 m/s. It seems that this velocity represents the cut-off point for the ΔOAPWL performance.

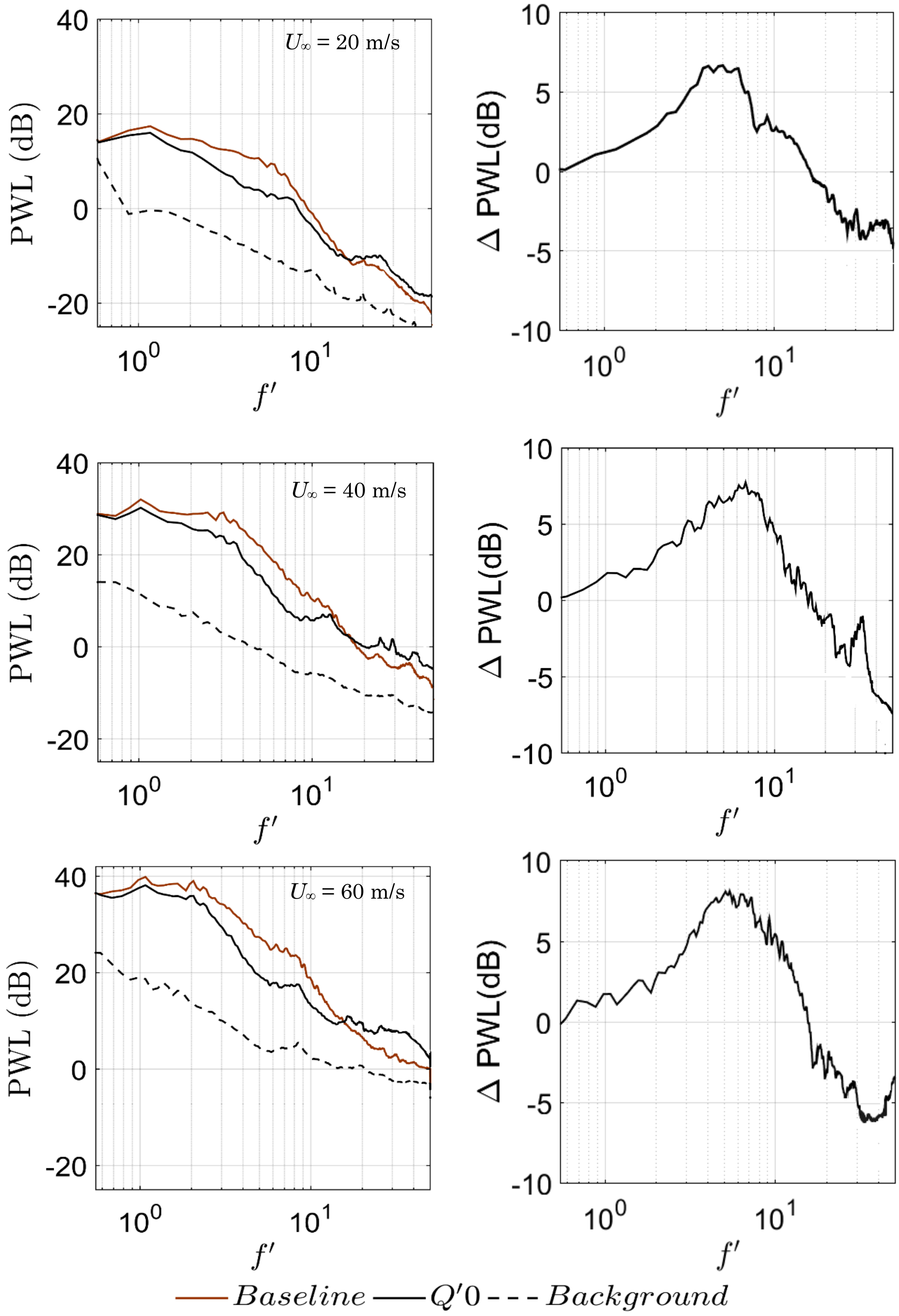

Figure 6-1: Comparison of PWL and ΔPWL as a function of normalised frequency f' produced by baseline ,serration *λ45A30* leading edges and background (black broken line) at U_∞ = 20-60 m/s. Note that the AoA for all cases is set at $\alpha = 0°$ with grid Tu = 4.5%.

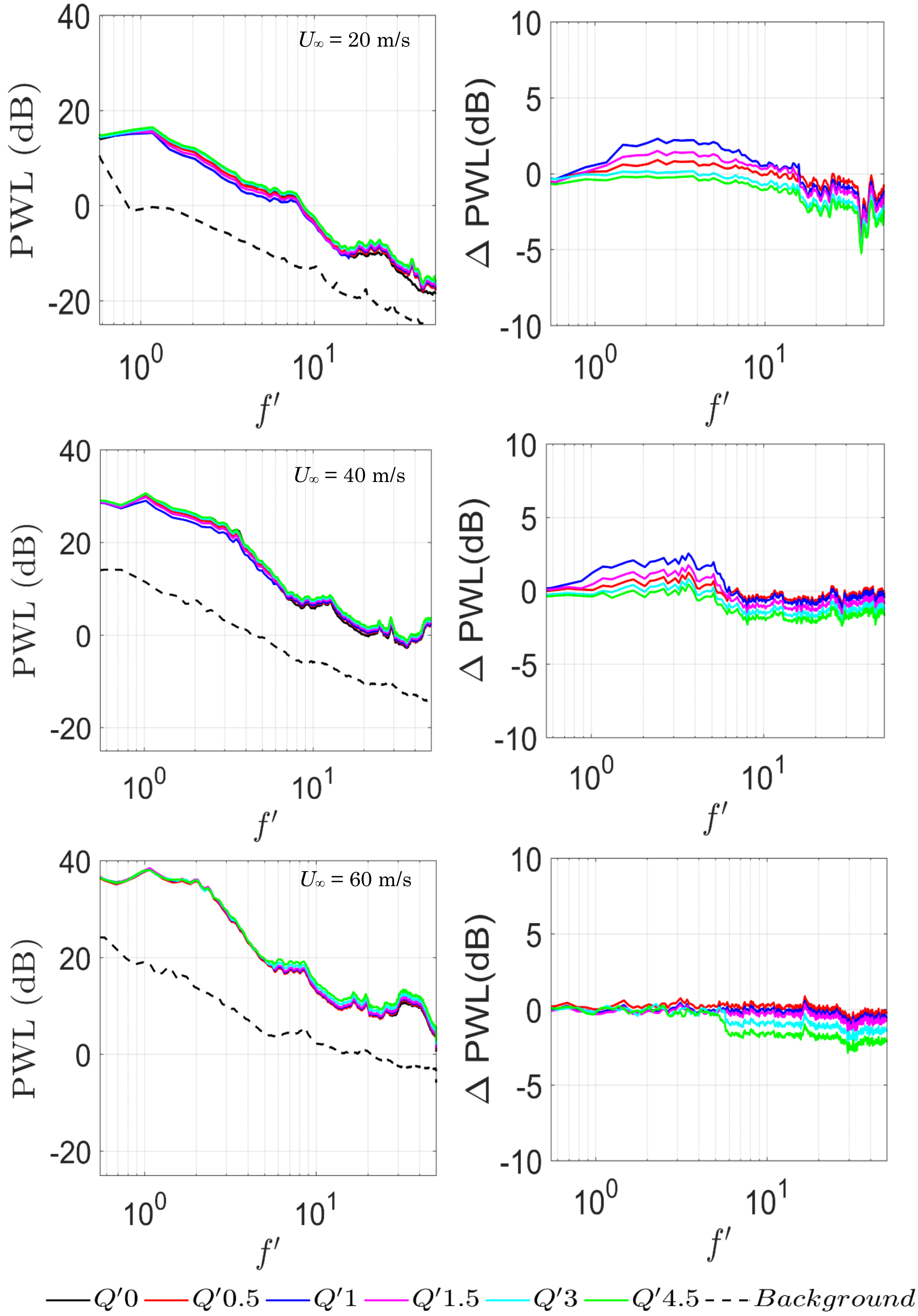

Figure 6-2: Comparison of PWL and ΔPWL as a function of normalised frequency f' produced by serration *λ45A30*, blowing leading edges and background (black broken line) at U_∞ = 20-60 m/s. Note that the AoA for all cases is set at $\alpha = 0°$ with grid Tu = 4.5%.

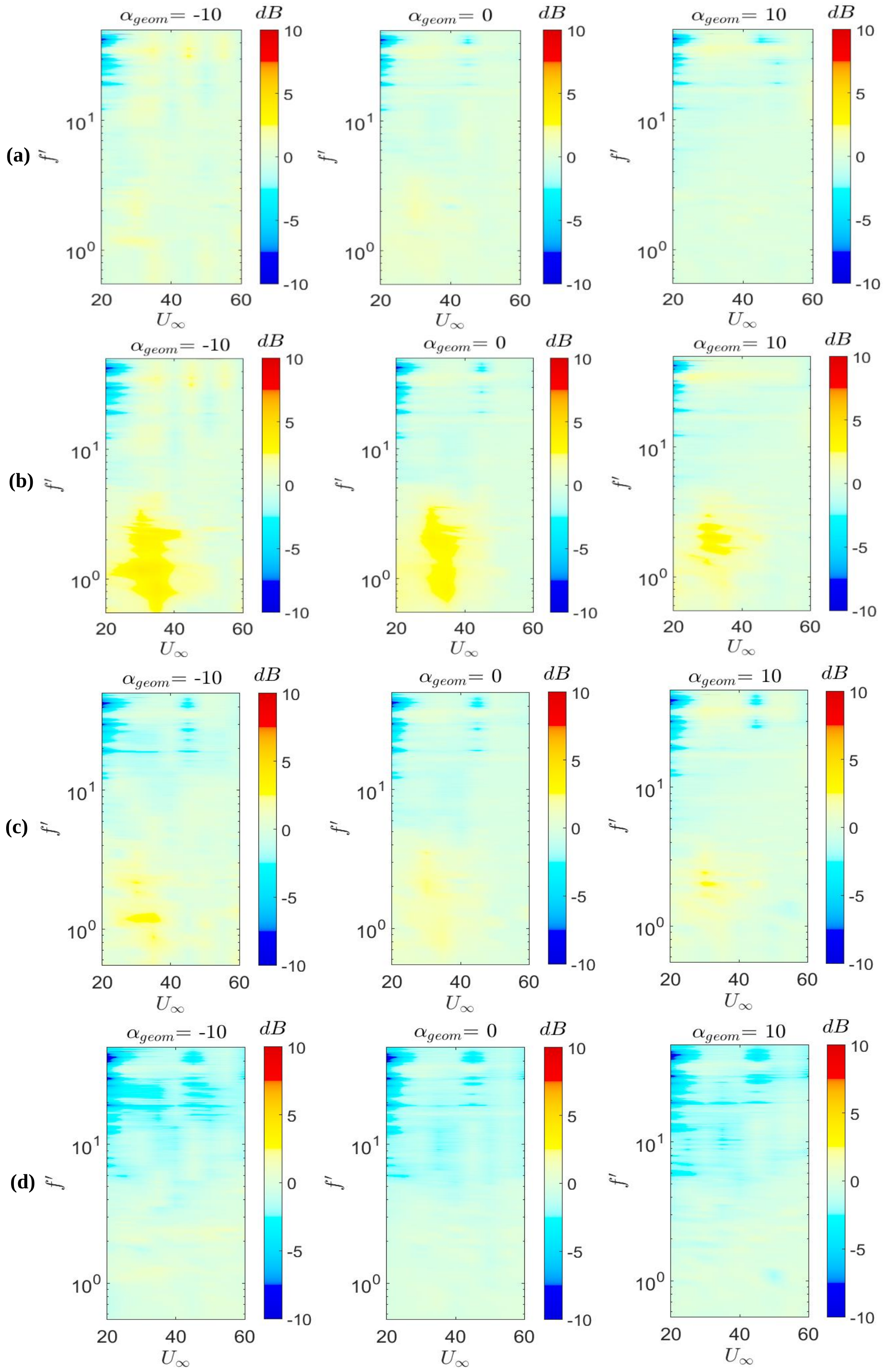

Figure 6-3: Comparison of ΔPWL as a function of normalised frequency f' produced by serration *λ45A30*, blowing leading edges and U_∞ at (α = 0 °, 10 °,-10 °) when Tu = 4.5 %, under Q' = 0.5 (a), Q' = 1 (b) , Q' = 1.5 (c) and Q' = 4.5 (d) liter/min.

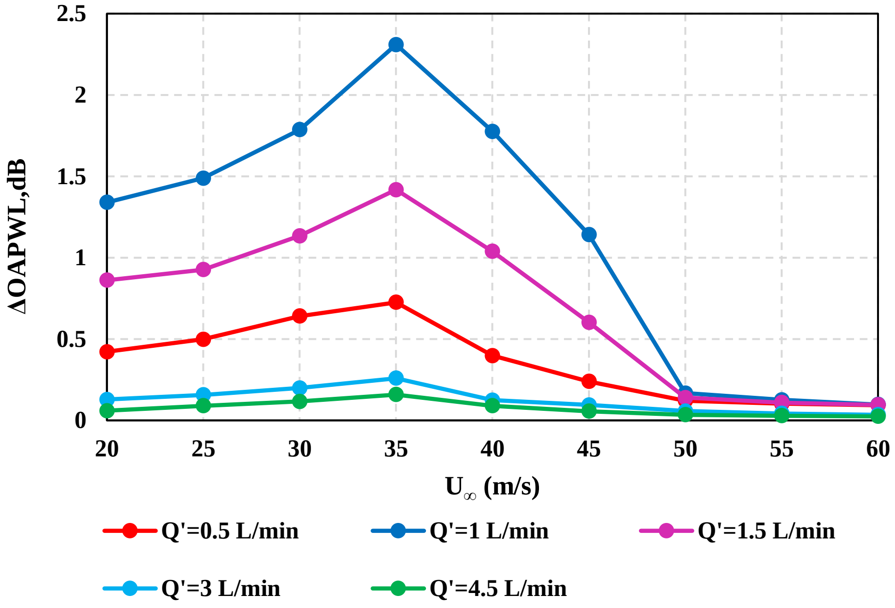

Figure 6-4: Variation of ΔOAPWL for hybrid device *λ45A30*, and different Q' at U_∞ = 20-60 m/s, α = 0° and Tu = 4.5%.

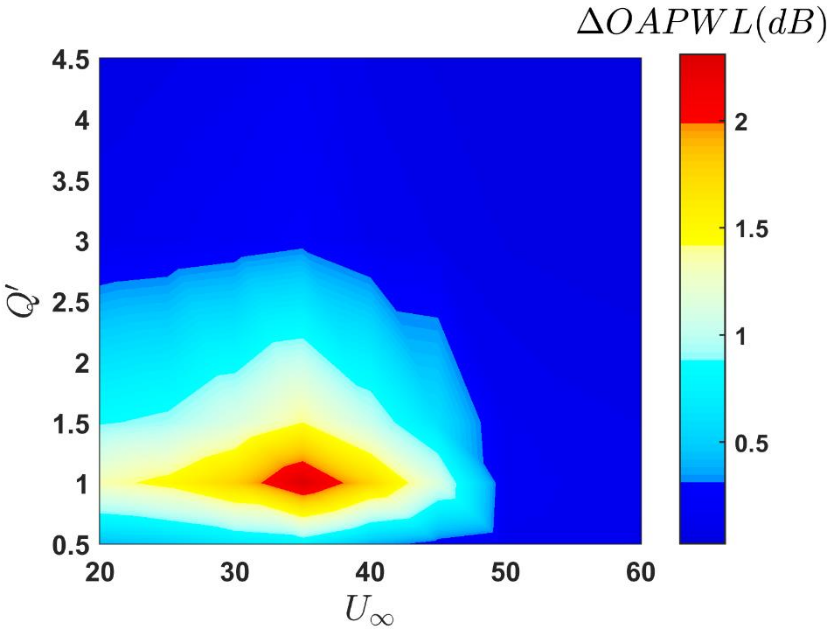

Figure 6-5: Contour map of ΔOAPWL, dB (noise reduction in the turbulence–leading edge interaction) with velocity for various Q' values, produced by the hybrid device *λ45A30*, and Tu = 4.5% at α = 0°.

6.4.1.2 Low turbulence intensities

Effect of hybrid device with different blowing rates (Q′)

Similar to the results presented in chapter 4, when the turbulence grid is removed, the main noise source switches to the trailing edge where the radiated noise will be prodominantly tonal, and is embedded with multiple discrete tones. Discussion on the mechanism can be found in chapter 4. In addition, the capability of both the passive device (serrated leading edge) and active device (blowing leading edge) to suppress this type of noise has also been demonstrated. The mechanism underpinning the reduction is due to the streamwise vortices generated by both the serration and entrained-jet, respectively. The rational is based on the assumption that the jet produced from the orifices situated at the roots and tips of the *λ45A30* serration can be entrained back to the aerofoil surface in the form of streamwise vortices. Such addition of the secondary flow structure is expected to enhance the level of suppression of the separation bubbles at the trailing edge. Thereby depriving further the viscous amplification between the Tollmien-schlichting instability and the separation bubbles. As a result, the radiated tonal noise level is expected to decrease even further.

The main objectives of this section are to identify the optimum blow rate of this hybrid device, and to investigate the sensitivity of the radiated noise subjected to the hybrid device over a range of angles of attack and velocity.

First, it is necessary to demonstrate the response of the trailing edge instability tonal noise that is subjected to serrated leading edge (*λ45A30).* Figure 6-6 compares the PWL and ΔPWL produced by the baseline (straight leading edge) and *λ45A30* (serrated leading edge). It is very clear from the figure that the instability tonal noise that is produced by the non-serrated, non-aerofoil can be suppressed effectively by the *λ45A30* serrated aerofoil.

Figure 6-7 compares the PWL and ΔPWL between the baseline (i.e. Q'= 0 liter/min) and the hybrid aerofoil with Q'= 0.5-4.5 liter/min. Several interesting trends can be found in the comparison. First, adding jet blowing at the root and tip regions for the serration can affect the noise performance of the otherwise passive device in a non-linear way. At Q'= 0.5 liter/min, the hybrid device already begains to perform better (i.e. ΔPWL > 0) across a large range of frequency up to *f*≈ 8 or 9. It becomes even better at *Q*′= 1 liter/min, before drops its performance at *Q*′= 1.5 liter/min. However, from *Q*′= 2.5 liter/min onwards, the PWL partaining to the hybrid device, and their corresponding ΔPWL, deteriorate significantly. Second, the above trend is completely opposite to the case of straight blowing leading edge instability tonal noise is proportional to the level of *Q*′.

One important aspect that needs to bear in mind is that the mere used of *λ45A30* aerofoil itself can already suppress the trailing edge instability tonal noise significantly. Because of the relatively large serration wavelength (*λ45*), for the hybrid device the total number of streamwise vortices generated by the serration will be relatively less than that with a smaller serration wavelength. For *Q*′ up to about 1.5 liter/min, it is conjectured that the extra streamwise vortices generated as a result of the blowing will help to suppress the separation bubble at the trailing edge even more, thus achieving further reduction of noise as demonstrated in Figure 6-7. However, it is not expected to further reduce the noise level by increasing the level of *Q*′ because the radiated spectra are unlikely to contain any traces of the instability noise. Rather, the increase level of the *Q*′ will produce stronger streamwise vortices where by themselves represent a new noise source when reaching the trailing edge. As a result, the stronger streamwise votices will no longer just a feature to supress the separation bubble near the trailing edge. These new mechanism is expected to be prominent at frequency up to *f*≈ 8 or 9. Beyond which, the jet noise radiated from the orifices of the hybrid device remains to be the dominant noise source.

The sensitivity of the ΔPWL by the hybrid device against the angle of attack and velocity at a range of *Q*′ is demonstrated in Figure 6-8. It can be seen that the trend observed in Figure 6-7 are largely applicable to other angles of attack and velocities up to 35 m/s. This further confirms the validity of the conjecture described earlier.

Finally, assessment of the overall acoustic performance for the hybrid device is shown in Figure 6-9 and Figure 6-10 in the form of ΔOAPWL. The OAPWL is obtained by integrating the sound power level across frequency range of 0.5 $\leq f' \leq 10$. The results only show up to Q' =1.5 liter/min as the focus is on the Q' level where further trailing edge noise reduction can still be achieved. The results folllow the expectation that the optimum Q' is the 1 liter/min and is the most effective at 30 m/s.

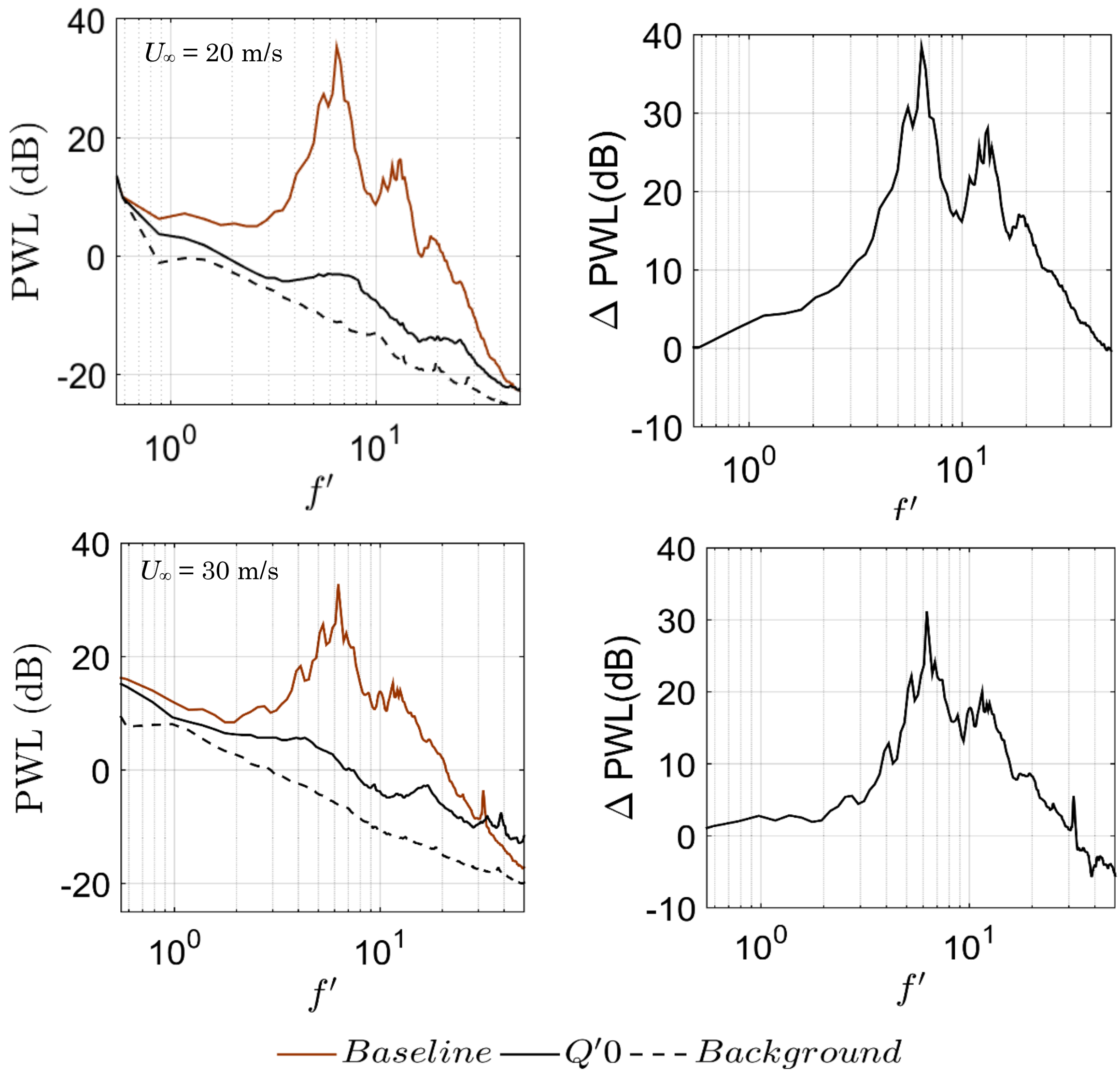

Figure 6-6: Comparison of PWL and ΔPWL as a function of normalised frequency f' produced by baseline ,serration *λ45A30* leading edges and background (black broken line) at U_∞ = 20 m/s on the top and U_∞ = 30 m/s bottom. Note that the AoA for all cases is set at α = 0° without grid Tu = 0.2%.

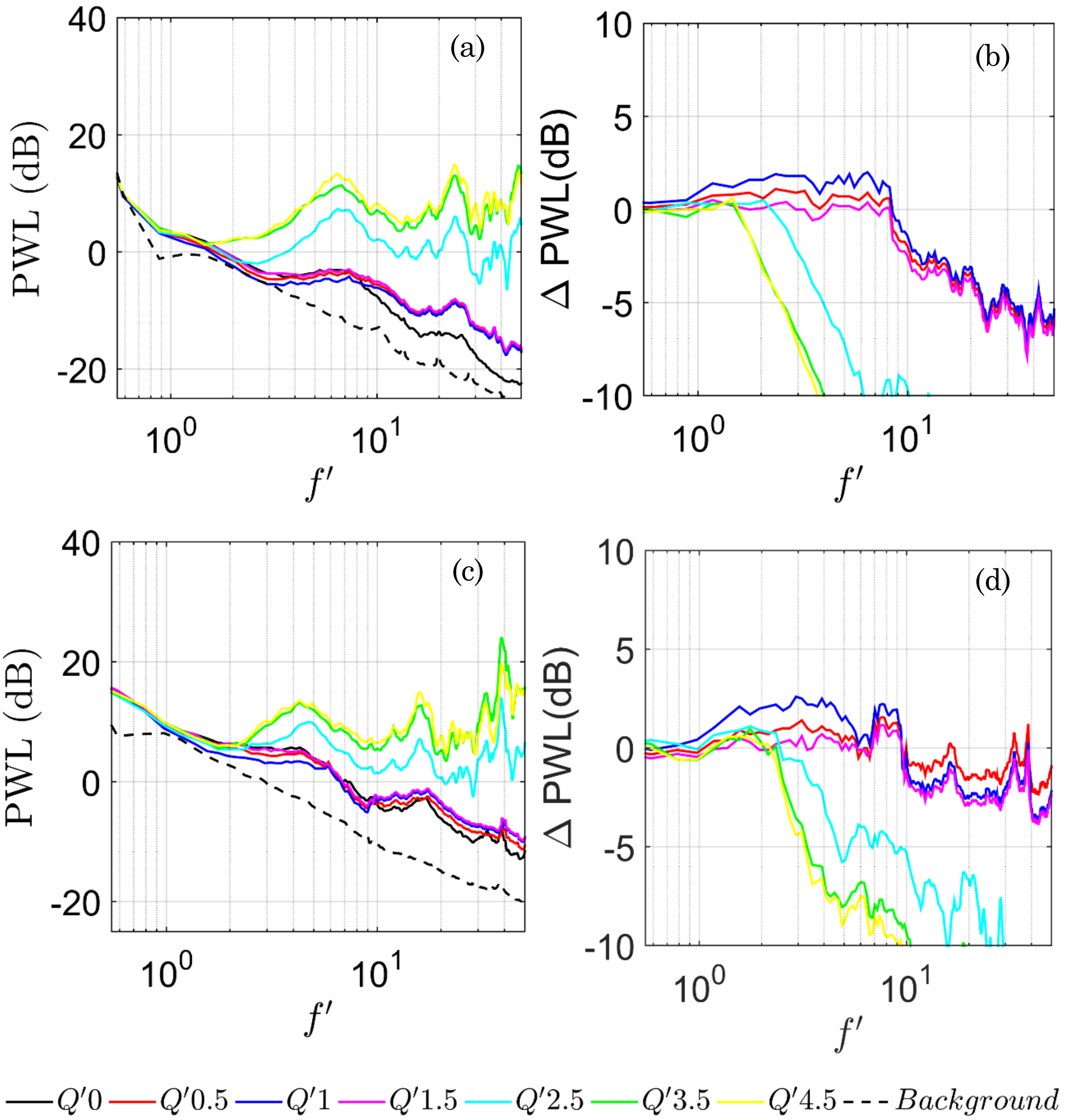

Figure 6-7: Comparison of PWL and ΔPWL as a function of normalised frequency f' produced by serration *λ45A30*, blowing leading edges and background (black broken line) at (a-b) $U_\infty = 20$ and (c-d) $U_\infty = 30$ m/s. Note that the AoA for all cases is set at $\alpha = 0°$ when $Tu = 0.2\%$.

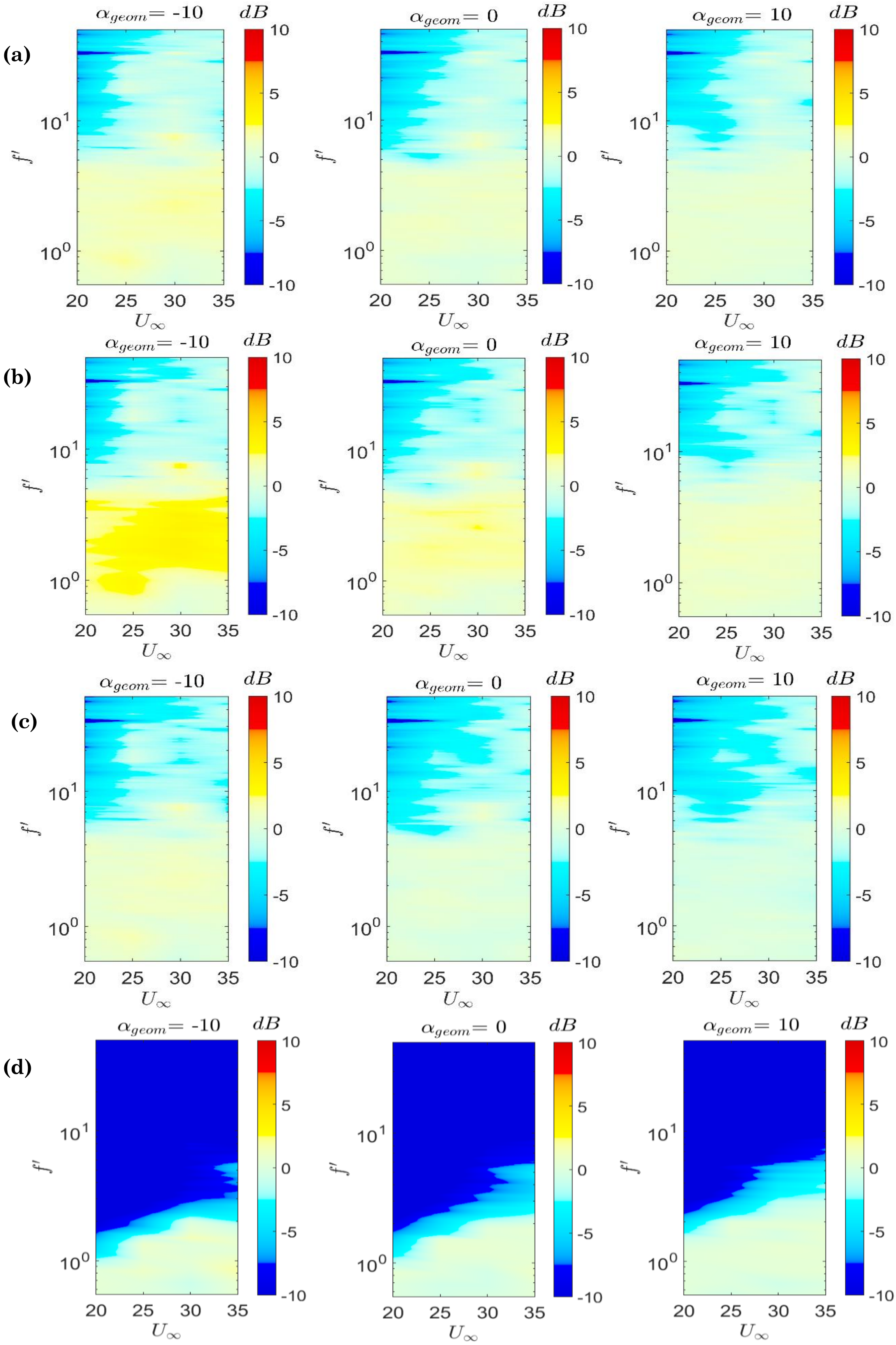

Figure 6-8: Comparison of ΔPWL as a function of normalised frequency f' produced by serration *λ45A30*, blowing leading edges and U_∞ at (α = 0 °, 10 °,-10 °) when *Tu* = 0.2 %, under *Q´* = 0.5 (a), *Q´* = 1 (b) , *Q´* = 1.5 (c) and *Q´* = 4.5 (d) liter/min.

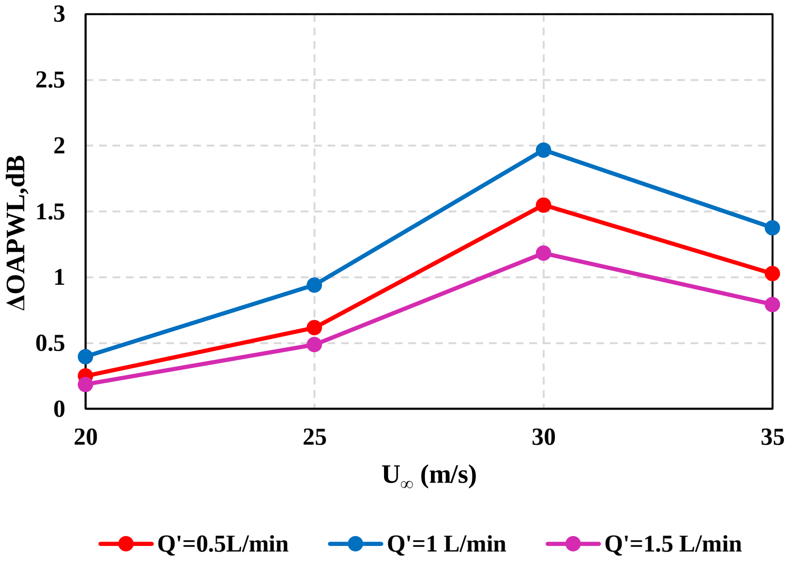

Figure 6-9: Variation of ΔOAPWL for hybrid device *λ45A30*, and different Q' at U_∞ = 20-35 m/s, $\alpha = 0°$ and $Tu = 0.2\%$.

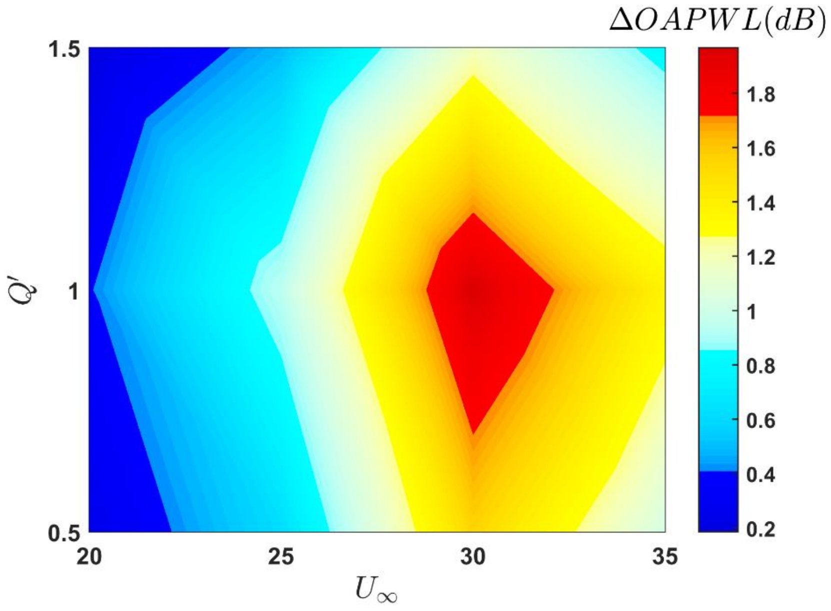

Figure 6-10: Contour map of ΔOAPWL, dB (noise reduction in the low turbulence–leading edge) with velocity for various Q′ values, produced by the serrated-blowing leading edges *λ45A30*, and $Tu = 0.2\%$ at $\alpha = 0°$.

6.4.2 Aerodynamic Results Produced by Serration-Blowing Leading Edge

Perviously, in the comparison of the lift, drag coefficients, and stall AoA, the effects of variation in serration amplitude and wavelength and the blowing rates Q' are investigated respectively. Similarly, these aerodynamic performances are investigated for the hybrid device where the serration and leading edge blowing co-exist.

The hybrid device has exactly the same configuration as the one studied for the acoustic tests described earlier. The aerodynamic performance of the hybrid device is investigated under low and high turbulence intensity turbulence inflow conditions. It is worth noting that there is an ambiguity in the description of the planform area when considering a wing with leading edge serrations. One of the popular definitions is dependent on the baseline area of the planform. It enables a direct contrast between standard rectangular and changed cut serrated leading edge geometries. With this popular concept, it is regarded the same baseline planform area as the one met with the standard rectangular wing geometry.

6.4.2.1 High Inflow Turbulence Intensities (4.5%)

This section presents the CL and CD for various types of the hybrid device at a range of AoA $-15° \leq \alpha \leq 15°$. Note that the symbol α in this section refers to the “effective” AoA, as the aerodynamic force measurements were performed in a closed-section wind tunnel with a relatively large cross-sectional area. The freestream velocity was set at 25 m/s, equivalent to the Reynolds number of 0.25×10^5 based on the aerofoil chord. Note that the planform area remains constant during the calculation for the CL and CD, irrespective of whether it is a baseline serrated, or hybrid leading edges. The CL slope (dCL/dα) is also one of the significant parameters in the description of a wing’s aerodynamic performance. The following discussion deals with the effect of blowing rate Q' on the characteristic values of CL_{max} against the AoA, as well as the lift-curve slope and post-stall behaviour. Table 6-1 summaries the results for CL_{max} and stall angle produced by $Q' = 1$, $Q' = 2$, $Q' = 3$ and $Q' = 4$ liter/min for the hybrid device with a constant amplitude of A = 30mm and wavelength λ =

45m. It can be clearly seen that the variation of blowing rate *Q′* on the hybrid device is an influencing factor for the aerodynamic performance. Lower *Q′* blowing rate can achieve an increase in CL_{max} up to 11%, as well as a delay in stall, compared with the baseline and *λ45A30* aerofoil. As shown in the table, the performance in lift generation deteorates when *Q′* increases. Therefore, similar to the aeroacoustics performance, the level of *Q′* in the hybrid configuration can either enhance or deteorates the aerodynamic performances, Figure 6-11 presents the compreison of the CL distributions against α for various combinations of *Q′*. It can be seen that lift curve attributed to the baseline leading edge largely follows the classical thin aerofoil theory, with a lift curve slope of 2π was estimated in the linear region, i.e., between $-1° \leq \alpha \leq 7°$. At $\alpha > 8°$, the aerofoil begins to stall and the CL begins to decrease. The CL at $\alpha < -6°$ does not vary significantly with an increasingly negative α. For the serrated leading edge (*λ45A30),* both the CL_{max} and stall angle are better than the baseline leading edge. The CL of the serrated leading edge is also slightly lower than the baseline at the pre-stall, positive α range for the hybrid aerofoil, a lower *Q′* is observed to achieve even better performance than the (*λ45A30)* aerofoil for the CL, CL_{max} and stall angles. The aerodynamic performance become deteorated as *Q′* increases. For the most extreme case, i.e. *Q′*=4 liter/min, there are significant losses in the CL_{max} and stall angle if compared to the *λ45A30* aerofoil. Furthermore, the level of lift curve slope for this case has been reduced to $dCL/d\alpha = 0.076$, which is significantly lower than the value close to 0.1 for the baseline.

The analysis of the CD characteristics in Figure 6-12 confirms that the hybrid device is capable of producing different performance. All curves have almost the same point of interception at zero AoA, with a value of CD = 0.033. Unlike their counter port in the CL distribution, lower CD tends to associate with largest *Q′*. This relationship remains the square across the entire angle of attack range investigated here.

Combining the results of CL and CD against α for the hybrid aerofoil, the following observations can be made:

1- At small of *Q′*, the jet leaving the orifices at the serration roots and tips will be entrained back to land on the aerofoil suction surface.

Table 6-1: Summarizes the changes produced by hybrid leading edge geometries on NACA 65(12)-10 aerofoil aerodynamic performance at high turbulent intensity (4.5%).

High turbulent intensity 4.5%			
Configuration	**Stall angle (α)**	**CL(max)**	**ΔCL(max)**
Baseline	9	1.28	reference
λ45A30	12	1.32	0.04
Q′1	13	1.43	0.15
Q′2	12	1.38	0.10
Q′2.5	11	1.31	0.03
Q′3	10	1.21	-0.07
Q′3.5	9	1.15	-0.13
Q′4	8	1.09	-0.19
Q′4.5	8	1.04	-0.24

2- These-entrained jets will form streamwise vortices and propagate all the way down to the trailing edge. If there is a separation bubble, the streamwise vortices generated by the jet will help to suppress it. As a result, the CL performance will be improved, as well as the stall angle. These streamwise vortices by themselves do not contribute in the generation of CD too significantly.

At high level of Q', the jet leaving the orifices at the serration roots and tips will not be entrained back. Rather, they will continue to oppose the incoming flow until fully dissipated. During the process, leading edge stagnation point could be altered, thereby producing a new flow circulation around the aerofoil. Although it remains a conjecture, it is reasonable to believe that the change in circulation reduces the pressure leading on the aerofoil surface and violated the classic thin aerofoil theory. Therefore at high level of the Q' the deviations of CL and CD from those produced by a baseline aerofoil become significant.

Figure 6-13 shows the blow rate (Q' effect in performance in terms of ΔCL (CL_{hybrid} –$CL_{Baseline}$); it can be seen that where there is a decrease in blow rate, an increase in performance generally occurs. Figure 6-13 gives a clearer understanding of the hybrid leading edge performance across the range of the angle of attack. The profile shows a discontinuity of ΔCL between α = 1-10°, which refers to the pre-stall region. This emphasises that the hybrid leading edge produces the largest impact in the post-stall region, whilst maintaining the CL performance in the pre-stall region.

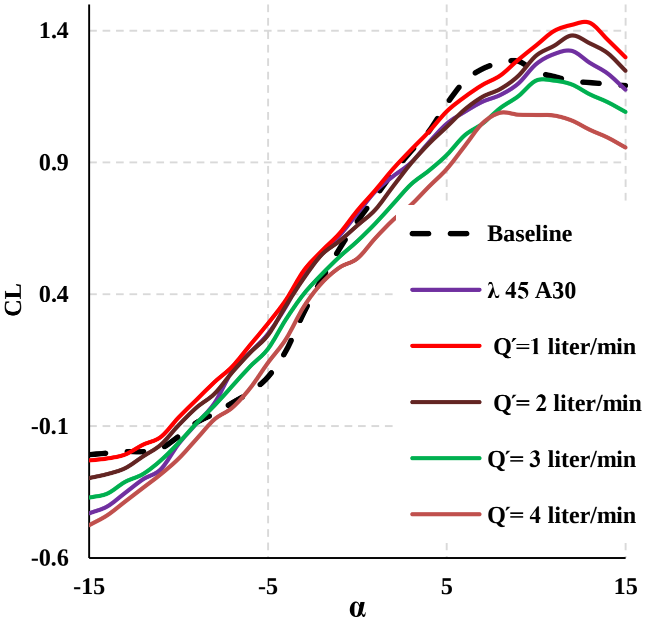

Figure 6-11: Lift coefficient curve at the case of U_∞ = 25 m/s, corresponding to Tu = 4.5 %, produced by the hybrid leading edges when blowing at a range of 1-4 liter/min.

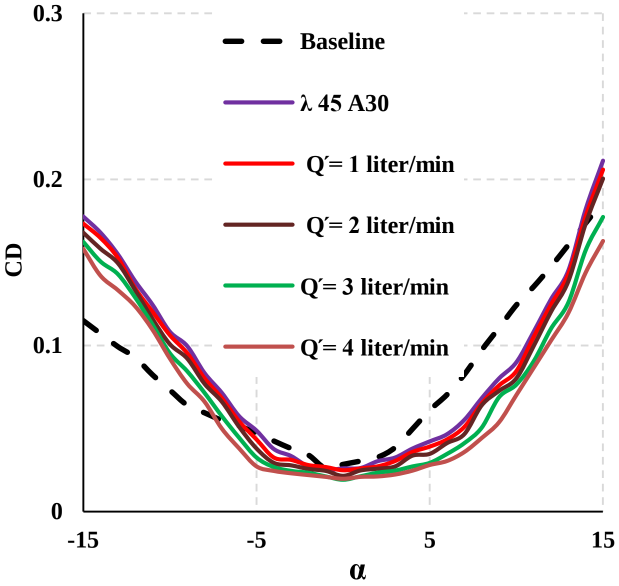

.

Figure 6-12: Drag coefficient curve at the case of U_∞ = 25 m/s, corresponding to Tu = 4.5 %, produced by the hybrid leading edges when blowing at a range of 1-4 liter/min.

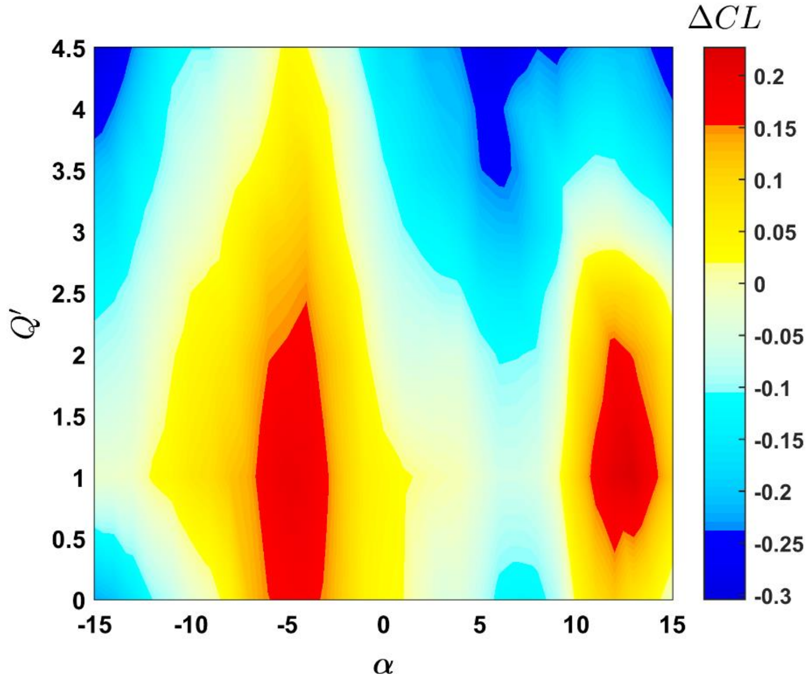

Figure 6-13: Contour maps of ΔCL at different AoA (α) at the case of U_∞ = 25 m/s, corresponding to Tu = 4.5%, produced by the hybrid leading edges when blowing at a range of 1-4.5 liter/min.

6.4.2.2 Low Turbulence Intensities (0.2%)

In addition to the investigation of the aerodynamic measurements, the results of the aerodynamic measurements, including lift and drag coefficients for the NACA65(12)-10 aerofoil at low turbulent intensity Tu = 0.2%, are presented and discussed. The objective of this experiment is to identify the effects of hybrid device compared to the baseline case. Therefore, the baseline leading edge acts as a reference case in this research. Figure 6-14 presents the results of lift coefficients for the aerofoil with hybrid device leading edge over the AoA range of -15°≤ α ≤15°, and the same velocity used in pervious section as Reynolds number of 0.25 x 10^5. Results are presented for hybrid device with different blowing rates of Q' = 1 liter/min, Q' = 2 liter/min Q' = 3 liter/min and Q' = 4 liter/min, with a constant wavelength λ/C = 0.3 of and amplitude A/C = 0.2. The aim of this comparison is to provide information on how the hybrid device influences the lift coefficient in the designated AoA range. The baseline leading edge acts as a reference for the observation of aerodynamic performance of the different leading edges. According to equation 3-20 (see

Table 6-2), this would lead to a higher CL (up to 9%), depending on the blowing rates. In the following passage the lift curved is analysed. The results show individual post-stall characteristics for each blowing rate (Q') and indicate a clear tendency in slope $dCL/d\alpha$ characteristics. The CL_{max} vary with various patterns. It can be seen that larger blowing rate decreases the slope up to 24% and lowers the maximum CL up to 9.6%, while the smaller blowing rate Q' = 1 liter/min experiences a sharp stall and unsteady post-stall behaviour; smaller blow rate shows a significant increase in the maximum stall angle. The hybrid device leading edge Q' = 4 liter/min (highest blowing rate) affects the curve progression by delaying the stall angle up to 7°, with lower lift coefficient (CL = 0.995) and smoother stall characteristics compared to the untreated NACA65(12)-10.

The conclusion that can be drawn from these findings is that the application of hybrid device significantly delays the stall flow field, while reducing the lift coefficient. Thus, lower blowing rate achieves the highest stall, and shows decent behaviour after CL_{max}. Larger blowing rate leads to a high loss in lift, and causes unsteady post-stall performance.

The analysis of the CD characteristics for the serrated-blowing rate (Figure 6-15) confirms the constant influence of the blowing rate (Q'). All curves have the same point of interception at zero AoA with a value of CD = 0.031. The single curves are slightly tilted anticlockwise with increasing blowing rate. While the smallest blow rate Q' = 1 liter/min shows high drag at positive range AoA, higher blow rate causes a lower drag in the positive AoA range, and reduced drag in the negative AoA range (by up to 41% compared to the baseline LE). The drag increase in the post-stall area is particularly noticeable. On the other hand, the CD value decreases in the lower range of AoA (1-8°) for higher blow rates (more than 2 liter/min).

The results of the experimental drag data indicate that the hybrid device have a good impact on CD, and lead to a shift in the curve progression. The experimental results are summarised in Table 6-2.

Table 6-2: Summary of changes produced by hybrid device geometries on NACA 65(12)-10 aerofoil aerodynamic performance at low turbulent intensity (0.2%).

Low turbulent intensity 0.2%			
Configuration	**Stall angle (α)**	**CL(max)**	**ΔCL(max)**
Baseline	8	1.24	reference
λ45A30	11	1.25	0.01
Q′1	12	1.34	0.10
Q′2	11	1.29	0.05
Q′2.5	10	1.22	-0.02
Q′3	9	1.14	-0.10
Q′3.5	8	1.07	-0.17
Q′4	8	1.03	-0.21
Q′4.5	7	1	-0.24

Lower lift coefficients are noted when the incoming flow is of low turbulence intensity. However, it can be observed that when the freestream turbulence intensity is low, the CL distributions of hybrid device are less accurate compared to those under high turbulence intensity.

Figure 6-16 illustrates the blow rate effect on performance in terms of ΔCL ($CL_{hybrid}–CL_{Baseline}$). It can be seen that a reduction in blow rate is associated with increased performance. The leading edge flow separation for smooth configuration anticipates a drop in turbulent intensity, thereby avoiding increased trailing edge separation during the pre-stall stage. Thus, minimizing the blow rate influence in increasing flow separation at the trailing edge has the advantage of increasing ΔCL caused by the three-dimensional bubble mechanism in the post-stall area (Figure 6-14). To confirm the measured lift ratio and to enhance the understanding of the ΔCL, the resulting profile shows a standard deviation with relatively high homogeneity. Conversely, the profile still shows deviation along the vertical direction, especially at α = 3-4° where a drop of the ΔCL occurs. These contours show that for the serrated-blowing configurations studied there is an optimum blow rate-to-AoA relationship. The biggest difference in the lift coefficient between the baseline and hybrid aerofoil ΔCL = 0.1829 was produced at $\alpha = -5°$, and the lowest ΔCL = -0.289 was produced at the AoA α

= -15°. In summary, serrated edge with low blow rate is beneficial for aerodynamic lift, the delay in stall AoA can be noticed. The flow jet from the orifices will be backed to surface of the aerofoil these will be formed a separation bubble the jets will help to suppress it, therefore CL performance will be increased and the stall angle of attack will be enhanced. However, at high blow rate jet will be opposed the incoming flow until fully dissipated.

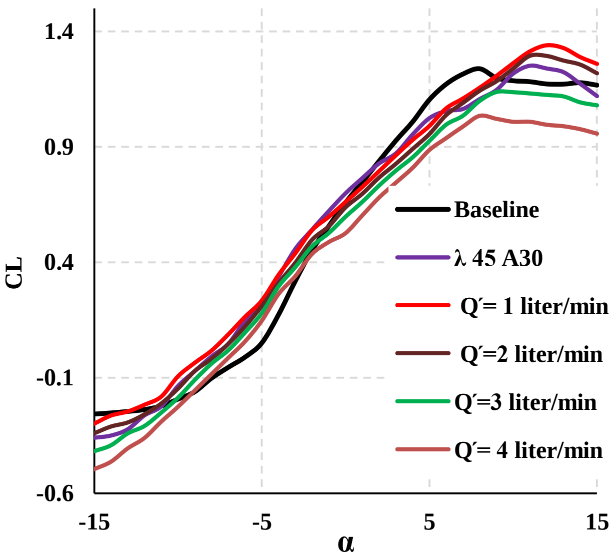

Figure 6-14: Lift coefficient curve at the case of U_∞ = 25 m/s, corresponding to Tu = 0.2 %, produced by the hybrid leading edges when blowing at a range of 1-4 liter/min.

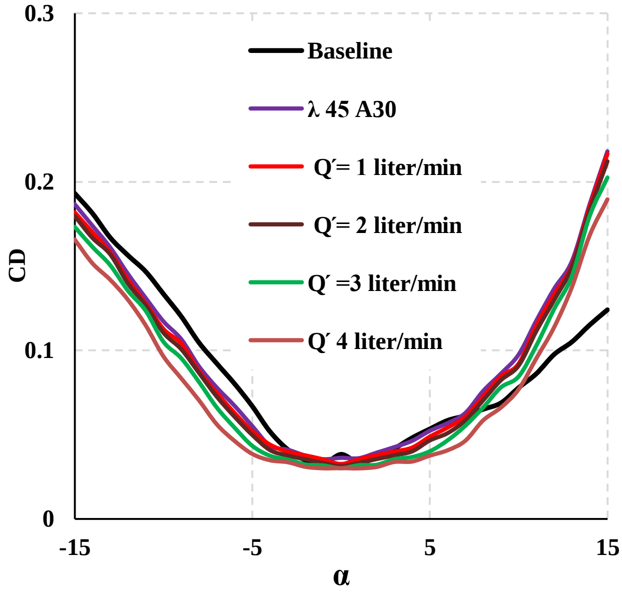

Figure 6-15: Drag coefficient curve at the case of U_∞ = 25 m/s, corresponding to Tu = 0.2 %, produced by the hybrid leading edges when blowing at a range of 1-4 liter/min.

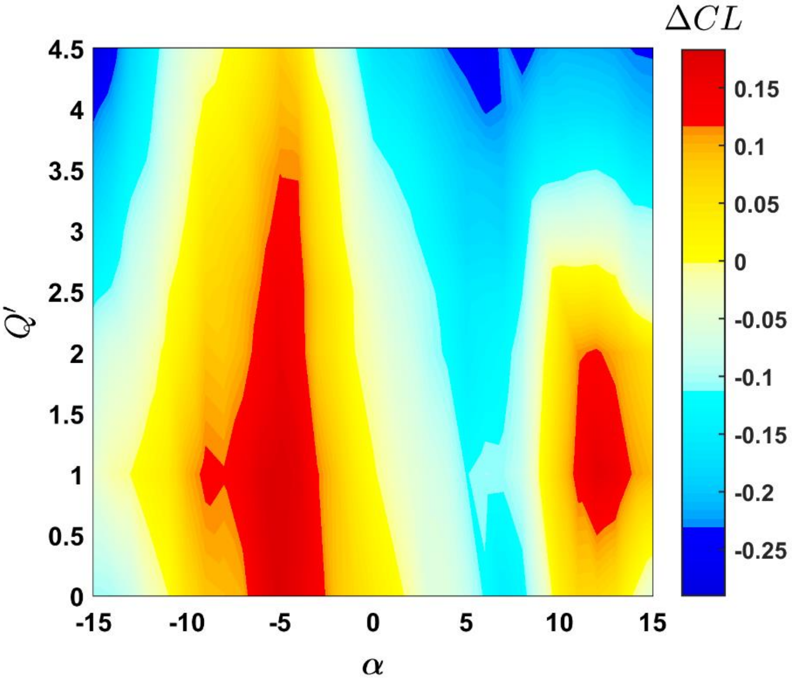

Figure 6-16: Contour maps of ΔCL at different AoA (α) at the case of U_∞ = 25 m/s, corresponding to Tu = 0.2%, produced by the hybrid leading edges when blowing at a range of 1-4.5 liter/min.

Chapter 7 : Conclusions and Future Work

7.1. Introduction

This thesis presents results of a study on the application of leading edges serration as a passive flow-control device, blowing as a active flow-control and both active and passive (hybrid) flow control for enhancing aerofoil performance aerodynamic and aeroacoustic depends strongly on the level of turbulence intensity (4.5%) at the high and used the low turbulence intensity (0.2%). The aim of this study was to describe the influence of blowing, serrated and serrated-blowing leading edges on aerofoil performance and on the streamwise flow pattern downstream of the edges and . Therefore an aerodynamic study was conducted where eight different leading edges of a NACA65(12)-10 aerofoil were tested in an open-circuit suction type wind tunnel to gain more information about the aerodynamic characteristics.

7.2. Conclusions overview

Firstly, the thesis presented a detailed investigation in the behaviour of the aerofoil noise, injection of mass flow from the leading edge (against the incoming flow) could potentially be an effective mechanism to decrease the turbulence intensity, hence the level of turbulence–leading edge interaction noise radiation. After the injection of air from the leading edge and mixed with the incoming flow, the mass flow can be entrained back and propagated as streamwise vortices in the downstream direction along the aerofoil surface. These streamwise vortices generated indirectly as a result of the leading edge blowing could also be effective in the suppression of boundary layer separation. On the other hand, leading edge serration is now a well-established effective passive control device for the reduction of turbulence–leading edge interaction noise and suppression of boundary layer separation, also resulting in the reduction of instability tonal noise. The aeroacoustics performance of a NACA 65(12)-10 aerofoil subjected to leading edge blowing. The inflow conditions were set at low and high turbulence intensity at the freestream, creating two mechanisms for the aerofoil noise radiation (trailing edge noise and leading noise, respectively). It was found that leading edge blowing can be very effective to reduce these two different noise sources, but the requirement in the optimal blowing rate and spanwise concentration of the orifices will be different. It is envisaged that leading edge blowing, an active flow control approach, could produce the same mechanisms as those produced by a serrated leading edge to enhance the aerodynamic and aeroacoustics performances of aerofoil. An explicit relationship between the A and Q', as well as for the aerodynamic performance low blow rate and low spanwise concentration of orifices are the effective configuration to inhibit the boundary layer separation at large angle of attack, increase the stall angle, increase the lift coefficient and reduce the drag coefficient. Aeroacoustically, it can also be concluded at this chapter that there exists a correlation between the A and Q' for the noise reduction. Unlike the serration counterpart, the effectiveness of the leading edge noise reduction by blowing is found to be very sensitive to the choice of Q', and to some extents, λ' as well. Nevertheless, it can be confirmed that the serration effect on aerofoil can be mimicked by leading edge blowing. Further studies are necessary to fully establish the sensitivities of ΔPWL, as well as the change in lift and drag coefficients, to the (λ, A) and (Q', λ'). The concept of the leading edge blowing is to minimise the interaction of an incoming turbulent flow with the leading edge of the aerofoil. Through blowing, the leading edge jet continuously opposes, and possibly dissipates the incoming turbulent eddies by either displacing the leading edge stagnation point of the aerofoil, or creating a "buffer zone" over the region around the aerofoil leading edge. It seems that one, or possibly both of these mechanisms could be very sensitive to the blowing volume flow rate, which is related to the exit jet velocity, ΔPWL as high as 9 dB can be achieved by one of the leading edge blowing configurations when λ'=5mm and Q'=1 liter/min. However for low turblent intensity the noise is sensitive to the straight blowing of the leading edge in the high frequency range, which suggests thus clearly that spanwise hole air on the leading edge can reduce the trailing edge noise. Reductions in tonal noise of up to 18.5 dB can be achieved by the $\lambda' = 5$ mm, which are comparable to those obtained with large λ'=10mm is about 5dB at 30 m/s, the level of noise reduction incresed with increasing velocity and reduced the spanwise hole air on the leading edge from 10 to 5mm. This effect is certainly due to modification to the boundary layer caused by the leading edge blowing.

The inflow conditions were set at low and high turbulence intensity at the freestream, creating two mechanisms. It was found that leading edge blowing can be very effective to reduce drag and enhancement lift, but the requirement in the optimal blowing rate and spanwise concentration of the orifices will be different.

There is an explicit relationship between A and Q', as well as λ and λ', for the aerodynamic lift and drag coefficients across a wide range of AoA. Aerodynamically, low blow rate and low spanwise concentration of orifices are the most effective configuration to inhibit the boundary layer separation at large angle of attack, increase stall angle, increase lift coefficient, and reduce drag coefficient.

Secondly, chapter six presents the aeroacoustic results of a NACA65(12)-10 hybrid devices. In particular, the (hybrid) serrated-blowing leading edge *Q′1* with holes inserts around serrated represent the core of investigation. The noise measurements at high and low turbulent intensity, as well as the speed flow measurement on the leading edge, were executed inside an aeroacoustic wind tunnel. The use of *λ45A30* hybrid device will result in sound power level reduction of the noise up to 3.7 dB for low turbulent intensity. However, the jet noise from the air holes becomes dominant and overtakes the aerofoil noise. As a result, negative value of ΔPWL (i.e. noise increase), especially for the Q'=4.5 liter/min case. Adding jet blowing at the root and tip regions for the serration can affect the noise performance of the otherwise passive device in a non-linear way. At Q'= 0.5 liter/min, the hybrid device already begains to perform better (i.e. ΔPWL > 0) across quite a large range of frequency up to $f \approx$ 8 or 9. It becomes even better at Q'= 1 liter/min, before drops its performan at Q'= 1.5 liter/min. Furthermore, from Q'= 2.5 liter/min onwards, the PWL partaining to the hybrid device, and their corresponding ΔPWL, deteriorate significantly, the above trend is completely opposite to the case of straight blowing leading edge instability tonal noise is proportional to the level of Q'.

On the other hand, the sound power level reduction of the noise up to 4 dB for high turbulent intensity when the velocity reach to 35 m/s. There is a good aerodynamic performance if these hybrid device are integrated to the aerofoil body. A trend discernible from the current results is that the *Q′*=1 liter/min hybrid leading edge (with a low blowing rate) performs better aerodynamically and acoustically than the *Q′*=4 liter/min counterpart. And the studied the effect of turbulent intensity on the aerodynamic performance. For all the leading edge device experimented, one main groups can be created depended on the noise performances. The group (*Q′0.5, Q′1* and *Q′1.5*) is characterized by a hybrid device and every member within this case consistently established a significant trailing edge noise reduction at low turbulent intensity. The second case (*Q′0.5, Q′1* and *Q′1.5*), where every member within this case uses a hybrid, offers benefit on the noise reduction at high turbulent intensity even though it shares the same parameters of the first case. This can be explained by the turbulence's acoustic efficiency on a hybrid device (serration-blowing). In chapter six deals with a hybrid concept wher the jet orifice were placed at the root and tip regions of the serration. The premises of this configuration are:

A- Jet produced at the roots (as well as at the tips) can further reduce the level of interaction with the inflow turbulence.

B- Jet produced at the tips (and/or the roots) can increase the number of streamwise vortices, thereby enhance the level of suppression of separation bubble to achieve a greater level of instability tonal noise reduction.

7.3. Future work

The definition of blowing leading edges could further be developed to improve the technological willingness level. A viable path for the continuation of the work is a parametric analysis of different the serration geometries and various blowing rates for leading and trailing edges. The suggestions for future work are outlined below:

1- Design and test a straight blowing leading edge and serrated trailing edge and study the combined effect for quieter low noise aerofoils and aerodynamic performance at high and low turblent intensity.

2- Design and test a serrated blowing leading edge for different wavelengthes λ and amplitudes A with straight and sawtooth trailing edge for the reduction of trailing edge noise and aerodynamic performance. More precisely, the serration angle (φ) and the serration length (2h) are changed where S1, S2 and S3 share the same 2A=20mm) but differ in φ (=7°,12° and 25° respectively) and one baseline straight trailing edge S0.

3- Turbulence and noise produced by a wing section inserted in the wake of a cylindrical rod are changed by adding blowing close the aerofoil's leading edge.

4- Design and test trailing edge blowing Influences on the performance and noise reduction of a propeller. In order to provide a better performance.

5- Develop a mixed leading and trailing edge blowing for slower low noise aerofoils.

6- Apply CFD techniques to better understand the noise reduction process of the leading edge geometries suggested in this thesis.

7- Measurements in the near wake of the aerofoil showed the structure of the counter-rotating vortices. It was possible to illustrate the single velocity components of these vortices and get an understanding of the mode of operation.

8- The ability of these flow structures to reduce tonal noise at the trailing edge is left for future work.

9- In future studying, The angle in which the jets exit may be significant parameter to optimise.

10- Replicate the experiment with tandem aerofoil on a rotating fan device by adjusting the fan blade's trailing edge and the front of the outlet guide vannes (OGV).

11- Measurements of the unsteady surface-pressure on both sides of a blowing-serration would be useful to study the validity of the Kutta condition on the leading edge in the presence of blowing, so that a noise-reduction mechanism can be established defnittively.

References

[1] European Commission, 2012. Research & Innovation Transport ACARE Goals Progress Evaluation. [Online] Available at: http://ec.europa.eu/research/transport/projects/items/agape_en.htm [Accessed 12 07 2016].

[2] ACARE, 2015. Annual Report, Activity Summary 2014-15, s.l.: Advisory Council for Aviation Research and Innovation in Europe.

[3] European Commission, 2011. “Flightpath 2050. Europe’s Vision for Aviation, ” Luxembourg: Report of the High Level Group on Aviation Research, Publications Office of the European Union.

[4] Oerlemans, S., 2011. “Wind turbine noise: primary noise sources”, s.l.: National Aerospace Laboratory NLR.

[5] Schmitt, O. H., 1969. “Some interesting and useful biomimetic transforms”. Proc. 3rd Int. Biophysics Congress, Boston, MA: p. 297.

[6] Galvez, D.J., 2018. “Owl Inspired Leading Edge Serrations for Gliding Flight” (Doctoral dissertation, Mississippi State University).

[7] Fish, F. E. & Battle, J. M., 1995. “Hydrodynamic Design of the Humpback Whale Flipper, ” s.l.: Journal of Morphology Vol. 225, No. 1.

[8] Jude Hislop, 2017. “Humpback whale flippers inspire Canadian design of highly efficient wind turbine blade,” Progress Evaluation. [Online] Available at: https://energi.media/innovation/canadian-inventors-turbine-humpback-whales-increasing-wind-efficiency/

[9] Astley, R.J., Agarwal, A., Joseph, P.F., Self, R.H., Smith, M.G., Sugimoto, R. and Tester, B.J., 2007. “Predicting and reducing aircraft noise,” In 14th International Congress on Sound and Vibration..

[10] Amiet, R.K., 1975. “Acoustic radiation from an airfoil in a turbulent stream”. Journal of Sound and vibration, 41(4), pp.407-420.

[11] Clair, V., Polacsek, C., Le Garrec, T., Reboul, G., Gruber, M. and Joseph, P., 2013. “Experimental and numerical investigation of turbulence-airfoil noise reduction using wavy edges”. AIAA journal, 51(11), pp.2695-2713.

[12] Narayanan, S., Chaitanya, P., Haeri, S., Joseph, P., Kim, J.W. and Polacsek, C., 2015. “Airfoil noise reductions through leading edge serrations”. Physics of Fluids, 27(2), p.025109.

[13] Kim, J.W. and Haeri, S., 2015. An advanced synthetic eddy method for the computation of aerofoil–turbulence interaction noise. Journal of Computational Physics, 287, pp.1-17.

[14] Kim, J.W., Haeri, S. and Joseph, P.F., 2016. On the reduction of aerofoil–turbulence interaction noise associated with wavy leading edges. Journal of Fluid Mechanics, 792, pp.526-552.

[15] Johari, H., Henoch, C.W., Custodio, D. and Levshin, A., 2007. “Effects of leading-edge protuberances on airfoil performance,” AIAA journal, 45(11), pp.2634-2642.

[16] Miklosovic, D.S., Murray, M.M., Howle, L.E. and Fish, F.E., 2004. “Leading-edge tubercles delay stall on humpback whale (Megaptera novaeangliae) flippers”. Physics of fluids, 16(5), pp.L39-L42.

[17] Hansen, K.L., 2012. “Effect of leading edge tubercles on airfoil performance” (Doctoral dissertation).

[18] Skillen, A., Revell, A., Pinelli, A., Piomelli, U. and Favier, J., 2014. Flow over a wing with leading-edge undulations. Aiaa Journal, 53(2), pp.464-472.

[19] Cattafesta, L., Bahr, C. and Mathew, J., 2010. “Fundamentals of wind-tunnel design”. Encyclopedia of Aerospace Engineering.

[20] Cebeci, T. and Cousteix, J., 2005. “Modeling and Computation of Boundary-Layer Flows”, Long Beach.

[21] Gad-el-Hak, M., 1990. Control of low-speed airfoil aerodynamics. AIAA journal, 28(9), pp.1537-1552.

[22] Lin, J.C., 2002. Review of research on low-profile vortex generators to control boundary-layer separation. Progress in Aerospace Sciences, 38(4-5), pp.389-420.

[23] Godard, G and Stanislas, M 2006, “Control of a decelerating boundary layer. Part 1: optimization of passive vortex generators,” Aerospace Science and Technology, 10, pp. 181–191.

[24] Lin, J., Howard, F. and Selby, G., 1991, January. “Exploratory study of vortex-generating devices for turbulent flow separation control,” In 29th aerospace sciences meeting (p. 42).

[25] Kuethe, A.M., 1972. “Effect of streamwise vortices on wake properties associated with sound generation,” Journal of Aircraft, 9(10), pp.715-719.

[26] Soderman, P.T., 1972. “Aerodynamic effects of leading-edge serrations on a two-dimensional airfoil,”.

[27] Thompson, D.H., 1997. “Effect of the Leading-Edge Extension (LEX) Fence on the Vortex Structure over the F/A-18 (No. DSTO-TR-0489),” DEFENCE SCIENCE AND TECHNOLOGY ORGANIZATION CANBERRA (AUSTRALIA).

[28] Lee, B.H., Brown, D., Zgela, M. and Poirel, D., 1990. "Wind tunnel investigation and flight tests of tail buffet on the CF-18 aircraft," NATIONAL AERONAUTICAL ESTABLISHMENT OTTAWA (ONTARIO).

[29] Simons, M., 1999. "Model Aircraft Aerodynamic: London," Special interest model books.

[30] Werle, M.J., ATERSON, R. and Resz, W.M., 1987. "Trailing-edge separation/stall alleviation," AIAA journal, 25(4), pp.624-626.

[31] Zverkov, I. . Zanin, B. and Kozlov, V., 2008. "Disturbances growth in boundary layers on classical and wavy surface wings," AIAA journal, 46(12), pp.3149-3158.

[32] Meyer, R., Bechert, D.W. and Hage, W., 1999. "Wind tunnel experiments with artificial bird feathers for passive separation control on airfoils," In IUTAM Symposium on Mechanics of Passive and Active Flow Control (pp. 99-100). Springer, Dordrecht.

[33] Anderson, G.W., 1973, "An experimental investigation of a high lift device on the owl wing," (No. GAM/AE/73-6). AIR FORCE INST OF TECH WRIGHT-PATTERSON AFB OH SCHOOL OF ENGINEERING.

[34] Carpenter, P. and Garrad, A.D., 1986, "The hydrodynamic stability of flow over Kramer-type compliant surfaces. Part 2. Flow-induced surface instabilities," Journal of Fluid Mechanics, 170, pp.199-232.

[35] Gaster, M., 1988, "Is the dolphin a red herring?," In Turbulence management and relaminarisation (pp. 285-304). Springer, Berlin, Heidelberg.

[36] Gad-el-Hak, M., 2000, "Flow Control, passive, active and reactive management," Cambridge University Press, 11, pp.17-26.

[37] Carpenter, P.W., Davies, C. and Lucey, A.D., 2000, "Hydrodynamics and compliant walls: Does the dolphin have a secret?," Current Science, pp.758-765.

[38] Bar-Sever, A., 1989, "Separation control on an airfoil by periodic forcing," AIAA journal, 27(6), pp.820-821.

[39] Vakili, A.D. and Gauthier, C., 1994, "Control of cavity flow by upstream mass-injection," Journal of Aircraft, 31(1), pp.169-174.

[40] Bueno, P., Unalmis, O., Clemens, N. and Dolling, D., 2002, December. The effects of upstream mass injection on a Mach 2 Cavity Flow. In 40th AIAA Aerospace Sciences Meeting & Exhibit (p. 663).

[41] Zhuang, N., Alvi, F.S., Alkislar, M.B. and Shih, C., 2006. Supersonic cavity flows and their control. AIAA journal, 44(9), pp.2118-2128.

[42] Ukeiley, L., Sheehan, M., Coiffet, F., Alvi, F., Arunajatesan, S. and Jansen, B., 2008. Control of pressure loads in geometrically complex cavities. Journal of Aircraft, 45(3), pp.1014-1024.

[43] Arunajatesan, S., Kannepalli, C., Sinha, N., Sheehan, M., Alvi, F., Shumway, G. and Ukeiley, L., 2009. Suppression of cavity loads using leading-edge blowing. AIAA journal, 47(5), pp.1132-1144.

[44] Khurana, K.C., 2009. Aviation management: global perspectives. Global India Publications.

[45] Orlady, H., 2017. Human factors in multi-crew flight operations. Routledge.

[46] Swatton, P.J., 2011. Principles of flight for pilots (Vol. 42). John Wiley & Sons.

[47] Torenbeek, E., 2013. Synthesis of subsonic airplane design: an introduction to the preliminary design of subsonic general aviation and transport aircraft, with emphasis on layout, aerodynamic design, propulsion and performance. Springer Science & Business Media.

[48] Koumoutsakos, P and Mezic, I 2006, Control of fluid flow, Springer-Verlag, Berlin.

[49] Gilarranz, J.L., Traub, L.W. and Rediniotis, O.K., 2002. Characterization of a compact, high-power synthetic jet actuator for flow separation control. In AIAA Aerospace Sciences Meeting & Exhibit, 40 th, Reno, NV.

[50] Tuck, A. and Soria, J., 2004, December. Active flow control over a NACA 0015 airfoil using a ZNMF jet. In 15th Australasian fluid mechanics conference (pp. 13-17).

[51] Dingle, L., Tooley, M. (2005) - Aircraft Engineering Principles, pp. 541-593, Butterworth Heinemann, ISBN 0-7506-5015-X, Oxford.

[52] Gad-el-Hak, M., 1990. Control of low-speed airfoil aerodynamics. AIAA journal, 28(9), pp.1537-1552.

[53] Johnson, S.J. and Berg, D.E., 2008. Active load control techniques for wind turbines.

[54] Khan, ZU and Johnson, JP 2000, “On vortex generating jets,”International Journal of Heat and Fluid Flow, 21, pp. 506-511.

[55] Compton, D.A. and Johnston, J.P., 1992. Streamwise vortex production by pitched and skewed jets in a turbulent boundary layer. AIAA journal, 30(3), pp.640-647.

[56] Seifert, A., Bachar, T., Koss, D., Shepshelovich, M. and Wygnanskil, I., 1993. Oscillatory blowing: a tool to delay boundary-layer separation. AIAA journal, 31(11), pp.2052-2060.

[57] Huang, L., Maestrello, L. and Bryant, T., 1987, June. Separation control over an airfoil at high angles of attack by soundemanating from the surface. In 19th AIAA, Fluid Dynamics, Plasma Dynamics, and Lasers Conference (p. 1261).

[58] Hsiao, F.B., SHYU, J.Y. and LIU, C.F., 1990. Control of wall-separated flow by internal acoustic excitation. AIAA journal, 28(8), pp.1440-1446.

[59] Ahuja, K. and Burrin, R., 1984. Control of flow separation by sound. In 9th Aeroacoustics Conference (p. 2298).

[60] Corke, T., Jumper, E., Post, M., Orlov, D. and McLaughlin, T., 2002, January. Application of weakly-ionized plasmas as wing flow-control devices. In 40th AIAA Aerospace Sciences Meeting & Exhibit (p. 350).

[61] Goeksel, B, Rechenberg, I, Greenblatt, D and Paschereit, C 2006, "Steady and unsteady plasma wall jets for separation and circulation control," Presented at 3rd AIAA Flow Control Conference, San Francisco, AIAA paper number 2006-3686.

[62] Wilkinson, S.P., 2003. Investigation of an oscillating surface plasma for turbulent drag reduction.

[63] Corke, T.C., Enloe, C.L. and Wilkinson, S.P., 2010. Dielectric barrier discharge plasma actuators for flow control. Annual review of fluid mechanics, 42, pp.505-529.

[64] Enloe, C.L., McLaughlin, T.E., Van Dyken, R.D., Kachner, K.D., Jumper, E.J. and Corke, T.C., 2004. Mechanisms and responses of a single dielectric barrier plasma actuator: plasma morphology. AIAA journal, 42(3), pp.589-594.

[65] Corke, T. and Post, M., 2005, January. Overview of plasma flow control: concepts, optimization, and applications. In 43rd AIAA Aerospace Sciences Meeting and Exhibit (p. 563).

[66] Grundmann, S, Frey, M and Tropea, C 2009, "Unmanned aerial vehicle (UAV) with plasma actuators for separation control," Presented at 47th AIAA Aerospace Sciences Meeting, 5 - 8 January, Orlando, Florida, AIAA paper no. 2009-698.

[67] Roth, J.R., 2003. Aerodynamic flow acceleration using paraelectric and peristaltic electrohydrodynamic effects of a one atmosphere uniform glow discharge plasma. Physics of plasmas, 10(5), pp.2117-2126.

[68] Seifert, A., 2007. Closed-loop active flow control systems: actuators. In Active Flow Control (pp. 85-102). Springer, Berlin, Heidelberg.

[69] Nosenchuck, D.M., Brown, G.L., Culver, H.C., Eng, T.I. and Huang, I.S., 1995. Spatial and temporal characteristics of boundary layers controlled with the Lorentz force. In 12th Australian Fluid Mechanics Conference (pp. 93-96).

[70] Curle, N., 1955. The influence of solid boundaries upon aerodynamic sound. Proceedings of the Royal Society of London. Series A. Mathematical and Physical Sciences, 231(1187), pp.505-514.

[71] Lighthill, M.J., 1952. On sound generated aerodynamically I. General theory. Proceedings of the Royal Society of London. Series A. Mathematical and Physical Sciences, 211(1107), pp.564-587.

[72] Geyer, T., Sarradj, E. and Giesler, J., 2012. Application of a beamforming technique to the measurement of airfoil leading edge noise. Advances in Acoustics and Vibration, 2012.

[73] Oerlemans, S. and Migliore, P., 2004, May. Aeroacoustic wind tunnel tests of wind turbine airfoils. In 10th AIAA/CEAS Aeroacoustics Conference (p. 3042).

[74] Roger, M., Schram, C. and De Santana, L., 2013. Reduction of airfoil turbulence-impingement noise by means of leading-edge serrations and/or porous material. In 19th AIAA/CEAS aeroacoustics conference (p. 2108).

[75] Blake, W.K., 1986. Mechanics of Flow-Induced Sound and Vibration V1: General Concepts and Elementary Sources. Academic Press.

[76] Carolus, T., 2013. Ventilatoren–Aerodynamischer Entwurf, Schallvorhersage, Konstruktion, Universität Siegen, 3rd revised Edition, DOI 10.1007/978-3-8348-2472-1, Springer Vieweg, Siegen, Germany.

[77] Gershfeld, J., 2004. Leading edge noise from thick foils in turbulent flows. The Journal of the Acoustical Society of America, 116(3), pp.1416-1426.

[78] Oerlemans, S., 2004. Wind tunnel aeroacoustic tests of six airfoils for use on small wind turbines. Report of the National Renewable Energy Laboratory NREL/SR-500-35339.

[79] Paterson, R. and Amiet, R., 1976, August. Acoustic radiation and surface pressure characteristics of an airfoil due to incident turbulence. In 3rd Aeroacoustics Conference (p. 571).

[80] Staubs, J.K., 2008. Real airfoil effects on leading edge noise (Doctoral dissertation, Virginia Tech).

[81] Howe, M., 2014. Acoustics and aerodynamic sound. Cambridge University Press.

[82] Min, J., Li, X., Bai, B. and Lin, D., 2012. Numerical simulation on the NACA0018 airfoil self-noise generation. Theoretical and Applied Mechanics Letters, 2(5), p.052004.

[83] Hersh, A.S. and Hayden, R.E., 1971. Aerodynamic sound radiation from lifting surfaces with and without leading-edge serrations.

[84] Tam, C.K., 1974. Discrete tones of isolated airfoils. The Journal of the Acoustical Society of America, 55(6), pp.1173-1177.

[85] Tam, C.K. and Ju, H., 2012. Aerofoil tones at moderate Reynolds number. Journal of Fluid Mechanics, 690, pp.536-570.

[86] Arbey, H. and Bataille, J., 1983. Noise generated by airfoil profiles placed in a uniform laminar flow. Journal of Fluid Mechanics, 134, pp.33-47.

[87] Nash, E., Lowson, M., McAlpine, A.: Boundary layer instability noise on airfoils, Journal of Fluid Mechanics, 382 (1999) 27-61: 1999.

[88] McAlpine, A., Nash, E.C. and Lowson, M.V., 1999. On the generation of discrete frequency tones by the flow around an aerofoil. Journal of Sound and Vibration, 222(5), pp.753-779.

[89] Desquesnes, G., Terracol, M. and Sagaut, P., 2007. Numerical investigation of the tone noise mechanism over laminar airfoils. Journal of Fluid Mechanics, 591, pp.155-182.

[90] Kingan, M.J. and Pearse, J.R., 2009. Laminar boundary layer instability noise produced by an aerofoil. Journal of Sound and Vibration, 322(4-5), pp.808-828.

[91] Paterson, R.W., Vogt, P.G., Fink, M.R. and Munch, C.L., 1973. Vortex noise of isolated airfoils. Journal of Aircraft, 10(5), pp.296-302.

[92] Brooks, T.F., Pope, D.S. and Marcolini, M.A., 1989. Airfoil self-noise and prediction.

[93] Powell, A., 1959. On the aerodynamic noise of a rigid flat plate moving at zero incidence. The Journal of the Acoustical Society of America, 31(12), pp.1649-1653.

[94] Williams, J.F. and Hall, L.H., 1970. Aerodynamic sound generation by turbulent flow in the vicinity of a scattering half plane. Journal of fluid mechanics, 40(4), pp.657-670.

[95] Chase, D.M., 1975. Noise radiated from an edge in turbulent flow. AIAA journal, 13(8), pp.1041-1047.

[96] Howe, M.S., 1978. A review of the theory of trailing edge noise. Journal of sound and vibration, 61(3), pp.437-465.

[97] Roger, M., Moreau, S. and Wang, M., 2002. An analytical model for predicting airfoil self-noise using wall-pressure statistics. Annual Research Brief, Center for Turbulence Research, Stanford University, 2002, pp.405-414.

[98] Lighthill, M.J., 1951. A new approach to thin aerofoil theory. The Aeronautical Quarterly, 3(3), pp.193-210.

[99] Lighthill, M.J., 1954. On sound generated aerodynamically II. Turbulence as a source of sound. Proceedings of the Royal Society of London. Series A. Mathematical and Physical Sciences, 222(1148), pp.1-32.

[100] Brooks, T., Marcolini, M. and Pope, D., 1984, October. Airfoil trailing edge flow measurements and comparison with theory, incorporating open wind tunnel corrections. In 9th Aeroacoustics Conference (p. 2266).

[101] Fink, M.R., 1975. Experimental evaluation of trailing edge and incidence fluctuation noise theories.

[102] McDonough, J.M., 2007. Introductory lectures on turbulence: physics, mathematics and modeling.

[103] Brooks, T.F. and Hodgson, T.H., 1981. Trailing edge noise prediction from measured surface pressures. Journal of sound and vibration, 78(1), pp.69-117.

[104] Blake, W.K. and Temkin, S., 1988. Mechanics of Flow-Induced Sound and Vibration. Vol. I: General Concepts and Elementary Sources by William K. Blake.

[105] ITO, S., 2009. Aerodynamic influence of leading-edge serrations on an airfoil in a low Reynolds number. Journal of Biomechanical Science and Engineering, 4(1), pp.117-123.

[106] Hansen, K.L., Kelso, R.M. and Dally, B.B., 2011. Performance variations of leading-edge tubercles for distinct airfoil profiles. AIAA journal, 49(1), pp.185-194.

[107] Watts, P. and Fish, F.E., 2001, August. The influence of passive, leading edge tubercles on wing performance. In Proc. Twelfth Intl. Symp. Unmanned Untethered Submers. Technol. Durham New Hampshire: Auton. Undersea Syst. Inst.

[108] Stein, B. and Murray, M.M., 2005. Stall mechanism analysis of humpback whale flipper models. Proceedings of Unmanned Untethered Submersible Technology (UUST), UUST05, 5.

[109] Levshin, A., Custodio, D., Henoch, C. and Johari, H., 2006, June. Effects of leading edge protuberances on airfoil performance. In 36th AIAA Fluid Dynamics Conference and Exhibit (p. 2868).

[110] Miklosovic, D.S., Murray, M.M. and Howle, L.E., 2007. Experimental evaluation of sinusoidal leading edges. Journal of aircraft, 44(4), pp.1404-1408.

[111] Stanway, M.J., 2008. Hydrodynamic effects of leading-edge tubercles on control surfaces and in flapping foil propulsion (Doctoral dissertation, Massachusetts Institute of Technology).

[112] Van Nierop, E.A., Alben, S. and Brenner, M.P., 2008. How bumps on whale flippers delay stall: an aerodynamic model. Physical review letters, 100(5), p.054502.

[113] Bearman, P.W. and OWen, J.C., 1998. Reduction of bluff-body drag and suppression of vortex shedding by the introduction of wavy separation lines. Journal of Fluids and Structures, 12(1), pp.123-130.

[114] Polacsek, C., Reboul, G., Clair, V., Le Garrec, T. and Deniau, H., 2011, July. Turbulence-airfoil interaction noise reduction using wavy leading edge: An experimental and numerical study. In Proc. of Inter-Noise.

[115] Hansen, K.L., Kelso, R.M. and Dally, B.B., 2009. The effect of leading edge tubercle geometry on the performance of different airfoils. World.

[116] Fish, F. and Lauder, G.V., 2006. Passive and active flow control by swimming fishes and mammals. Annu. Rev. Fluid Mech., 38, pp.193-224.

[117] Custodio, D.S., 2007. The Effect of Humpback Whale-like Protuberances on Hydrofoil Performance.

[118] Carreira Pedro, H. and Kobayashi, M., 2008, January. Numerical study of stall delay on humpback whale flippers. In 46th AIAA aerospace sciences meeting and exhibit (p. 584).

[119] Weber, P.W., Howle, L.E. and Murray, M.M., 2010. Lift, drag, and cavitation onset on rudders with leading-edge tubercles. Marine technology, 47(1), pp.27-36.

[120] Hersh, A.S., Sodermant, P.T. and Hayden, R.E., 1974. Investigation of acoustic effects of leading-edge serrations on airfoils. Journal of Aircraft, 11(4), pp.197-202.

[121] Longhouse, R.E., 1977. Vortex shedding noise of low tip speed, axial flow fans. Journal of sound and vibration, 53(1), pp.25-46.

[122] Arndt, R., 1972. Effect of leading edge serrations on noise radiation from a model rotor. In Society of Naval Architects and Marine Engineers, and US Navy, Advanced Marine Vehicles Meeting (p. 655).

[123] Lau, A.S.H. and Kim, J.W., 2013. The Effects of Wavy Leading Edges on Airfoil-Gust Interaction Noise. In 19th AIAA/CEAS Aeroacoustics Conference (p. 2120).

[124] Haeri, S., Kim, J.W., Narayanan, S. and Joseph, P., 2014. 3D calculations of aerofoil-turbulence interaction noise and the effect of wavy leading edges. In 20th AIAA/CEAS Aeroacoustics Conference (p. 2325).

[125] Chong, T.P., Vathylakis, A., McEwen, A., Kemsley, F., Muhammad, C. and Siddiqi, S., 2015. Aeroacoustic and aerodynamic performances of an aerofoil subjected to sinusoidal leading edges. In 21st AIAA/CEAS Aeroacoustics Conference (p. 2200).

[126] Biedermann, T., Chong, T.P. and Kameier, F., 2016. Statistical-empirical modelling of aerofoil noise subjected to leading edge serrations and aerodynamic

identification of noise reduction mechanisms. In 22nd AIAA/CEAS Aeroacoustics Conference (p. 2757).

[127] Melo De Sousa, J. and Camara, J., 2013, January. Numerical study on the use of a sinusoidal leading edge for passive stall control at low Reynolds number. In 51st AIAA Aerospace Sciences Meeting including the New Horizons Forum and Aerospace Exposition (p. 62).

[128] Narayanan, S., Joseph, P., Haeri, S. and Kim, J.W., 2014. Noise reduction studies from the leading edge of serrated flat plates. In 20th AIAA/CEAS Aeroacoustics Conference (p. 2320).

[129] Chong, T.P., Biedermann, T., Koster, O. and Hasheminejad, S.M., 2018. On the Effect of Leading Edge Serrations on Aerofoil Noise Production. In 2018 AIAA/CEAS Aeroacoustics Conference (p. 3289).

[130] Lacagnina, G., Paruchuri, C., Berk, T.A., Joseph, P., Hasheminejad, S.M., Stalnov, O., Chong, T.P. and Ganapathisubramani, B., 2018. Effect of Leading Edge serrations in reducing aerofoil noise near stall conditions. In 2018 AIAA/CEAS Aeroacoustics Conference (p. 3285).

[131] Biedermann, T. and Kameier, F., 2016, August. Statistical-empirical modelling of aerofoil noise and performance subjected to leading edge serrations. In INTER-NOISE and NOISE-CON Congress and Conference Proceedings (Vol. 253, No. 8, pp. 632-643). Institute of Noise Control Engineering.

[132] Paruchuri, C., Gill, J.R., Subramanian, N., Joseph, P., Vanderwel, C., Zhang, X. and Ganapathisubramani, B., 2015. Aerofoil geometry effects on turbulence interaction noise. In 21st AIAA/CEAS Aeroacoustics Conference (p. 2830).

[133] Chen, W., Qiao, W., Wang, L., Tong, F. and Wang, X., 2015. Rod-airfoil interaction noise reduction using leading edge serrations. In 21st AIAA/CEAS aeroacoustics conference (p. 3264).

[134] Weiland, C.J. and Vlachos, P.P., 2006, January. Modification of Blade Vortex Interactions Using Leading Edge Blowing. In ASME 2006 2nd Joint US-European Fluids Engineering Summer Meeting Collocated With the 14th International Conference on Nuclear Engineering (pp. 425-435). American Society of Mechanical Engineers.

[135] Malovrh, B. and Gandhi, F., 2005. Sensitivity of helicopter blade-vortex-interaction noise and vibration to interaction parameters. Journal of aircraft, 42(3), pp.685-697.

[136] Slomski, J., 2009. Reducing vortex shedding sound from a trailing edge above a wall jet. In 47th AIAA Aerospace Sciences Meeting including The New Horizons Forum and Aerospace Exposition (p. 778).

[137] McManus, K. and Magill, J., 1996. Separation control in incompressible and compressible flows using pulsed jets. In Fluid Dynamics Conference (p. 1948).

[138] Rao, P., Strganac, T. and Rediniotis, O., 2000. Control of aeroelastic response via synthetic jet actuators. In 41st Structures, Structural Dynamics, and Materials Conference and Exhibit (p. 1415).

[139] Williams, R.M. and Howe, H.J., 1970. Two dimensional subsonic wind tunnel tests on a 20 percent thick, 5 percent cambered circulation control airfoil (No. TN-AL-176). DAVID W TAYLOR NAVAL SHIP RESEARCH AND DEVELOPMENT CENTER BETHESDA MD.

[140] Abramson, J., 2004. Characteristics of a Cambered Circulation Control Airfoil Having Both Upper and Lower Surface Trailing Edge Slots (No. NSWCCD-50-TR-2004/030). NAVAL SURFACE WARFARE CENTER CARDEROCK DIV BETHESDA MD.

[141] Kobayashi, R. and Fujisawa, N., 1983. Curvature effects on two-dimensional turbulent wall jets. Ingenieur-Archiv, 53(6), pp.409-417.

[142] Colonius, T. and Williams, D.R., 2011. Control of vortex shedding on two- and three-dimensional aerofoils. Philosophical Transactions of the Royal Society A: Mathematical, Physical and Engineering Sciences, 369(1940), pp.1525-1539.

[143] Kweder, J., Clarke, M.A. and Smith, J.E., 2010, January. Effect of Leading Edge Blowing Slots on Stall Angles of a 10: 1 Elliptical Airfoil. In ASME 2010 International Mechanical Engineering Congress and Exposition (pp. 137-143). American Society of Mechanical Engineers Digital Collection.

[144] Lusk, T., Cattafesta, L. and Ukeiley, L., 2012. Leading edge slot blowing on an open cavity in supersonic flow. Experiments in fluids, 53(1), pp.187-199.

[145] Wolf, W.R., Azevedo, J.L.F. and Lele, S.K., 2012. Convective effects and the role of quadrupole sources for aerofoil aeroacoustics. Journal of Fluid Mechanics, 708, pp.502-538.

[146] Wolf, W.R. and Lele, S.K., 2011. Aeroacoustic integrals accelerated by fast multipole method. AIAA journal, 49(7), pp.1466-1477.

[147] Biedermann, T., 2015. Aerofoil Noise Subjected to Leading Edge Serration. Düsseldorf, September.

[148] Abbott, I.H., Von Doenhoff, A.E. and Stivers, L.S., 1945. Summary of Airfoil Data, Report no. 824.

[149] Vathylakis, A., Kim, J. H. & Chong, T. P., 2014. Design of a low-noise aeroacoustic wind tunnel facility at Brunel University, School of Engineering and Design, Brunel University, London, UK: AIAA Aviation.

[150] Chong, T.P., Joseph, P.F. and Davies, P.O.A.L., 2009. Design and performance of an open jet wind tunnel for aero-acoustic measurement. Applied acoustics, 70(4), pp.605-614.

[151] Bruun, H., 2002. Hot-wire anemometry : principles and signal analysis. New York: Oxford Unversity Press, Oxford.

[152] Dantec Dynamics, n.d., 2015. Probes for Hot-wire Anemometry, DENMARK: Dantec Dynamics A/S Nova Instruments.

[153] Marko, M., Milan, D., Emina, P. and Jelena, M., 2012. Turblence intensity in smoth tube measuring. DAS-29, 29th Danubia-Adria Symposium, University of Belgrade, Serbia.

[154] Jørgensen, F.E., 2002. How to measure turbulence with hot-wire anemometers-a practical guide, Dantec dynamics.

[155] Bruun, E., 1995. Bandwidth optimization of a low power, high speed CMOS current op amp. Analog Integrated Circuits and Signal Processing, 7(1), pp.11-19.

[156] Perry, A. E., 1982. Hot-Wire Anemometry. Oxford: Oxford University Press.

[157] Schade, H. & Kunz, E., 2007. Strömungslehre 3., neu bearbeitete Auflage. Berlin, Germany: Walter de Gruyter.

[158] Laws, E. M. & Livesey, J. L., 1978. FLOW THROUGH SCREENS, England: Department of Aeronautical and Mechanical Engineering, University of Salford, In: Annu.Rev.Fluid Mech. 1978.10:247-266.

[159] Plint & Partners LTD Engineers, 1986. Operating Instructions TE.81/D, s.l.: PLINT.

[160] Crites, R. and Steinle, r, F., 1995, January. Wall interference reduction methods for subsonic wind tunnels. In 33rd Aerospace Sciences Meeting and Exhibit (p. 107).

[161] Glauert, H., 1933. Wind tunnel interference on wings, bodies and airscrews (No. ARC-R/M-1566). AERONAUTICAL RESEARCH COUNCIL LONDON (UNITED KINGDOM).

[162] Allen, H.J. and Vincenti, W.G., 1944. Wall interference in a two-dimensional-flow wind tunnel with consideration of the effect of compressibility (No. NACA-WR-A-63). NATIONAL AERONAUTICS AND SPACE ADMINISTRATION MOFFETT FIELD CA AMES RESEARCH CENTER.

[163] Gruber, M., 2012. Airfoil noise reduction by edge treatments (Doctoral dissertation, University of Southampton).

[164] Chong, T.P., Biedermann, T., Koster, O. and Hasheminejad, S.M., 2018. On the Effect of Leading Edge Serrations on Aerofoil Noise Production. In 2018 AIAA/CEAS Aeroacoustics Conference (p. 3289).

[165] Jacobs, E.N. and Sherman, A., 1937. Airfoil section characteristics as affected by variations of the Reynolds number.

[166] Loth, J.L., Fanucci, J.B. and Roberts, S.C., 1976. Flight performance of a circulation controlled STOL aircraft. Journal of Aircraft, 13(3), pp.169-173.4).

Appendices

Appendix A: High Turbulence Intensities

Effect of Angle of Attack (AOA)

$\lambda' = 5$ mm

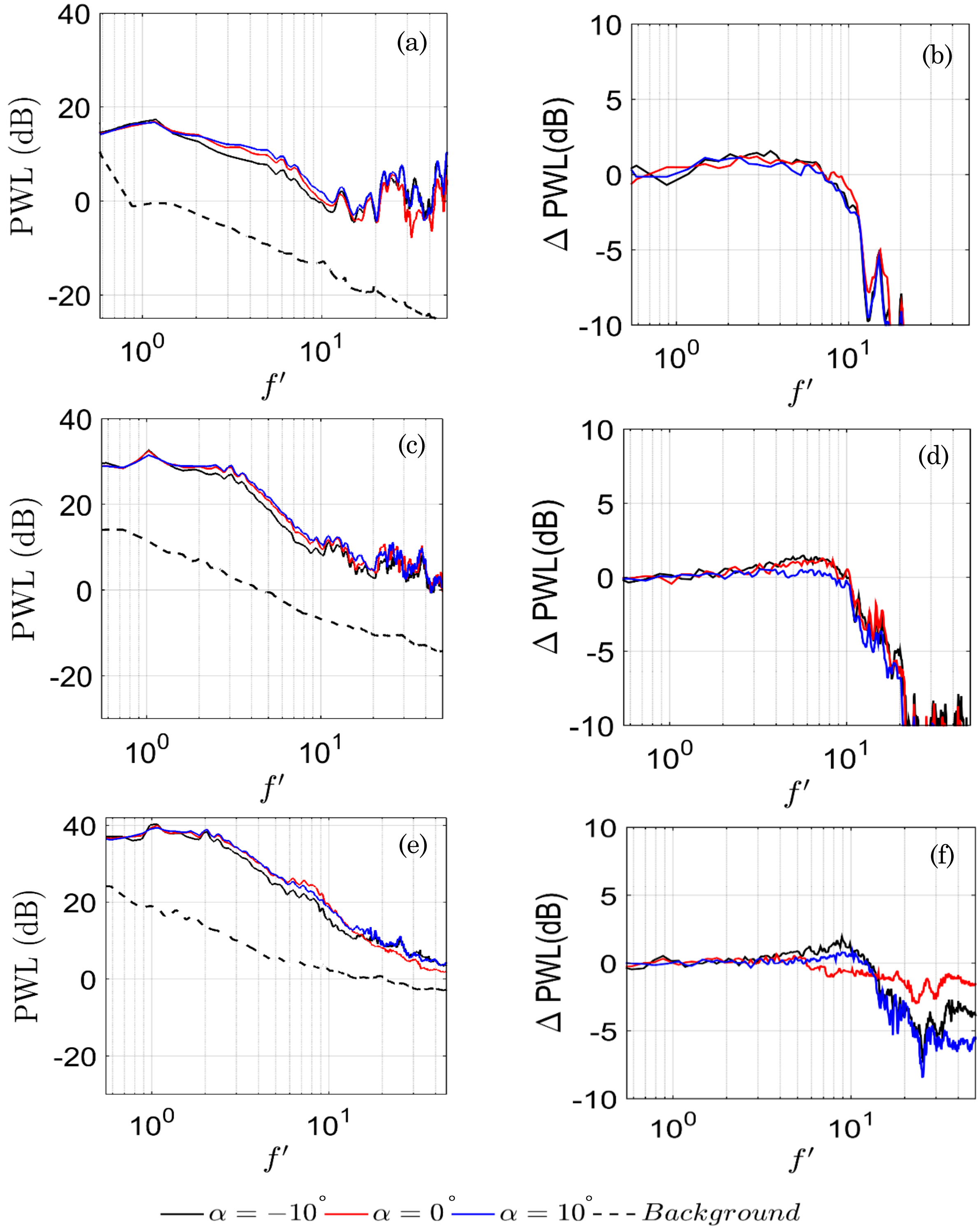

Figure A1: Comparison of PWL and ΔPWL as a function of normalised frequency f' at (a, b) $U_\infty = 20$ m/s, (c, d) $U_\infty = 40$ m/s and (e, f) $U_\infty = 60$ m/s when $Q' = 3.5$ litre/min and $Tu = 4.5\%$.

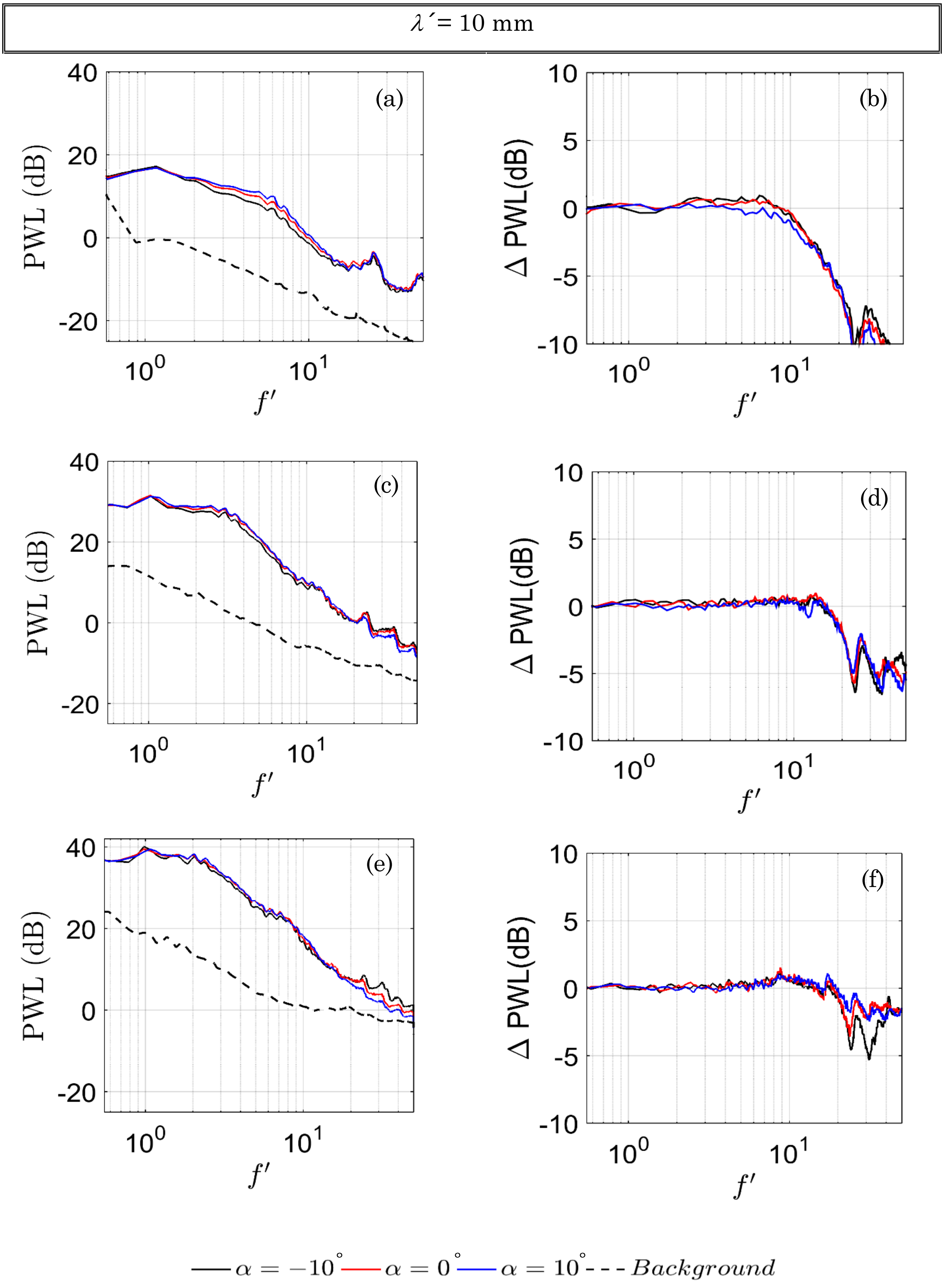

Figure A2: Comparison of PWL and ΔPWL as a function of normalised frequency f' at (a, b) U_∞ = 20 m/s, (c, d) U_∞ = 40 m/s and (e, f) U_∞ = 60 m/s when Q' = 3.5 litre/min and Tu = 4.5%.

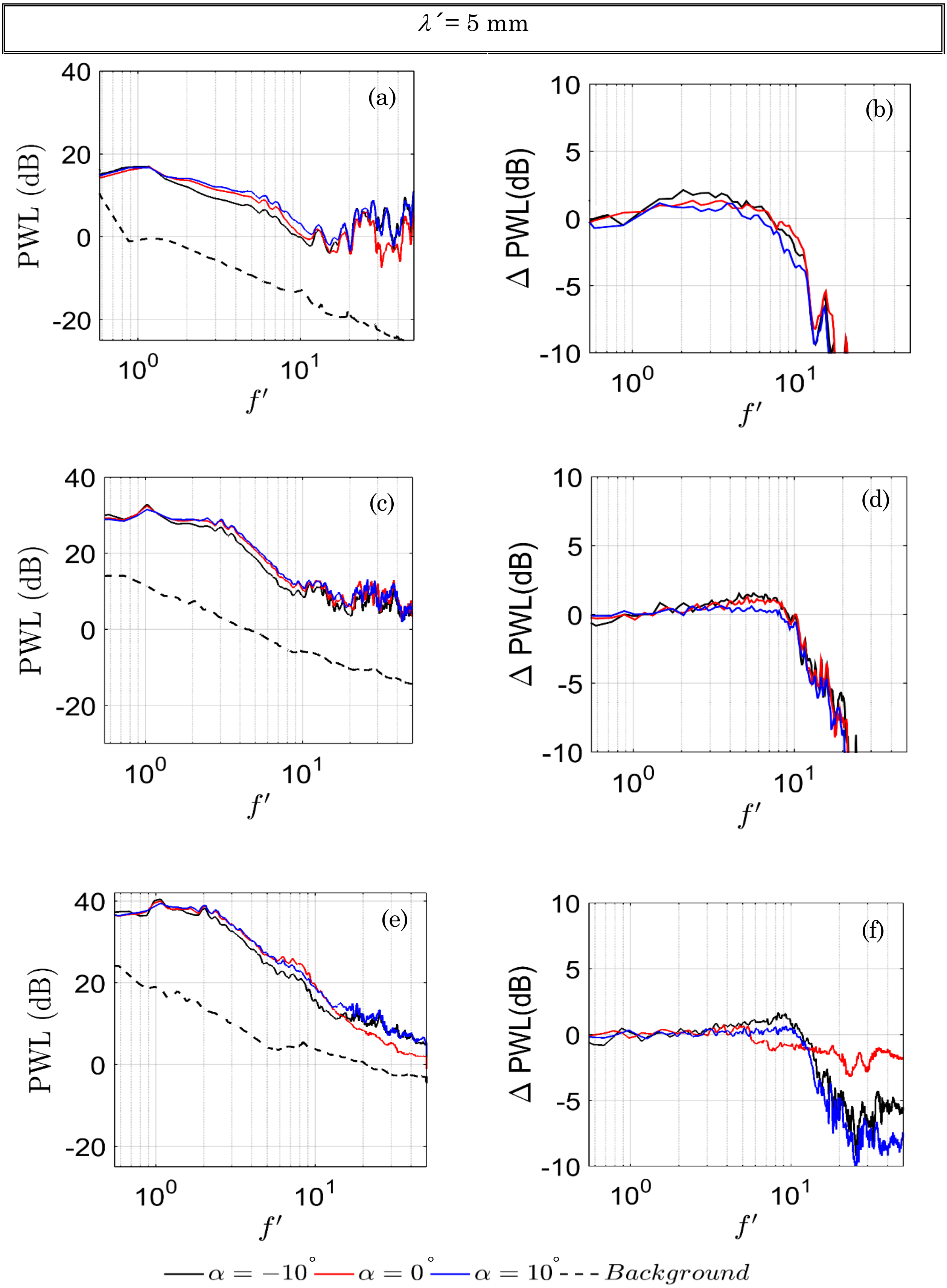

Figure A3: Comparison of PWL and ΔPWL as a function of normalised frequency f' at (a, b) U_∞ = 20 m/s, (c, d) U_∞ = 40 m/s and (e, f) U_∞ = 60 m/s when Q' = 4.5 litre/min and Tu = 4.5%.

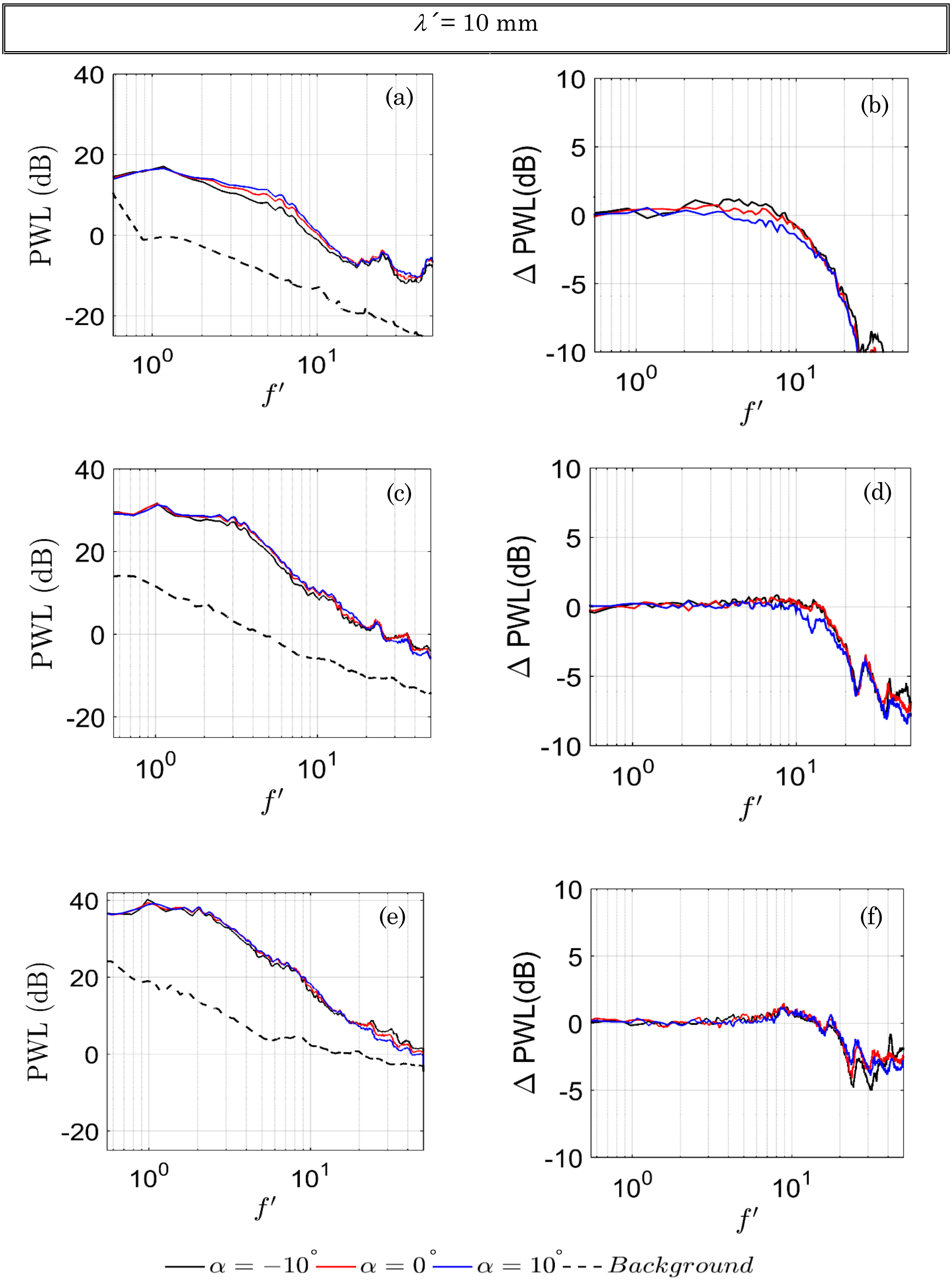

Figure A4: Comparison of PWL and ΔPWL as a function of normalised frequency f' at (a, b) U_∞ = 20 m/s, (c, d) U_∞ = 40 m/s and (e, f) U_∞ = 60 m/s when Q' = 4.5 litre/min and Tu = 4.5%.

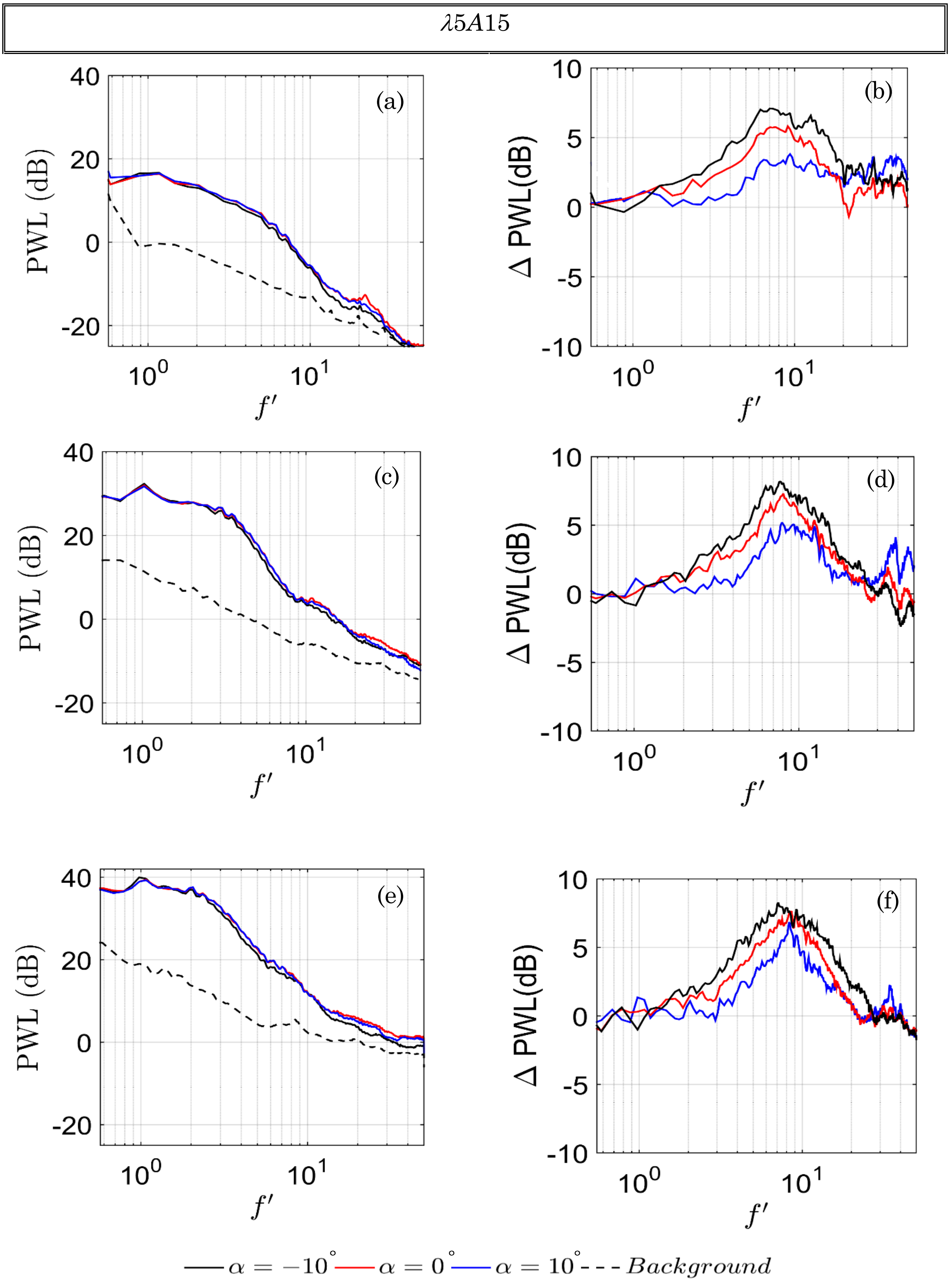

Figure A5: Comparison of PWL and ΔPWL as a function of normalised frequency f' at (a, b) $U_\infty = 20$ m/s, (c, d) $U_\infty = 40$ m/s and (e, f) $U_\infty = 60$ m/s and $Tu = 4.5\%$.

$\lambda 5A30$

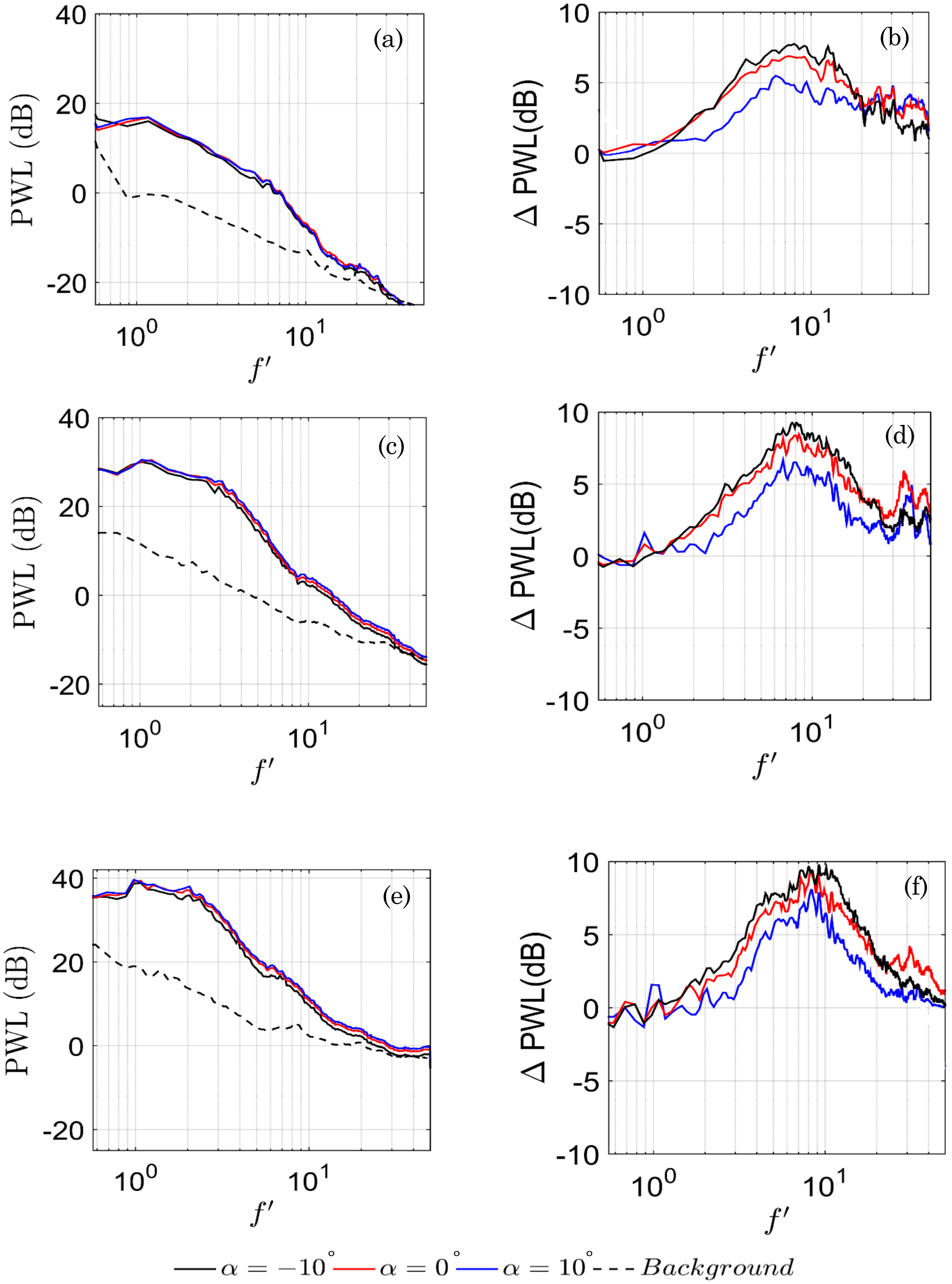

Figure A6: Comparison of PWL and ΔPWL as a function of normalised frequency f' at (a, b) $U_\infty = 20$ m/s, (c, d) $U_\infty = 40$ m/s and (e, f) $U_\infty = 60$ m/s and $Tu = 4.5\%$.

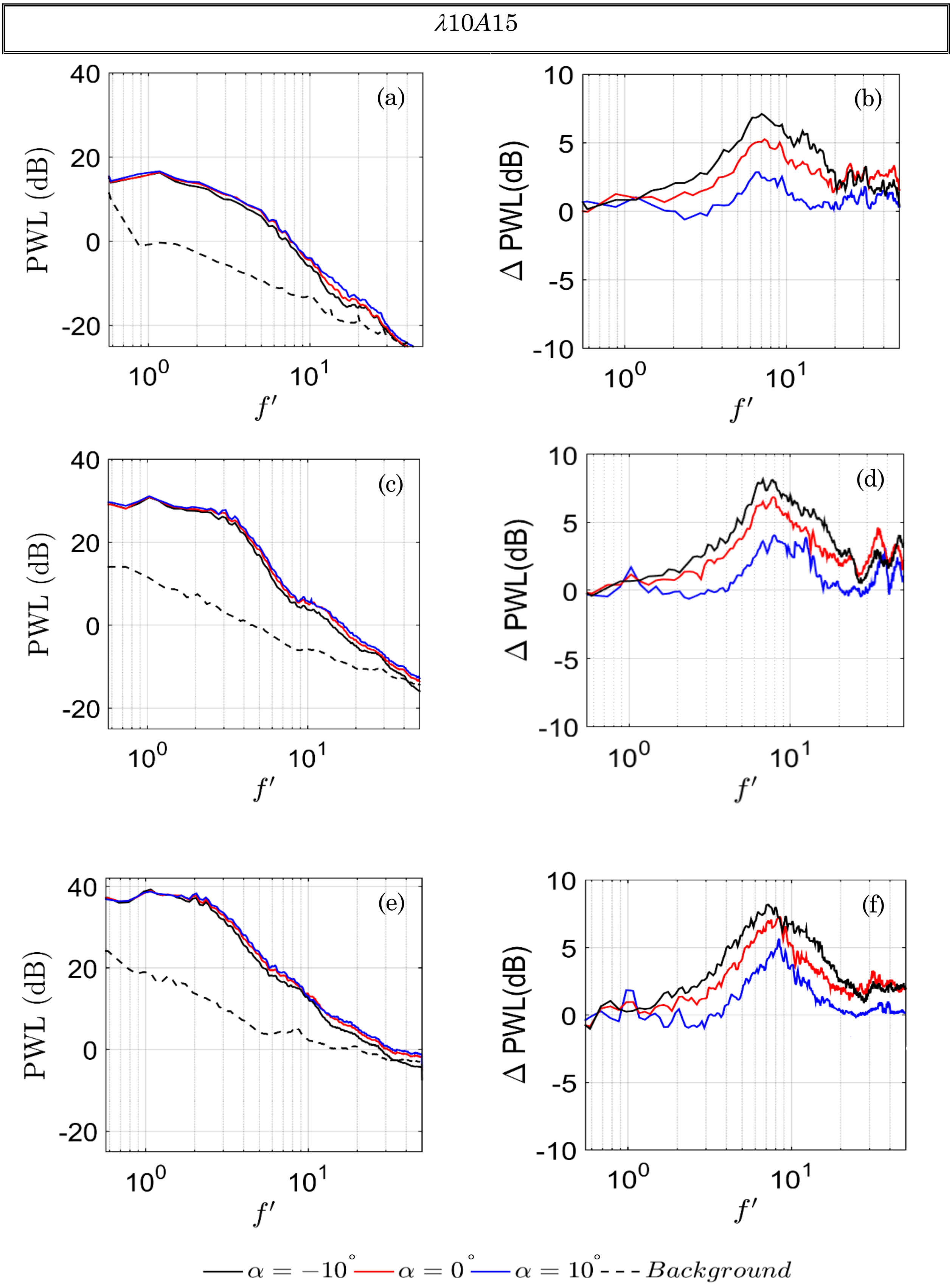

Figure A7: Comparison of PWL and ΔPWL as a function of normalised frequency f' at (a, b) U_∞ = 20 m/s, (c, d) U_∞ = 40 m/s and (e, f) U_∞ = 60 m/s and Tu = 4.5%.

$\lambda 10A30$

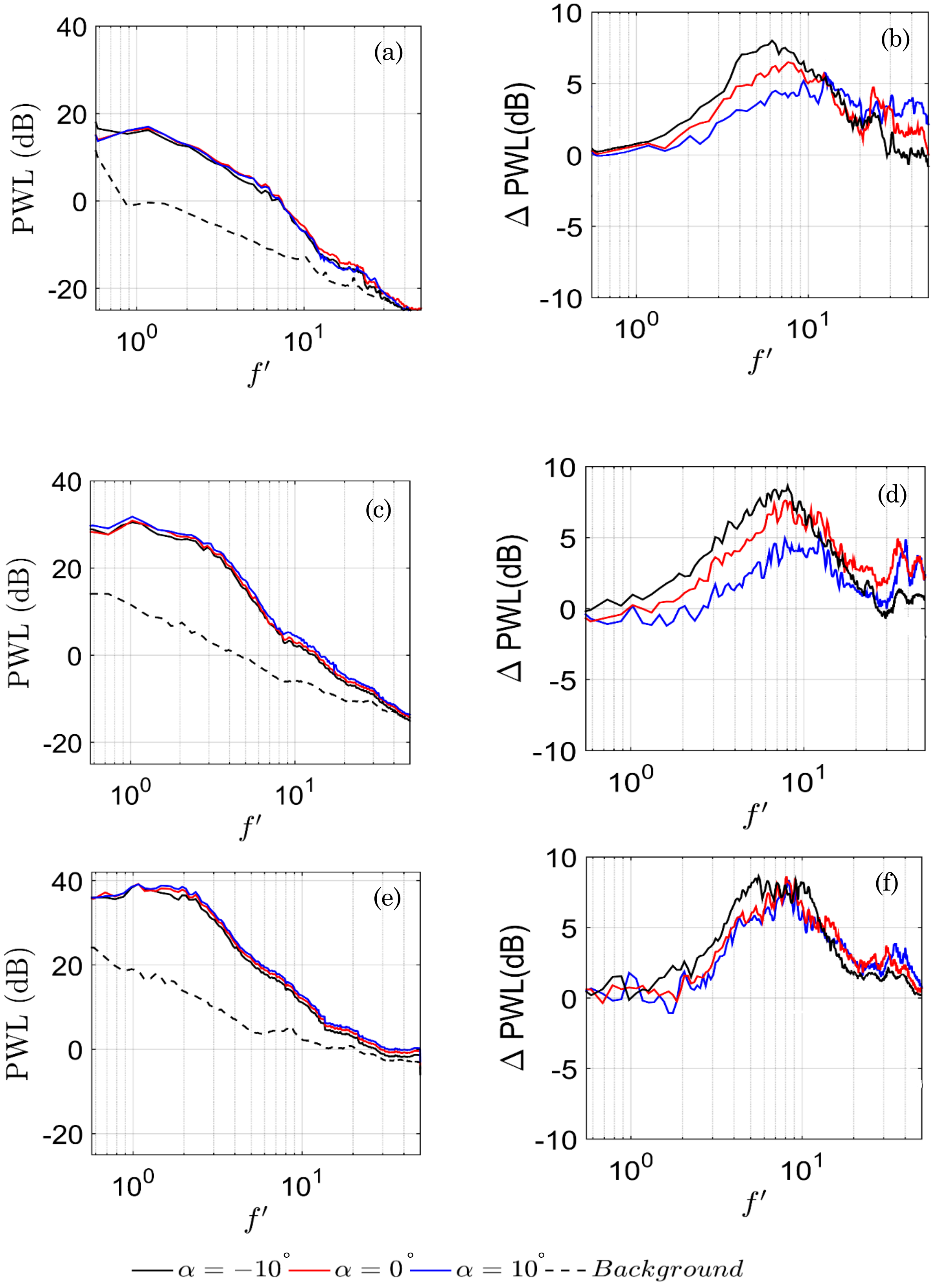

Figure A8: Comparison of PWL and ΔPWL as a function of normalised frequency f' at (a, b) U_∞ = 20 m/s, (c, d) U_∞ = 40 m/s and (e, f) U_∞ = 60 m/s and Tu = 4.5%.

Appendix B: Low Turbulence Intensities

<u>Effect angle of attack (AOA)</u>

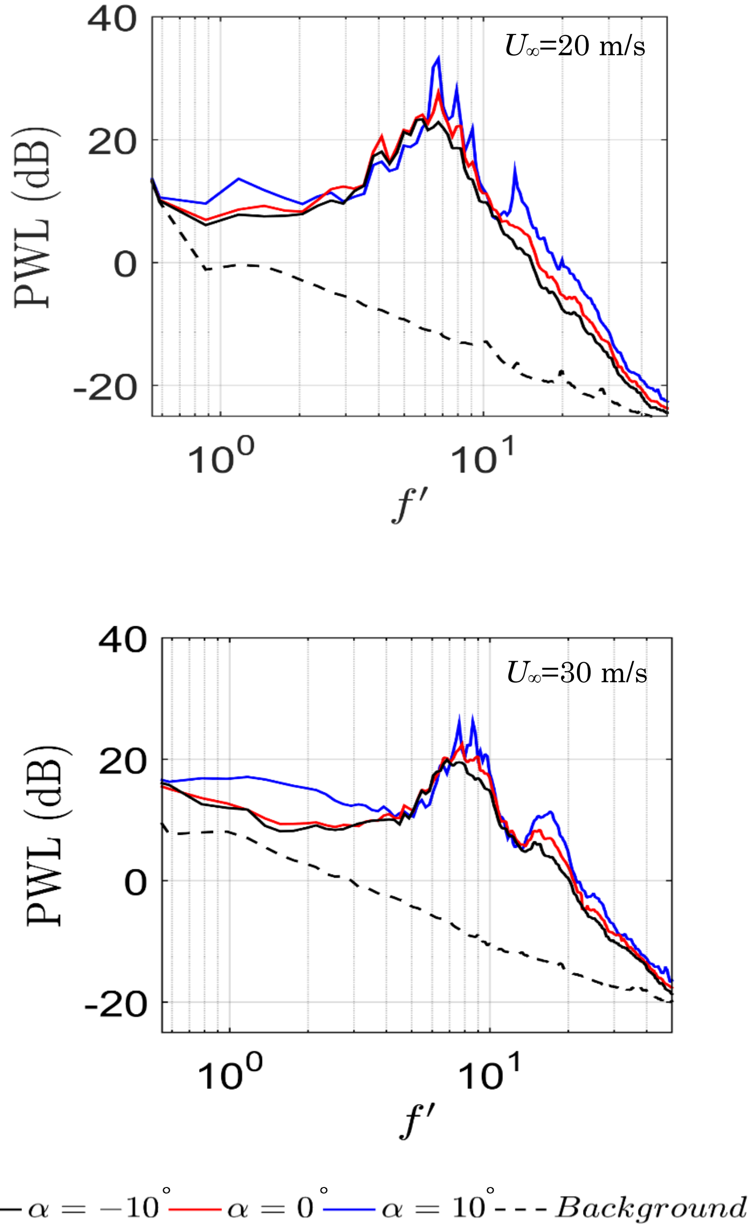

Figure B1: Comparison of PWL as a function of normalised frequency f' at U_∞ = 20-60 m/s when Q' = 0 litre/min and Tu = 0.2%.

$\lambda' = 5$ mm

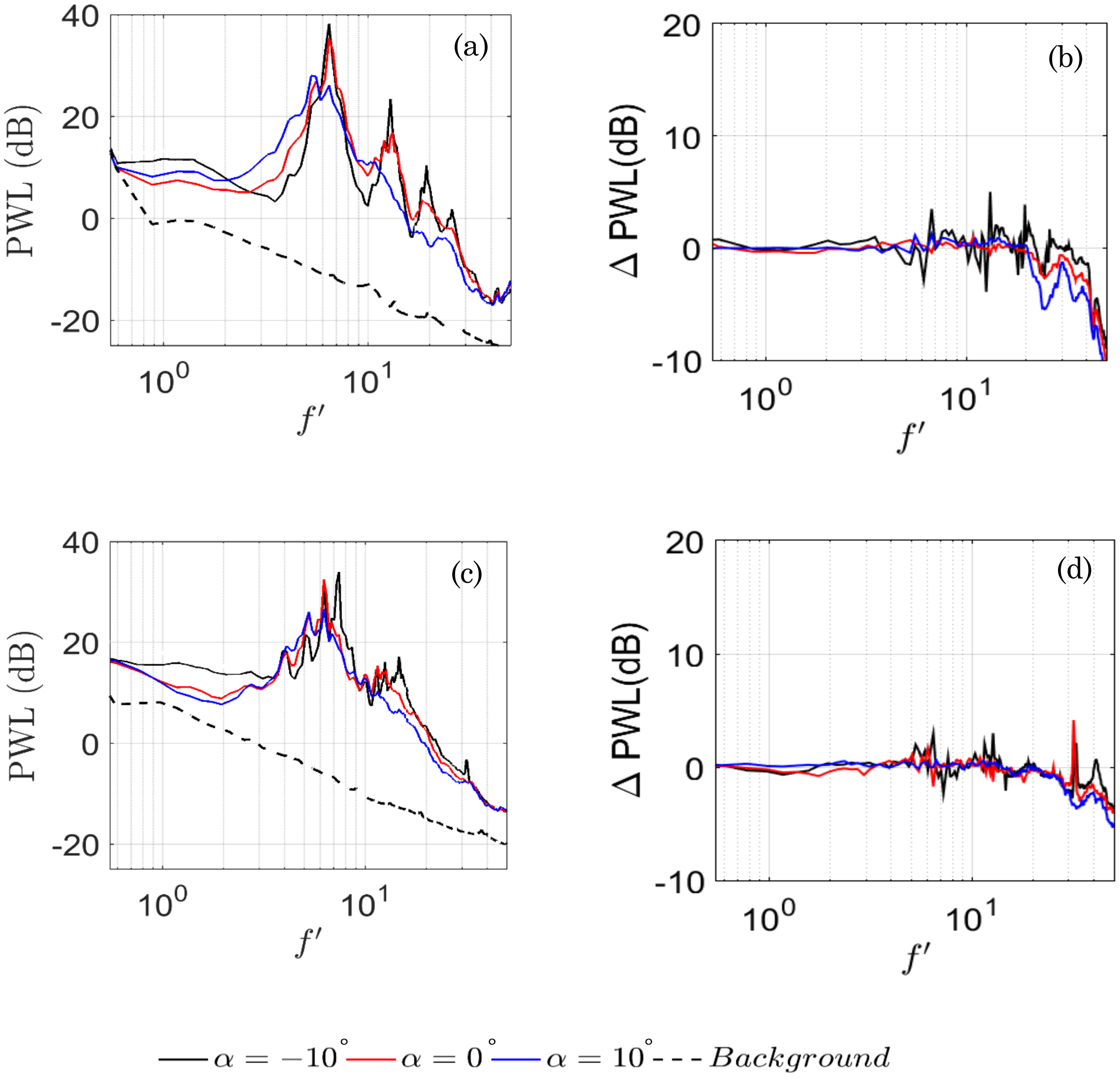

Figure B2: Comparison of PWL and ΔPWL as a function of normalised frequency f' at (a, b) U_∞ = 20 m/s and (c, d) U_∞ = 30 m/s when Q' = 1 litre/min and Tu = 0.2%.

$\lambda' = 10$ mm

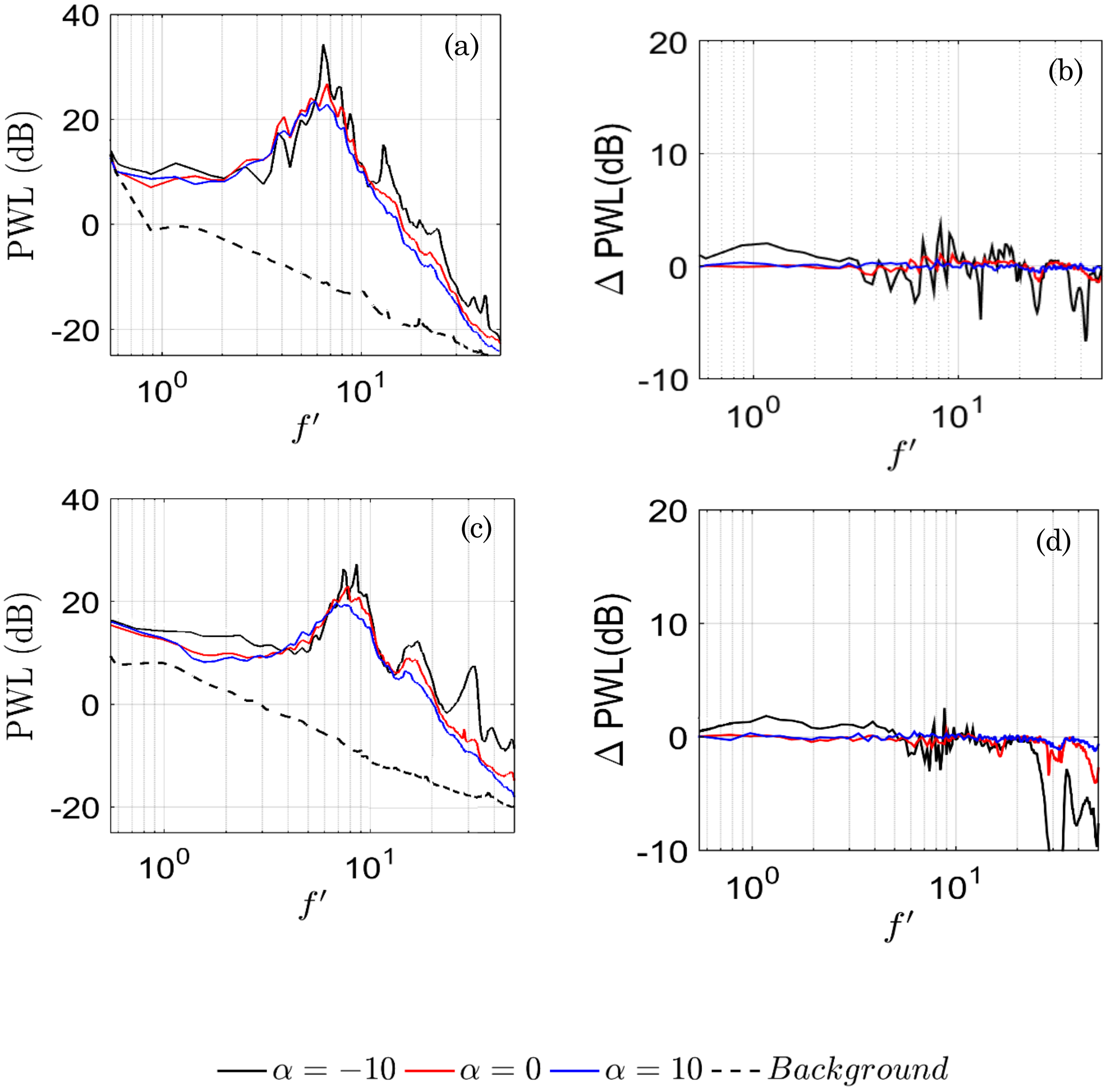

Figure B3: Comparison of PWL and ΔPWL as a function of normalised frequency f' at (a, b) U_∞ = 20 m/s and (c, d) U_∞ = 30 m/s when Q' = 1 litre/min and Tu = 0.2%.

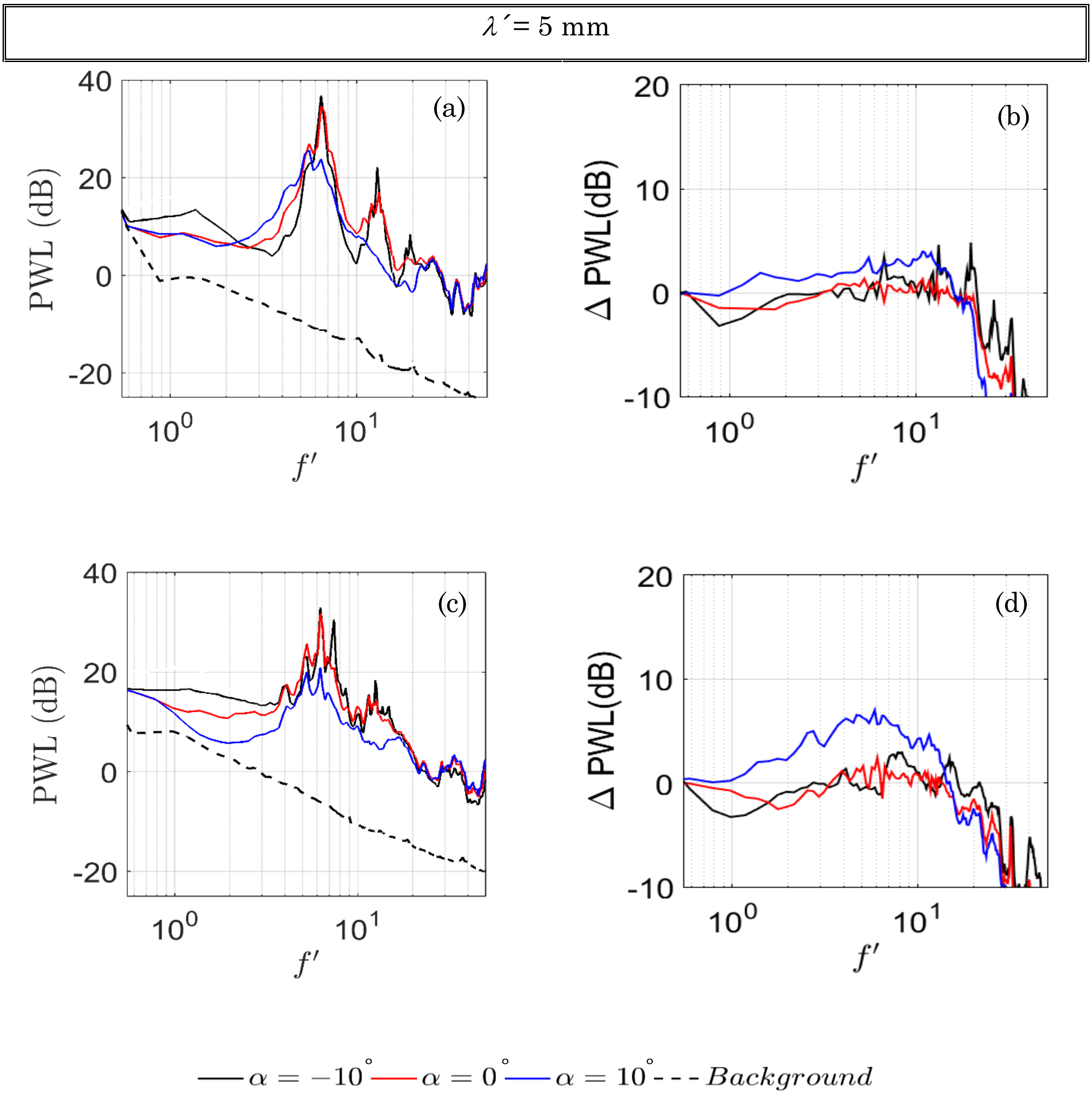

Figure B4: Comparison of PWL and ΔPWL as a function of normalised frequency f' at (a, b) U_∞ = 20 m/s and (c, d) U_∞ = 30 m/s when Q' = 2.5 litre/min and Tu = 0.2%.

$\lambda' = 10$ mm

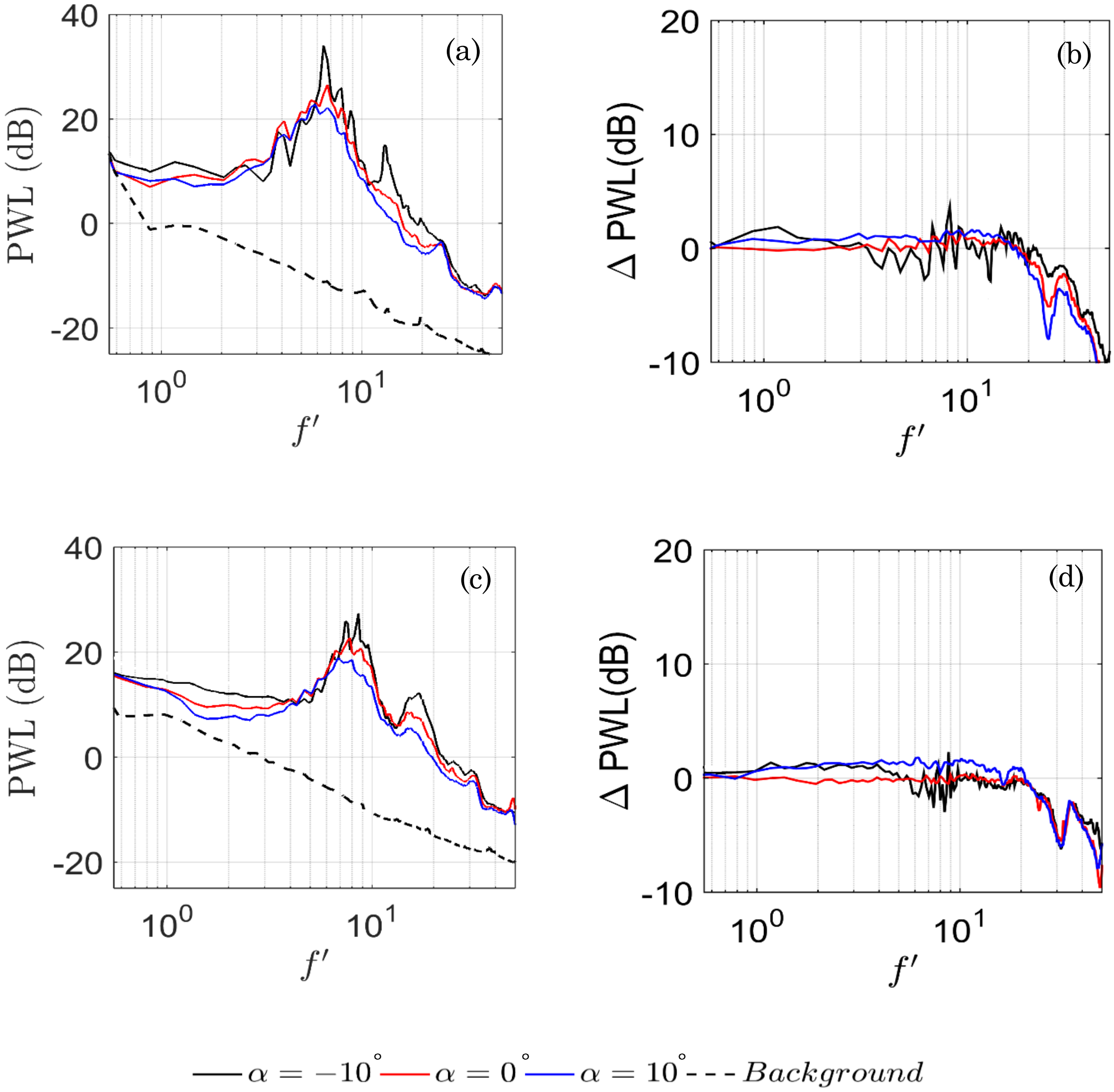

Figure B5: Comparison of PWL and ΔPWL as a function of normalised frequency f' at (a, b) U_∞ = 20 m/s and (c, d) U_∞ = 30 m/s when Q' = 2.5 litre/min and Tu = 0.2%.

$\lambda' = 5$ mm

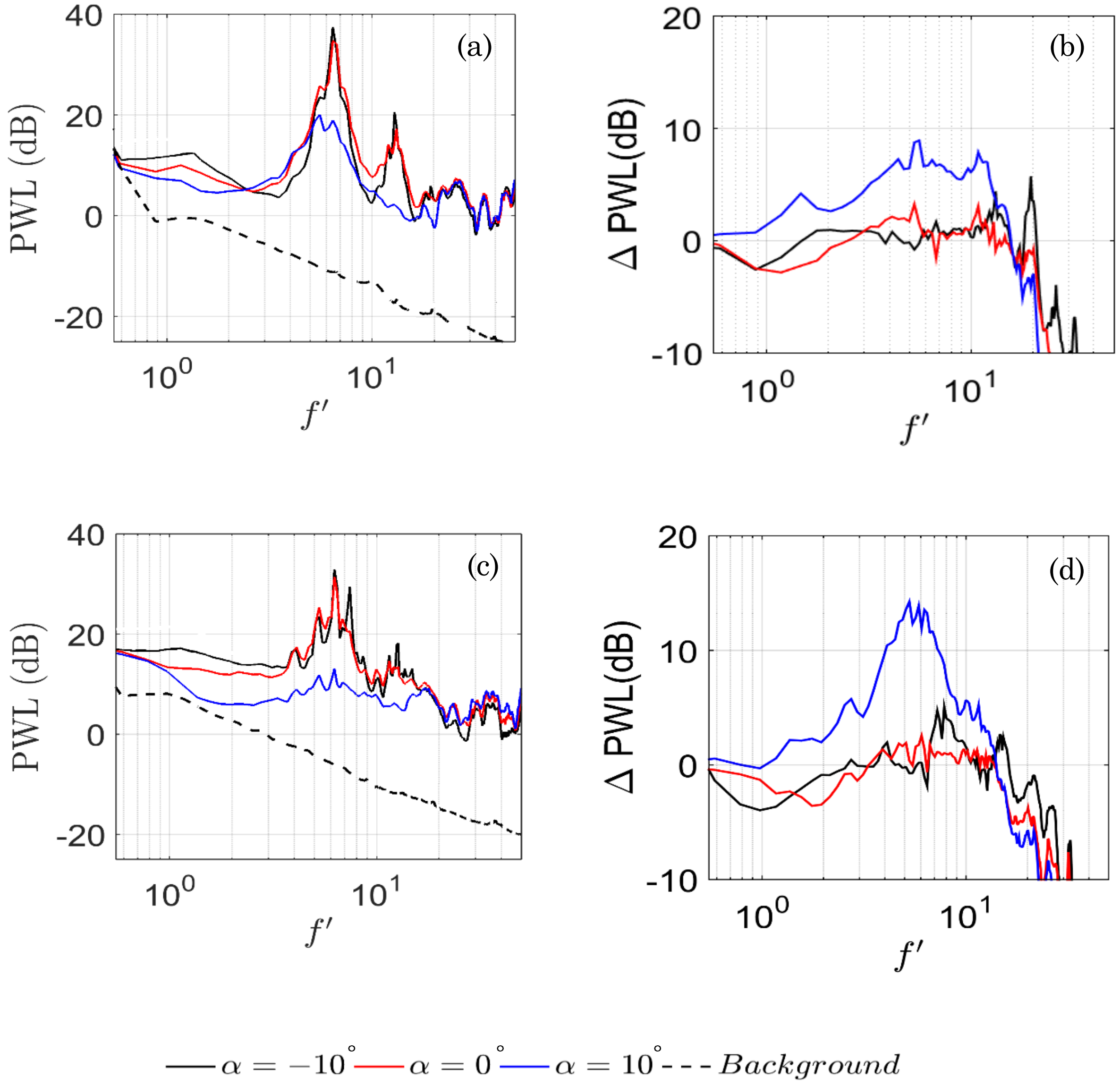

Figure B6: Comparison of PWL and ΔPWL as a function of normalised frequency f' at (a, b) U_∞ = 20 m/s and (c, d) U_∞ = 30 m/s when Q' = 3.5 litre/min and Tu = 0.2%.

$\lambda' = 10$ mm

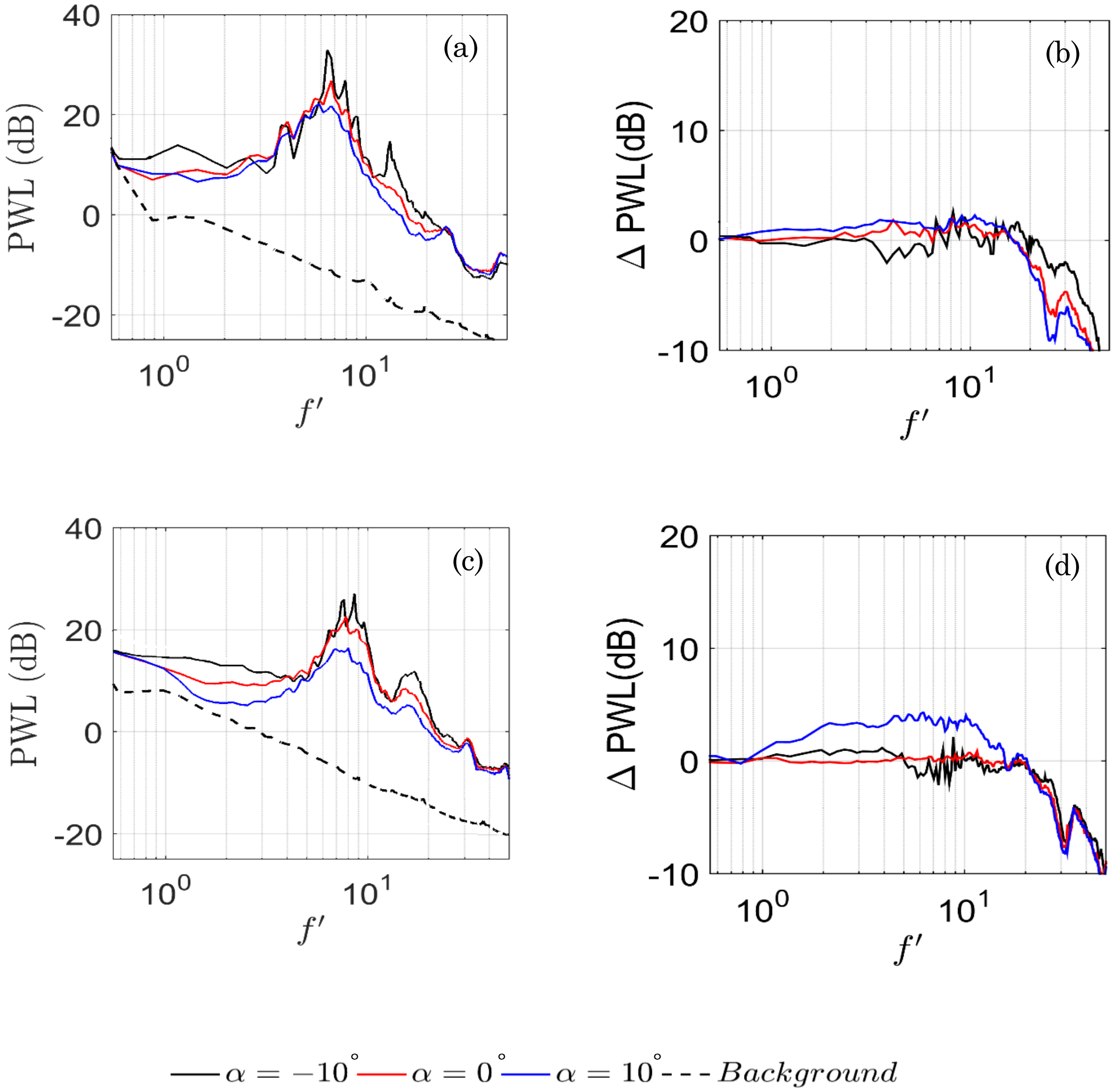

Figure B7: Comparison of PWL and ΔPWL as a function of normalised frequency f' at (a, b) $U_\infty = 20$ m/s and (c, d) $U_\infty = 30$ m/s when $Q' = 3.5$ litre/min and $Tu = 0.2\%$.

$\lambda 5A15$

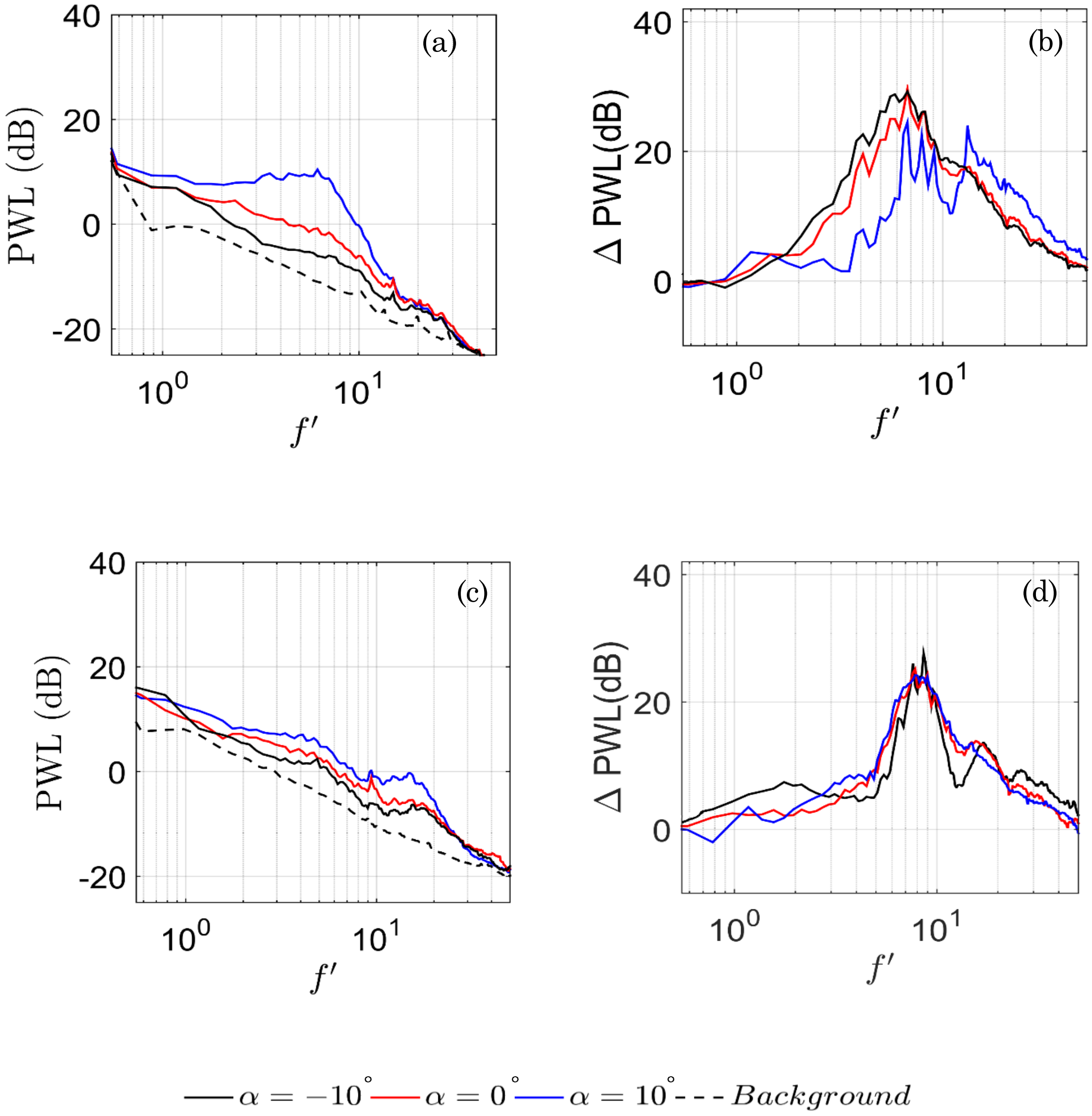

Figure B8: Comparison of PWL and ΔPWL as a function of normalised frequency f' at (a, b) U_∞ = 20 m/s and (c, d) U_∞ = 30 m/s when Tu=0.2%.

$\lambda 5A30$

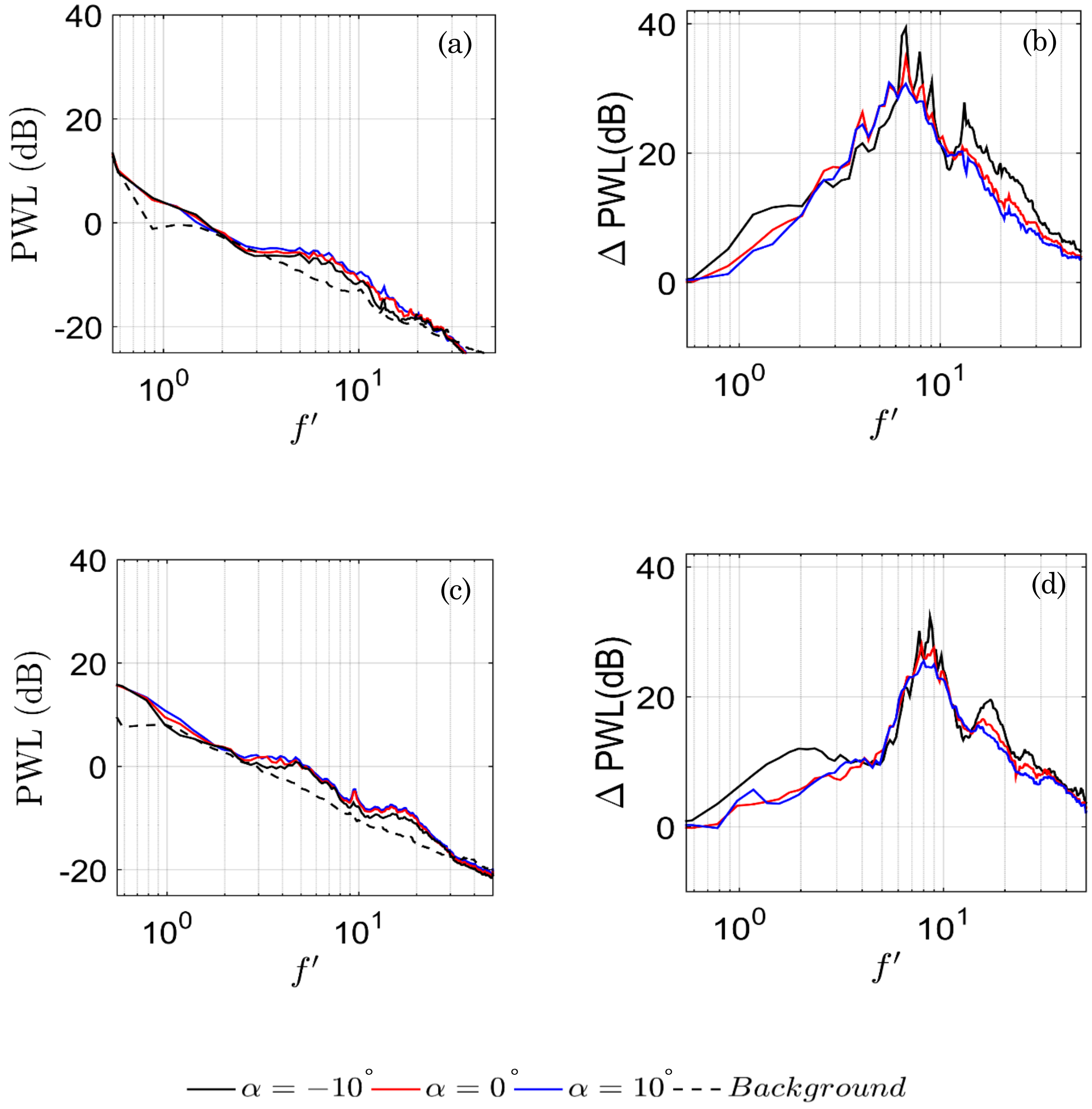

Figure B9: Comparison of PWL and ΔPWL as a function of normalised frequency f' at (a, b) U_∞ = 20 m/s and (c, d) U_∞ = 30 m/s when Tu=0.2%.

$\lambda 10A15$

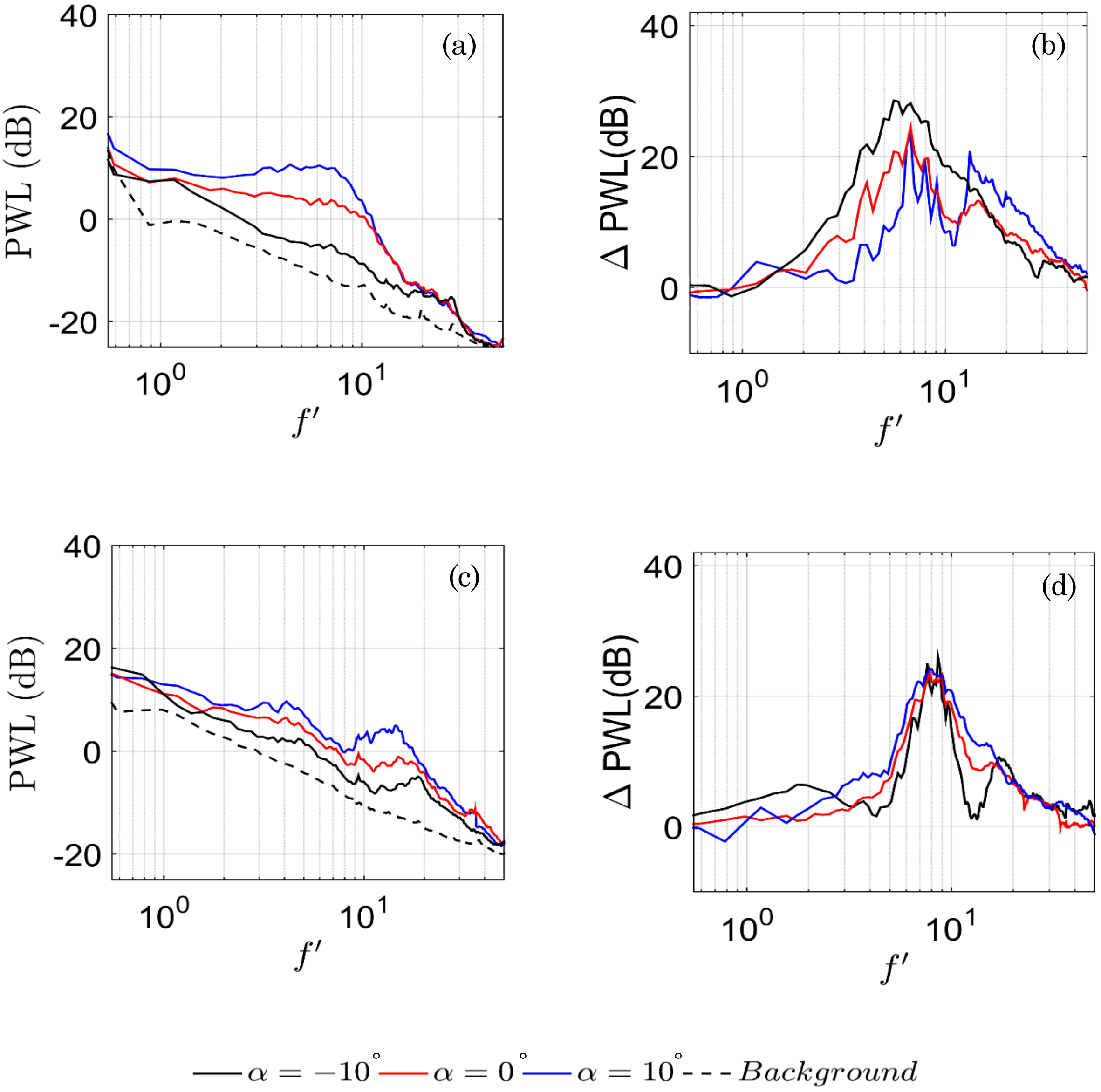

Figure B10: Comparison of PWL and ΔPWL as a function of normalised frequency f' at (a, b) U_∞ = 20 m/s and (c, d) U_∞ = 30 m/s when Tu=0.2%.

$\lambda 10A30$

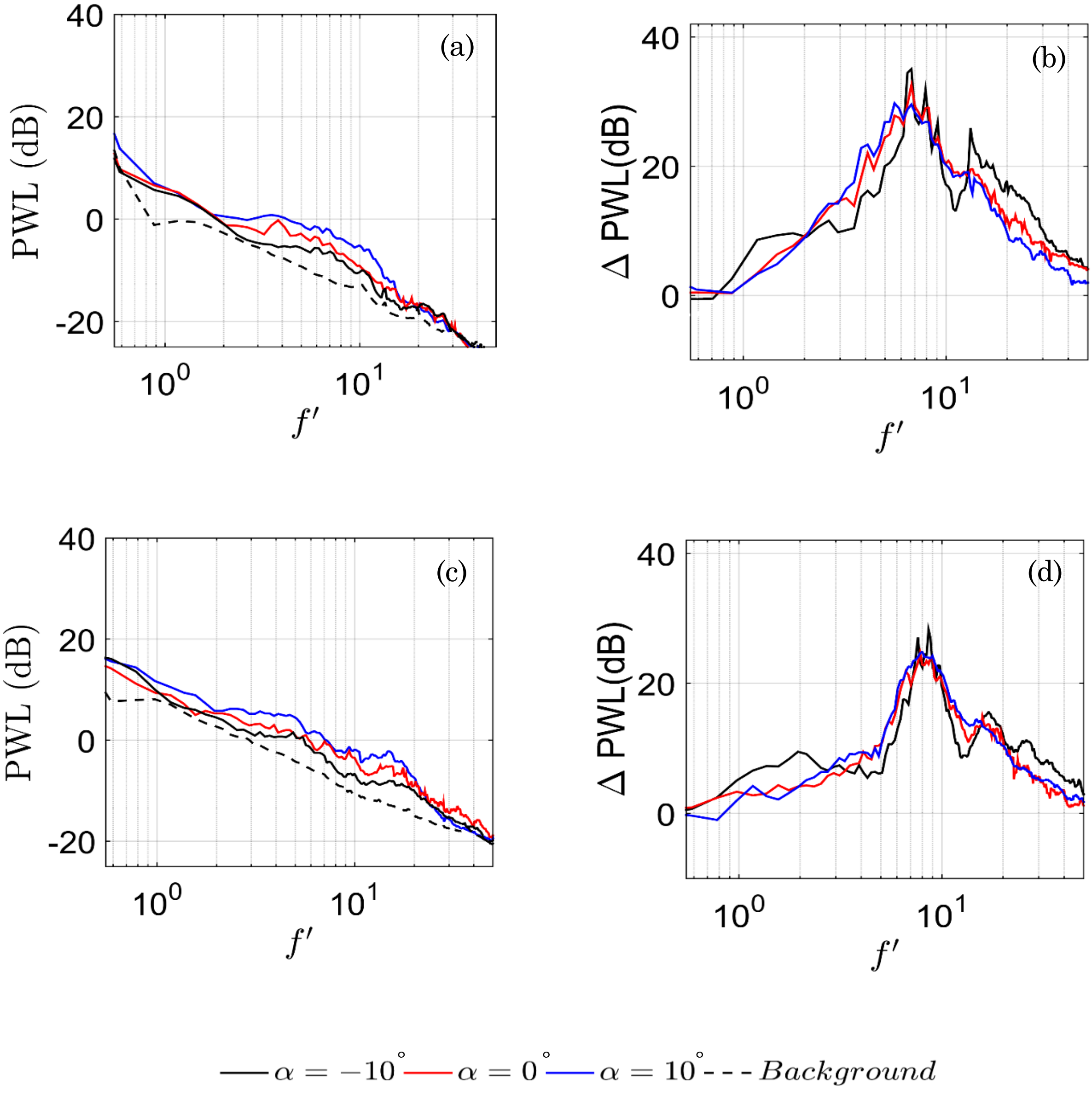

Figure B11: Comparison of PWL and ΔPWL as a function of normalised frequency f' at (a, b) U_∞ = 20 m/s and (c, d) U_∞ = 30 m/s when Tu=0.2%.